UNIVERSITY OF CALIFORNIA

Los Angeles

The Biogeochemistry of Methane Cycling and its Clumped Isotope Effects

A dissertation submitted in partial satisfaction of the

requirements for the degree Doctor of Philosophy

in Geochemistry

by

Jiarui Liu

2024

ABSTRACT OF THE DISSERTATION

The Biogeochemistry of Methane Cycling and its Clumped Isotope Effects

by

Jiarui Liu

Doctor of Philosophy in Geochemistry

University of California, Los Angeles, 2024

Professor Tina Irene Treude, Chair

Methane is a major greenhouse gas and a key component of global biogeochemical cycles. Its emissions are largely governed by microbial production and oxidation of methane. While the mechanisms and isotope effects of these processes have been extensively studied, important questions continue to arise. These include (1) the clumped isotope effects associated with microbial methane metabolisms in anoxic environments, specifically anaerobic oxidation of methane (AOM) and methanogenesis, and (2) the environmental controls on the electron acceptors involved in AOM.

The first question is addressed through a combination of laboratory microbial incubations and methane samples from natural environments. We found that with high metabolic reversibility of methanogenesis and AOM, the distribution of carbon and hydrogen isotopes among methane molecules is consistent with thermodynamic equilibrium. These near-equilibrium methane isotopologue signatures result from isotope exchange operating under conditions of near-threshold free energy, catalyzed by the methyl-coenzyme M reductase enzyme. When the thermodynamic driving force is elevated, methanogenesis and AOM can generate more negative and positive isotopologue signatures, respectively. We propose that clumped isotopes of methane provide a proxy for characterizing the bioenergetics of environments for methane production and consumption. Together, these observations demonstrate clumped isotopes of methane as a powerful tool to better understand the relation between methane metabolisms and the energy landscape in natural environments. We further applied this approach to track coupled hydrocarbon biodegradation and secondary methanogenesis in terrestrial mud volcanoes.

The second question is addressed through comprehensive porewater and solid-phase geochemical analyses, along with microbial radiotracer incubations, in hypersaline coastal wetland sediment. We demonstrate that, despite the high concentrations of sulfate, AOM is not associated with sulfate reduction but is instead coupled with the reduction of an unconventional electron acceptor—iron oxides—in subsurface sediment. This finding highlights the role of wetland sediments enriched in iron oxides as an effective sink for the greenhouse gas methane. Iron-dependent AOM in sulfate-free sediments has been extensively studied. Extending these observations into sulfate-rich sediments significantly advances the earlier observations and hypotheses, while suggesting that iron-AOM is an under-considered sink for methane in wetlands.

The dissertation of Jiarui Liu is approved.

Edward Donald Young

Edwin Arthur Schauble

Daniele Bianchi

Tina Irene Treude, Committee Chair

University of California, Los Angeles

2024

Table of Contents

List of Figures

List of Tables

Acknowledgments

I would like to express my deepest gratitude to my incredible advisors, Tina Treude and Edward Young, for introducing me to the stunning world of isotope and marine biogeochemistry. I feel incredibly fortunate to have been your student and to have had the opportunity to learn from your expertise. I am grateful for the encouragement and the freedom you gave me to explore new ideas and pursue them. Your scientific curiosity, optimism, and integrity are qualities I greatly admire and hope to emulate. With support from both of you, I have developed into a more complete researcher, and I am truly thankful for that. I look forward to continuing our journey together, unraveling the mysteries of strange isotopes and stinky mud in the future.

I also wish to thank my thesis committee members, Daniele Bianchi and Edwin Schauble, for their valuable insights and genuine interest in my projects. Many members of the EPSS department at UCLA have generously contributed their time and ideas to my research. I would particularly like to thank Sebastian Krause, Emily Klonicki, George Vetushko, Kira Homola, David Yousavich, De'Marcus Robinson, Jeana Drake, Laetitia Guibourdenche, Lauren Tafla, and Sarah Marcum for their friendship. I would like to acknowledge those who have offered valuable guidance, mentorship, or contribution throughout the course of my PhD research: William Leavitt, David Valentine, Bill Schopf, An Yin, Haolan Tang, Peng Ni, Lisa Levin, Victoria Orphan, Shana Goffredi, Peter Girguis, Andreas Teske, Barbara Sherwood Lollar, James Ferry, Jeanine Ash, Rachel Harris, Jabrane Labidi, Divya Prakash, Oliver Warr, Orhan Abbasov, Elnur Baloglanov, Qianhui Qin, and Eric Wessenauer. I would like to acknowledge the crews of the research vessel *Atlantis*, the *Alvin* submersible team, and the funding sources for my research, with particular thanks to NASA, the NSF, and the Simons Foundation.

My publications would largely be a collection of white pages if not for all the fruitful collaborations. I have had the privilege of working in several labs around the world before the start of my PhD program. I am deeply grateful to Bo Barker Jørgensen, André Pellerin, Alyssa Findlay, Hans Røy, Matthias Egger, Sasha Turchyn, Gilad Antler, Shuhei Ono, Gareth Izon, David Wang, Mandy Joye, Guangchao Zhuang, and Sabine Kasten.

I would like to express my gratitude to Jiasheng Wang, my undergraduate advisor, for introducing me to the field of marine biogeochemistry and guiding me through the early stages of my academic journey. I wish to thank many teachers and students in China who have supported me, with special thanks to Dong Feng, Zhou Wang, Xingqian Cui, Genming Luo, Chao Li, Caixiang Zhang, Jie Zhao, Qi Lin, Xiaoping Liao, Zihu Zhang, Shanggui Gong, Xudong Wang, Xiting Liu, Zhiyong Lin, and Keqing Xiao.

I feel especially fortunate to have built new and maintained old friendships along the way. To all the close friends, I particularly wish to thank Ming Zhao, Fengyu Wang, Jiawen Li, Jiahao Zhao, Xiuyuan Ding, Shujun Zhou, Bidong Zhang, Tianji Jiang, Yuxuan Li, Hanzhang Chen, Zijin Zhang, Zesen Huang, Xinyang Tong, Mingxin Qu, Ao Zhang, and Jiaqi Chen.

Finally, I want to express my heartfelt gratitude to my parents, the unsung heroes of my life. My research would not have been possible without your unconditional love and support. I feel incredibly fortunate to have such wonderful parents and to share my life with you. Although I have spent less time with you since college, I want you to know that I love you deeply, and my debt to you is beyond measure. You have always been a constant source of joy, inspiration, and guidance in my life.

To myself: great job! Remember to always *Think Big, Start Small, and Move Fast*.

Vita/Biographical Sketch

Jiarui Liu

Education

University of California, Los Angeles 2021

Master of Science in Geochemistry

China University of Geosciences (Wuhan) 2018

Bachelor of Science in Geology

Selected Publications

Liu J., Treude T., Abbasov O.R., Baloglanov E.E., Aliyev A.A., Harris C.M., Leavitt W.D. and Young E.D. (2024) Clumped isotope evidence for microbial alteration of thermogenic methane in terrestrial mud volcanoes. *Geology* **52**, 22-26 (COVER IMAGE).

Liu J., Harris R.L., Ash J.L., Ferry J.G., Krause S.J.E., Labidi J., Prakash D., Sherwood Lollar B., Treude T., Warr O. and Young E.D. (2023) Reversibility controls on extreme methane clumped isotope signatures from anaerobic oxidation of methane. *Geochimica et Cosmochimica Acta* **348**, 165-186.

Liu J., Pellerin A., Wang J., Rickard D., Antler G., Zhao J., Wang Z., Jørgensen B.B. and Ono S. (2022) Multiple sulfur isotopes discriminate organoclastic and methane-based sulfate reduction by sub-seafloor pyrite formation. *Geochimica et Cosmochimica Acta* **316**, 309-330.

Liu J., Pellerin A., Antler G., Izon G., Findlay A.J., Røy H., Ono S., Kasten S., Turchyn A.V. and Jørgensen B.B. (2021) Early diagenesis of sulfur in Bornholm Basin sediments: The role of upward diffusion of isotopically "heavy" sulfide. *Geochimica et Cosmochimica Acta* **313**, 359-377.

Liu J., Antler G., Pellerin A., Izon G., Dohrmann I., Findlay A.J., Røy H., Ono S., Turchyn A.V., Kasten S. and Jørgensen B.B. (2021) Isotopically "heavy" pyrite in marine sediments due to high sedimentation rates and non-steady-state deposition. *Geology* **49**, 816-821 (COVER IMAGE).

Liu J., Pellerin A., Antler G., Kasten S., Findlay A.J., Dohrmann I., Røy H., Turchyn A.V. and Jørgensen B.B. (2020) Early diagenesis of iron and sulfur in Bornholm Basin sediments: The role of near-surface pyrite formation. *Geochimica et Cosmochimica Acta* **284**, 43-60.

Liu J., Pellerin A., Izon G., Wang J., Antler G., Liang J., Su P., Jørgensen B.B. and Ono S. (2020) The multiple sulphur isotope fingerprint of a sub-seafloor oxidative sulphur cycle driven by iron. *Earth and Planetary Science Letters* **536**, 116165.

Liu J., Izon G., Wang J., Antler G., Wang Z., Zhao J. and Egger M. (2018) Vivianite formation in methane-rich deep-sea sediments from the South China Sea. *Biogeosciences* **15**, 6329-6348.

Selected Awards

Simons Postdoctoral Fellowships in Marine Microbial Ecology. 2025–2027.

Future Investigator in NASA Earth and Space Science and Technology (FINESST) Award, Planetary Science Division. 2021–2024.

Chapter 1: Introduction

1. Sources and sinks of methane

1.1. Overview

Methane, the simplest hydrocarbon, holds significant economic, social, and environmental importance. It is the primary constituent of natural gas, which serves as a critical energy source for electricity generation, heating, and industrial processes worldwide. Its abundance and relatively clean combustion compared to coal and oil have positioned natural gas as a key player in the global transition toward lower-carbon energy solutions (Howarth, 2014; Faramawy et al., 2016).

As a major player in the global carbon cycle, methane significantly influences the exchange of carbon among the atmosphere, oceans, and land (Reeburgh, 2007a). It is a powerful greenhouse gas and ranks as the second-largest contributor to global warming, following carbon dioxide (Mitchell, 1989; Dlugokencky et al., 2011; Nisbet et al., 2019). Its thermal potency as a greenhouse gas—approximately 30 times more effective than carbon dioxide over a 100-year period—makes it a critical factor in accelerating global warming and amplifying climate change impacts (Forster et al., 2021). Since the beginning of industrialization, methane concentration in the Earth's atmosphere has increased significantly, largely driven by human activities such as agriculture, fossil fuel production and use, and waste disposal (Fig. 1; Wuebbles and Hayhoe, 2002).

Methane has also been detected on other solar system bodies including Mars and the moons of the outer planets, where its presence holds significant implications for astrobiology (Fig. 2; Formisano et al., 2004; Yung et al., 2018). The discovery of methane elsewhere in the solar system

fuels ongoing research into whether the gas originates from geological activity or could be a potential indicator of past or present life (Lefèvre and Forget, 2009; Webster et al., 2015).

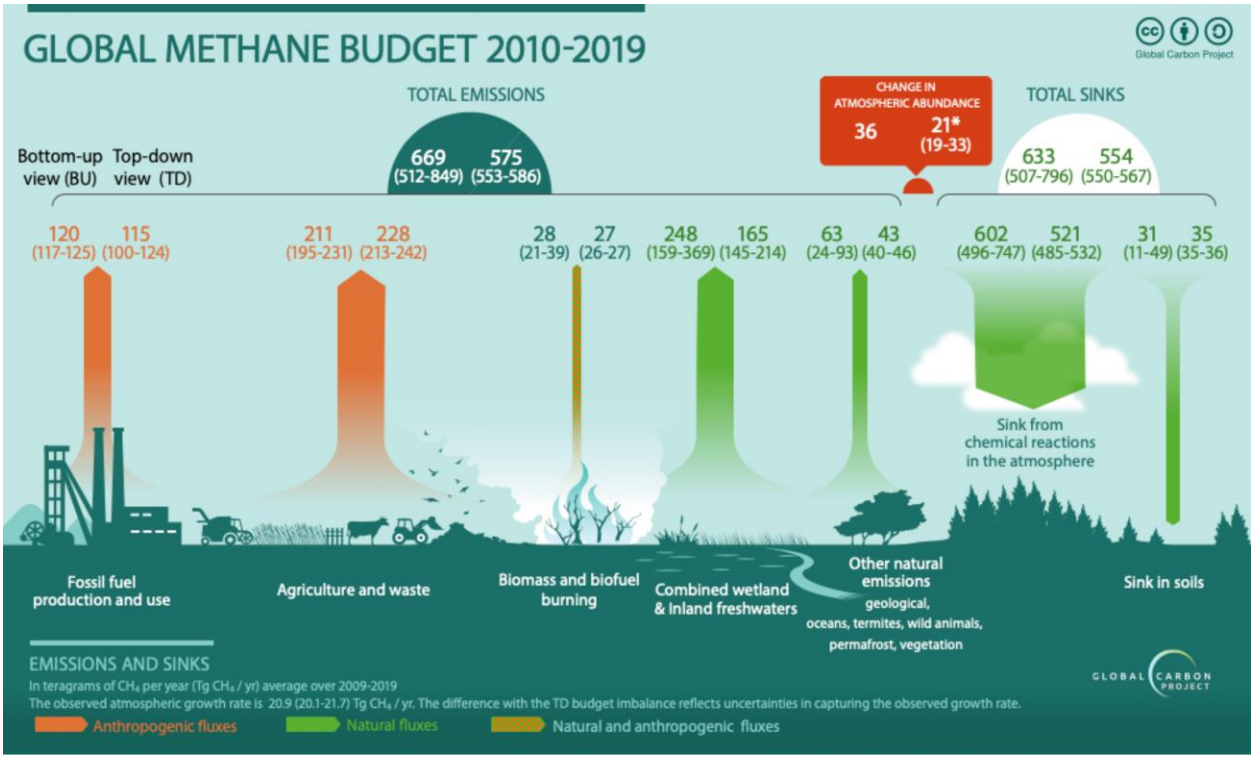

Fig. 1-1 Global Methane Budget for the 2010-2019 decade. Bottom-up estimates (left) and top-down estimates (right) are presented for each emission and sink category in Tg CH_4 yr^{-1}, along with total emissions and total sinks. Figure taken from Saunois et al. (2024).

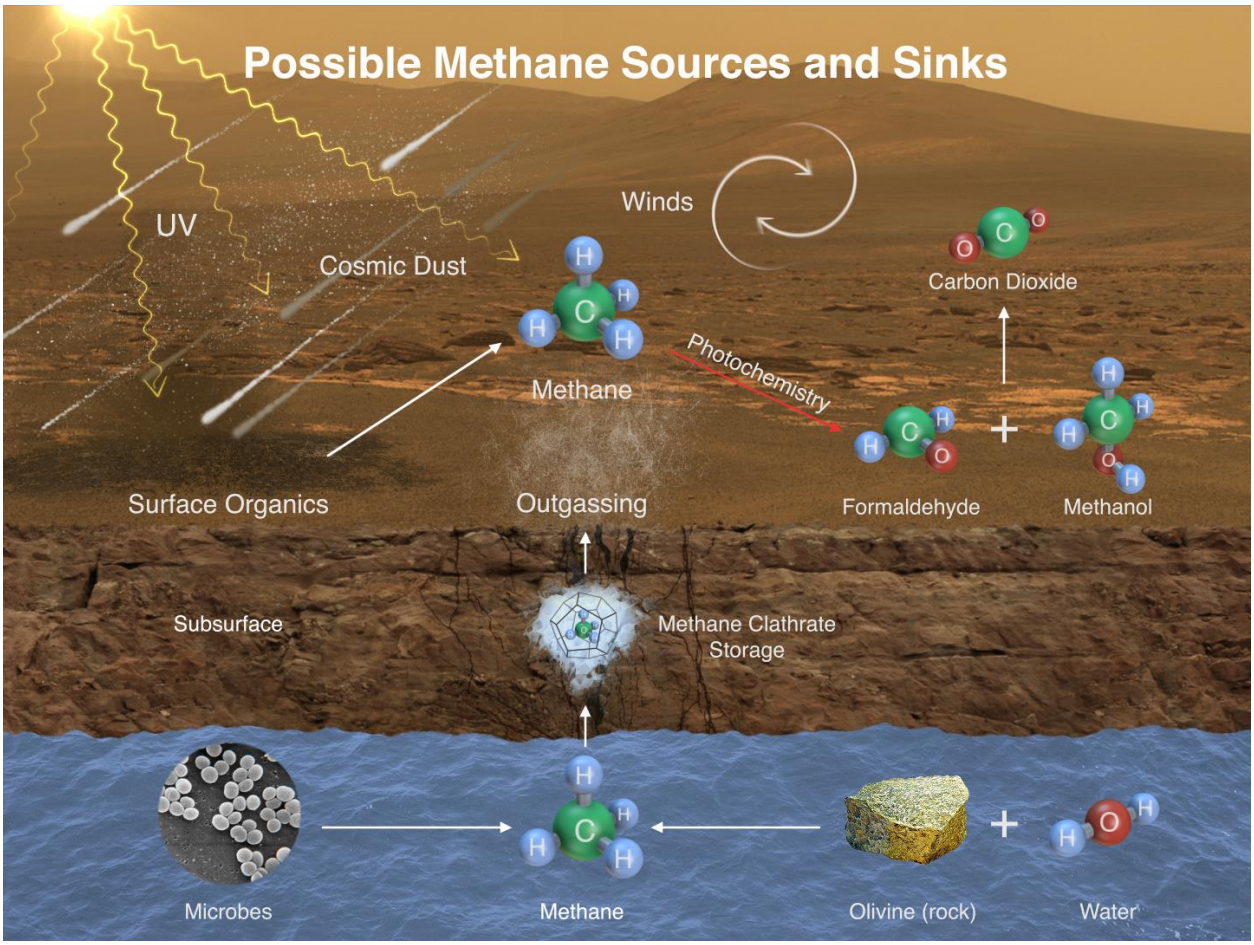

Fig. 1-2 Possible sources and sinks of methane on Mars. This illustration depicts potential processes that methane might be added to Mars' atmosphere (sources) and removed from the atmosphere (sinks). Image credit: NASA/JPL-Caltech.

1.2. Global methane budget

Methane arises from both natural sources and human activities. In 2022, the average surface dry air mole fraction of methane reached 1912 ppb in the atmosphere, which is 2.6 times higher than its estimated pre-industrial level in 1750 (Saunois et al., 2024). This rise is largely attributed to increased anthropogenic emissions. For the decade spanning 2010 to 2019, global

methane emissions were estimated at 575 Tg CH_4 per year using top-down methods, and 669 Tg CH_4 per year using bottom-up approaches (Fig. 1; Saunois et al., 2024). Approximately 60% of current methane emissions stem from human activities, with the remaining portion originating from natural processes (Kirschke et al., 2013; Saunois et al., 2020). Natural and indirect anthropogenic sources include wetlands, inland freshwater systems (lakes, ponds, reservoirs, streams, rivers), land sources (geological, wild animals, termites, wildfires, permafrost soils, vegetation), and coastal and oceanic sources (biogenic and geological) (Reeburgh, 2007a). Direct anthropogenic sources include agriculture (enteric fermentation and manure, rice cultivation), landfills and waste, fossil fuels (coal mining, oil and natural gas system), and biomass and biofuel burning (Reeburgh, 2007a). The main methane sink for atmospheric methane is photocatalytic oxidation by the hydroxyl radical (OH), mostly in the troposphere (Ehhalt, 1974). Other sinks are by photochemistry in the stratosphere (reactions with chlorine atoms (Cl) and excited atomic oxygen), by photochemistry in the marine boundary layer (reaction with Cl), and microbial aerobic oxidation in soils (Curry, 2007; Dutaur and Verchot, 2007; Thornton et al., 2010).

Notably, wetlands stand out as the predominant natural contributor to atmospheric methane globally, making them a significant focal point in addressing climate change concerns (Bartlett and Harriss, 1993; Bridgham et al., 2013). Wetlands are characterized by ecosystems featuring water-saturated or inundated soils or peats, where anaerobic conditions beneath the water table foster the production of methane and significantly influence soil biogeochemistry and ecosystem species composition (Matthews and Fung, 1987). These vital ecosystems also provide essential services, such as water filtration, flood protection, and habitat for diverse wildlife, making them crucial for maintaining ecological balance and supporting human livelihoods (Mitsch and Gosselink, 2000).

Methane emissions are dictated by its production and oxidation. In the following sections, I will discuss the microbial pathways involved in both the production and consumption of methane by microorganisms, which apply to wetlands as well as a range of other environments on Earth.

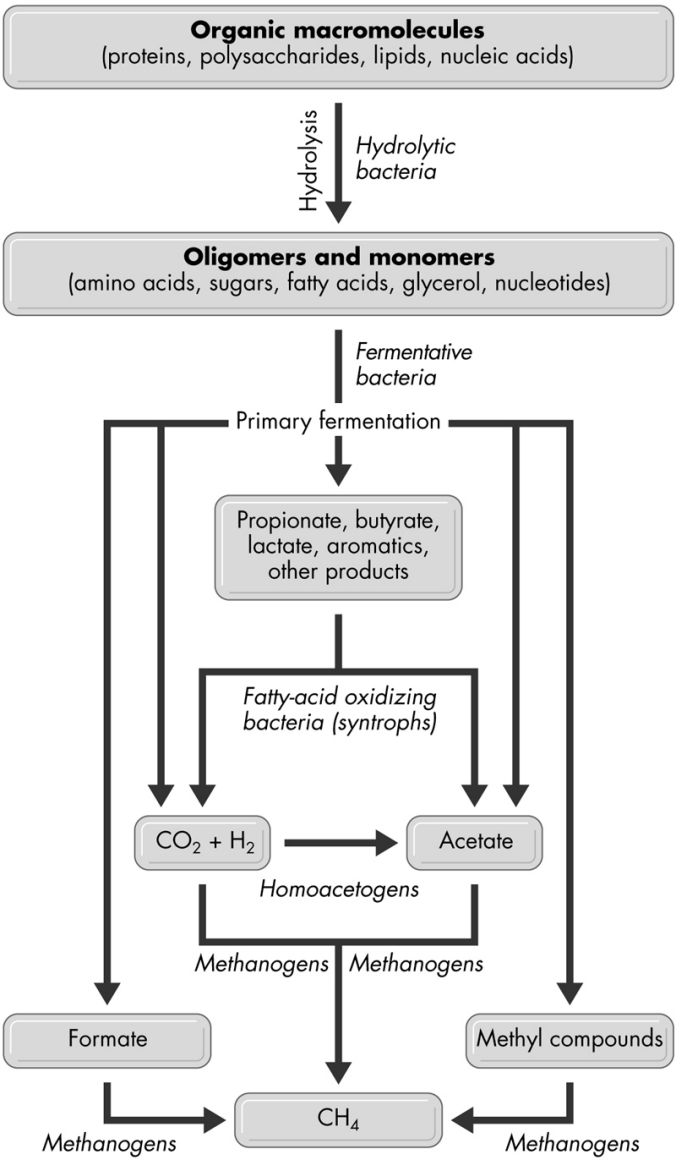

Fig. 1-3 The overall process of organic matter degradation to methane. Complex organic macromolecules are gradually broken down into simpler substrates, and ultimately converted to methane, through the cooperative interactions of multiple species within a syntrophic community. Figure taken from Konhauser (2009).

1.3. Microbial methanogenesis

Methanogenesis is the biological process through which methane is produced, primarily by microorganisms known as methanogenic archaea (Fig. 3). These archaea thrive in anaerobic environments, such as sediments, landfills, and the guts of ruminant animals, where they convert organic matter into methane (Thauer et al., 2008). This process is a crucial component of the global carbon cycle, playing a significant role in both energy production and greenhouse gas emissions. Microbial methanogenesis contributes more than half of annual emissions to the atmosphere (Kirschke et al., 2013; Saunois et al., 2020).

Methanogenic archaea use a range of substrates to produce methane under anoxic conditions (Reeburgh, 2007a). Three primary pathways for methanogenesis are known based on the types of carbon sources catabolized: hydrogenotrophic methanogenesis, which uses carbon dioxide and hydrogen; acetoclastic methanogenesis, which relies on acetate; and methylotrophic methanogenesis, which utilizes methylated compounds, such as methanol and methylamines (Thauer et al., 2008; Welte and Deppenmeier, 2014; Vanwonterghem et al., 2016). In sulfate-rich environments, sulfate-reducing bacteria often outcompete methanogens for common substrates, such as hydrogen and acetate, and thus suppress hydrogenotrophic and acetoclastic methanogenesis, due to their greater affinity and higher energy yield (Lovley and Klug, 1983; Jørgensen, 2021). As a result, microbial methane production is commonly found in the deeper layers of marine sediments, where sulfate levels are low and sulfate reduction is absent, allowing methane to accumulate below the penetration depth of sulfate.

While hydrogenotrophic and acetoclastic methanogenesis is largely suppressed in sulfate-reducing zones, methanogenesis can persist through methylotrophic pathways, as methanogens can use a range of methylated compounds that sulfate-reducing bacteria typically do not

metabolize (Oremland et al., 1982; Lovley and Klug, 1986; Maltby et al., 2016; Zhuang et al., 2016; Xiao et al., 2018; Krause and Treude, 2021). Therefore, the distribution and activity of methanogens in sediments are shaped not only by their competition with sulfate-reducing bacteria for hydrogen and acetate but also by the availability of these non-competitive methylated substrates.

Figure 4 illustrates the key metabolic pathways involved in methanogenesis. In the hydrogenotrophic pathway, carbon dioxide is reduced to methane through seven consecutive enzymatic reactions, involving four reduction steps facilitated by the electron carriers ferredoxin, coenzyme F_{420}, and coenzyme B (Thauer et al., 2008). In acetoclastic methanogenesis, acetate is first converted to acetyl-CoA, after which its methyl group is transferred to tetrahydromethanopterin and enters the hydrogenotrophic pathway, while the carbonyl group is oxidized to carbon dioxide (Welte and Deppenmeier, 2014). In the methylotrophic pathway, the methyl group is transferred directly from methanol to coenzyme B, forming methyl coenzyme M. This intermediate is then either reduced to methane or oxidized to carbon dioxide, typically occurring at a ratio of approximately 3:1 (Vanwonterghem et al., 2016). Methyl-coenzyme M reductase (MCR) is the essential enzyme in microbial methane production, used by all methanogenic archaea (Ermler et al., 1997). It catalyzes the exergonic reaction that converts methylcoenzyme M and coenzyme B into methane, along with the formation of the heterodisulfide of coenzyme M and coenzyme B.

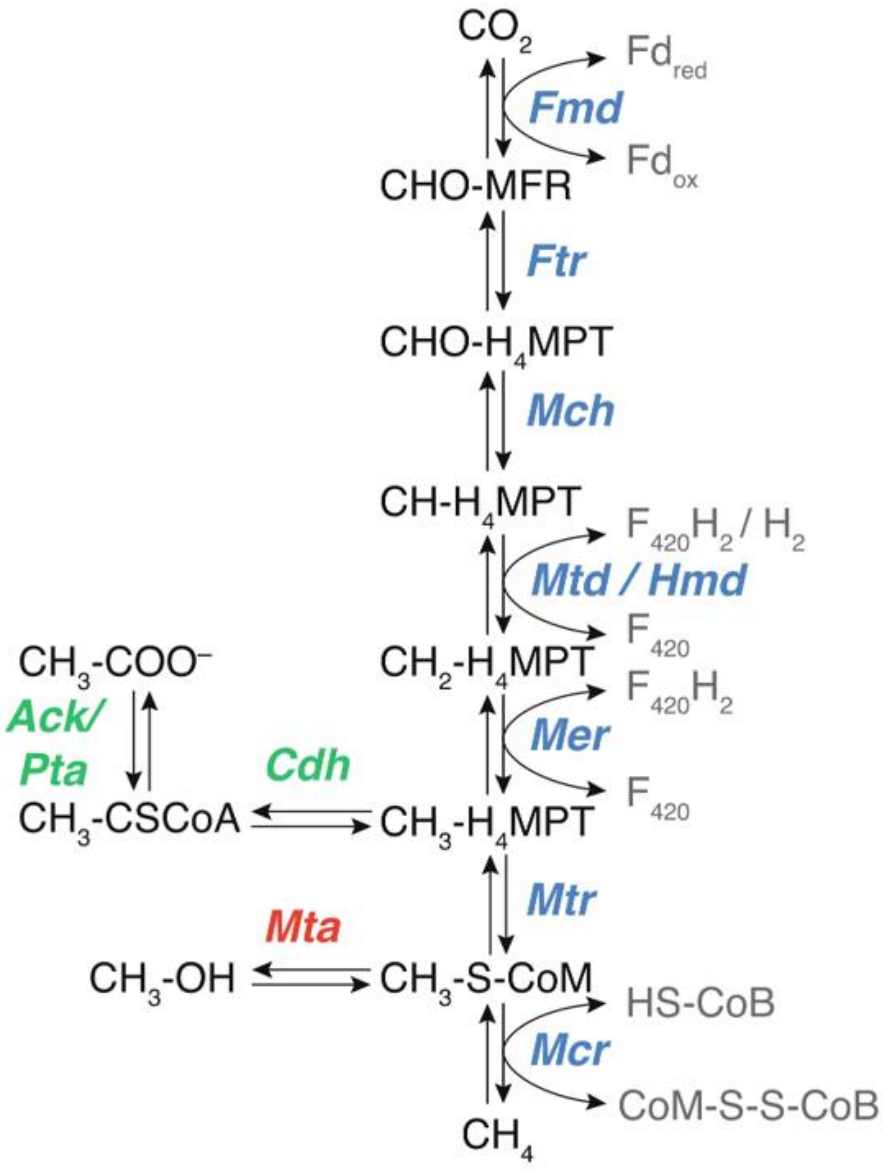

Fig. 1-4 Metabolic pathways of methanogenesis and anaerobic oxidation of methane. Metabolites are shown in black, electron carriers in gray, and enzymes in bold, italicized colored fonts. Reactions specific to the acetoclastic pathway are highlighted in green, while those unique to the methylotrophic pathway are in red. Reactions in blue represent the hydrogenotrophic and anaerobic oxidation pathways, which overlap with both the acetoclastic and methylotrophic pathways. All reactions are assumed to be potentially fully reversible. Figure taken from Gropp et al. (2021).

Aside from the three common groups of methanogenic substrates, recent studies have demonstrated that methanogens can independently produce methane from complex methoxylated aromatic compounds and oil hydrocarbons without relying on syntrophic partnership (Mayumi et al., 2016; Zhou et al., 2022). Methoxydotrophic methanogenesis likely plays a key role in the formation of coal-bed methane by breaking down aromatic compounds derived from lignin, while alkylotrophic methanogens may have a crucial role in converting petroleum compounds into methane.

A group of aerobic phytoplankton can also generate methane in oxygenated water bodies (Karl et al., 2008; Repeta et al., 2016). Methane concentrations in near-surface waters across much of the global ocean are often supersaturated relative to the atmosphere, suggesting in-situ methanogenesis and a net release of methane into the atmosphere (Lamontagne et al., 1973). Several hypotheses have been suggested to explain the methane supersaturation observed in surface ocean. The aerobic degradation of methyl compounds, such as methylphosphonate (via C-P lyase), dimethylsulfoniopropionate, or methylamines, along with non-enzymatic methane formation driven by reactive oxygen species and free iron, have been proposed as key mechanisms promoting methane production in oxic aquatic environments (Karl et al., 2008; Repeta et al., 2016; Ernst et al., 2022).

1.4. Methanotrophy

Microbial oxidation of methane, a.k.a. “methanotrophy,” can be categorized into the aerobic oxidation of methane (AeOM) and the anaerobic oxidation of methane (AOM). Aerobic oxidation is carried out by a group of bacteria that use oxygen to convert methane into carbon

dioxide and water. These methane-oxidizing bacteria thrive in oxic sediments and water columns of most marine and freshwater environments where oxygen is present (Oremland and Culbertson, 1992; Ding and Valentine, 2008; Rahalkar et al., 2009; Steinle et al., 2015; Mao et al., 2022). Methane entering the water column or surface soil may undergo partial or complete aerobic oxidation before eventually being released into the atmosphere (Le Mer and Roger, 2001; Chowdhury and Dick, 2013).

Aerobic methanotrophs are classified into three main groups, Type I, Type II, and Type X, based on their phylogeny, carbon assimilation pathways, and intracellular membrane structures (Bowman, 2006). Types I and X methanotrophs belong to the class Gammaproteobacteria and use the Ribulose Monophosphate (RuMP) pathway to incorporate formaldehyde into biomass, while Type II methanotrophs, classified under Alphaproteobacteria, use the Serine pathway for this purpose (Hanson and Hanson, 1996). Recently, the isolation of thermophilic, acidophilic methanotrophs from the phylum Verrucomicrobia has expanded the taxonomic and physiological diversity of aerobic methanotrophy (Murrell, 2010). The initial step of aerobic oxidation, where methane is converted to methanol, is catalyzed by the enzyme methane monooxygenase, which exists in either a soluble or particulate form (Stanley et al., 1983; Prior and Dalton, 1985; Ross and Rosenzweig, 2017).

Methane can be oxidized by AOM in anoxic environments, depending on the availability of electron acceptors (Knittel and Boetius, 2009; Chadwick et al., 2022). Geochemical and microbiological evidence, together with mass balance calculations, suggest that AOM efficiently consumes over 90% of the methane produced in marine sediments, thereby significantly reducing the atmospheric methane efflux from the ocean (Reeburgh, 2007b). AOM operates through a modified reverse-methanogenesis pathway, using the same enzymes involved in hydrogenotrophic

methanogenesis to catalyze methane oxidation (Thauer, 2011; Timmers et al., 2017). Common electron acceptors for AOM include sulfate, metal oxides, nitrate, nitrite, and humic substances (Beal et al., 2009; Knittel and Boetius, 2009; Ettwig et al., 2010; Haroon et al., 2013; Scheller et al., 2016).

Sulfate-dependent AOM is ubiquitous in coastal and marine environments. In methane-rich marine sediments, methane diffusing upward reacts with sulfate diffusing downward, fueling sulfate reduction coupled to AOM at the sulfate-methane transition zone (Martens and Berner, 1977; Niewöhner et al., 1998; Borowski et al., 1999; Treude et al., 2005). Sulfate-driven AOM is typically performed by consortia of anaerobic methanotrophic (ANME) archaea and sulfate-reducing bacteria (Hinrichs et al., 1999; Boetius et al., 2000; McGlynn et al., 2015; Wegener et al., 2015). One of the most intriguing aspects of ANME metabolism is the mechanism of electron transfer between ANME and their sulfate-reducing partners (e.g., Chadwick et al., 2022). This interspecies electron transfer seems to necessitate the formation of unique multicellular aggregates involving both microorganisms (e.g., Knittel and Boetius, 2009). Earlier investigations proposed mechanisms for AOM syntrophy based on the diffusion of small molecules, such as hydrogen, acetate, and zero-valent sulfur (Hoehler et al., 1994; Valentine and Reeburgh, 2000; Milucka et al., 2012). Subsequent studies have demonstrated that direct interspecies electron transfer occurs through electrical connections involving multiheme cytochrome c proteins and pili nanowire structures (McGlynn et al., 2015; Wegener et al., 2015).

AOM can also be coupled to the reduction of various heavy metals, such as Fe(III), Mn(IV), Cr(VI), As(V), and Se(VI) (Beal et al., 2009; He et al., 2018; Shi et al., 2020). Fe-mediated AOM can be performed by methanotrophs, such as ANME-2d archaea ("*Ca. Methanoperedens*"), which oxidize methane nonsyntropically, exploiting soluble, nanophase, or solid-phase ferric Fe as

electron acceptors (Ettwig et al., 2016; Scheller et al., 2016; Cai et al., 2018; Yan et al., 2018). Similar to sulfate-driven AOM, electrons can be shuttled to Fe(III) via membrane-bound cytochromes (Scheller et al., 2016). Incubation experiments demonstrated that Fe-AOM has the potential to reduce a range of solid-phase ferric Fe, from highly reactive Fe oxides such as ferrihydrite to poorly reactive Fe minerals such as hematite and magnetite (Beal et al., 2009; Bar-Or et al., 2017). By employing tracer incubation of sediment slurries, modeling of porewater profiles and the identification of authigenic minerals, the presence of Fe-AOM has been documented in diverse aquatic settings, encompassing both marine and freshwater environments (Beal et al., 2009; Sivan et al., 2011; Wankel et al., 2012; Norði et al., 2013; Riedinger et al., 2014; Treude et al., 2014; Egger et al., 2015; Liu et al., 2018; Aromokeye et al., 2020).

Nitrate- and nitrite-dependent AOM has mainly been observed in freshwater environments (e.g., Raghoebarsing et al., 2006). Nitrate-dependent AOM is mediated by specific members of the ANME clade (ANME-2d, "*Ca. Methanoperedens*"), operating in a syntrophic relationship with nitrite consumers or performing denitrification independently (Haroon et al., 2013; Yao et al., 2024). Nitrite-dependent AOM, on the other hand, is performed by oxygen-producing intra-aerobic bacteria known as "*Methylomirabilis oxyfera*" from the NC10 group, which reduce nitrite and concurrently produce oxygen as an intermediate, facilitating the oxidation of methane (Ettwig et al., 2010). Humic substances, such as anthraquinone 2,6-disulfonate (AQDS), have been employed as electron sinks for AOM in short-term experiments, whereas their environment significance is yet to be thoroughly investigated (Scheller et al., 2016; Bai et al., 2019; Yu et al., 2022).

2. Methane clumped isotopologues

2.1. Early research on the origins of methane

Naturally occurring methane originates from three primary sources: microbial, thermogenic, and abiotic. Microbial methane is produced through microbial degradation of organic matter, while thermogenic methane forms via the thermocatalytic decomposition of organic material (e.g., Reeburgh, 2007a). Primary microbial gas is generated from dispersed organic matter in relatively shallow sediments, whereas secondary microbial gas results from the biodegradation of petroleum accumulations (e.g., Milkov, 2011). Abiotic methane is produced by magmatic and gas-water-rock reactions, such as the Sabatier reaction and serpentinization (e.g., Etiope and Sherwood Lollar, 2013).

The origins of methane are commonly inferred using diagrams plotting molecular ratios of alkanes against the bulk carbon ($^{13}C/^{12}C$) and hydrogen (D/H) isotopic compositions of methane. The diagram of $\delta^{13}C\text{-}CH_4$ versus $C_1/(C_2 + C_3)$ is one of the most commonly used tools for interpreting the origin of hydrocarbon gases (Fig. 5). This diagram was first presented by Bernard et al. (1976) and Bernard et al. (1977) (Fig. 5A). The empirical genetic fields were further refined by Whiticar (1999) and Milkov and Etiope (2018) as additional experimental and field data come to light (Fig. 5B–C).

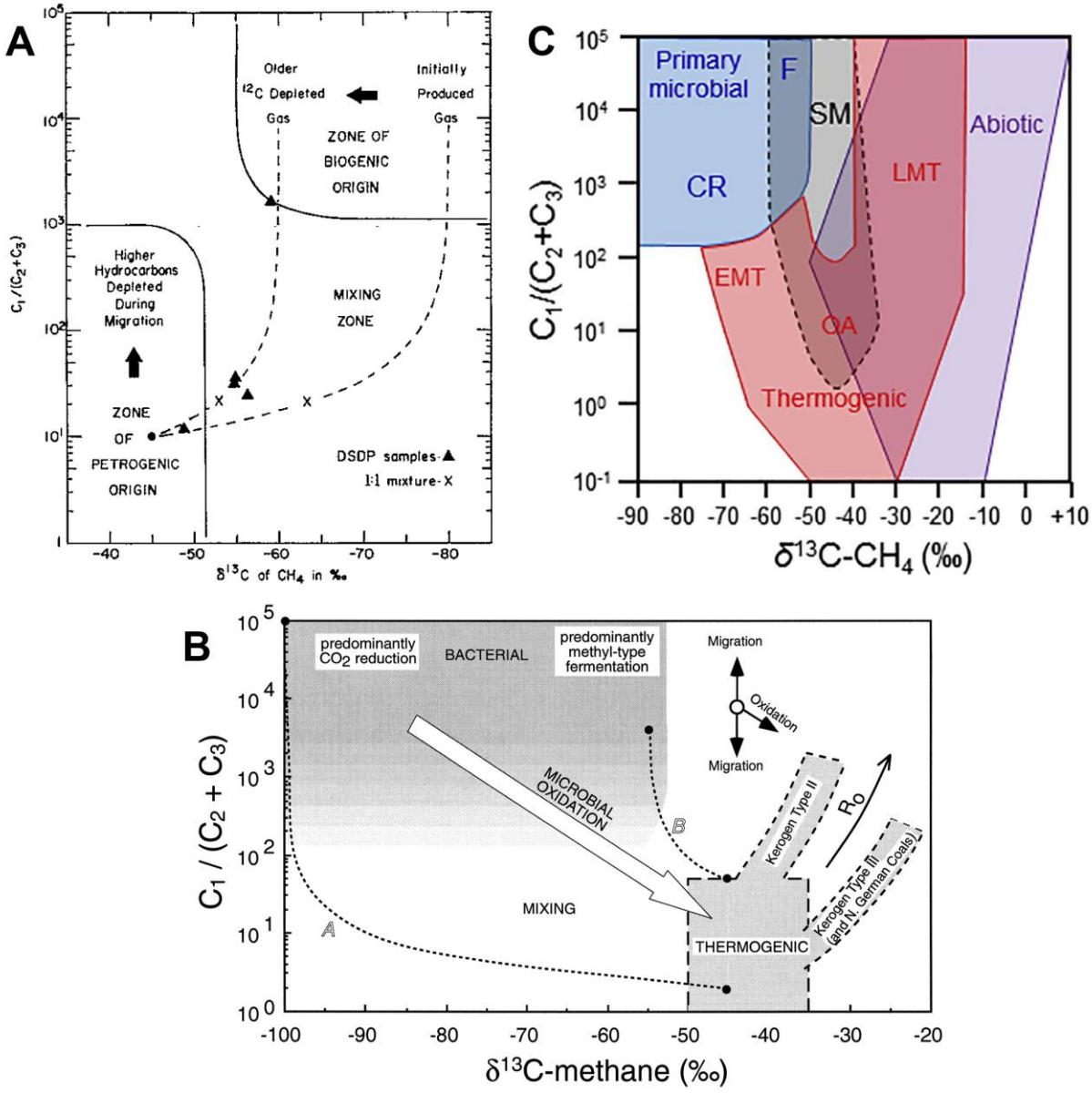

Fig. 1-5 Genetic diagrams of δ^{13}C-CH_4 versus $C_1/(C_2 + C_3)$. Panels A–C taken from Bernard et al. (1977), Whiticar (1999), and Milkov and Etiope (2018), respectively.

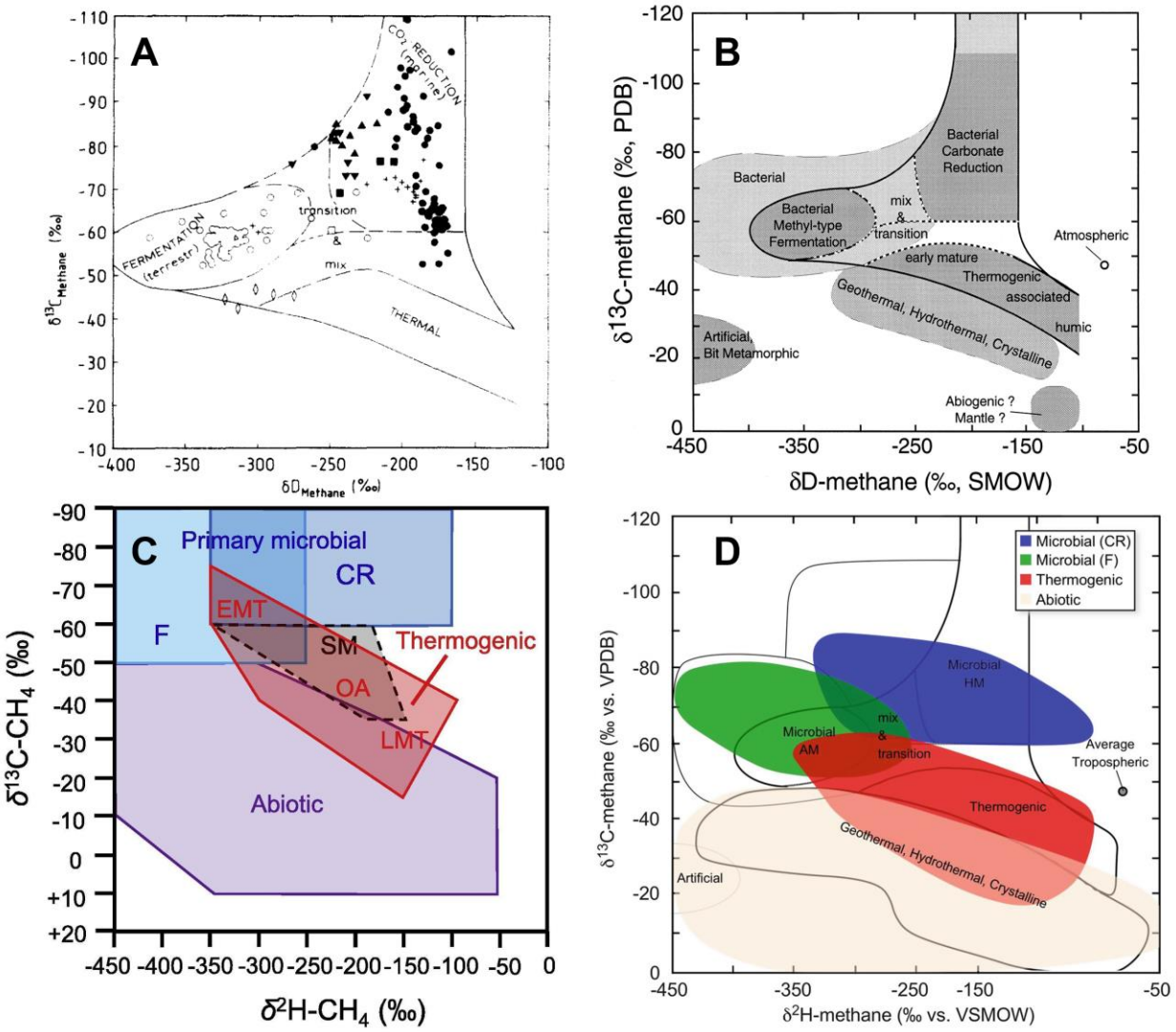

Fig. 1-6 Methane genetic diagrams based on $\delta^{13}C$-CH_4 versus δD-CH_4. Panels A–D taken from Whiticar et al. (1986), Whiticar (1999), Milkov and Etiope (2018), and Whiticar (2020), respectively.

Strong isotopic discrimination during methane formation has driven the extensive application of conventional stable carbon and hydrogen isotope ratios in distinguishing microbial from thermogenic and abiotic methane (Fig. 6). Schoell (1980, 1983) suggested interpreting the

origin of hydrocarbon-bearing gases using a genetic diagram based on $\delta^{13}C$ and δD of methane. Whiticar et al. (1986) and Whiticar (1999) later revised this diagram by simplifying the field of thermogenic gases and distinguishing between microbial methane produced through hydrogenotrophic and acetoclastic methanogenesis. These isotopic tools also facilitate the construction of global methane budgets and the assessment of methane's climatic impacts (Nisbet et al., 2016; Schwietzke et al., 2016). However, these molecular ratio and bulk isotope approaches relies predominantly on empirical observations, and distinct origins of methane often result in overlapping characteristic isotope signals (Fig. 6; Milkov and Etiope, 2018; Whiticar, 2020). Furthermore, empirical fields in $\delta^{13}C$ vs. δD space are linked to the isotopic signature of the source materials coupled with the formation processes, which are strongly affected by mixing and secondary alteration processes (Etiope and Sherwood Lollar, 2013).

2.2. Fundamentals of methane isotopologues

Beyond conventional bulk isotope ratios, the exploration of doubly substituted "clumped" isotopologues has emerged as a cutting-edge approach for understanding methane sources and sinks (Stolper et al., 2014a; Wang et al., 2015; Young et al., 2017). This innovative method capitalizes on recent advances in high-resolution gas-source isotope ratio mass spectrometry and spectroscopic techniques, unlocking a wealth of previously inaccessible information contained in the distribution of isotopes among methane molecules (Ono et al., 2014; Stolper et al., 2014b; Young et al., 2016). An isotopologue is a molecular entity that differs only in isotopic composition (i.e., number of isotopic substitutions). For example, $^{13}CH_4$ and $^{12}CH_3D$ are "singly substituted" isotopologues and $^{13}CH_3D$ and $^{12}CH_2D_2$ are "doubly substituted" isotopologues (Fig. 7). Doubly

substituted isotopologues are less abundant compared to singly substituted isotopologues in natural systems (Table 1).

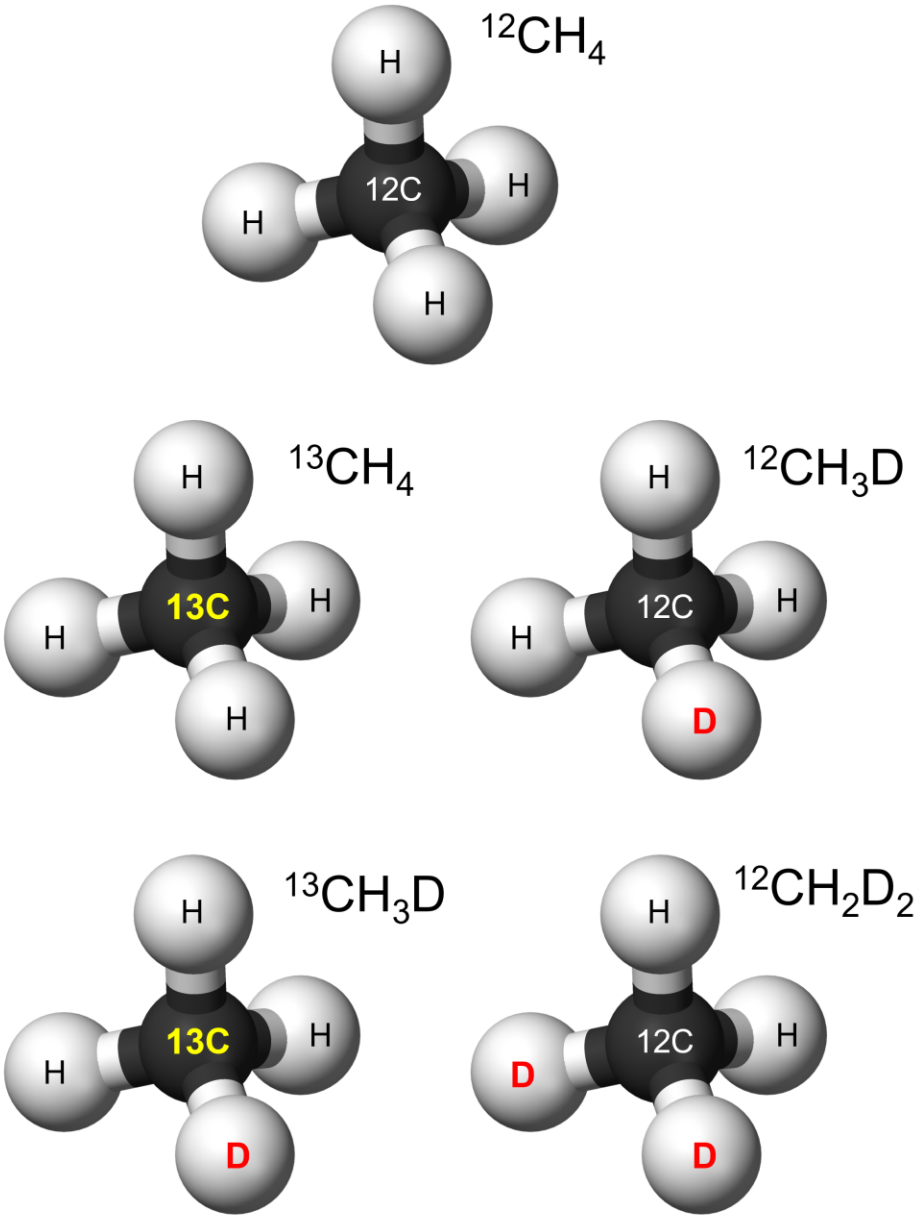

Fig. 1-7 **Ball-and-stick models of methane isotopologues.** The mass-16, -17, and -18 isotopologues are shown from top to bottom.

Table 1-1 Relative abundances and masses of the isotopologues of methane (Stolper et al., 2014b).

Cardinal mass	Isotopologue	Proportional relative abundance of CH_4*	Exact mass (amu)
16	$^{12}CH_4$	$9.88^{*}10^{-1}$	16.031
17	$^{13}CH_4$	$1.11^{*}10^{-2}$	17.035
	$^{12}CH_3D$	$6.16^{*}10^{-4}$	17.038
18	$^{13}CH_3D$	$6.92^{*}10^{-6}$	18.041
	$^{12}CH_2D_2$	$1.44^{*}10^{-7}$	18.044
19	$^{13}CH_2D_2$	$1.62^{*}10^{-9}$	19.047
	$^{12}CHD_3$	$1.49^{*}10^{-11}$	19.050
20	$^{13}CHD_3$	$1.68^{*}10^{-13}$	20.053
	$^{12}CD_4$	$5.82^{*}10^{-16}$	20.056
21	$^{13}CD_4$	$6.54^{*}10^{-18}$	21.060

* Assumes that isotopes are randomly distributed throughout all isotopologues and that $\delta^{13}C = 0‰$ and $\delta D = 0‰$ (relative to VPDB and VSMOW respectively).

A methane molecule that contains a "clump" of two heavy, stable isotopes is more thermodynamically stable than those with only one heavy isotope (carbon-13 and/or deuterium). The increased stability arises from the reduction in vibrational frequency, caused by the presence of two heavy isotopes together. The vibrational frequency, ν, is inversely proportional to the square root of the reduced mass, μ, which is greater for bonds involving heavy isotopes: $\nu \propto \mu^{-1/2}$ (Wang et al., 2004; Eiler, 2007; Young et al., 2025). The reduction in energy is most pronounced at lower temperatures, making the clumping of heavy isotopes strongly dependent on temperature. For example, $^{13}CH_3D$ is slightly more stable at low temperature than $^{12}CH_3D$. The slight increase in stability leads to a higher abundance of the multiply substituted isotopologue as temperature decreases (Fig. 8; Ma et al., 2008; Webb and Miller, 2014; Liu and Liu, 2016). The relative abundances of doubly substituted methane isotopologues are expressed as $\Delta^{13}CH_3D$ and $\Delta^{12}CH_2D_2$

values (Equations 1 and 2), representing deviations from a stochastic standard in which distributions of isotopes across all isotopologues are effectively random (Fig. 8). The latter is the expected state at sufficiently high temperatures (>1000 K). If isotopic equilibration is not reached, kinetic isotope fractionation of clumped isotopologues may generate signatures diagnostic of specific reaction mechanisms (Eiler, 2007; Young et al., 2025).

$$\Delta^{13}CH_3D = [(^{13}CH_3D\ /^{12}CH_4)_{sample}/(^{13}CH_3D\ /^{12}CH_4)_{stochastic} - 1] \times 1000 \quad (1)$$

$$\Delta^{12}CH_2D_2 = [(^{12}CH_2D_2/^{12}CH_4)_{sample}/(^{12}CH_2D_2/^{12}CH_4)_{stochastic} - 1] \times 1000 \quad (2)$$

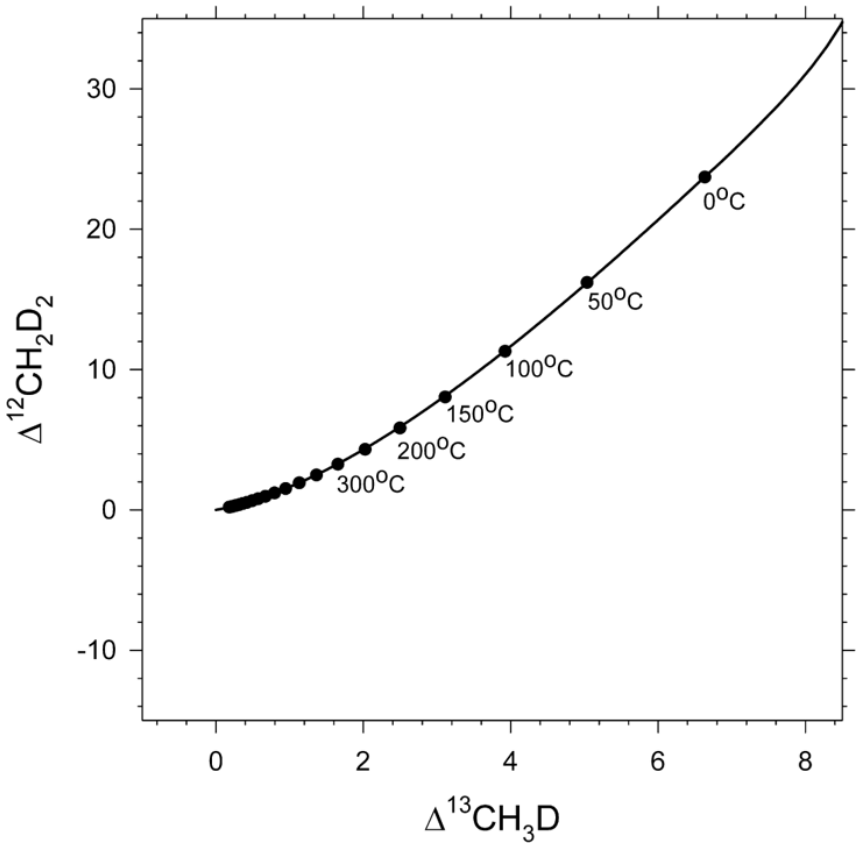

Fig. 1-8 Thermodynamic equilibrium curve in $\Delta^{13}CH_3D$ versus $\Delta^{12}CH_2D_2$ space, with both axes expressed in per mil. Figure taken from Young et al. (2017).

The significance of clumped isotopologues lies in the fact that their distribution offers an intra-molecular or intra-phase isotope signal, without needing to reference other species (Young et al., 2025). In contrast, stable isotope ratios typically require comparison with ratios in a different phase or molecule for interpretation. In other words, isotopic bond ordering, or "clumping", is a tracer for the processes involved in the formation of molecules, as well as subsequent consumption or re-equilibration. This unique characteristic makes clumped isotopologues a powerful tool for investigating methane formation and oxidation processes, both on Earth and beyond (Young, 2019).

2.3. Clumped isotope effects of methane sources and sinks

The abundances of clumped isotopologues in thermogenic methane make it possible to record its formation temperatures of approximately 100–250 °C at which C–H bonds reached equilibrium (Fig. 9; Stolper et al., 2014a; Young et al., 2017; Xie et al., 2021). The abundances of clumped isotopologues of microbial methane, on the other hand, differ from thermodynamic equilibrium in cultures and in non-marine natural environments, meaning that their distribution does not reflect the temperature at which the methane was formed (Fig. 9; Stolper et al., 2015; Wang et al., 2015; Douglas et al., 2016; Young et al., 2017; Gruen et al., 2018; Giunta et al., 2019). Meanwhile, microbial methanogenesis in some environments, especially in marine sediments, appears to generate methane that approaches thermodynamic equilibrium at low temperatures (Fig. 9; Stolper et al., 2015; Wang et al., 2015). The $\Delta^{13}CH_3D$ and $\Delta^{12}CH_2D_2$ values of microbial methane can be modeled as the result of the combination of equilibrium and kinetic isotope effects, as well as the combinatorial effect, during the enzymatically facilitated formation of methane (Yeung, 2016; Cao et al., 2019; Young, 2019; Taenzer et al., 2020; Gropp et al., 2022; Ono et al., 2022).

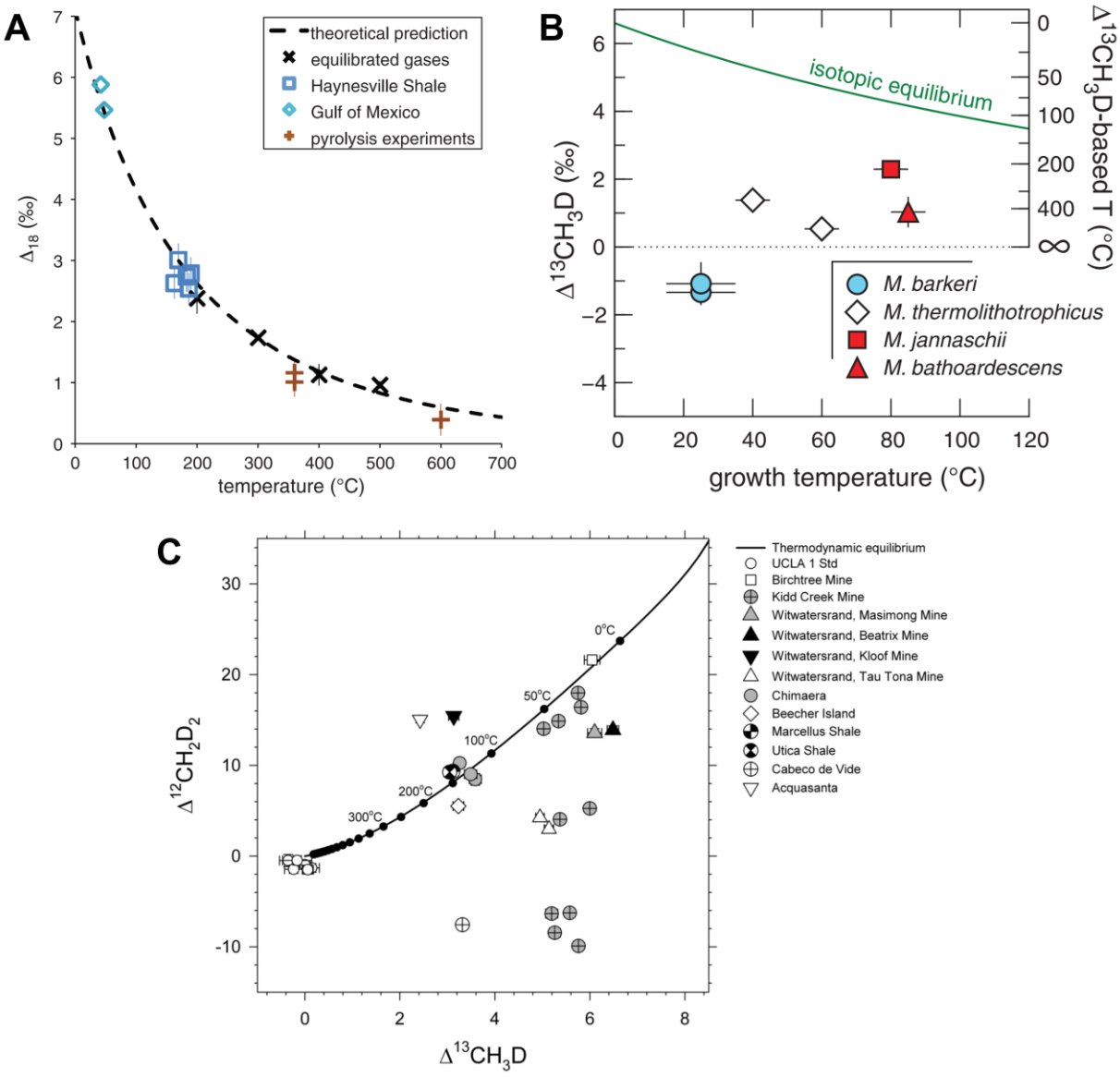

Fig. 1-9 Different approaches to investigate mass-18 methane isotopologues. (A) Formation/reservoir temperatures versus Δ_{18} values. (B) $\Delta^{13}CH_3D$ values of methane produced by hydrogenotrophic methanogens in batch cultures. (C) $\Delta^{13}CH_3D$ versus $\Delta^{12}CH_2D_2$ of various natural samples. Panels A–C taken from Stolper et al. (2014a), Wang et al. (2015), and Young et al. (2017), respectively.

While the ability to define a methane isotopologue signature related to microbial methanogenesis is promising, there are caveats. One is that abiotic methane and low-maturity thermogenic methane has been found with deficits in $\Delta^{12}CH_2D_2$ compared with equilibrium values in methane gas (Young et al., 2017; Dong et al., 2021; Warr et al., 2021; Xie et al., 2021). The extremely negative $\Delta^{12}CH_2D_2$ values are a result of the combinatorial effect during the formation of microbial, thermogenic, and abiotic methane. This effect is a mathematical consequence of incorporating multiple isotopic pools of a given element during the construction of a molecule (Röckmann et al., 2016; Yeung, 2016). For methane, using hydrogen from multiple pools with different D/H ratios to construct the molecule can result in negative $\Delta^{12}CH_2D_2$ values (Young et al., 2017). The effect has been experimentally confirmed for methane in the laboratory (Taenzer et al., 2020; Dong et al., 2021).

After methane formation, both biotic and abiotic consumption processes have the potential to modify the relative abundances of clumped isotopologues. This alteration could simulate the presumed microbial methanogenesis signature, introducing a layer of complexity in discerning the true origin of methane. For example, AOM exhibits both kinetic and equilibrium behaviors. Remarkably high $\Delta^{13}CH_3D$ and $\Delta^{12}CH_2D_2$ values have been observed in both laboratory AOM incubations and natural settings exhibiting vigorous AOM activity (Ono et al., 2021; Giunta et al., 2022). When AOM is less active, thermodynamic isotopic bond-order equilibrium is achieved in methane from deep subsurface sediments (Ash et al., 2019).

Another major microbial methane sink occurs through aerobic oxidation. Laboratory experiments reveal that methane oxidation with oxygen is accompanied by significant shifts in methane clumping. The clumped isotopologue fractionations result in either distinctly negative $\Delta^{13}CH_3D$ and $\Delta^{12}CH_2D_2$ values within a Rayleigh-type closed system or markedly positive

$\Delta^{12}CH_2D_2$ with unchanging $\Delta^{13}CH_3D$ values in a steady state characterized by simultaneous production and oxidation (Wang et al., 2016; Giunta et al., 2022; Krause et al., 2022). A reservoir effect, controlled by the ratio of oxidation rate within cells to the transport rate of methane into the cells, can lead to deviations from the traditional closed-system Rayleigh distillation fractionation during aerobic oxidation (Li et al., 2024). Similarly, the clumped isotopologue effect of photocatalytic oxidation in the atmosphere resembles that of microbial aerobic oxidation. Ab initio modeling and laboratory experiments demonstrated that methane oxidation by OH or Cl radicals leads to significant changes in methane clumping (Haghnegahdar et al., 2017; Whitehill et al., 2017). The effects of radicals on atmospheric methane isotopologue ratios, as previously predicted, have been confirmed through measurements of the relative abundances of $^{13}CH_3D$ and $^{12}CH_2D_2$ in the atmosphere (Haghnegahdar et al., 2023; Sivan et al., 2024).

Despite notable progress over the past decade, our understanding of methane clumped isotopologue effects is still incomplete due to a limited number of studies. The scarcity of data hinders our grasp of microbial metabolic mechanisms that lead to inconsistencies of methane isotopologue distribution with respect to thermodynamic equilibrium. Figure 10 illustrates our current understanding of methane clumped isotopologues, with various zonations and trajectories that are primarily derived from a limited number of laboratory cultures or specific natural environments. Therefore, it is essential to map the manifestations of all microbial processes across diverse environments that could affect the abundances of these species in $\Delta^{13}CH_3D$ vs. $\Delta^{12}CH_2D_2$ space.

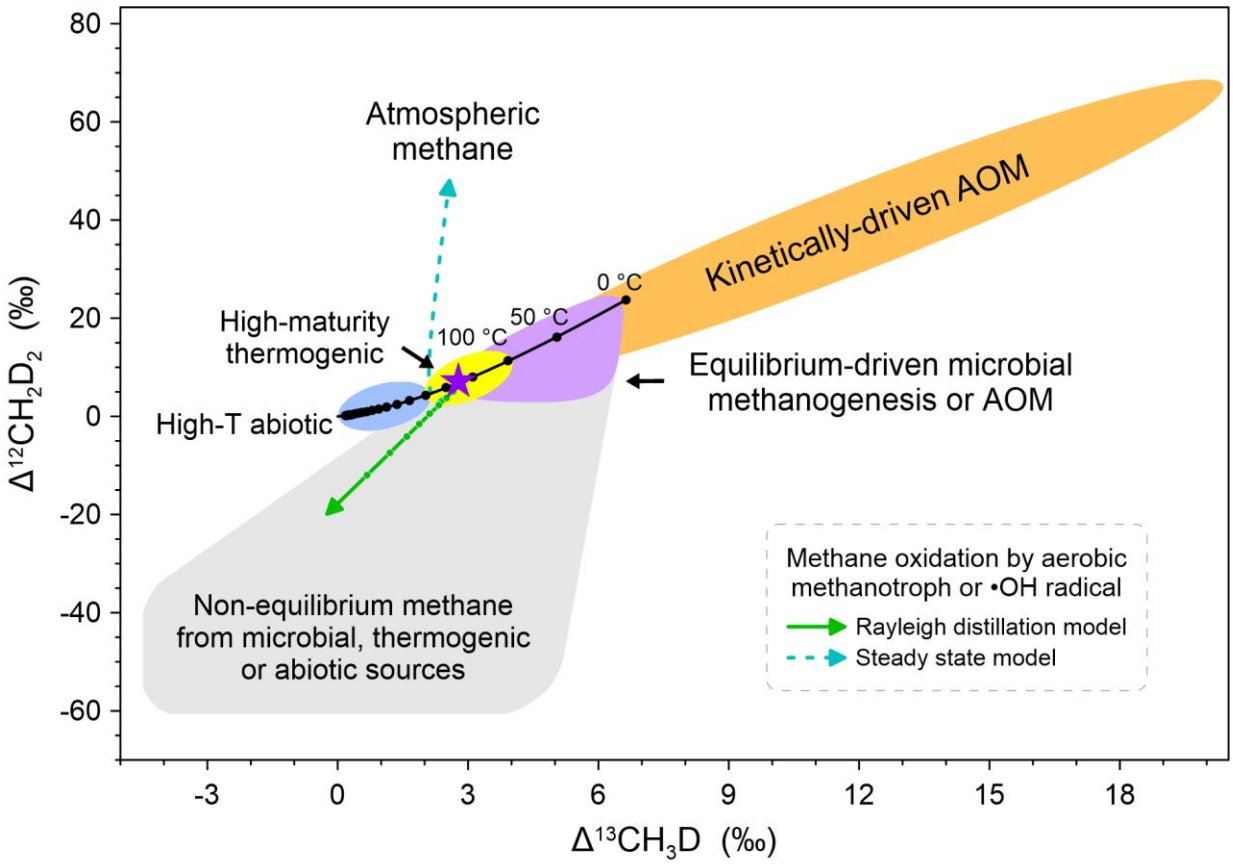

Fig. 1-10 A schematic representation of methane clumped isotope signatures of diverse methane sources and sinks. The solid black line depicts theoretical thermodynamic equilibrium abundances of methane isotopologues, along with corresponding temperatures. The zonation of methane sources is adopted from Young et al. (2017), Young (2019), Dong et al. (2021), Xie et al. (2021), Gropp et al. (2022), Ono et al. (2022), etc. The zonation and trajectories of methane sinks are based on an initial gas of thermogenic origin, depicted as a purple star. Two scenario trajectories for the aerobic oxidation of methane are presented: the solid line represents the Rayleigh distillation model, while the dashed line denotes the steady state model (Krause et al., 2022). The trajectories for methane oxidation with ·OH radical, which is the primary methane sink in the atmosphere, exhibit similarities to those observed in aerobic oxidation of methane (Haghnegahdar et al., 2023).

3. Dissertation outlook

The dissertation begins with this introductory chapter, followed by four separate manuscripts, and ends with a concluding chapter. Each manuscript presents original research, either published or submitted to scientific journals. Chapter 2, published in *Geochimica et Cosmochimica Acta* (Liu et al., 2023), presents methane clumped isotopologue data on AOM from laboratory microbial incubations and natural environments. We hypothesize that the range of clumped isotope effects caused by AOM is controlled by the reversibility of its intracellular pathways. Chapter 3, published in *Geology* (Liu et al., 2024), presents methane clumped isotopologue data from Azerbaijanian mud volcanoes. We hypothesize that methane clumped isotopes can be used to identify secondary methanogenesis and determine the exact evolution stages of natural gases. Chapter 4 presents methane clumped isotopologue data on methanogenesis from laboratory incubations and natural environments. We hypothesize that the range of clumped isotope effects associated with methanogenesis is governed by reaction reversibility and the availability of chemically accessible energy. We further hypothesize that clumped isotope effects of methane metabolisms are linked to the energy landscape of natural environments.

Chapter 5 presents geochemical data and radiotracer incubation results from a hypersaline pool in a coastal wetland to investigate the electron acceptors involved in AOM. We hypothesize that the occurrence of iron-driven AOM depends on both the availability and reactivity of iron oxides, as well as the balance between iron(III) and sulfide. We further hypothesize that iron-driven AOM may act as an effective methane sink in wetland sediments. The final chapter summarizes the key findings and conclusions of the research and places them in a broader context. It highlights the relevance of the results to the interdisciplinary fields of Earth science, chemistry, and microbiology, emphasizing their potential to influence future research directions.

References

Aromokeye D.A., Kulkarni A.C., Elvert M., Wegener G., Henkel S., Coffinet S., Eickhorst T., Oni O.E., Richter-Heitmann T., Schnakenberg A., Taubner H., Wunder L., Yin X., Zhu Q., Hinrichs K.-U., Kasten S. and Friedrich M.W. (2020) Rates and Microbial Players of Iron-Driven Anaerobic Oxidation of Methane in Methanic Marine Sediments. *Front. Microbiol.* **10**.

Ash J.L., Egger M., Treude T., Kohl I., Cragg B., Parkes R.J., Slomp C.P., Sherwood Lollar B. and Young E.D. (2019) Exchange catalysis during anaerobic methanotrophy revealed by 12CH2D2 and 13CH3D in methane. *Geochemical Perspectives Letters* **10**, 26-30.

Bai Y.-N., Wang X.-N., Wu J., Lu Y.-Z., Fu L., Zhang F., Lau T.-C. and Zeng R.J. (2019) Humic substances as electron acceptors for anaerobic oxidation of methane driven by ANME-2d. *Water Res.* **164**, 114935.

Bar-Or I., Elvert M., Eckert W., Kushmaro A., Vigderovich H., Zhu Q., Ben-Dov E. and Sivan O. (2017) Iron-coupled anaerobic oxidation of methane performed by a mixed bacterial-archaeal community based on poorly reactive minerals. *Environ. Sci. Technol.* **51**, 12293-12301.

Bartlett K.B. and Harriss R.C. (1993) Review and assessment of methane emissions from wetlands. *Chemosphere* **26**, 261-320.

Beal E.J., House C.H. and Orphan V.J. (2009) Manganese-and iron-dependent marine methane oxidation. *Science* **325**, 184-187.

Bernard B., Brooks J.M. and Sackett W.M. (1977) A Geochemical Model For Characterization Of Hydrocarbon Gas Sources In Marine Sediments, Offshore Technology Conference, pp. 435-438.

Bernard B.B., Brooks J.M. and Sackett W.M. (1976) Natural gas seepage in the Gulf of Mexico. *Earth Planet. Sci. Lett.* **31**, 48-54.

Boetius A., Ravenschlag K., Schubert C.J., Rickert D., Widdel F., Gieseke A., Amann R., Jørgensen B.B., Witte U. and Pfannkuche O. (2000) A marine microbial consortium apparently mediating anaerobic oxidation of methane. *Nature* **407**, 623-626.

Borowski W.S., Paull C.K. and Ussler Iii W. (1999) Global and local variations of interstitial sulfate gradients in deep-water, continental margin sediments: Sensitivity to underlying methane and gas hydrates. *Mar. Geol.* **159**, 131-154.

Bowman J. (2006) The Methanotrophs — The Families Methylococcaceae and Methylocystaceae, in: Dworkin M., Falkow S., Rosenberg E., Schleifer K.-H., Stackebrandt E. (Eds.), The Prokaryotes: Volume 5: Proteobacteria: Alpha and Beta Subclasses. Springer New York, New York, NY, pp. 266-289.

Bridgham S.D., Cadillo-Quiroz H., Keller J.K. and Zhuang Q. (2013) Methane emissions from wetlands: biogeochemical, microbial, and modeling perspectives from local to global scales. *Global Change Biol.* **19**, 1325-1346.

Cai C., Leu A.O., Xie G.-J., Guo J., Feng Y., Zhao J.-X., Tyson G.W., Yuan Z. and Hu S. (2018) A methanotrophic archaeon couples anaerobic oxidation of methane to Fe(III) reduction. *The ISME Journal* **12**, 1929-1939.

Cao X., Bao H. and Peng Y. (2019) A kinetic model for isotopologue signatures of methane generated by biotic and abiotic CO2 methanation. *Geochim. Cosmochim. Acta* **249**, 59-75.

Chadwick G.L., Skennerton C.T., Laso-Pérez R., Leu A.O., Speth D.R., Yu H., Morgan-Lang C., Hatzenpichler R., Goudeau D., Malmstrom R., Brazelton W.J., Woyke T., Hallam S.J., Tyson G.W., Wegener G., Boetius A. and Orphan V.J. (2022) Comparative genomics

reveals electron transfer and syntrophic mechanisms differentiating methanotrophic and methanogenic archaea. *PLoS Biol.* **20**, e3001508.

Chowdhury T.R. and Dick R.P. (2013) Ecology of aerobic methanotrophs in controlling methane fluxes from wetlands. *Applied Soil Ecology* **65**, 8-22.

Curry C.L. (2007) Modeling the soil consumption of atmospheric methane at the global scale. *Global Biogeochem. Cycles* **21**.

Ding H. and Valentine D.L. (2008) Methanotrophic bacteria occupy benthic microbial mats in shallow marine hydrocarbon seeps, Coal Oil Point, California. *Journal of Geophysical Research: Biogeosciences* **113**.

Dlugokencky E.J., Nisbet E.G., Fisher R. and Lowry D. (2011) Global atmospheric methane: budget, changes and dangers. *Philosophical Transactions of the Royal Society A: Mathematical, Physical and Engineering Sciences* **369**, 2058-2072.

Dong G., Xie H., Formolo M., Lawson M., Sessions A. and Eiler J. (2021) Clumped isotope effects of thermogenic methane formation: Insights from pyrolysis of hydrocarbons. *Geochim. Cosmochim. Acta* **303**, 159-183.

Douglas P.M.J., Stolper D.A., Smith D.A., Walter Anthony K.M., Paull C.K., Dallimore S., Wik M., Crill P.M., Winterdahl M., Eiler J.M. and Sessions A.L. (2016) Diverse origins of Arctic and Subarctic methane point source emissions identified with multiply-substituted isotopologues. *Geochim. Cosmochim. Acta* **188**, 163-188.

Dutaur L. and Verchot L.V. (2007) A global inventory of the soil CH4 sink. *Global Biogeochem. Cycles* **21**.

Egger M., Rasigraf O., Sapart C.l.J., Jilbert T., Jetten M.S., Röckmann T., van der Veen C., Bândă N., Kartal B. and Ettwig K.F. (2015) Iron-mediated anaerobic oxidation of methane in brackish coastal sediments. *Environ. Sci. Technol.* **49**, 277-283.

Ehhalt D.H. (1974) The atmospheric cycle of methane. *Tellus* **26**, 58-70.

Eiler J.M. (2007) "Clumped-isotope" geochemistry—The study of naturally-occurring, multiply-substituted isotopologues. *Earth Planet. Sci. Lett.* **262**, 309-327.

Ermler U., Grabarse W., Shima S., Goubeaud M. and Thauer R.K. (1997) Crystal Structure of Methyl-Coenzyme M Reductase: The Key Enzyme of Biological Methane Formation. *Science* **278**, 1457-1462.

Ernst L., Steinfeld B., Barayeu U., Klintzsch T., Kurth M., Grimm D., Dick T.P., Rebelein J.G., Bischofs I.B. and Keppler F. (2022) Methane formation driven by reactive oxygen species across all living organisms. *Nature* **603**, 482-487.

Etiope G. and Sherwood Lollar B. (2013) ABIOTIC METHANE ON EARTH. *Rev. Geophys.* **51**, 276-299.

Ettwig K.F., Butler M.K., Le Paslier D., Pelletier E., Mangenot S., Kuypers M.M.M., Schreiber F., Dutilh B.E., Zedelius J., de Beer D., Gloerich J., Wessels H.J.C.T., van Alen T., Luesken F., Wu M.L., van de Pas-Schoonen K.T., Op den Camp H.J.M., Janssen-Megens E.M., Francoijs K.-J., Stunnenberg H., Weissenbach J., Jetten M.S.M. and Strous M. (2010) Nitrite-driven anaerobic methane oxidation by oxygenic bacteria. *Nature* **464**, 543-548.

Ettwig K.F., Zhu B., Speth D., Keltjens J.T., Jetten M.S. and Kartal B. (2016) Archaea catalyze iron-dependent anaerobic oxidation of methane. *P. Natl. Acad. Sci. USA* **113**, 12792-12796.

Faramawy S., Zaki T. and Sakr A.A.E. (2016) Natural gas origin, composition, and processing: A review. *Journal of Natural Gas Science and Engineering* **34**, 34-54.

Formisano V., Atreya S., Encrenaz T., Ignatiev N. and Giuranna M. (2004) Detection of Methane in the Atmosphere of Mars. *Science* **306**, 1758-1761.

Forster P., Storelvmo T., Armour K., Collins W., Dufresne J.-L., Frame D., Lunt D., Mauritsen T., Palmer M., Watanabe M., Wild M. and Zhang H. (2021) Chapter 7: The Earth's energy budget, climate feedbacks, and climate sensitivity. Open Access Te Herenga Waka-Victoria University of Wellington.

Giunta T., Young E.D., Labidi J., Sansjofre P., Jézéquel D., Donval J.-P., Brandily C. and Ruffine L. (2022) Extreme methane clumped isotopologue bio-signatures of aerobic and anaerobic methanotrophy: Insights from the Lake Pavin and the Black Sea sediments. *Geochim. Cosmochim. Acta* **338**, 34-53.

Giunta T., Young E.D., Warr O., Kohl I., Ash J.L., Martini A., Mundle S.O.C., Rumble D., Pérez-Rodríguez I., Wasley M., LaRowe D.E., Gilbert A. and Sherwood Lollar B. (2019) Methane sources and sinks in continental sedimentary systems: New insights from paired clumped isotopologues 13CH3D and 12CH2D2. *Geochim. Cosmochim. Acta* **245**, 327-351.

Gropp J., Iron M.A. and Halevy I. (2021) Theoretical estimates of equilibrium carbon and hydrogen isotope effects in microbial methane production and anaerobic oxidation of methane. *Geochim. Cosmochim. Acta* **295**, 237-264.

Gropp J., Jin Q. and Halevy I. (2022) Controls on the isotopic composition of microbial methane. *Sci. Adv.* **8**, eabm5713.

Gruen D.S., Wang D.T., Könneke M., Topçuoğlu B.D., Stewart L.C., Goldhammer T., Holden J.F., Hinrichs K.-U. and Ono S. (2018) Experimental investigation on the controls of clumped isotopologue and hydrogen isotope ratios in microbial methane. *Geochim. Cosmochim. Acta* **237**, 339-356.

Haghnegahdar M.A., Schauble E.A. and Young E.D. (2017) A model for 12CH2D2 and 13CH3D as complementary tracers for the budget of atmospheric CH4. *Global Biogeochem. Cycles* **31**, 1387-1407.

Haghnegahdar M.A., Sun J., Hultquist N., Hamovit N.D., Kitchen N., Eiler J., Ono S., Yarwood S.A., Kaufman A.J., Dickerson R.R., Bouyon A., Magen C. and Farquhar J. (2023) Tracing sources of atmospheric methane using clumped isotopes. *P. Natl. Acad. Sci. USA* **120**, e2305574120.

Hanson R.S. and Hanson T.E. (1996) Methanotrophic bacteria. *Microbiological Reviews* **60**, 439-471.

Haroon M.F., Hu S., Shi Y., Imelfort M., Keller J., Hugenholtz P., Yuan Z. and Tyson G.W. (2013) Anaerobic oxidation of methane coupled to nitrate reduction in a novel archaeal lineage. *Nature* **500**, 567-570.

He Z., Zhang Q., Feng Y., Luo H., Pan X. and Gadd G.M. (2018) Microbiological and environmental significance of metal-dependent anaerobic oxidation of methane. *Sci. Total Environ.* **610**, 759-768.

Hinrichs K.-U., Hayes J.M., Sylva S.P., Brewer P.G. and DeLong E.F. (1999) Methane-consuming archaebacteria in marine sediments. *Nature* **398**, 802-805.

Hoehler T.M., Alperin M.J., Albert D.B. and Martens C.S. (1994) Field and laboratory studies of methane oxidation in an anoxic marine sediment: Evidence for a methanogen-sulfate reducer consortium. *Global Biogeochem. Cycles* **8**, 451-463.

Howarth R.W. (2014) A bridge to nowhere: methane emissions and the greenhouse gas footprint of natural gas. *Energy Science & Engineering* **2**, 47-60.

Jørgensen B.B. (2021) Sulfur Biogeochemical Cycle of Marine Sediments. *Geochem. Perspect.* **10**, 145-146.

Karl D.M., Beversdorf L., Björkman K.M., Church M.J., Martinez A. and Delong E.F. (2008) Aerobic production of methane in the sea. *Nat. Geosci.* **1**, 473-478.

Kirschke S., Bousquet P., Ciais P., Saunois M., Canadell J.G., Dlugokencky E.J., Bergamaschi P., Bergmann D., Blake D.R., Bruhwiler L., Cameron-Smith P., Castaldi S., Chevallier F., Feng L., Fraser A., Heimann M., Hodson E.L., Houweling S., Josse B., Fraser P.J., Krummel P.B., Lamarque J.-F., Langenfelds R.L., Le Quéré C., Naik V., O'Doherty S., Palmer P.I., Pison I., Plummer D., Poulter B., Prinn R.G., Rigby M., Ringeval B., Santini M., Schmidt M., Shindell D.T., Simpson I.J., Spahni R., Steele L.P., Strode S.A., Sudo K., Szopa S., van der Werf G.R., Voulgarakis A., van Weele M., Weiss R.F., Williams J.E. and Zeng G. (2013) Three decades of global methane sources and sinks. *Nat. Geosci.* **6**, 813-823.

Knittel K. and Boetius A. (2009) Anaerobic oxidation of methane: progress with an unknown process. *Annu. Rev. Microbiol.* **63**, 311-334.

Konhauser K.O. (2009) Introduction to geomicrobiology. John Wiley & Sons.

Krause S.J.E., Liu J., Young E.D. and Treude T. (2022) Δ13CH3D and Δ12CH2D2 signatures of methane aerobically oxidized by Methylosinus trichosporium with implications for deciphering the provenance of methane gases. *Earth Planet. Sci. Lett.* **593**, 117681.

Krause S.J.E. and Treude T. (2021) Deciphering cryptic methane cycling: Coupling of methylotrophic methanogenesis and anaerobic oxidation of methane in hypersaline coastal wetland sediment. *Geochim. Cosmochim. Acta* **302**, 160-174.

Lamontagne R.A., Swinnerton J.W., Linnenbom V.J. and Smith W.D. (1973) Methane concentrations in various marine environments. *J. Geophys. Res.* **78**, 5317-5324.

Le Mer J. and Roger P. (2001) Production, oxidation, emission and consumption of methane by soils: A review. *European Journal of Soil Biology* **37**, 25-50.

Lefèvre F. and Forget F. (2009) Observed variations of methane on Mars unexplained by known atmospheric chemistry and physics. *Nature* **460**, 720-723.

Li J., Chiu B.K., Piasecki A.M., Feng X., Landis J.D., Marcum S., Young E.D. and Leavitt W.D. (2024) The evolution of multiply substituted isotopologues of methane during microbial aerobic oxidation. *Geochim. Cosmochim. Acta* **381**, 223-238.

Liu J., Harris R.L., Ash J.L., Ferry J.G., Krause S.J.E., Labidi J., Prakash D., Sherwood Lollar B., Treude T., Warr O. and Young E.D. (2023) Reversibility controls on extreme methane clumped isotope signatures from anaerobic oxidation of methane. *Geochim. Cosmochim. Acta* **348**, 165-186.

Liu J., Izon G., Wang J., Antler G., Wang Z., Zhao J. and Egger M. (2018) Vivianite formation in methane-rich deep-sea sediments from the South China Sea. *Biogeosciences* **15**, 6329-6348.

Liu J., Treude T., Abbasov O.R., Baloglanov E.E., Aliyev A.A., Harris C.M., Leavitt W.D. and Young E.D. (2024) Clumped isotope evidence for microbial alteration of thermogenic methane in terrestrial mud volcanoes. *Geology* **52**, 22-26.

Liu Q. and Liu Y. (2016) Clumped-isotope signatures at equilibrium of CH4, NH3, H2O, H2S and SO2. *Geochim. Cosmochim. Acta* **175**, 252-270.

Lovley D.R. and Klug M.J. (1983) Sulfate Reducers Can Outcompete Methanogens at Freshwater Sulfate Concentrations. *Appl. Environ. Microbiol.* **45**, 187-192.

Lovley D.R. and Klug M.J. (1986) Model for the distribution of sulfate reduction and methanogenesis in freshwater sediments. *Geochim. Cosmochim. Acta* **50**, 11-18.

Ma Q., Wu S. and Tang Y. (2008) Formation and abundance of doubly-substituted methane isotopologues (13CH3D) in natural gas systems. *Geochim. Cosmochim. Acta* **72**, 5446-5456.

Maltby J., Sommer S., Dale A.W. and Treude T. (2016) Microbial methanogenesis in the sulfate-reducing zone of surface sediments traversing the Peruvian margin. *Biogeosciences* **13**, 283-299.

Mao S.-H., Zhang H.-H., Zhuang G.-C., Li X.-J., Liu Q., Zhou Z., Wang W.-L., Li C.-Y., Lu K.-Y., Liu X.-T., Montgomery A., Joye S.B., Zhang Y.-Z. and Yang G.-P. (2022) Aerobic oxidation of methane significantly reduces global diffusive methane emissions from shallow marine waters. *Nat. commun.* **13**, 7309.

Martens C.S. and Berner R.A. (1977) Interstitial water chemistry of anoxic Long Island Sound sediments. 1. Dissolved gases. *Limnol. Oceanogr.* **22**, 10-25.

Matthews E. and Fung I. (1987) Methane emission from natural wetlands: Global distribution, area, and environmental characteristics of sources. *Global Biogeochem. Cycles* **1**, 61-86.

Mayumi D., Mochimaru H., Tamaki H., Yamamoto K., Yoshioka H., Suzuki Y., Kamagata Y. and Sakata S. (2016) Methane production from coal by a single methanogen. *Science* **354**, 222-225.

McGlynn S.E., Chadwick G.L., Kempes C.P. and Orphan V.J. (2015) Single cell activity reveals direct electron transfer in methanotrophic consortia. *Nature* **526**, 531.

Milkov A.V. (2011) Worldwide distribution and significance of secondary microbial methane formed during petroleum biodegradation in conventional reservoirs. *Org. Geochem.* **42**, 184-207.

Milkov A.V. and Etiope G. (2018) Revised genetic diagrams for natural gases based on a global dataset of >20,000 samples. *Org. Geochem.* **125**, 109-120.

Milucka J., Ferdelman T.G., Polerecky L., Franzke D., Wegener G., Schmid M., Lieberwirth I., Wagner M., Widdel F. and Kuypers M.M. (2012) Zero-valent sulphur is a key intermediate in marine methane oxidation. *Nature* **491**, 541.

Mitchell J.F.B. (1989) The "Greenhouse" effect and climate change. *Rev. Geophys.* **27**, 115-139.

Mitsch W.J. and Gosselink J.G. (2000) The value of wetlands: importance of scale and landscape setting. *Ecol. Econ.* **35**, 25-33.

Murrell J.C. (2010) The Aerobic Methane Oxidizing Bacteria (Methanotrophs), in: Timmis K.N. (Ed.), Handbook of Hydrocarbon and Lipid Microbiology. Springer Berlin Heidelberg, Berlin, Heidelberg, pp. 1953-1966.

Niewöhner C., Hensen C., Kasten S., Zabel M. and Schulz H.D. (1998) Deep Sulfate Reduction Completely Mediated by Anaerobic Methane Oxidation in Sediments of the Upwelling Area off Namibia. *Geochim. Cosmochim. Acta* **62**, 455-464.

Nisbet E.G., Dlugokencky E.J., Manning M.R., Lowry D., Fisher R.E., France J.L., Michel S.E., Miller J.B., White J.W.C., Vaughn B., Bousquet P., Pyle J.A., Warwick N.J., Cain M., Brownlow R., Zazzeri G., Lanoisellé M., Manning A.C., Gloor E., Worthy D.E.J., Brunke E.-G., Labuschagne C., Wolff E.W. and Ganesan A.L. (2016) Rising atmospheric methane: 2007–2014 growth and isotopic shift. *Global Biogeochem. Cycles* **30**, 1356-1370.

Nisbet E.G., Manning M.R., Dlugokencky E.J., Fisher R.E., Lowry D., Michel S.E., Myhre C.L., Platt S.M., Allen G., Bousquet P., Brownlow R., Cain M., France J.L., Hermansen O., Hossaini R., Jones A.E., Levin I., Manning A.C., Myhre G., Pyle J.A., Vaughn B.H., Warwick N.J. and White J.W.C. (2019) Very Strong Atmospheric Methane Growth in the 4 Years 2014–2017: Implications for the Paris Agreement. *Global Biogeochem. Cycles* **33**, 318-342.

Norði K.à., Thamdrup B. and Schubert C.J. (2013) Anaerobic oxidation of methane in an iron-rich Danish freshwater lake sediment. *Limnol. Oceanogr.* **58**, 546-554.

Ono S., Rhim J.H., Gruen D.S., Taubner H., Kölling M. and Wegener G. (2021) Clumped isotopologue fractionation by microbial cultures performing the anaerobic oxidation of methane. *Geochim. Cosmochim. Acta* **293**, 70-85.

Ono S., Rhim J.H. and Ryberg E.C. (2022) Rate limits and isotopologue fractionations for microbial methanogenesis examined with combined pathway protein cost and isotopologue flow network models. *Geochim. Cosmochim. Acta* **325**, 296-315.

Ono S., Wang D.T., Gruen D.S., Sherwood Lollar B., Zahniser M.S., McManus B.J. and Nelson D.D. (2014) Measurement of a Doubly Substituted Methane Isotopologue, 13CH3D, by Tunable Infrared Laser Direct Absorption Spectroscopy. *Anal. Chem.* **86**, 6487-6494.

Oremland R.S. and Culbertson C.W. (1992) Importance of methane-oxidizing bacteria in the methane budget as revealed by the use of a specific inhibitor. *Nature* **356**, 421-423.

Oremland R.S., Marsh L.M. and Polcin S. (1982) Methane production and simultaneous sulphate reduction in anoxic, salt marsh sediments. *Nature* **296**, 143-145.

Prior S.D. and Dalton H. (1985) The Effect of Copper Ions on Membrane Content and Methane Monooxygenase Activity in Methanol-grown Cells of Methylococcus capsulatus (Bath). *Microbiology* **131**, 155-163.

Raghoebarsing A.A., Pol A., van de Pas-Schoonen K.T., Smolders A.J.P., Ettwig K.F., Rijpstra W.I.C., Schouten S., Damsté J.S.S., Op den Camp H.J.M., Jetten M.S.M. and Strous M. (2006) A microbial consortium couples anaerobic methane oxidation to denitrification. *Nature* **440**, 918-921.

Rahalkar M., Deutzmann J., Schink B. and Bussmann I. (2009) Abundance and Activity of Methanotrophic Bacteria in Littoral and Profundal Sediments of Lake Constance (Germany). *Appl. Environ. Microbiol.* **75**, 119-126.

Reeburgh W.S. (2007a) Global Methane Biogeochemistry, in: Holland H.D., Turekian K.K. (Eds.), Treatise on Geochemistry. Pergamon, Oxford, pp. 1-32.

Reeburgh W.S. (2007b) Oceanic methane biogeochemistry. *Chem. Rev.* **107**, 486-513.

Repeta D.J., Ferrón S., Sosa O.A., Johnson C.G., Repeta L.D., Acker M., DeLong E.F. and Karl D.M. (2016) Marine methane paradox explained by bacterial degradation of dissolved organic matter. *Nat. Geosci.* **9**, 884-887.

Riedinger N., Formolo M.J., Lyons T.W., Henkel S., Beck A. and Kasten S. (2014) An inorganic geochemical argument for coupled anaerobic oxidation of methane and iron reduction in marine sediments. *Geobiology* **12**, 172-181.

Röckmann T., Popa M.E., Krol M.C. and Hofmann M.E.G. (2016) Statistical clumped isotope signatures. *Scientific Reports* **6**, 31947.

Ross M.O. and Rosenzweig A.C. (2017) A tale of two methane monooxygenases. *JBIC Journal of Biological Inorganic Chemistry* **22**, 307-319.

Saunois M., Martinez A., Poulter B., Zhang Z., Raymond P., Regnier P., Canadell J.G., Jackson R.B., Patra P.K., Bousquet P., Ciais P., Dlugokencky E.J., Lan X., Allen G.H., Bastviken D., Beerling D.J., Belikov D.A., Blake D.R., Castaldi S., Crippa M., Deemer B.R., Dennison F., Etiope G., Gedney N., Höglund-Isaksson L., Holgerson M.A., Hopcroft P.O., Hugelius G., Ito A., Jain A.K., Janardanan R., Johnson M.S., Kleinen T., Krummel P., Lauerwald R., Li T., Liu X., McDonald K.C., Melton J.R., Mühle J., Müller J., Murguia-Flores F., Niwa Y., Noce S., Pan S., Parker R.J., Peng C., Ramonet M., Riley W.J., Rocher-Ros G., Rosentreter J.A., Sasakawa M., Segers A., Smith S.J., Stanley E.H., Thanwerdas J., Tian H., Tsuruta A., Tubiello F.N., Weber T.S., van der Werf G., Worthy D.E., Xi Y., Yoshida Y., Zhang W., Zheng B., Zhu Q., Zhu Q. and Zhuang Q. (2024) Global Methane Budget 2000-2020. *Earth Syst. Sci. Data Discuss.* **2024**, 1-147.

Saunois M., Stavert A.R., Poulter B., Bousquet P., Canadell J.G., Jackson R.B., Raymond P.A., Dlugokencky E.J., Houweling S., Patra P.K., Ciais P., Arora V.K., Bastviken D., Bergamaschi P., Blake D.R., Brailsford G., Bruhwiler L., Carlson K.M., Carrol M., Castaldi S., Chandra N., Crevoisier C., Crill P.M., Covey K., Curry C.L., Etiope G., Frankenberg C., Gedney N., Hegglin M.I., Höglund-Isaksson L., Hugelius G., Ishizawa M., Ito A., Janssens-Maenhout G., Jensen K.M., Joos F., Kleinen T., Krummel P.B., Langenfelds R.L., Laruelle G.G., Liu L., Machida T., Maksyutov S., McDonald K.C., McNorton J., Miller P.A., Melton J.R., Morino I., Müller J., Murguia-Flores F., Naik V., Niwa Y., Noce S., O'Doherty S., Parker R.J., Peng C., Peng S., Peters G.P., Prigent C., Prinn R., Ramonet M., Regnier P., Riley W.J., Rosentreter J.A., Segers A., Simpson I.J., Shi H., Smith S.J., Steele L.P., Thornton B.F., Tian H., Tohjima Y., Tubiello F.N., Tsuruta A., Viovy N., Voulgarakis A., Weber T.S., van Weele M., van der Werf G.R., Weiss R.F.,

Worthy D., Wunch D., Yin Y., Yoshida Y., Zhang W., Zhang Z., Zhao Y., Zheng B., Zhu Q., Zhu Q. and Zhuang Q. (2020) The Global Methane Budget 2000–2017. *Earth Syst. Sci. Data* **12**, 1561-1623.

Scheller S., Yu H., Chadwick G.L., McGlynn S.E. and Orphan V.J. (2016) Artificial electron acceptors decouple archaeal methane oxidation from sulfate reduction. *Science* **351**, 703-707.

Schoell M. (1980) The hydrogen and carbon isotopic composition of methane from natural gases of various origins. *Geochim. Cosmochim. Acta* **44**, 649-661.

Schoell M. (1983) Genetic Characterization of Natural Gases. *AAPG Bulletin* **67**, 2225-2238.

Schwietzke S., Sherwood O.A., Bruhwiler L.M.P., Miller J.B., Etiope G., Dlugokencky E.J., Michel S.E., Arling V.A., Vaughn B.H., White J.W.C. and Tans P.P. (2016) Upward revision of global fossil fuel methane emissions based on isotope database. *Nature* **538**, 88-91.

Shi L.-D., Guo T., Lv P.-L., Niu Z.-F., Zhou Y.-J., Tang X.-J., Zheng P., Zhu L.-Z., Zhu Y.-G., Kappler A. and Zhao H.-P. (2020) Coupled anaerobic methane oxidation and reductive arsenic mobilization in wetland soils. *Nat. Geosci.* **13**, 799-805.

Sivan M., Röckmann T., van der Veen C. and Popa M.E. (2024) Extraction, purification, and clumped isotope analysis of methane (Δ13CDH3 and Δ12CD2H2) from sources and the atmosphere. *Atmos. Meas. Tech.* **17**, 2687-2705.

Sivan O., Adler M., Pearson A., Gelman F., Bar-Or I., John S.G. and Eckert W. (2011) Geochemical evidence for iron-mediated anaerobic oxidation of methane. *Limnol. Oceanogr.* **56**, 1536-1544.

Stanley S.H., Prior S.D., Leak D.J. and Dalton H. (1983) Copper stress underlies the fundamental change in intracellular location of methane mono-oxygenase in methane-oxidizing organisms: Studies in batch and continuous cultures. *Biotechnol. Lett.* **5**, 487-492.

Steinle L., Graves C.A., Treude T., Ferré B., Biastoch A., Bussmann I., Berndt C., Krastel S., James R.H., Behrens E., Böning C.W., Greinert J., Sapart C.-J., Scheinert M., Sommer S., Lehmann M.F. and Niemann H. (2015) Water column methanotrophy controlled by a rapid oceanographic switch. *Nat. Geosci.* **8**, 378-382.

Stolper D.A., Lawson M., Davis C.L., Ferreira A.A., Neto E.V.S., Ellis G.S., Lewan M.D., Martini A.M., Tang Y., Schoell M., Sessions A.L. and Eiler J.M. (2014a) Formation temperatures of thermogenic and biogenic methane. *Science* **344**, 1500-1503.

Stolper D.A., Martini A.M., Clog M., Douglas P.M., Shusta S.S., Valentine D.L., Sessions A.L. and Eiler J.M. (2015) Distinguishing and understanding thermogenic and biogenic sources of methane using multiply substituted isotopologues. *Geochim. Cosmochim. Acta* **161**, 219-247.

Stolper D.A., Sessions A.L., Ferreira A.A., Santos Neto E.V., Schimmelmann A., Shusta S.S., Valentine D.L. and Eiler J.M. (2014b) Combined 13C–D and D–D clumping in methane: Methods and preliminary results. *Geochim. Cosmochim. Acta* **126**, 169-191.

Taenzer L., Labidi J., Masterson A.L., Feng X., Rumble D., Young E.D. and Leavitt W.D. (2020) Low Δ12CH2D2 values in microbialgenic methane result from combinatorial isotope effects. *Geochim. Cosmochim. Acta* **285**, 225-236.

Thauer R.K. (2011) Anaerobic oxidation of methane with sulfate: on the reversibility of the reactions that are catalyzed by enzymes also involved in methanogenesis from CO2. *Curr. Opin. Microbiol.* **14**, 292-299.

Thauer R.K., Kaster A.-K., Seedorf H., Buckel W. and Hedderich R. (2008) Methanogenic archaea: ecologically relevant differences in energy conservation. *Nature Reviews Microbiology* **6**, 579-591.

Thornton J.A., Kercher J.P., Riedel T.P., Wagner N.L., Cozic J., Holloway J.S., Dubé W.P., Wolfe G.M., Quinn P.K., Middlebrook A.M., Alexander B. and Brown S.S. (2010) A large atomic chlorine source inferred from mid-continental reactive nitrogen chemistry. *Nature* **464**, 271-274.

Timmers P.H.A., Welte C.U., Koehorst J.J., Plugge C.M., Jetten M.S.M. and Stams A.J.M. (2017) Reverse Methanogenesis and Respiration in Methanotrophic Archaea. *Archaea* **2017**, 22.

Treude T., Krause S., Maltby J., Dale A.W., Coffin R. and Hamdan L.J. (2014) Sulfate reduction and methane oxidation activity below the sulfate-methane transition zone in Alaskan Beaufort Sea continental margin sediments: Implications for deep sulfur cycling. *Geochim. Cosmochim. Acta* **144**, 217-237.

Treude T., Niggemann J., Kallmeyer J., Wintersteller P., Schubert C.J., Boetius A. and Jørgensen B.B. (2005) Anaerobic oxidation of methane and sulfate reduction along the Chilean continental margin. *Geochim. Cosmochim. Acta* **69**, 2767-2779.

Valentine D.L. and Reeburgh W.S. (2000) New perspectives on anaerobic methane oxidation. *Environ. Microbiol.* **2**, 477-484.

Vanwonterghem I., Evans P.N., Parks D.H., Jensen P.D., Woodcroft B.J., Hugenholtz P. and Tyson G.W. (2016) Methylotrophic methanogenesis discovered in the archaeal phylum Verstraetearchaeota. *Nature Microbiology* **1**, 16170.

Wang D.T., Gruen D.S., Lollar B.S., Hinrichs K.-U., Stewart L.C., Holden J.F., Hristov A.N., Pohlman J.W., Morrill P.L., Könneke M., Delwiche K.B., Reeves E.P., Sutcliffe C.N., Ritter

D.J., Seewald J.S., McIntosh J.C., Hemond H.F., Kubo M.D., Cardace D., Hoehler T.M. and Ono S. (2015) Nonequilibrium clumped isotope signals in microbial methane. *Science* **348**, 428-431.

Wang D.T., Welander P.V. and Ono S. (2016) Fractionation of the methane isotopologues 13CH4, 12CH3D, and 13CH3D during aerobic oxidation of methane by Methylococcus capsulatus (Bath). *Geochim. Cosmochim. Acta* **192**, 186-202.

Wang Z., Schauble E.A. and Eiler J.M. (2004) Equilibrium thermodynamics of multiply substituted isotopologues of molecular gases. *Geochim. Cosmochim. Acta* **68**, 4779-4797.

Wankel S.D., Adams M.M., Johnston D.T., Hansel C.M., Joye S.B. and Girguis P.R. (2012) Anaerobic methane oxidation in metalliferous hydrothermal sediments: influence on carbon flux and decoupling from sulfate reduction. *Environ. Microbiol.* **14**, 2726-2740.

Warr O., Young E.D., Giunta T., Kohl I.E., Ash J.L. and Sherwood Lollar B. (2021) High-resolution, long-term isotopic and isotopologue variation identifies the sources and sinks of methane in a deep subsurface carbon cycle. *Geochim. Cosmochim. Acta* **294**, 315-334.

Webb M.A. and Miller T.F. (2014) Position-Specific and Clumped Stable Isotope Studies: Comparison of the Urey and Path-Integral Approaches for Carbon Dioxide, Nitrous Oxide, Methane, and Propane. *The Journal of Physical Chemistry A* **118**, 467-474.

Webster C.R., Mahaffy P.R., Atreya S.K., Flesch G.J., Mischna M.A., Meslin P.-Y., Farley K.A., Conrad P.G., Christensen L.E., Pavlov A.A., Martín-Torres J., Zorzano M.-P., McConnochie T.H., Owen T., Eigenbrode J.L., Glavin D.P., Steele A., Malespin C.A., Archer P.D., Sutter B., Coll P., Freissinet C., McKay C.P., Moores J.E., Schwenzer S.P., Bridges J.C., Navarro-Gonzalez R., Gellert R. and Lemmon M.T. (2015) Mars methane detection and variability at Gale crater. *Science* **347**, 415-417.

Wegener G., Krukenberg V., Riedel D., Tegetmeyer H.E. and Boetius A. (2015) Intercellular wiring enables electron transfer between methanotrophic archaea and bacteria. *Nature* **526**, 587.

Welte C. and Deppenmeier U. (2014) Bioenergetics and anaerobic respiratory chains of aceticlastic methanogens. *Biochim. Biophys. Acta* **1837**, 1130-1147.

Whitehill A.R., Joelsson L.M.T., Schmidt J.A., Wang D.T., Johnson M.S. and Ono S. (2017) Clumped isotope effects during OH and Cl oxidation of methane. *Geochim. Cosmochim. Acta* **196**, 307-325.

Whiticar M.J. (1999) Carbon and hydrogen isotope systematics of bacterial formation and oxidation of methane. *Chem. Geol.* **161**, 291-314.

Whiticar M.J. (2020) The Biogeochemical Methane Cycle, in: Wilkes H. (Ed.), Hydrocarbons, Oils and Lipids: Diversity, Origin, Chemistry and Fate. Springer International Publishing, Cham, pp. 1-78.

Whiticar M.J., Faber E. and Schoell M. (1986) Biogenic methane formation in marine and freshwater environments: CO2 reduction vs. acetate fermentation—Isotope evidence. *Geochim. Cosmochim. Acta* **50**, 693-709.

Wuebbles D.J. and Hayhoe K. (2002) Atmospheric methane and global change. *Earth-Sci. Rev.* **57**, 177-210.

Xiao K.-Q., Beulig F., Røy H., Jørgensen B.B. and Risgaard-Petersen N. (2018) Methylotrophic methanogenesis fuels cryptic methane cycling in marine surface sediment. *Limnol. Oceanogr.* **63**, 1519-1527.

Xie H., Dong G., Formolo M., Lawson M., Liu J., Cong F., Mangenot X., Shuai Y., Ponton C. and Eiler J. (2021) The evolution of intra- and inter-molecular isotope equilibria in natural gases with thermal maturation. *Geochim. Cosmochim. Acta* **307**, 22-41.

Yan Z., Joshi P., Gorski C.A. and Ferry J.G. (2018) A biochemical framework for anaerobic oxidation of methane driven by Fe (III)-dependent respiration. *Nat. commun.* **9**.

Yao X., Wang J., He M., Liu Z., Zhao Y., Li Y., Chi T., Zhu L., Zheng P., Jetten M.S.M. and Hu B. (2024) Methane-dependent complete denitrification by a single Methylomirabilis bacterium. *Nature Microbiology* **9**, 464-476.

Yeung L.Y. (2016) Combinatorial effects on clumped isotopes and their significance in biogeochemistry. *Geochim. Cosmochim. Acta* **172**, 22-38.

Young E.D. (2019) A Two-Dimensional Perspective on CH4 Isotope Clumping: Distinguishing Process from Source, in: Orcutt B.N., Daniel I., Dasgupta R. (Eds.), Deep Carbon: Past to Present. Cambridge University Press, Cambridge, pp. 388-414.

Young E.D., Kohl I.E., Lollar B.S., Etiope G., Rumble D., Li S., Haghnegahdar M.A., Schauble E.A., McCain K.A., Foustoukos D.I., Sutclife C., Warr O., Ballentine C.J., Onstott T.C., Hosgormez H., Neubeck A., Marques J.M., Pérez-Rodríguez I., Rowe A.R., LaRowe D.E., Magnabosco C., Yeung L.Y., Ash J.L. and Bryndzia L.T. (2017) The relative abundances of resolved 12CH2D2 and 13CH3D and mechanisms controlling isotopic bond ordering in abiotic and biotic methane gases. *Geochim. Cosmochim. Acta* **203**, 235-264.

Young E.D., Labidi J. and Kohl I.E. (2025) Advances in measuring multiply-substituted isotopologues of gas molecules with geochemical applications, in: Anbar A., Weis D. (Eds.), Treatise on Geochemistry (Third edition). Elsevier, Oxford, pp. 645-670.

Young E.D., Rumble D., Freedman P. and Mills M. (2016) A large-radius high-mass-resolution multiple-collector isotope ratio mass spectrometer for analysis of rare isotopologues of O2, N2, CH4 and other gases. *Int. J. Mass spectrom.* **401**, 1-10.

Yu H., Skennerton C.T., Chadwick G.L., Leu A.O., Aoki M., Tyson G.W. and Orphan V.J. (2022) Sulfate differentially stimulates but is not respired by diverse anaerobic methanotrophic archaea. *The ISME Journal* **16**, 168-177.

Yung Y.L., Chen P., Nealson K., Atreya S., Beckett P., Blank J.G., Ehlmann B., Eiler J., Etiope G., Ferry J.G., Forget F., Gao P., Hu R., Kleinböhl A., Klusman R., Lefèvre F., Miller C., Mischna M., Mumma M., Newman S., Oehler D., Okumura M., Oremland R., Orphan V., Popa R., Russell M., Shen L., Sherwood Lollar B., Staehle R., Stamenković V., Stolper D., Templeton A., Vandaele A.C., Viscardy S., Webster C.R., Wennberg P.O., Wong M.L. and Worden J. (2018) Methane on Mars and Habitability: Challenges and Responses. *Astrobiology* **18**, 1221-1242.

Zhou Z., Zhang C.-j., Liu P.-f., Fu L., Laso-Pérez R., Yang L., Bai L.-p., Li J., Yang M., Lin J.-z., Wang W.-d., Wegener G., Li M. and Cheng L. (2022) Non-syntrophic methanogenic hydrocarbon degradation by an archaeal species. *Nature* **601**, 257-262.

Zhuang G.-C., Elling F.J., Nigro L.M., Samarkin V., Joye S.B., Teske A. and Hinrichs K.-U. (2016) Multiple evidence for methylotrophic methanogenesis as the dominant methanogenic pathway in hypersaline sediments from the Orca Basin, Gulf of Mexico. *Geochim. Cosmochim. Acta* **187**, 1-20.

Chapter 2

Reversibility controls on extreme methane clumped isotope signatures from anaerobic oxidation of methane

Jiarui Liu [a, *], Rachel L. Harris [b], Jeanine L. Ash [c], James G. Ferry [d], Sebastian J.E. Krause [a], Jabrane Labidi [e], Divya Prakash [f], Barbara Sherwood Lollar [e, g], Tina Treude [a, h], Oliver Warr [g], Edward D. Young [a]

[a] Department of Earth, Planetary and Space Sciences, University of California, Los Angeles, CA, USA.

[b] Department of Organismic and Evolutionary Biology, Harvard University, Cambridge, MA, USA.

[c] Department of Earth, Environmental and Planetary Sciences, Rice University, Houston, TX, USA.

[d] Department of Biochemistry and Molecular Biology, Pennsylvania State University, University Park, PA, USA.

[e] Université de Paris, Institut de Physique du Globe de Paris, CNRS, Paris, France.

[f] School of Chemical and Biomolecular Sciences, Southern Illinois University, Carbondale, IL, USA.

[g] Department of Earth Sciences, University of Toronto, Toronto, Ontario, Canada.

[h] Department of Atmospheric and Oceanic Sciences, University of California, Los Angeles, CA, USA.

* Corresponding author. Email: jiaruiliu@ucla.edu (J.L.).

Abstract

Microbial anaerobic oxidation of methane (AOM) substantially mitigates atmospheric methane emissions on Earth and is a process to consider for astrobiological targets where methane has been detected. The measurement of doubly substituted, or "clumped", methane isotopes has proven useful in tracing processes of methane formation and oxidation. Both near-equilibrium and extreme disequilibrium methane clumped isotope signatures can be attributed to AOM, but, to date, understanding the mechanistic and environmental controls on those signatures has been lacking. We report measurements of methane clumped isotope compositions of residual methane in AOM-active microbial incubations using sediment slurries from Svalbard and Santa Barbara Channel methane seeps. Incubation experiments of Svalbard sediment slurries resulted in residual methane with very high $\Delta^{13}CH_3D$ and $\Delta^{12}CH_2D_2$ values up to 19.5‰ and 65.1‰, respectively. We found similarly high $\Delta^{13}CH_3D$ and $\Delta^{12}CH_2D_2$ values in fluid samples from the Chamorro Seamount, a serpentinite mud volcano in the Mariana forearc, suggesting that minimal reversibility of AOM intracellular reactions leads to kinetic fractionation of clumped isotopologues. When conditions were consistent with a low thermodynamic drive for AOM, however, methane isotopologues approached intra-species quasi-equilibrium. This was clearly observed in isotope exchange

experiments with methyl-coenzyme M reductase (Mcr) and in microbial incubations of the Santa Barbara Channel sediment slurries. Using an isotopologue fractionation model, we highlight the critical role of reversibility in controlling the trajectory of gases in $\Delta^{13}CH_3D$ vs. $\Delta^{12}CH_2D_2$ space during AOM. The near-equilibrium methane isotopologue signatures are generalized as a result of the Mcr-catalyzed intracellular isotope exchange operating under near-threshold free energy conditions, as shown in the deep-biosphere incubations. Our results show that the reversibility of the Mcr-catalyzed reaction is central to understanding the meaning of methane isotopologue ratios affected by microbial production and oxidation.

Keywords: methane isotopologues; methyl-coenzyme M reductase; kinetic fractionation; equilibrium fractionation; isotopic bond re-ordering.

1. Introduction

Methane, the simplest of all hydrocarbons, is a gas with economic, societal, and environmental relevance. It is the main component of natural gas, a key component of the global carbon cycle (Reeburgh, 2007), and a primary target for understanding the relative role of geologic processes and potential extinct/extant life elsewhere in the universe (e.g., Yung et al., 2018). As a potent greenhouse gas, methane contributes to climate change and its concentration in the atmosphere has been increasing since the beginning of industrialization (IPCC, 2021). The main "biological" processes forming methane are microbial degradation (microbialgenic) and pyrolysis (thermogenic) of organic matter (e.g., Reeburgh, 2007; Repeta et al., 2016). Abiotic methane can be formed through various types of water-rock interactions (Etiope and Sherwood Lollar, 2013 and references therein) under a range of both low-temperature and high-temperature conditions. Identifying the sources and processes of methane emission is vital for constraining fluxes from major reservoirs contributing to climate change, and more broadly, for understanding the biogeochemical dynamics of the planet's critical zone. Traditionally, microbial and thermogenic methane gases are interpreted by their carbon ($\delta^{13}C$) and hydrogen (δD) isotopic compositions (e.g., Schoell, 1983; Whiticar, 1999). However, applying $\delta^{13}C$ and δD as a diagnostic framework alone has significant limitations, most notably circumstances in which isotopic signatures of methane sources are not sharply demarcated, exhibit some degree of overlap, and such empirical frameworks are inevitably redefined as additional experimental and field data come to light (Sherwood Lollar et al., 2006; Douglas et al., 2017). In addition, empirical fields in $\delta^{13}C$ vs. δD space are inherently linked to the isotopic signature of the source materials coupled with the formation processes, which in turn are strongly affected by mixing and secondary alteration processes (Etiope and Sherwood Lollar, 2013 and references therein).

Recently, sophisticated instrumentation has become available to resolve the abundances of doubly substituted, "clumped", isotopologues of methane gas, including $^{13}CH_3D$ and $^{12}CH_2D_2$ (Ono et al., 2014; Stolper et al., 2014b; Young et al., 2016; Eldridge et al., 2019; Gonzalez et al., 2019; Dong et al., 2021; Zhang et al., 2021). The relative abundances of these two mass-18 methane isotopologues are expressed as $\Delta^{13}CH_3D$ and $\Delta^{12}CH_2D_2$ values, representing deviations from a stochastic standard in which distributions of isotopes across all isotopologues are effectively random. The latter is the expected state at sufficiently high temperatures (>1000 K). The relative abundances of doubly substituted methane isotopologues differ from the stochastic distribution at lower temperatures due to the enhanced thermodynamic stability of bonds involving the heavier isotopes (e.g., Ma et al., 2008; Webb and Miller, 2014; Liu and Liu, 2016). In principle, isotopic bond ordering, or clumping, is a tracer of the processes attending the formation of the molecules, coupled with any consumption and/or re-equilibration processes, and therefore gives the potential for their application to discern processes of methane formation and oxidation both on Earth and beyond (Young, 2019). The utility of $\Delta^{13}CH_3D$ and $\Delta^{12}CH_2D_2$ lies in the fact that the values should be sensitive to process, and interpretations of their significance may not dependent upon long-lost isotope exchange partners (e.g., water). In practice, kinetically controlled methane clumped isotope compositions can be sensitive to hydrogen sources of methane that differ in δD (Taenzer et al., 2020).

In some cases, $\Delta^{13}CH_3D$ has been used to reconstruct the formation temperatures of thermogenic methane (Stolper et al., 2014a; Stolper et al., 2015; Wang et al., 2015; Douglas et al., 2016; Lalk et al., 2022) and the combination of $\Delta^{13}CH_3D$ and $\Delta^{12}CH_2D_2$ has been used to verify that the molecules record equilibrium at a given temperature (Young et al., 2017; Giunta et al., 2019; Gonzalez et al., 2019; Thiagarajan et al., 2020; Xie et al., 2021). The abundances of mass-

18 isotopologues of microbial methane, on the other hand, have been shown to be inconsistent with thermodynamic equilibrium, meaning that their distribution does not reflect the temperature at which the methane was formed (Stolper et al., 2015; Wang et al., 2015; Young et al., 2017; Ash et al., 2019; Giunta et al., 2019; Warr et al., 2021). The $\Delta^{13}CH_3D$ and $\Delta^{12}CH_2D_2$ of microbial methane can be modeled as the result of the combination of equilibrium and kinetic steps during the enzymatically facilitated formation of methane (Cao et al., 2019; Young, 2019; Gropp et al., 2021; Gropp et al., 2022; Ono et al., 2022). In particular, the extremely negative $\Delta^{12}CH_2D_2$ values are most likely due to the combinatorial effect of accessing multiple sources of hydrogen with significantly different hydrogen isotopic signatures during the formation of methane (Röckmann et al., 2016; Yeung, 2016; Young, 2019; Taenzer et al., 2020).

While the ability to define a methane isotopologue signature related to microbial methanogenesis is promising, there are caveats. One is that abiotic methane and low-maturity thermogenic methane has been found with deficits in $\Delta^{12}CH_2D_2$ compared with equilibrium values in methane gas, which is further confirmed by pyrolysis experiments on n-octadecane (Douglas et al., 2017; Young et al., 2017; Dong et al., 2021; Warr et al., 2021; Xie et al., 2021). On the other hand, abiotic or biotic consumption processes could potentially alter the relative abundances of the mass-18 isotopologues in ways that might mimic the putative microbial methanogenesis signature. Laboratory experiments and *ab initio* modeling indicate that methane oxidation in the atmosphere by OH or Cl radicals is accompanied by large shifts in methane clumping down to very negative $\Delta^{13}CH_3D$ and $\Delta^{12}CH_2D_2$ values due to Rayleigh distillation (Haghnegahdar et al., 2017; Whitehill et al., 2017; Young, 2019). Similarly, both $\Delta^{13}CH_3D$ and $\Delta^{12}CH_2D_2$ values of residual methane in microbial culture were observed to decrease during the aerobic oxidation of methane (Wang et al., 2016; Krause et al., 2022).

Photocatalytic oxidation and aerobic microbial oxidation of methane occur in the atmosphere and oxygenated environments. Therefore, these processes are in principle separated spatially from microbial methanogenesis, which operates almost exclusively under anoxic, and thus reducing, conditions. Anaerobic oxidation of methane (AOM), however, is closely related to methanogenesis both spatially and metabolically. For example, concurrent methanogenesis and AOM have been found in near-surface sediments and at the sulfate–methane transition (Xiao et al., 2017; Beulig et al., 2019; Krause and Treude, 2021). Anaerobic methanotrophic (ANME) archaea are close relatives of methanogenic archaea and have the full enzymatic machinery of methanogenesis working in reverse (Timmers et al., 2017). Methanogens belonging to *Methanosarcina* can reverse key reactions of methanogenesis coupled to ferric iron reduction (Yan et al., 2018; Yu et al., 2022). The prospect of a methanotroph (ANME-1) from natural sediments conducting methanogenesis further underscores the potential versatility of methanoarchaeal enzymes (Beulig et al., 2019; Kevorkian et al., 2021). Factors forcing these enzymes to operate in either direction need further investigation. However, even when operating in full AOM mode with the highest net turnover of methane, ANME archaea demonstrate some fraction (~4–15%) of net reversibility, defined as the ratio of the backward to forward fluxes (Treude et al., 2007; Holler et al., 2011; Wegener et al., 2021). Back flux of material during the enzymatic reactions of AOM has implications for isotope fractionation, leading to carbon isotope ($^{13}C/^{12}C$) equilibration between methane and intracellular metabolites, in particular when AOM is operating close to thermodynamic limitations where the methyl-coenzyme M reductase (Mcr)-catalyzed reaction is near equilibrium (Hoehler et al., 2000; Holler et al., 2011; Yoshinaga et al., 2014; Chuang et al., 2019; Wegener et al., 2021).

The precise mechanisms that are responsible for $\Delta^{13}CH_3D$ vs. $\Delta^{12}CH_2D_2$ effects of AOM are largely unknown, and further laboratory incubation experiments under different environmental conditions are required. The overarching goal is to develop these intra-methane isotopologue signals as tracers for the origin and processing of methane in general, and AOM in particular. One of the biggest challenges for understanding the isotopologue composition of natural samples is limited knowledge of how isotopic bond re-ordering caused by AOM can overwrite formation-process signatures. Given the high level of reversibility of Mcr-catalyzed reactions during AOM, Ash et al. (2019), Giunta et al. (2019), and Warr et al. (2021) suggested that AOM could be responsible for thermodynamic isotopic bond-order equilibrium in methane found in sulfate-depleted Baltic Sea sediments, sedimentary basins, and the deep subsurface, respectively. Recently, Ono et al. (2021) found that the methane clumped isotopologue $^{13}CH_3D$ exhibits kinetic fractionation in an ANME-1 sediment-free enrichment culture with a high sulfate concentration (28 mM), where $\Delta^{13}CH_3D$ values increased by up to 5.8‰. Importantly, Wegener et al. (2021) demonstrated a sulfate dependence of the net bulk isotope fractionation by virtue of the thermodynamic drive of the intracellular reactions of AOM. Based on the earlier studies, therefore, it appears that the reversibility of intracellular reactions of AOM is responsible for the observed discrepancy between the kinetic isotopologue fractionation in a sulfate-replete culture (Ono et al., 2021) and the intra-species isotope equilibrium in sulfate-depleted settings (Ash et al., 2019; Giunta et al., 2019; Warr et al., 2021).

To document the range of effects that AOM may have on modifying methane isotopologue signatures, we collected a suite of marine sediments and fracture fluids from diverse marine and terrestrial settings that showed different degrees of ANME abundance and AOM activity (Fig. 1). We performed microbial incubations using these samples to evaluate the relationship between the

reversibility of intracellular reactions of AOM and the methane isotopologue fractionation/re-ordering, and to elucidate the unknown fractionation factors for $^{12}CH_2D_2/^{12}CH_4$. We also collected natural fluids from the South Chamorro Seamount where AOM is known to substantially consume abiotic source methane (Wheat et al., 2020), in order to examine whether the isotopologue fractionation differs between laboratory incubations and endogenous AOM in natural environments. In combination, our work aims to address how environmental conditions can potentially affect isotopologue fractionation, as well as rates and magnitudes of isotopic bond re-ordering during AOM. This information will improve our ability to distinguish primary signatures of methane formation from biologically-driven overprinting to maximize the utility of $^{13}CH_3D/^{12}CH_4$ and $^{12}CH_2D_2/^{12}CH_4$ as tracers of methane formation and subsequent processing.

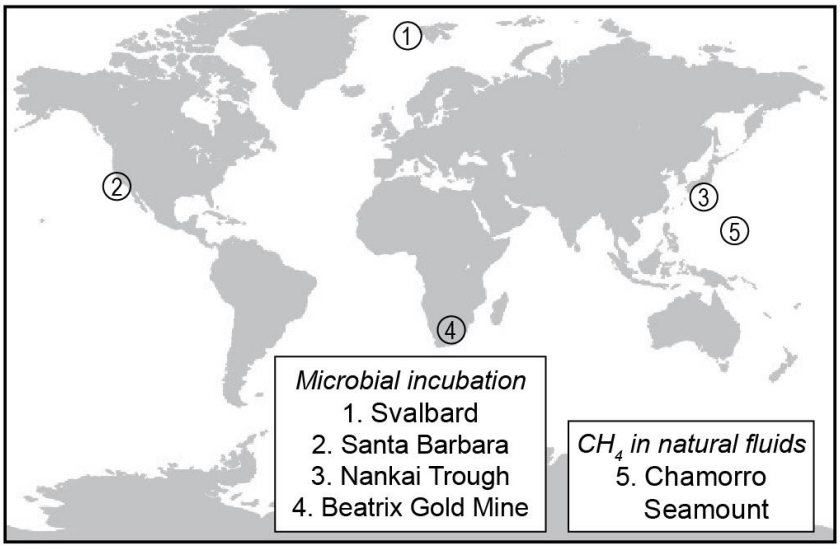

Fig. 2-1 Global map showing sampling sites for this study. Marine sediments or fracture fluids were collected for slurry or fluid incubations at (1) Svalbard methane seeps, (2) Santa Barbara Channel methane seeps, (3) Nankai Trough (International Ocean Discovery Program Hole C0023A), and (4) Beatrix Gold Mine, South Africa. Methane in natural fluids was collected from

a sub-seafloor borehole observatory (Ocean Drilling Program Hole 1200C) on (5) South Chamorro Seamount, a serpentinite mud volcano in the Mariana forearc.

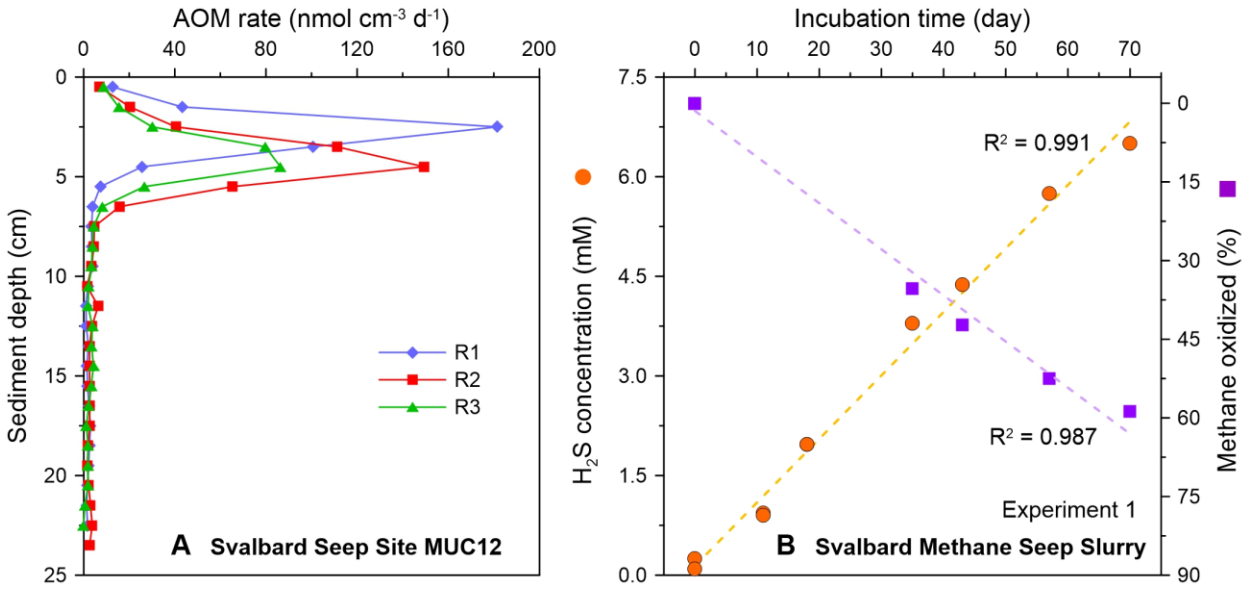

Fig. 2-2 Geochemistry of the Svalbard methane seep sediment and slurry. (A) *Ex-situ* AOM rates determined by $^{14}CH_4$ radiotracer at Site MUC12 offshore Svalbard (Melaniuk et al., 2022). R1–3 represents replicate one through three. (B) Evolution of dissolved sulfide concentration and percentage of methane oxidized in the Svalbard methane seep sediment slurry with a starting sulfate concentration of 20 mM. Linear regressions are shown in panel B.

2. MATERIALS AND METHODS

2.1. Incubation of methane seep sediment slurry from Svalbard

Marine sediments were collected in summer 2011 with a video-guided multicorer from active methane seeps covered by a dense sulfur-bacteria mat offshore northwestern Svalbard

during the R/V *Poseidon* cruise 419 (Site MUC 12; 79°00.417' N, 06°54.131' E, 1235 m water depth). Details of the sampling site, including *ex-situ* activity of AOM (Fig. 2A) and sulfate reduction and geochemical parameters in replicate sediment cores, can be found in Melaniuk et al. (2022). Sediment used for the present study was collected from the top 10 cm of a replicate multicorer core (10 cm inner diameter) and filled headspace-free into 100- and 250-ml borosilicate bottles with butyl stoppers. The sediment was stored anoxically at 4 °C in the dark for 9 years without methane or sulfate addition. The AOM community in the sediment was reactivated in the laboratory at UCLA in April 2020 by mixing with anoxic artificial seawater medium at a ratio of 1:1 (v:v) (Widdel and Bak, 1992; Laso-Pérez et al., 2018) and a methane gas headspace as the sole amended carbon source in a 2-L glass bottle. The cultivation procedures of Laso-Pérez et al. (2018) were followed.

We performed a set of sulfide analyses to confirm the activity of AOM before starting the actual experiments. Sulfide concentration was measured after Cord-Ruwisch (1985) using a Shimadzu UV-Spectrophotometer (UV-1800). The relative standard deviation (RSD) of sulfide analysis was better than 5%. Sulfide concentration in the supernatant started to increase two months after the addition of substrates (sulfate and methane). Further, sulfide concentration increased ca. 0.07 mM per day between the 134th and 205th days since reactivation. The supernatant of the sediment slurry was replaced with fresh anoxic medium with seawater sulfate concentration (28 mM) when sulfide concentration approached 11 mM. After that, sulfide concentration continued to increase ca. 0.07 mM per day between the 206th and 283rd days since reactivation. Sulfide production from sulfate reduction with non-methane substrates was excluded by the control experiment (see below). The linear increase in sulfide concentration over time indicates that the ANME community was successfully reactivated in the sediment slurry. Thus, the

homogenized slurry was equally distributed to two 600-ml culture bottles in replicate and filled up completely with an anoxic artificial seawater medium (Laso-Pérez et al., 2018). Sixty ml of the medium volume was replaced with ca. 200 kPa of methane (Airgas), and both incubations were performed under excess sulfate (ca. 10 mmol) over methane (5.4 mmol) (cf. Ono et al., 2021). The sediment slurry was then stored horizontally at 4 °C in the dark. Methane isotopologue compositions were analyzed on days 1, 36, 44, 58, and 71 of the incubation. After the first experiment, we reset the slurry for longer incubation through medium replacement and bubbling with N_2/CO_2 gas. Methane isotopologue compositions were analyzed on days 1, 60, 90, and 168 of the incubation.

To further confirm and quantify the activity of AOM and sulfate reduction, we measured turnover rates with ^{14}C- and ^{35}S-radiotracer techniques, respectively, in the high-sulfate experiment. AOM rate was determined by injecting 20 µL of ^{14}C-methane tracer (dissolved in MilliQ water, activity 0.7 kBq, specific activity 185 MBq $mmol^{-1}$) into two 13 ml headspace-free sub-samples of the sediment slurry. Sulfate reduction rate was determined by injecting 10 µL of carrier-free ^{35}S-sulfate tracer (dissolved in MilliQ water, activity 234 kBq, specific activity 37 TBq $mmol^{-1}$) into a 10 ml sub-sample of the sediment slurry. The vials were incubated for two days at 4 °C in the dark. After incubation, sulfate reduction activity was terminated by transferring the sample from the glass vial to a centrifuge tube filled with 20 ml 20% zinc acetate followed by freezing at −30°C. Sulfate reduction rate was analyzed and calculated according to the cold chromium distillation method (Kallmeyer et al., 2004). To terminate AOM activity, samples were transferred to 50 ml glass vials filled with 20 ml 5% sodium hydroxide. The vials were sealed with rubber stoppers immediately and shaken thoroughly. AOM rate was determined according to Treude et al. (2005) and Joye et al. (2004).

After the high-sulfate experiment described above, the supernatant in the slurry was replaced with low-sulfate artificial seawater medium (1 mM) four times. The sulfate concentration in the slurry decreased over time due to medium replacement and microbial consumption. The produced sulfide was maintained at low concentrations (<1 mM) through medium replacement and bubbling with N_2/CO_2 gas. The culture bottle was then filled up completely with the low-sulfate medium, reaching a sulfate concentration of 0.4 mM in the slurry. Sixty ml of the medium volume was replaced with ca. 200 kPa of methane (Airgas), allowing the incubation to be performed under excess methane (5.4 mmol) over sulfate (<0.2 mmol). The low-sulfate experiment was performed identically to the high-sulfate experiment with sulfate concentration as the only variable at the beginning of each incubation. Towards the end of the low-sulfate experiment, sulfate was depleted (0.01 mM) in the slurry. Thus, an additional concentrated anoxic sulfate solution (2.5 ml) was added to the culture bottle by a syringe without opening the bottle, reaching a final sulfate concentration of 0.4 mM again in the slurry. Sulfate concentration was analyzed by ion chromatography (Metrohm 761). Alkalinity was determined by acid titration with a Metrohm 876 Dosimat Plus (Dale et al., 2015). The concentrations were calibrated against the IAPSO standard seawater (n=10) with RSD of sulfate and alkalinity analyses better than 2%. In addition, pH was determined by a pH meter (VWR sympHony B10P).

Methane concentration and isotopologue abundance were determined during the incubations on a vacuum line interfaced with a gas chromatograph, and the Panorama mass spectrometer, respectively, as described below in section 2.6. Given the known volume and porosity of the slurry, the amounts of methane that dissolved in the liquid phase were calculated using Henry's law and the Bunsen solubility coefficient (Yamamoto et al., 1976). For porosity analysis, the homogenized slurry was sampled using a syringe. Porosity was measured from the

volume of slurry and water weight loss after drying at 60 °C until a constant weight was reached. The total amounts of methane in the culture bottle were therefore the sum of methane in the headspace and the liquid phase.

The liquid phase was also sampled to determine the $\delta^{13}C$ of dissolved inorganic carbon (DIC) and the δD of water in the slurry (Atekwana and Krishnamurthy, 1998; Kopec et al., 2019). In brief, analysis of $\delta^{13}C_{DIC}$ was performed in 12 ml Labco Exetainer vials on a Thermo Scientific GasBench II coupled to a Thermo Finnigan Delta Plus XL isotope-ratio mass spectrometer (IRMS) at the UC Davis Stable Isotope Facility. Isotopic values are reported in δ-notation relative to the Vienna Pee Dee Belemnite (VPDB) standard. Analytical precision for $\delta^{13}C$ is better than 0.1‰ (1σ) based on replicate analyses of laboratory standards. Analysis of hydrogen isotopic composition of water was conducted at the Stable Isotope Laboratory at Dartmouth College. The δD values of water were measured using an H-Device, in which water was reduced by hot chromium (850 °C), and the resulting hydrogen gas was measured by a Thermo Delta Plus XL IRMS. Isotopic ratios are reported in δ-notation relative to the Standard Mean Ocean Water (VSMOW) standard. Analytical precision for δD is better than 0.5‰ (1σ) based on replicate analyses of laboratory standards.

A control incubation was set up to assess potential microbial methanogenesis and organoclastic sulfate reduction in the same sediment slurry. The control experiment was prepared by replacing the supernatant with a new methane-free anoxic artificial seawater medium and a 60-ml headspace was left to monitor methane concentration. The slurry was then bubbled thoroughly with N_2/CO_2 (80:20) three times (3 hours in total) to get rid of the residual dissolved methane and sulfide from the previous experiments. The slurry was stirred during and between flushing to drive the dissolved methane into the headspace. The control experiment slurry was stored in the dark at

4 °C for three months. The slurry supernatant was collected for sulfide and sulfate concentrations at the start and end of the control incubation. Methane concentration in the gas phase was measured by gas chromatography throughout the three months.

2.2. Incubation of methane seep sediment slurries from the Santa Barbara Channel

Marine sediments were collected with four push cores from the Coal Oil Point seep field (Rostocker Seep and Isla Vista Super Seep) in the Santa Barbara Channel in 2017 (Jordan et al., 2020). The top 12.5 cm sediment of the cores was transferred to 300 ml culture bottles at UCLA following the same procedure as detailed in the Svalbard slurry section above. Low sulfate (< 1 mM) and high sulfate (> 28 mM) concentrations were achieved in the sediment slurry by either dilution steps with anoxic artificial seawater (without sulfate) or additions of concentrated sodium sulfate solution (100 mM). The sediment slurry was incubated in the dark with a 4.4 ml headspace of methane at ca. 100 kPa and 20 °C on a shaker. The methane gas bubble from the sediment slurry was extracted at the end of each experiment and geochemistry analyses were performed as described in the Svalbard slurry section. A similar control experiment followed the Svalbard slurry section with a 4.4 ml Argon headspace.

2.3. Incubations of sediment slurry and fracture fluid from the deep biosphere (Nankai Trough and Beatrix Gold Mine)

Hole C0023A (32°22.0018′ N, 134°57.9844′ E), located in the Nankai Trough on the subduction boundary between the Philippine Sea and Eurasian plates, was drilled during International Ocean Discovery Program (IODP) Expedition 370 in 2016 (Heuer et al., 2017).

Marine sediments from 257 m below seafloor (mbsf) were sampled anoxically with rigorous contamination control (see Heuer et al., 2017) and utilized for sediment incubation. In brief, whole-round cores (WRCs) were prepared from recovered sections under super-clean and anoxic conditions onboard the *Chikyu* Drilling Vessel. X-ray computed tomography was performed on all WRCs for lithological identification and to assess core quality on board. Samples without drilling disturbances were designated for incubation and were subjected to secondary scraping to minimize the potential for contamination.

At South Africa's Beatrix Gold Mine (28 ˚14.1′ S, 26˚47.7′ E), fracture fluid was collected in 2016 from the BE326-BH2 borehole, from 1390 m below land surface (mbls) in shaft 3, level 26. A detailed description of the study site and sample collection has been published in Lau et al. (2016). Briefly, fracture fluid was filtered using a 0.2 µm hollow fiber MediaKap®-10 filter. The microorganisms on the filter were anoxically back-flushed into sterile, capped, N_2-sparged 160-ml borosilicate serum vials to a final cell concentration of ~ 10^7 cells ml^{-1}. Samples were stored at 4 °C upon return to the surface and used for incubation.

Incubations were set up inside a clean anoxic glove bag at Princeton University. Sterile aluminum foil was placed on the working surface of the glove bag and sterile nitrile gloves were used over the glove bag's butyl rubber gloves to minimize potential contamination of low-biomass samples. The surface of C0023A samples was scraped using a sterile scalpel to remove sediment exposed to gas-tight packaging. A total of 10 g (wet weight) of interior sediment was weighed out from sample source core C0023A-5F02 (top depth 257.3 mbsf) and transferred into combusted 160-ml borosilicate serum vials containing 100 ml artificial sulfate-free seawater medium modified from the recipe by Widdel and Bak (1992). For the BE326-BH2 incubation, 10 ml of fracture fluid was added to 90 ml of artificial sulfate-free seawater medium. Serum vials were

sealed with 0.1 N NaOH-boiled butyl rubber stoppers and aluminum crimps, and the headspace was subsequently replaced with 100% methane. Each incubation was supplemented with 10 mM of one of the following electron acceptors: NO_3^-, NO_2^-, SO_4^{2-}, or Fe^{3+} (in the form of hydrous ferric oxide). A control without added electron acceptors was included to assess endogenous microbial activity from remnant electron acceptors available in the inoculum, and an autoclaved sample was included as a killed control. Serum vials containing sediment slurry or fracture fluid were incubated upside-down at an approximate *in-situ* temperature of 40 °C. At UCLA, the collected residual methane was purified for isotopologue analysis following the method described in section 2.6.

Electron acceptor depletion was monitored using Dionex IC25 ion chromatography coupled to an MSQ-quadruple mass spectrometer (Thermo Scientific). The sediment slurry or fracture fluid was also subsampled to monitor the $\delta^{13}C$ of DIC. Briefly, 500 µl aliquots were anoxically transferred to combusted, amber borosilicate serum vials treated with saturated $HgCl_2$ and aluminum-crimped sealed with butyl rubber stoppers. Following sample transfer, vials were over-pressurized with ultra-high purity N_2 gas, supplemented with 0.5 N H_3PO_4, and heated overnight in a water bath at 70 °C to extract all DIC out of the solution. Isotopic composition of the headspace was analyzed using a Picarro cavity ring-down spectrometer equipped with a G2101-I Isotopic CO_2 analyzer in CO_2 focus mode.

2.4. Methyl-coenzyme M reductase (Mcr) experiments

The experiment was performed as described previously with the Mcr enzyme purified from *Methanothermobacter marburgensis* (Mahlert et al., 2002; Scheller et al., 2010) at Pennsylvania

State University. Mcr that was used for this assay had absorbance maxima at 387 nm, corresponding to the enzyme's active (Ni^{+}) form. Coenzyme B (HS-CoB) was prepared from the symmetric disulfide CoB-S-S-CoB by reaction with $NaBH_4$. Methyl-coenzyme M (CH_3-S-CoM) was synthesized from coenzyme M (sodium salt) by methylation with methyl iodide. The complete reaction mixture (4 ml) contained 5 mM CH_3-S-CoM, 2.5 mM HS-CoB and 32.3 mg of Mcr in 50 mM phosphate buffer (pH 7.6). This allowed isotope exchange of the methyl moiety in methyl-coenzyme M and methane to occur. The reaction mixtures were incubated at 20 °C for 48 hours or 60 ºC for 2–6 hours in a stoppered 10-ml serum vial with a methane headspace of ca. 100 kPa. The difference in incubation times is due to more rapid reaction at 60 ºC. Control reactions contained the complete reaction mixture minus enzyme. At UCLA, the collected gas was purified for isotopologue analysis following the method detailed in section 2.6.

2.5. Methane-bearing natural fluids at the South Chamorro Seamount

South Chamorro Seamount is an active serpentinite mud volcano at ca. 3150 m water depth in the Mariana forearc. In 2001, Hole 1200C was drilled to 266 mbsf and cased during Ocean Drilling Program (ODP) Leg 195 in the summit knoll of South Chamorro Seamount (Fryer and Salisbury, 2006). An oceanic borehole observatory, commonly called a CORK (Circulation Obviation Retrofit Kit), was deployed for subsequent fluid sampling (Wheat et al., 2008). The discharged fluids were largely altered relative to seawater composition, displaying a high pH up to 12.3 with abundant dissolved methane up to 33 mM (Wheat et al., 2008; Wheat et al., 2020). In January 2009, pristine crustal fluids were collected directly as they discharged at Hole 1200C with a remotely operated vehicle (ROV) *HyperDolphin* (HPD Dives 941–947) during Cruise NT09-01 (Wheat et al., 2020). Isobaric gas-tight samplers (Seewald et al., 2002) were used for fluid

sampling. Immediately upon recovery of the ROV, fluid samples were subsampled for liquid and gas analyses. Gas extraction from fluid samples was conducted using previously reported techniques (Seewald et al., 2002). At UCLA, the collected gas was purified for isotopologue analysis following the method detailed in the next section.

2.6. Doubly substituted isotopologue measurements and isotope notation

Methane isotopologue abundances of methane gas samples were measured using the Panorama (Nu Instruments) high-mass-resolution gas-source isotope ratio mass spectrometer housed at UCLA. Details surrounding the purification and measurement of methane gas were previously published (Young et al., 2016; Young et al., 2017) and are briefly summarized here. Methane sample gases were purified on a vacuum line interfaced with a gas chromatograph (GC). Samples were delivered to the vacuum line through a septum by a gas-tight syringe and trapped on silica gel at liquid nitrogen temperature. The Helium carrier gas was then used to flush the sample to the GC. Separation was accomplished with a 3-meter 1/8-inch OD stainless steel column packed with 5 Å molecular sieve, followed in series by a 2-meter 1/8-inch OD stainless steel column packed with HayeSep D porous polymer. Peaks were identified using an in-line, passive thermal conductivity detector (TCD). Once methane collection was complete, the sample was transferred to an evacuated sample tube filled with silica gel at liquid nitrogen temperature. Methane in this tube was introduced to the inlet of the mass spectrometer where it was warmed to 40 °C and expanded into the bellow of the instrument.

The Panorama mass spectrometer was set to a mass resolving power of ~40,000 or greater, allowing the measurement of ion currents for resolved $^{12}CH_4^+$, $^{13}CH_4^+$, $^{12}CH_3D^+$, $^{13}CH_3D^+$, and

$^{12}CH_2D_2^+$. Isotopologues of masses 16 and 17 were measured using Faraday collectors with amplifier resistors of 10^{11} Ω. Both doubly substituted mass-18 isotopologues, $^{13}CH_3D^+$ and $^{12}CH_2D_2^+$, were measured with an electron multiplier as the axial collector. The measured ratios of these ion currents yield values for bulk $^{13}C/^{12}C$ and D/H as well as for both $\Delta^{13}CH_3D$ and $\Delta^{12}CH_2D_2$. The isotopic compositions of carbon and hydrogen are reported as deviations from the carbon and hydrogen reference materials VPDB and VSMOW. Standard delta notation is used to express the fractional differences in per mil units:

$$\delta^{13}C = [(^{13}C/^{12}C)_{sample}/(^{13}C/^{12}C)_{VPDB} - 1] \times 1000 \quad (1)$$

$$\delta D = [(D/H)_{sample}/(D/H)_{VSMOW} - 1] \times 1000 \quad (2)$$

The relative abundances of the two mass-18 isotopologues of methane are reported relative to the stochastic reference frame expressed in per mil using the capital delta notation:

$$\Delta^{13}CH_3D = [(^{13}CH_3D/^{12}CH_4)_{sample}/(^{13}CH_3D/^{12}CH_4)_{stochastic} - 1] \times 1000 \quad (3)$$

$$\Delta^{12}CH_2D_2 = [(^{12}CH_2D_2/^{12}CH_4)_{sample}/(^{12}CH_2D_2/^{12}CH_4)_{stochastic} - 1] \times 1000 \quad (4)$$

Analytical uncertainties are estimated from the long-term reproducibility of the thermogenic Utica Shale gas through the same purification process (n=22). External precision for $\delta^{13}C$, δD, $\Delta^{13}CH_3D$, and $\Delta^{12}CH_2D_2$ is found to be approximately 0.1‰, 0.3‰, 0.3‰ and 0.7‰, respectively (1σ). The relationship between temperature and both $\Delta^{13}CH_3D$ and $\Delta^{12}CH_2D_2$ has been predicted through *ab initio* calculations based on the harmonic approximation and can be expressed by the following equations (Young et al., 2017):

$$\Delta^{13}CH_3D\ (T) \approx 1000\ \ln(1 + 0.0355502/T - 433.038/T^2 + 1270210.0/T^3 - 5.94804 \times 10^8/T^4 + 1.196630 \times 10^{11}/T^5 - 9.07230 \times 10^{12}/T^6) \quad (5)$$

$$\Delta^{12}CH_2D_2\ (T) \approx 1000\ \ln(1 + 0.183798/T - 785.483/T^2 + 1056280.0/T^3 + 9.37307 \times 10^7/T^4 - 8.919480 \times 10^{10}/T^5 + 9.901730 \times 10^{12}/T^6) \quad (6)$$

where T is in Kelvin. Eqs. (5) and (6) show that $\Delta^{13}CH_3D$ and $\Delta^{12}CH_2D_2$ values are both positive when methane is formed at thermodynamic equilibrium, and approach 0‰ at high temperatures (>1000 K).

2.7. Calculation of isotope fractionation factors using Rayleigh equation

Incubations were performed in glass bottles with frequent shaking and the headspace methane was considered a well-mixed source in a closed system. Although methane in the headspace was extracted once or twice between the start and end of each experiment, the amount of methane extracted was minor (<3%) compared to the amount of methane in the whole bottle, resulting in a negligible deviation from a strictly closed system. Thus, the Rayleigh fractionation equation (Mariotti et al., 1981) was used to extract fractionation factors for the $^{13}CH_4$, $^{12}CH_3D$, $^{13}CH_3D$, and $^{12}CH_2D_2$ isotopologues relative to $^{12}CH_4$ resulting from anaerobic fractionation:

$$\frac{R_t}{R_0} = \left(\frac{[^{12}CH_4]_t}{[^{12}CH_4]_0} \right)^{\alpha - 1} \quad (7)$$

where R refers to the ratio of isotopologues of interest in the gas phase (e.g., $^{13}CH_3D/^{12}CH_4$, $^{12}CH_2D_2/^{12}CH_4$), the subscript *0* signifies the initial property, and the ratio of methane abundance at time *t* relative to the initial methane abundance is commonly referred to as F (fraction remaining). For kinetic fractionations, the fractionation factor α is simply the ratio of the rate constant associated with the reaction of an isotopically substituted isotopologue relative to the rate constant of the unsubstituted isotopologue. These can include ratios of symmetry numbers. For the sake of

simplification, the isotopologue fractionation factor for $^{13}CH_3D$ and $^{12}CH_2D_2$ relative to $^{12}CH_4$ are termed $^{13D}\alpha$ and $^{D2}\alpha$, respectively. By convention, $\alpha < 1$ signifies that the reaction favors the isotopically light species, leaving the residue enriched in the heavy isotope or isotopologue. On a plot of $-\ln F$ vs. $\ln(R/R_0)$, the slope (often termed ε) provides the fractionation factor ($^{13}\varepsilon = 1-{}^{13}\alpha$ or $^{D}\varepsilon = 1-{}^{D}\alpha$). Fractionations and their uncertainties (95% confidence interval) are calculated by the weighted least square method (York et al., 2004). Errors for methane concentrations are estimated to be 0.4% of the measured value. Note that the F ratio was only measured in the incubation experiment of the Svalbard methane seep sediments.

At zeroth order, the relationship among isotopologue fractionation factors would follow the rule of the geometric mean (Bigeleisen, 1955), in which a stochastic distribution of isotopes occurs among the isotopologues. This would be the case where there is no energetic preference for forming doubly substituted isotopologues as opposed to randomly distributing isotopes among bonds (e.g., $^{13D}\alpha \approx {}^{13}\alpha \cdot {}^{D}\alpha$). Under these circumstances, the fractionation factors for the doubly substituted species are simply the products of the fractionation factors for the individual isotopes (i.e., the square of the geometric mean of the fractionation factors for doubly substituted species). The deviation from the rule of the geometric mean can be characterized by the kinetic clumped isotopologue fractionation factor, γ, yielding (cf. Wang et al., 2016):

$$^{13D}\alpha = {}^{13D}\gamma \cdot {}^{13}\alpha \cdot {}^{D}\alpha \tag{8}$$

$$^{D2}\alpha = {}^{D2}\gamma \cdot {}^{D}\alpha \cdot {}^{D}\alpha \tag{9}$$

2.8. Open system model — steady-state between transport and oxidation of moving methane

In natural environments, Rayleigh-type methane oxidation is rarely observed because replenishment of methane, facilitated by advection or diffusion, usually applies. We will consider two end-member environmental scenarios: a steady-state open system model presented in this section and a time-dependent closed system model with a methane source and sink in the next section.

In the open system model, methane is transported into and out of the system via advection with concurrent AOM. A steady state between oxidation and supply is assumed to have been attained. A mass balance equation at steady state can be expressed as (Hayes, 2001; Wang et al., 2016):

$$R_0 = (1 - \varphi)\, R_{SS} + R_{SS}\, \varphi\, \alpha \tag{10}$$

where R_0 is the initial isotopologue ratio, R_{SS} is the steady-state value, φ is the fraction of methane removed via oxidation relative to that which flows through, and α is the kinetic fractionation factor associated with the oxidation reaction. Such a steady state will occur where the supply and sink occur at constant rates. Here, advection is assumed to have no isotope effect (Alperin et al., 1988), whereas AOM has associated fractionation factors $^{13}\alpha$, $^{D}\alpha$, $^{13D}\gamma$, and $^{D2}\gamma$. The fractional contribution of AOM to the total sink, φ, is physically related to the Damköhler number, i.e., *Da*, the ratio of the residence time in the flow system to the characteristic reaction time ($Da = \tau_{flow} / \tau_{reaction}$). For a first-order reaction, the dimensionless Damköhler number can be simplified to $\tau_{flow} \times k$ where τ_{flow} is the residence time and k is the reaction rate constant with units of inverse time. The φ values are normalized *Da* values, as in $\varphi = Da/(1+Da)$. Therefore, if k is large in comparison to τ, *Da* is large and φ approaches 1. At this extreme, a balance between production and oxidation is achieved in a closed system as described in the next section. Conversely, if k is small in comparison to τ, φ approaches 0 and the isotopologue ratio does not change. Values in between

these extrema cause the steady-state values to be intermediate between the initial isotopologue ratios and the values at $\varphi = 1$.

2.9. Closed system model — formation of methane balanced against oxidation

In the closed system model, the time-dependent evolution of the moles of an isotopologue of methane can be described in terms of a constant rate of production and a rate of oxidation that behaves as a first-order reaction with an invariable rate constant (Haghnegahdar et al., 2017). In this simplest model, where the balance is only between production and consumption, the system can be described as:

$$\frac{dn_i}{dt} = E_i - k_i n_i, \tag{11}$$

where n_i is the moles of the isotopic species of interest, E_i is the source term for i (e.g., rate of abiotic or microbial methanogenesis), and k_i is the rate constant for the sink i (i.e., the rate constant for oxidation). The solution to Eq. (11) yields:

$$n_i(t) = n_i^0 \mathrm{e}^{-k_i t} + \frac{E_i}{k_i}\left(1 - \mathrm{e}^{-k_i t}\right), \tag{12}$$

where n_i^0 is the initial moles of i. The moles of species i at steady state are obtained by evaluation Eq. (12) where $t \to \infty$, and thus $e^{-k_i t} \to 0$, yielding:

$$n_i(t \sim \infty) = \frac{E_i}{k_i}. \tag{13}$$

Considering *i* to be the major isotopologue, the steady-state amount of methane is controlled by the ratio of the production rate and the rate constant for oxidation. The steady-state ratio of two isotopologues can therefore be expressed as:

$$\frac{n_j(t \sim \infty)}{n_i(t \sim \infty)} = \frac{E_j}{E_i}\frac{k_i}{k_j} \tag{14}$$

where *n* is the moles of the two isotopologues *i* and *j*. The steady-state isotopologue ratio depends on the isotopologue ratio of the methane produced (E_j/E_i) and the reciprocal of the fractionation due to oxidation (k_i/k_j), independent of the absolute rates.

2.10. Comparison between measured and theoretically estimated isotope fractionation factors

To understand the meaning of the measured isotope fractionation factors from the Svalbard experiment, we used two methods to estimate the fractionation factors with mechanistic implications. Firstly, if the kinetics is dominated by rupture of single carbon-hydrogen bonds comprising the reaction coordinate, the fractionation factors can be estimated by the square root of the inverse ratios of relevant reduced masses, $\sqrt{\mu / \mu'}$. Here the μ' values are the reduced masses for ^{13}C-H and ^{12}C-D as required, μ is the reduced mass for ^{12}C-H, and the derived fractionation factors are those implied by these reduced masses, including the use of the rule of the geometric mean for the doubly-substituted species.

Secondly, we consider the ratio of the logarithm of rotational/vibrational partition functions for a crude estimate for the transition state of methane being dismantled by the Mcr-mediated reaction. The Q* values are estimated by calculating the partition function for methane at 4 °C

with the three asymmetric stretch modes (commonly referred to as ν_3) removed. The differences among the partition functions for the different isotopologues are evidenced clearly by writing their ratios where the prime superscript refers to the isotopically-substituted species (Bigeleisen and Mayer, 1947; Urey, 1947):

$$\frac{Q'}{Q} = \frac{\sigma}{\sigma'} \prod_i \frac{u_i'}{u_i} \frac{e^{-u_i'/2}}{1-e^{-u_i'}} \frac{1-e^{-u_i}}{e^{-u_i/2}} \tag{15}$$

We used the vibrational frequencies calculated by Lee et al. (1995). For our rough estimate of a suitable transition state bound to Mcr (an imprecise exercise in its own right), we removed the ν_3 modes from Eq. (15). This approach provides a test of the possibility that it is the highest frequency modes, ν_3, that are most readily broken and dominate the kinetics (and thus are not counted in the vibrational partition functions). Ratios of vibrational frequencies, or the square root of the inverse ratio of reduced masses, are ratios of energies associated with a vibration. Values lnQ* are also proportional to energies, but represent the weighted mean across all vibrations not involved in bond rupture (Bigeleisen, 1952). The ratio is therefore an estimate of the relative energy associated with motions in the molecules.

3. RESULTS

Methane isotopologue data from laboratory experiments and natural fluids are presented in Figure 3. The $\Delta^{13}CH_3D$ and $\Delta^{12}CH_2D_2$ values from the Svalbard sediment slurry incubation and Chamorro Seamount natural fluids are higher than thermodynamic equilibrium values at their ambient temperature (>0 °C; Fig. 3A–C). Other incubations, including the Mcr-catalyzed isotope exchange and incubations of the Santa Barbara Channel sediment, Nankai Trough sediment, and

Beatrix Gold Mine fracture fluid, show moderate increases in $\Delta^{13}CH_3D$ but minimal increases in $\Delta^{12}CH_2D_2$ (Fig. 3D–F). Their apparent temperatures based on clumped isotopes are similar to the experimental temperatures, ranging from 20 °C to 60 °C. In the following sections, we first present the laboratory incubation data and then show natural fluid data for comparison.

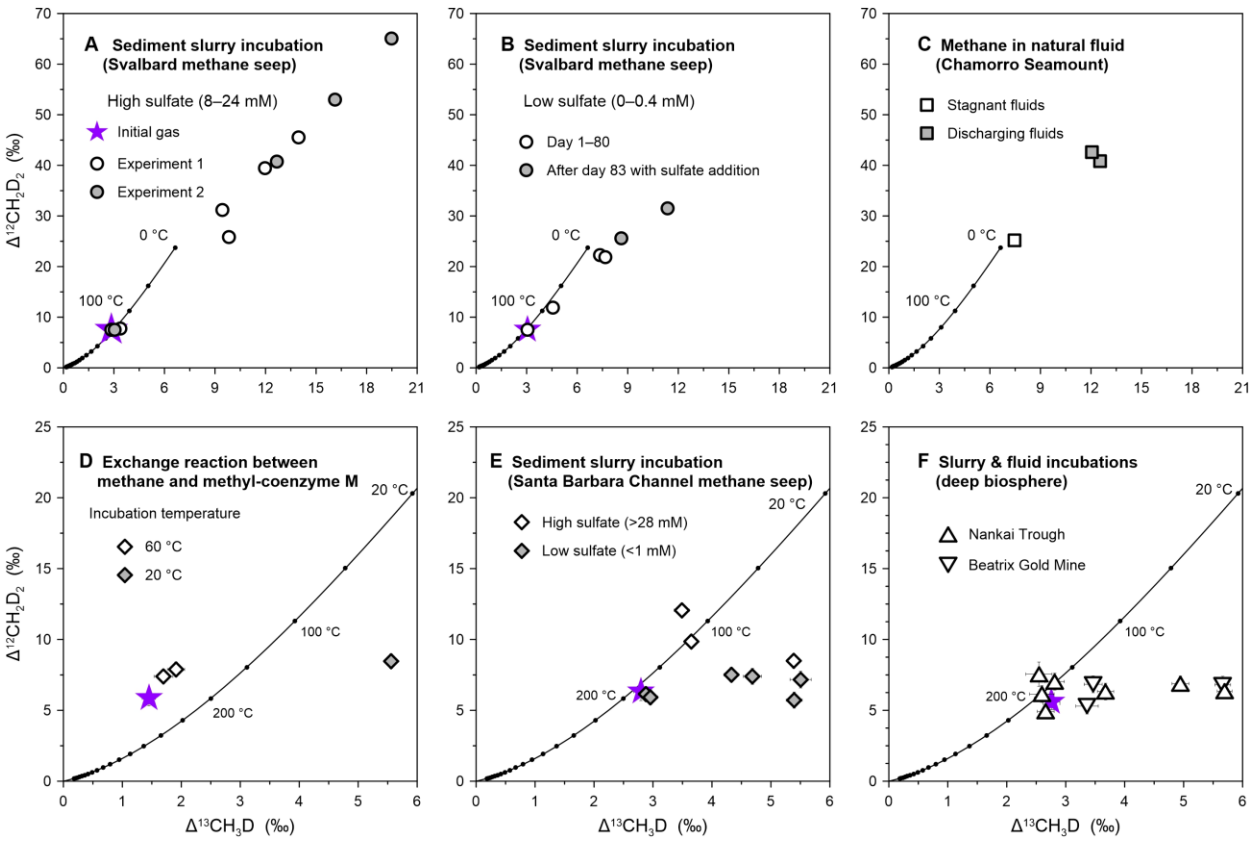

Fig. 2-3 Clumped isotope data of residual methane in AOM incubation experiments and natural fluids. (A–B) Incubation of the Svalbard methane seep sediment slurry with high sulfate concentration (8–24 mM; panel A) and low sulfate concentration (0–0.4 mM; panel B). (C) Methane in natural fluids collected from the South Chamorro Seamount. (D) Exchange reaction between methane and methyl-coenzyme M. (E) Incubation of the Santa Barbara Channel methane seep sediment slurry. (F) Incubations of the Nankai Trough sediment slurry and Beatrix Gold Mine

fracture fluid from the deep biosphere. The purple stars represent the initial tank gas. The solid black line depicts theoretical thermodynamic equilibrium abundances of methane isotopologues, along with corresponding temperatures. Error bars are one standard error. Note different scales between panels A–C and D–F.

3.1. Incubation of the Svalbard methane seep sediment slurries

Off-shore methane seep sediments from the Svalbard archipelago host high AOM activity. *Ex-situ* AOM rates determined by ^{14}C-radiotracer techniques peak at 182 nmol cm^{-3} d^{-1} at 2–5 cm below seafloor (Fig. 2A) (Melaniuk et al., 2022). In the reactivated sediment slurry with saturated methane and high sulfate concentrations (8–24 mM), dissolved sulfide concentrations increased linearly as methane concentrations decreased linearly (Fig. 2B). In addition, sulfate concentrations decreased, while alkalinity increased during the experiment (see the Supplementary Data). In the control experiment containing a headspace gas of N_2 and CO_2, no methane was detected and no increase in sulfide concentration was observed, indicating negligible methanogenesis and organoclastic sulfate reduction, respectively (Fig. S1A). Collectively, AOM is active in the sediment slurry and is the only mechanism for methane removal in the experiment. Accordingly, the *in-vitro* AOM rate determined by methane concentrations in the slurry incubation was 90 nmol of methane per cm^3 sediment slurry per day (Fig. 2B), translating into about 180 nmol per cm^3 of undiluted sediment per day. Furthermore, the *in-vitro* AOM and sulfate reduction rates determined by ^{14}C- and ^{35}S-radiotracers were 86 and 84 nmol cm^{-3} d^{-1}, respectively, in the slurry incubation, which are equivalent to roughly 172 and 168 nmol cm^{-3} d^{-1} for undiluted sediment. The *in-vitro* AOM rates are consistent with the *ex-situ* AOM rates of the same sediment measured by ^{14}C-

radiotracer (Fig. 2A) and other *in-vitro* AOM enrichment cultures (e.g., Ono et al., 2021; Wegener et al., 2021).

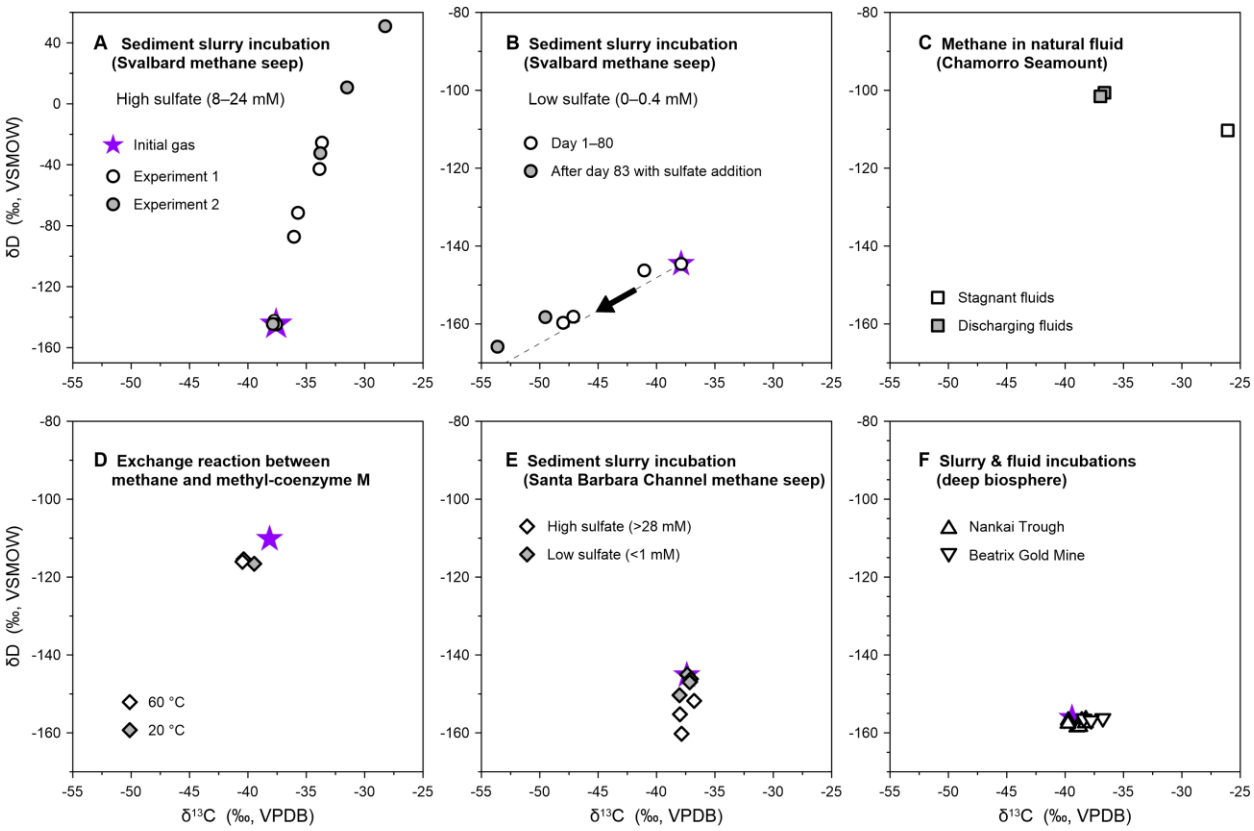

Fig. 2-4 Bulk isotope data of residual methane in AOM incubation experiments and natural fluids. (A–B) Incubation of the Svalbard methane seep sediment slurry with high sulfate concentration (8–24 mM; panel A) and low sulfate concentration (0–0.4 mM; panel B). The arrow and dashed line in panel B indicate the evolution of residual methane towards isotope equilibrium among CH_4, HCO_3^- and H_2O at 4 °C (Zhang et al., 1995; Turner et al., 2021). (C) Methane in natural fluids collected from the South Chamorro Seamount. (D) Exchange reaction between methane and methyl-coenzyme M. (E) Incubation of the Santa Barbara Channel methane seep sediment slurry. (F) Incubations of the Nankai Trough sediment slurry and Beatrix Gold Mine

fracture fluid from the deep biosphere. The purple stars represent the initial tank gas. Uncertainties of $\delta^{13}C$ and δD values are encompassed by individual data points.

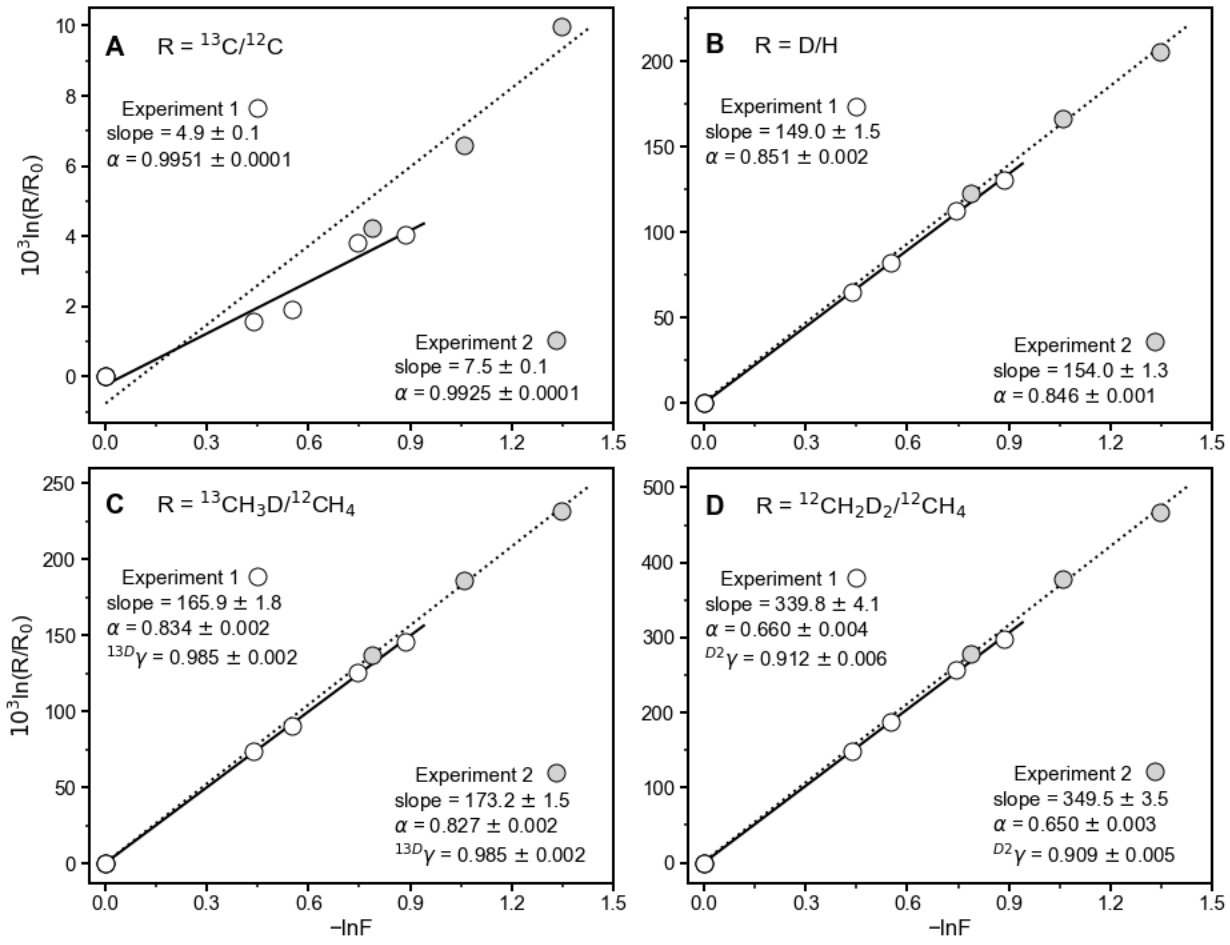

Fig. 2-5 Evolution of methane isotopologue ratios during methane consumption in the incubation of the Svalbard methane seep sediment slurry with high sulfate concentration (8–24 mM). Data from experiments 1 and 2 are shown in open and filled circles, respectively. F is the fraction of methane remaining and R is the ratio of isotopologues in the gas phase. α and γ represent the kinetic isotope fractionation factor and clumped isotopologue fractionation factor, respectively.

The linear regressions and 2σ errors are calculated by the weighted least square method of York et al. (2004).

In two experiments with high sulfate, the bulk $\delta^{13}C$ and δD values of residual methane increased by 9.6‰ and 195.4‰, respectively, with declining methane concentrations (Fig. 4A). Based on a Rayleigh distillation model, the respective carbon and hydrogen isotope fractionation factors, expressed in per mil, were found to be 4.9 ± 0.1‰ and 149.0 ± 1.5‰ in the first experiment, and 7.5 ± 0.1‰ and 154.0 ± 1.3‰ in the second experiment (Fig. 5A–B). With progressive methane consumption, $\Delta^{13}CH_3D$ and $\Delta^{12}CH_2D_2$ values increased by 16.4‰ and 57.6‰, reaching values of 19.5‰ and 65.1‰, respectively (Fig. 3A). These values are substantially higher than the values expected for isotopologue equilibrium at the incubation temperature of 4 °C. The kinetic clumped isotopologue fractionations (γ), defined as the ratio of the mass-18 isotopologue fractionation factors to the product of the bulk carbon and hydrogen fractionation factors, describe deviations from the rule of the geometric mean (Bigeleisen, 1955; Wang et al., 2016). The respective γ values for $^{13}CH_3D$ and $^{12}CH_2D_2$ defined by these data were 0.985 ± 0.002 and 0.912 ± 0.006 in the first experiment, and 0.985 ± 0.002 and 0.909 ± 0.005 in the second experiment (Fig. 5C–D). With declining methane concentrations, the $\delta^{13}C$ values of DIC decreased by 6‰ in the first experiment and 10‰ in the second experiment, whereas the δD values of water were more-or-less invariant (see the Supplementary Data).

The same sediment slurry was then incubated with low sulfate concentration (<0.35 mM) under the same conditions (e.g., saturated methane), resulting in a lower thermodynamic driving force for AOM. Methane isotopologue compositions were analyzed on days 1, 11, 58, and 79 of the incubation. In contrast to the high sulfate experiment, the bulk $\delta^{13}C$ and δD values of residual

methane decreased by 10.1‰ and 15.2‰, respectively (Fig. 4B). The $\Delta^{13}CH_3D$ and $\Delta^{12}CH_2D_2$ values, however, increased linearly by 4.6‰ and 14.8‰, respectively (Fig. 3B). There is no substantial difference in $\Delta^{13}CH_3D$ and $\Delta^{12}CH_2D_2$ values of residual methane taken on days 58 and 79, likely signaling a reduction in the AOM rate due to sulfate limitation (0.01 mM). To examine whether the residual methane will approach isotopologue equilibrium or overshoot it, additional sulfate was added on day 83, to increase the concentration again to 0.39 mM in the slurry. Isotopologue ratios of the residual methane were analyzed on days 92 and 178 of the incubation. Both $\Delta^{13}CH_3D$ and $\Delta^{12}CH_2D_2$ values increased up to 11.4‰ and 31.5‰, respectively (Fig. 3B). Net isotope fractionation factors are not reported here for low sulfate incubation because of the challenge of accurately quantifying methane consumption, limiting our ability to estimate the fraction of methane remaining in the Rayleigh process, and thus causing large errors, but both $^{13}\alpha$ and $^{D}\alpha$ are higher than 1.0, in contrast with the high sulfate incubation in which both $^{13}\alpha$ and $^{D}\alpha$ are lower than 1.0 (Figs. 4A–B, 5). The $\delta^{13}C$ values of DIC decreased by 2‰, less pronounced than the high-sulfate experiments, whereas the δD values of water remained constant (see the Supplementary Data).

3.2. Incubation of the Santa Barbara Channel methane seep sediment slurries

Analogous to the incubation of Svalbard sediment slurry, we conducted incubation with Santa Barbara Channel sediment slurries at 20 °C. However, the volume and pressure of headspace methane in the Santa Barbara slurry (4.4 ml under ca. 100 kPa) were much lower than those of the Svalbard slurry (60 ml under ca. 200 kPa), presumably leading to a lower thermodynamic driving force for AOM. An earlier study at the same sites of the Santa Barbara Channel found that the e*x-situ* AOM rates determined by ^{14}C-radiotracer techniques were relatively high, on the order of tens

to hundreds of nmol cm^{-3} d^{-1} (Treude and Ziebis, 2010). All incubations with methane headspace showed decreases in sulfate concentration and increases in dissolved sulfide concentration and alkalinity over time (see the Supplementary Data). Along with the e*x-situ* AOM rates reported in the earlier study and the control experiment (Fig. S1B), these trends indicate the activity of AOM. Some δD values of residual methane decreased by up to 15.0‰, whereas the $\delta^{13}C$ values remained roughly constant over time under both high and low sulfate conditions (Fig. 4E). In the high sulfate slurries (>28 mM), both $\Delta^{13}CH_3D$ and $\Delta^{12}CH_2D_2$ of residual methane increased, ranging from 3.5‰ to 5.4‰ for $\Delta^{13}CH_3D$ and from 8.5‰ to 12.1‰ for $\Delta^{12}CH_2D_2$ (Fig. 3E). In the low sulfate slurries (<1 mM), the $\Delta^{12}CH_2D_2$ values remained nearly constant over time (6.7 ± 0.9‰), while the $\Delta^{13}CH_3D$ increased by 2.7‰, reaching a value of 5.5 ± 0.2‰ relative to stochastic (Fig. 3E). For comparison, when methane molecules are at thermodynamic equilibrium at 20 °C, the respective $\Delta^{13}CH_3D$ and $\Delta^{12}CH_2D_2$ values would be 5.9‰ and 20.3‰ (Young et al., 2017).

3.3. Incubation of sediment slurries and fracture fluids from the deep biosphere

Marine sediments and fracture fluids were sampled from the deep subsurface of the Nankai Trough and the Beatrix Gold Mine, respectively. Metagenomics, metatranscriptomics, and fluorescent *in situ* Hybridization (FISH) of the Beatrix Gold Mine fluids were previously published and the results demonstrated that ANMEs are present and active in the incubations (Lau et al., 2016; Harris et al., 2018; Harris et al., 2021). In parallel to the natural abundance incubations described in Section 2.3, long-term (350 day) high-pressure (40 MPa) ^{13}C-CH_4 tracer incubations were performed on Nankai Trough sediment slurries (see Supplementary Methods and Fig. S2). Based on the production of ^{13}C-DIC (Fig. S3) and $\delta^{13}C_{DIC}$ measurements (Fig. S4), trace AOM activity was statistically distinguishable above background, albeit at very low rates (on the order

of pmol cm^{-3} day^{-1}). These findings agree with ^{14}C-CH_4 radiotracer experiments reported by Beulig et al. (2022), who found potential AOM activity near detection limits in the Nankai Trough sediments due to a high background of abiotic ^{14}C-CH_4 conversion to ^{14}C-CO_2 in the medium controls. These results collectively highlight the difficulty in quantifying AOM activity in these oligotrophic, low-biomass, deep biosphere sediments (see Heuer et al., 2020). Thus, only potential AOM activity has been observed and no explicit discussion can be made in this respect.

The bulk isotope data of incubation experiments are consistent with the sluggish nature of microbial activity in the deep subseafloor. Here, nearly all headspace methane showed no substantial changes in $\delta^{13}C$ and δD values (<2‰; Fig. 4F). However, substantial changes were found for clumped isotope ratios. In the Nankai Trough slurries with nitrate or nitrite as the added electron acceptors, only $\Delta^{13}CH_3D$ increased, reaching a value of 5.7 ± 0.1‰ as incubation time progressed (Figs. 3F, S5C). Similarly, when iron(III) in the form of hydrous ferric oxide was added as the electron acceptor in the Beatrix Gold Mine incubation, $\Delta^{13}CH_3D$ increased up to 5.7 ± 0.1‰, while there was less increase in $\Delta^{13}CH_3D$ when sulfate or no electron acceptor was added (Figs. 3F, S5D). Little variation in $\Delta^{12}CH_2D_2$ values was found in these experiments (Fig. 3F).

3.4. Incubation with methyl-coenzyme M reductase (Mcr) enzyme

We performed experiments with Mcr purified from *Methanothermobacter marburgensis* that catalyzes the exchange of the methyl moiety of methyl-coenzyme M with methane. The $\delta^{13}C$ and δD of residual methane decreased by up to 2.3‰ and 6.4‰ in all cases, respectively (Fig. 4D). Both $\Delta^{13}CH_3D$ and $\Delta^{12}CH_2D_2$ increased to different degrees relative to the initial methane isotopologue ratios (Fig. 3D). In detail, at 60 °C, the incubations lasted for 2–6 hours in which a

small increase of 0.5‰ in $\Delta^{13}CH_3D$ and 2.0‰ in $\Delta^{12}CH_2D_2$ were observed. At 20 °C, the incubation lasted for 48 hours and the $\Delta^{13}CH_3D$ of residual methane increased substantially by 4.1‰, reaching a value of 5.6 ± 0.1‰ relative to stochastic, while $\Delta^{12}CH_2D_2$ showed a modest increase of only 2.6‰, reaching a value of 8.5 ± 0.5‰.

3.5. Natural methane-rich fluids from the South Chamorro Seamount

Three fluid samples were collected from South Chamorro Seamount during *HyperDolphin* Dives 941, 945, and 947 in 2009. The general geochemical data were previously published (Wheat et al., 2020). In brief, the stagnant fluids collected during Dive 941 are rich in sulfate (12 mM) and methane (33 mM), whereas discharging fluids from Dives 945 and 947 have low sulfate concentrations (0.8 mM) and relatively low methane concentrations (23 mM). Further, sulfate and methane concentrations in the fluids were negatively correlated with aqueous sulfide concentration and alkalinity, indicating that the fluids were altered by AOM to different degrees (Wheat et al., 2020). The bulk $\delta^{13}C$ and δD values range from −37.0‰ to −26.1‰ and −110.3‰ to −100.6‰, respectively (Fig. 4C). The respective $\Delta^{13}CH_3D$ and $\Delta^{12}CH_2D_2$ values are 7.5‰ and 25.2‰ in the high-sulfate, high-methane fluid, but increase to 12.6‰ and 42.6‰ in low-sulfate, low-methane fluids (Fig. 3C). These values are analogous to the results from the Svalbard slurry incubations (Fig. 3A–B).

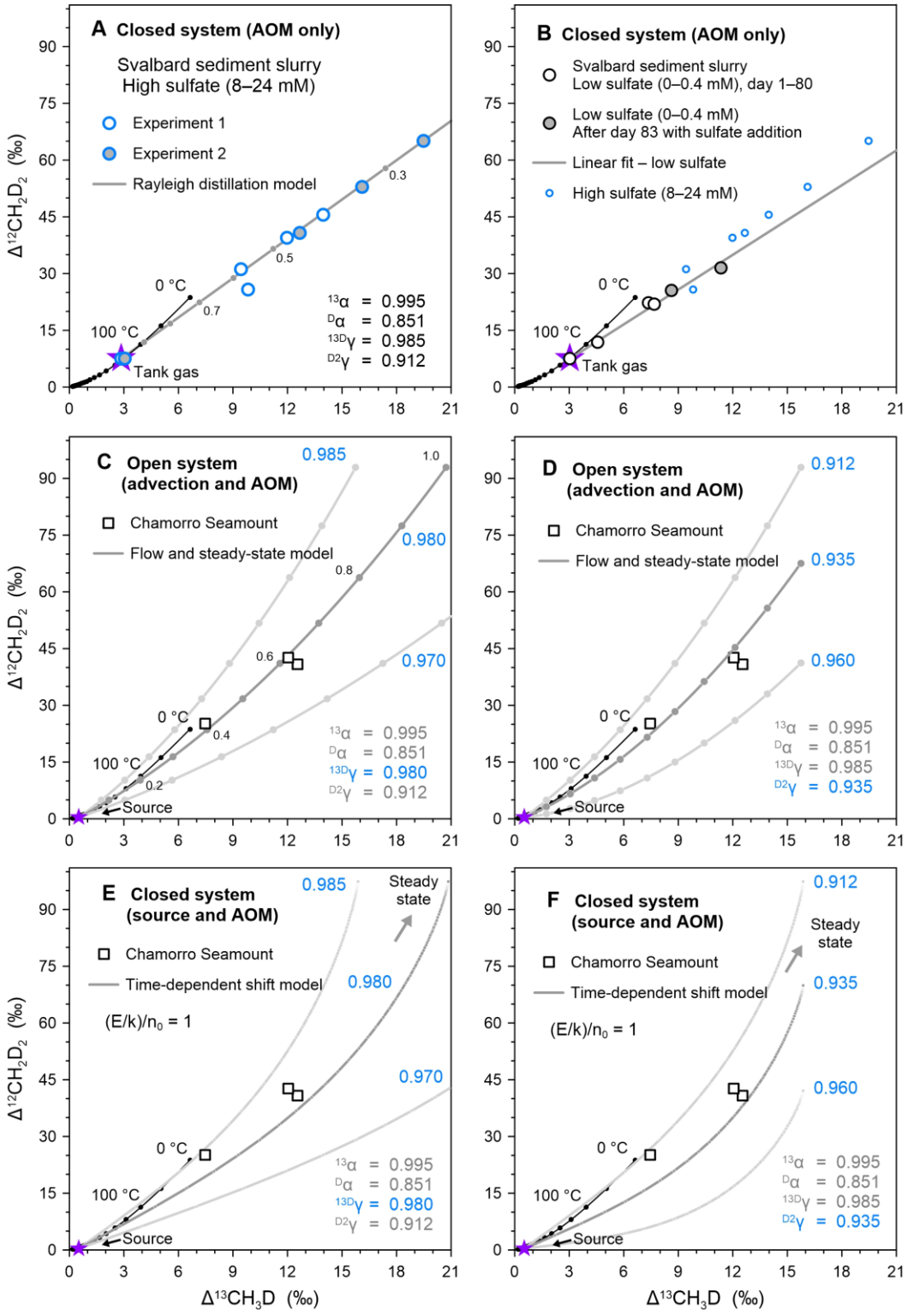

Fig. 2-6 Kinetically-driven methane isotopologue data of residual methane in AOM incubation experiments and methane in natural fluids. (A–B) Residual methane during

incubation of the Svalbard methane seep sediment slurry with high sulfate concentration (8–24 mM; panel A) and low sulfate concentration (0–0.4 mM; panel B). (C–F) Methane in natural fluids from the South Chamorro Seamount. Grey lines depict simulation outputs of the Rayleigh fractionation model (A), open-system flow and steady-state model (C–D), and closed-system time-dependent shift model (E–F). The fractionation factors used in each model are shown in each diagram. The purple stars represent the initial tank gas in panel A, and the source methane in panels C–F, respectively. This source methane is adopted from Young et al. (2017), representing abiotic methane gas formed through $Si_5C_{12}H_{36}$ decomposition experiments, which resembles methane production through serpentinization. In panel A, points along the Rayleigh fractionation line are marked at intervals of 0.1 in *f*, the fraction of initial methane remaining, while in panel C, points along the open-system model are marked at intervals of 0.1 in φ, the fraction of methane removed via oxidation. The modeled trajectories in panels E–F remain largely the same as $(E/k)/n_0$ increase from 10^{-10} to 10^{10} (data not shown), and we use 1 as an arbitrary representation. The solid black line depicts theoretical thermodynamic equilibrium abundances of methane isotopologues, along with corresponding temperatures. Uncertainties of $\Delta^{13}CH_3D$ and $\Delta^{12}CH_2D_2$ values are encompassed by individual data points.

4. DISCUSSION

4.1. Kinetic fractionations of methane clumped isotopologue during AOM

AOM was highly active in the sediment slurry from the Svalbard methane seep (Fig. 2). The high-sulfate incubation experiment showed progressive enrichment of methane isotopologues containing ^{13}C and D isotopes relative to the initial gas (Figs. 4A, 5), indicating a kinetic isotope

fractionation. Although the kinetic fractionation for D/H ratios is typical, the carbon isotope fractionation is slightly lower than previous studies, which are in the range of 11‰ to 39‰, suggesting a higher degree of reversibility of the carbon pathway in our AOM incubations (Holler et al., 2009; Wegener et al., 2021). The γ value for $^{13}CH_3D$ of 0.985 is lower than those obtained for other methane oxidation reactions such as aerobic oxidation and oxidation by OH and Cl radicals, while the γ values for $^{12}CH_2D_2$ of 0.909–0.912 are similar to those obtained for other methane oxidation reactions (Wang et al., 2016; Haghnegahdar et al., 2017; Whitehill et al., 2017; Ono et al., 2021; Krause et al., 2022). Lower absolute magnitudes of γ values imply larger magnitudes of clumped isotope effects and larger deviations in the clumped isotope fractionation factor relative to the product of the bulk isotope fractionation factors. Ono et al. (2021) proposed that the different γ values could be linked to the transition state structure of the reaction. For example, the C–H bond length of methyl-coenzyme M reductase (2.6 Å) and soluble methane monooxygenase (1.3 Å), the key enzymes involved in AOM and aerobic methanotrophy, respectively, are different, necessitating changes in the ^{13}C–D stretching vibrational mode and thus perhaps the difference in kinetic clumped isotopologue effects (Ono et al., 2021).

The extremely high $\Delta^{13}CH_3D$ and $\Delta^{12}CH_2D_2$ values up to 12.6‰ and 42.6‰, respectively, from the Chamorro Seamount, a serpentinite mud volcano in the Mariana forearc (Fig. 6C–F), as well as the high values seen in the Svalbard incubations (Fig. 6A), appear to be signatures of AOM. Based on samples from experiments and natural environments for which measurements currently exist, AOM is the only known process that drives methane isotopologue abundances substantially above equilibrium predictions for both $\Delta^{13}CH_3D$ and $\Delta^{12}CH_2D_2$. In the laboratory, we treat AOM as a Rayleigh process in which methane is consumed only by AOM in a closed system. This explains the trends in $\Delta^{13}CH_3D$ vs. $\Delta^{12}CH_2D_2$ space for the Svalbard incubations (Fig. 6A–B). For

the Chamorro Seamount, an open system that involves flow, is likely to be more suitable as a model for isotopologue fractionation. There, Wheat et al. (2020) demonstrated that methane production was abiotically fueled by hydrogen production from serpentinization and carbonate dissolution in the deep-sourced fluids, and the fluid compositions were largely altered by AOM as the fluid migrates upwards and encounters deposited pelagic sediment underlying South Chamorro Seamount. Although the pH of the collected fluids is 12, the pH of deep subsurface niches where ANME archaea live and AOM occurs can be lower, as observed in neighboring serpentinite mud volcanoes (Wheat et al., 2020). Earlier studies have shown that microorganisms can tolerate high-pH fluids and perform AOM at the Chamorro Seamount (Takai et al., 2005; Curtis et al., 2013; Kawagucci et al., 2018). These AOM-affected fluids make it to the seafloor where they discharge. Therefore, the environment where fluids are traversing through the seamount represents an open system, in which methane is transported into the subduction channel via advection and removed by both advection and AOM, likely resulting in a steady state, or at least a transient steady state. A simple mass balance model can be used to investigate the effects of simultaneous advection and oxidation (see Materials and Methods). Here, we assume that the serpentinite-sourced abiotic methane is in isotopologue equilibrium at its formation temperature (>250 °C; Wheat et al., 2020). Such near-zero clumped isotope compositions are consistent with the results from abiotic silane decomposition experiments at 300–600 °C reported in Young et al. (2017). We consider that the impact of diffusion in fluid transport on the $\Delta^{13}CH_3D$ and $\Delta^{12}CH_2D_2$ values is negligible within the subduction channel given the significantly smaller-scale molecular diffusion operates over advective processes (Wheat et al., 2020). Thus, AOM is assumed to be the only process for isotope fractionation.

The combined flow and oxidation steady-state models shown in Figure 6C–D largely reproduce the observed large $\Delta^{13}CH_3D$ and $^{12}CH_2D_2$ values at the Chamorro Seamount. Note that to achieve the best fit, a slightly lower γ value for $^{13}CH_3D$ of ~0.980 or a higher γ value for $^{12}CH_2D_2$ of ~0.935 than obtained from the experiments is needed. While the open system model is more suitable to describe these fluids, we also considered the scenario of a closed system in which the formation of methane is balanced against oxidation. In this model, isotopologue abundances vary with time, eventually reaching a steady state that is sensitive to the precise γ values (Fig. 6E–F). We set the ratio of the steady-state moles to initial moles of methane, $(E/k)/n_0$, to 1 since the modeled trajectories remain largely the same as $(E/k)/n_0$ varies. Here, $^{13}CH_3D$ γ values of 0.980–0.985 and $^{12}CH_2D_2$ γ values of 0.912–0.935 are needed to achieve the best fit in the closed system model. These estimated γ values for the Chamorro Seamount fluids from either the open- or closed-system model are largely consistent with those obtained from the Svalbard slurry incubations.

One caveat of these two models is the, to date, largely unknown bulk isotope fractionation factors. In Figure 6, we set $^{13}\alpha$ and $^{D}\alpha$ to be 0.995 and 0.851, respectively, based on experimental observations made in the Svalbard experiment. We then test the sensitivity of the models by varying the bulk isotope fractionation factors to allow depletion in heavy isotopes of methane (i.e., $^{13}\alpha$ and $^{D}\alpha > 1$). The model outputs remain largely the same, though with different curvatures (Fig. S6). This demonstrates that the trajectories in $\Delta^{13}CH_3D$ vs. $\Delta^{12}CH_2D_2$ space are much more sensitive to the relationship between the bulk α values (i.e., the γ factors) than to the absolute $^{13}\alpha$ and $^{D}\alpha$ values in these two models (Figs. 6, S6). Given the uncertainties in model inputs and limited data points, we stress that the estimated γ values are associated with large uncertainties but, overall, are significantly lower than unity.

Taken together, both open and closed system models display similar positive trajectories in $\Delta^{13}CH_3D$ vs. $\Delta^{12}CH_2D_2$ space, similar to the Rayleigh distillation model (Fig. 6), suggesting that extremely positive $\Delta^{13}CH_3D$ and $\Delta^{12}CH_2D_2$ values are potentially a clumped isotope signature of kinetically-dominated AOM. These positive values are the result of $\gamma < 1$ for both mass-18 isotopologues. Indeed, if $\gamma = 1$ for both rare isotopologues, and all else being equal, $\Delta^{13}CH_3D$ and $\Delta^{12}CH_2D_2$ would both decrease rather than increase with oxidation. In detail, the Rayleigh fractionation equation (Eq. 7) can be simplified to (Wang et al., 2016):

$$\Delta^{13}CH_3D = \Delta^{13}CH_3D_{init} + ({}^{13D}\gamma \cdot {}^{13}\alpha \cdot {}^{D}\alpha - {}^{13}\alpha - {}^{D}\alpha + 1) \cdot \ln f \quad (16)$$

$$\Delta^{12}CH_2D_2 = \Delta^{12}CH_2D_{2init} + ({}^{D2}\gamma \cdot {}^{D}\alpha^2 - 2 \cdot {}^{D}\alpha + 1) \cdot \ln f \quad (17)$$

where $\Delta^{13}CH_3D_{init}$ and $\Delta^{12}CH_2D_{2init}$ are the initial isotopologue compositions. Therefore, the threshold ${}^{13D}\gamma$ and ${}^{D2}\gamma$ for constant $\Delta^{13}CH_3D$ and $\Delta^{12}CH_2D_2$ values are $({}^{13}\alpha + {}^{D}\alpha - 1)/({}^{13}\alpha \cdot {}^{D}\alpha)$ and $(2 \cdot {}^{D}\alpha - 1)/{}^{D}\alpha^2$, respectively. Using the measured ${}^{13}\alpha$ and ${}^{D}\alpha$ from the high-sulfate Svalbard incubation, the calculated ${}^{13D}\gamma$ and ${}^{D2}\gamma$ thresholds are found to be 0.999 and 0.969, respectively. Any measured γ factors lower than the threshold conditions mean that both $\Delta^{13}CH_3D$ and $\Delta^{12}CH_2D_2$ values should evolve to more positive values in a closed system, and vice versa. Although the γ factors appear to be linked to the transition state structure of the enzyme-mediated reaction (Ono et al., 2021), the exact structures of transition states and their role in kinetic clumped isotopologue effect remain unknown. Further theoretical and experimental investigations are needed to elucidate the fundamental mechanism.

We note that with progressive AOM from the stagnant fluids to the discharging fluids at the Chamorro Seamount as indicated by alkalinity, methane, sulfate, and sulfide concentrations (Wheat et al., 2020), the $\delta^{13}C$ of residual methane decreases by 10.9‰ and δD increases by 9.7‰

in three fluid samples (Fig. 4C), resembling the ANME incubation under low-sulfate conditions (<1 mM) in Wegener et al. (2021). These authors determined radiotracer-based forward and backward AOM reaction rates at different sulfate concentrations and found that the net reversibility of the AOM reaction increases with decreasing sulfate concentration. They concluded that the net bulk isotope fractionations of AOM reflect a combination of expression of kinetic isotope effects (KIEs) and equilibrium isotope effects (EIEs) (Yoshinaga et al., 2014; Ono et al., 2021; Wegener et al., 2021). Indeed, when the Svalbard sediment slurry was incubated with even lower sulfate concentrations (<0.35 mM), both $\delta^{13}C$ and δD of residual methane decreased over time (Fig. 4B), suggestive of a greater expression of EIEs in both carbon and hydrogen pathways of AOM due to a lower net thermodynamic drive and thus relatively higher net reversibility of AOM. At 4 °C, the carbon and hydrogen equilibrium isotope fractionation factors between HCO_3^-(aq)–CH_4(g) and H_2O(l)–CH_4(g) are 1.091 and 1.216, respectively (Zhang et al., 1995; Turner et al., 2021). When inter-species isotope equilibrium is achieved, the $\delta^{13}C$ and δD of methane should be around −95‰ and −241‰ based on the measured $\delta^{13}C_{DIC}$ and δD_{H2O} values of −13.1‰ and −76.7‰ in the low-sulfate experiment.

Despite the fact that the residual methane in the low-sulfate incubation moves towards isotope equilibrium between both CH_4–CO_2 and CH_4–H_2O molecules (Fig. 4B), $\Delta^{13}CH_3D$ and $\Delta^{12}CH_2D_2$ increase linearly and fall on nearly the same Rayleigh fractionation line in $\Delta^{13}CH_3D$ vs. $\Delta^{12}CH_2D_2$ space as the high-sulfate incubation (Fig. 6B). In particular, the $\Delta^{13}CH_3D$ reaches 7.4‰ when sulfate is depleted (0.01 mM), which is higher than the value expected for intra-species isotope equilibrium at the experimental temperature ($\Delta^{13}CH_3D_{eq.}$ = 6.5‰ at 4 °C). This high $\Delta^{13}CH_3D$ value suggests a kinetic clumped isotopologue fractionation. We surmise that rather than representing unidirectional consumption of methane, the isotopic effects we observed appear to

reflect a convolution of transition-state kinetics and equilibrium isotopic effects. Furthermore, both $\Delta^{13}CH_3D$ and $\Delta^{12}CH_2D_2$ increase linearly again after new sulfate is added to the slurry (0.39 mM), indicating that the final $\Delta^{13}CH_3D$ and $\Delta^{12}CH_2D_2$ values in a methane-rich closed system depend on the electron acceptor concentration and availability. The last measured $\Delta^{13}CH_3D$ and $\Delta^{12}CH_2D_2$ values correspond to apparent temperatures lower than −34 °C (Fig. 6B), far below the incubation temperature of 4 °C. Collectively, our results from the Svalbard sediment slurry and the Chamorro Seamount show clear evidence for kinetic clumped isotopologue fractionation, with the bulk isotope ratios either increasing or decreasing with progressive methane consumption depending upon the availability of the electron acceptor.

4.2. Equilibrium between methane isotopologues during AOM

It has been proposed that AOM drives methane isotopologue abundances to thermodynamic isotopic bond-order equilibrium in a range of marine and continental settings (Ash et al., 2019; Giunta et al., 2019; Tyne et al., 2021; Warr et al., 2021; Ono et al., 2022). The initial step of AOM is the Mcr-catalyzed reversal of the final reaction in methanogenic pathways as shown for the enzyme from *M. marburgens*is (Eq. 18):

$$CH_4 + \text{CoM-S-S-CoB} \rightleftarrows CH_3\text{-S-CoM} + \text{HS-CoB} \quad (\Delta G^o = +30\ \text{kJ mol}^{-1}) \qquad (18)$$

where CoM-S-S-CoB is the heterodisulfide of coenzymes M and B, CH_3-S-CoM is methyl-coenzyme M, and HS-CoB is the reduced form of coenzyme B (Scheller et al., 2010). The reversibility of this reaction is evidently central to the mechanism for methane isotopologue equilibration by AOM. The *in-vitro* experiments that comprise exchange of methane and the methyl moiety in methyl-coenzyme M (CH_3-S-CoM) characterize the role of the Mcr enzyme in

reaction Eq. (18). At 60 °C, the optimal temperature for the thermophile-derived enzyme, both $\Delta^{13}CH_3D$ and $\Delta^{12}CH_2D_2$ values of residual methane increase slightly (Fig. 3D). At 20 °C, however, $\Delta^{13}CH_3D$ approaches the equilibrium value, while there is little change in $\Delta^{12}CH_2D_2$. This implies that carbon plays a larger role than hydrogen in the isotopologue selectivity for reaction with the Mcr enzyme at a temperature below optimal.

Incubations of slurry from the Santa Barbara Channel, with a lower amount of methane, further inform the assessment of the role of thermodynamic driving forces in determining the isotopologue signatures of AOM. There is a trend towards $\Delta^{13}CH_3D$ and/or $\Delta^{12}CH_2D_2$ values expected for isotopologue equilibrium at experimental temperature (Fig. 3E). Two of the high-sulfate incubations of the Santa Barbara sediments resemble the high-temperature Mcr experiments under the optimal condition, whereas the low-sulfate incubations resemble the low-temperature Mcr experiments (Fig. 3D–E). Importantly, the amounts of methane injected into the Santa Barbara slurry (0.5 mmol) are much lower than those into the Svalbard slurry (5.4 mmol), leading to a much lower thermodynamic drive for AOM for the former and an overall lower rate of reaction. Thus, the reversibility and isotope exchange during AOM in the Santa Barbara slurry may be much higher than the Svalbard slurry under either high- or low-sulfate conditions. This vigorous exchange ultimately allows methane isotopologues to react with Mcr reversibly, achieving partial intra-species isotope exchange in the Santa Barbara slurry incubations. The high reversibility may be exacerbated by the fact that the ANME community in coastal sandy Santa Barbara sediments with high depositional rates is less active with less biomass compared to that from the deep-sea fine-grained Svalbard methane seep sediments. The lower sedimentation rates at the Svalbard seep focus AOM in the same sediments for an extended period, allowing the ANME community to grow and enrich.

All experiments of the deep biosphere sediment and fluid incubations suggest that there is a trend toward equilibrium values for $\Delta^{13}CH_3D$ but little change in $\Delta^{12}CH_2D_2$ within experimental timescales, regardless of which electron acceptor is present (Fig. 3F). In detail, a positive correlation between incubation time (up to 500 days) and increase in $\Delta^{13}CH_3D$ values is found in incubation experiments of the Nankai Trough sediments (Fig. S5C), consistent with the well-documented sluggish nature of microbial activity in the deep subseafloor (Hoehler and Jørgensen, 2013; Heuer et al., 2020).

One may postulate that the $\Delta^{13}CH_3D$ values in our incubations that appear to approach equilibrium values would in fact continue to increase beyond the equilibrium value given sufficient time. However, this is probably not the case. The respective maximum observed for $\Delta^{13}CH_3D$ values is 5.56‰ (2 days), 5.50‰ (3 days), 5.70‰ (500 days), and 5.66‰ (350 days) in the Mcr experiment, and the incubations of the Santa Barbara Channel sediment, the Nankai Trough sediment, and the Beatrix Gold Mine fracture fluid (Fig. 3D–F). The apparent temperatures based on $\Delta^{13}CH_3D$ are 32 °C, 33 °C, 27 °C, and 28 °C, respectively (30 ± 3 °C, n = 4). These are all close to the ambient temperature under which these different incubations took place. Although it cannot be categorically ruled out that these $\Delta^{13}CH_3D$ values reflected ambient temperatures by happenstance during an ongoing kinetically driven trend, it would be fortuitous that this would occur four times in independent experimentation. Therefore, we conclude that the $\Delta^{13}CH_3D$ values increase over time towards equilibrium and indeed remain at thermodynamic equilibrium despite a large range of incubation times of 2 to 500 days in the above four experiments.

Given the observed intra-species isotope quasi-equilibrium, one may similarly expect inter-species isotope exchange to occur as seen in the low-sulfate Svalbard experiment (Fig. 4B). The residual methane in most of the Santa Barbara and deep biosphere incubations, however, showed

no substantial changes in $\delta^{13}C$ and δD values (Fig. 4E–F). Changes in bulk and clumped isotope compositions are decoupled in these incubations. While more experiments are needed to explicitly confirm the conditions under which this decoupling occurs, one tentative hypothesis is that, under certain conditions, the Mcr enzyme only mediates the exchange of isotopes among methane molecules without expressed bulk isotope fractionation, allowing $^{13}CH_3D$ and/or $^{12}CH_2D_2$ to be re-ordered to the incubation temperature via bond breaking and reformation. This hypothesis is analogous to the heating experiments in which methane intra-species equilibration is promoted by the presence of a metal catalyst at temperatures above 200 °C (Ono et al., 2014; Stolper et al., 2014b; Young et al., 2017). In our case, the Mcr enzyme may act as the catalyst and promote isotopic bond re-ordering with limited isotope exchange between CH_4–CO_2 and CH_4–H_2O molecules, as methane molecules are disassembled and reassembled. This hypothesis requires further experimental investigation.

4.3 A general model for methane isotopologue fractionation due to AOM

4.3.1 Model construction

To understand the mechanism of methane isotopologue fractionation and/or bond re-ordering during AOM, the methane isotopologue fractionation factors obtained in AOM laboratory incubation experiments can be used to construct a geochemical model with several simplifying assumptions for fractionation due to AOM. The result is a parsimonious model that explains most methane isotopologue data affected by anaerobic oxidation by ANMEs collected thus far. A crucial aspect of the model is the important role that reversibility has in controlling the trajectory of gases in $\Delta^{13}CH_3D$ vs. $\Delta^{12}CH_2D_2$ space during AOM.

The model addresses the most important single step, the potentially reversible cleaving of CH_4 molecules catalyzed by the Mcr enzyme to form co-enzyme hosted CH_3 and H in the ANME cells (e.g., Scheller et al., 2010). The relevant reaction can therefore be written succinctly as

$$\mathrm{CH_4} \underset{k_r}{\overset{k_f}{\rightleftharpoons}} \mathrm{CH_3 + H} \tag{19}$$

where the forward and reverse rate constants, k_f and k_r, are controlled by the kinetics of binding and bond rupture/formation in the first step of AOM. While there are a total of 280 isotopic isomer equivalents of the reaction in Eq. (19), with one exception (see below), we will focus on a simplified reaction network of isotopologues (as opposed to all isotopic isomers). This is necessitated by the fact that the measured fractionation factors convolve a number of isotopic effects, including the symmetry effects of all isomers. The sixteen reactions in terms of 12 isotopologues are

$$\begin{aligned}
&1.\ \mathrm{CH_4} \xrightarrow{k_1} \mathrm{CH_3 + H} \\
&2.\ \mathrm{CH_3D} \xrightarrow{k_2} \mathrm{CH_3 + D} \\
&3.\ \mathrm{CH_3D} \xrightarrow{k_3} \mathrm{CH_2D + H} \\
&4.\ \mathrm{CH_2D_2} \xrightarrow{k_4} \mathrm{CH_2D + D} \\
&5.\ \mathrm{CH_2D_2} \xrightarrow{k_5} \mathrm{CHD_2 + H} \\
&6.\ \mathrm{^{13}CH_4} \xrightarrow{k_6} \mathrm{^{13}CH_3 + H} \\
&7.\ \mathrm{^{13}CH_3D} \xrightarrow{k_7} \mathrm{^{13}CH_3 + D} \\
&8.\ \mathrm{^{13}CH_3D} \xrightarrow{k_8} \mathrm{^{13}CH_2D + H} \\
&9.\ \mathrm{CH_3 + H} \xrightarrow{k_9} \mathrm{CH_4} \\
&10.\ \mathrm{CH_3 + D} \xrightarrow{k_{10}} \mathrm{CH_3D} \\
&11.\ \mathrm{CH_2D + H} \xrightarrow{k_{11}} \mathrm{CH_3D} \\
&12.\ \mathrm{CH_2D + D} \xrightarrow{k_{12}} \mathrm{CH_2D_2} \\
&13.\ \mathrm{CHD_2 + H} \xrightarrow{k_{13}} \mathrm{CH_2D_2} \\
&14.\ \mathrm{^{13}CH_3 + H} \xrightarrow{k_{14}} \mathrm{^{13}CH_4} \\
&15.\ \mathrm{^{13}CH_3 + D} \xrightarrow{k_{15}} \mathrm{^{13}CH_3D} \\
&16.\ \mathrm{^{13}CH_2D + H} \xrightarrow{k_{16}} \mathrm{^{13}CH_3D}
\end{aligned} \tag{20}$$

where k_i are the relevant rate constants (first order for reactions 1 through 8, 2nd order for 9–16), and again we emphasize that the different isomers are embedded in the fractionation factors extracted from experiments.

Isotopologue fractionation factors for the first step in deconstructing methane isotopologues are in effect ratios of rate constants 1–8. We measured these fractionation factors for the Svalbard incubations in which the loss of methane gas due to AOM is consistent with an irreversible Rayleigh process. The derived fractionation factors, α, are listed in Table 1 together with relevant comparisons to be discussed. Here, the 3rd column is the square root of the inverse ratios of relevant reduced masses (^{12}C-H, ^{13}C-H, ^{12}C-D, etc.). These are the fractionation factors expected where the kinetics is dominated by rupture of single carbon-hydrogen bonds comprising the reaction coordinate. Note that the experimentally-derived fractionation factors are considerably closer to unity than those implied by the reduced masses.

Table 2-1 Measured and estimated fractionation factors relative to $^{12}CH_4$. The experimental data are from the Svalbard incubations. μ is reduced mass. Q* is rotational/vibrational partition functions for a crude estimate for the transition state of methane being dismantled by the Mcr-mediated reaction. The prime superscript refers to the isotopically-substituted species.

Species/$^{12}CH_4$	*Experiment*	$\sqrt{\mu/\mu'}$	*lnQ*'/lnQ**
$^{13}CH_4$	0.995	0.997	0.997
$^{12}CH_3D$	0.851	0.734	0.832
$^{13}CH_3D$	0.834	0.732	0.827
$^{12}CH_2D_2$	0.660	0.539	0.694

The 4th column in the table of fractionation factors is the ratio of the logarithm of rotational/vibrational partition functions for a crude estimate for the transition state of methane being dismantled by the Mcr-mediated reaction. We note that the measured fractionation factors are crudely similar, but not identical, to the lnQ*'/lnQ* ratios; the ratios of logs of partition functions provide better rationalizations for the measured fractionation factors than do reduced masses along individual bonds. We note further that this is evidently a characteristic of AOM as opposed to abiotic oxidation in the atmosphere and perhaps bacterial aerobic oxidation, where fractionation factors are significantly closer to the square root of the inverse ratios of relevant reduced masses (Haghnegahdar et al., 2017; Whitehill et al., 2017; Krause et al., 2022). For example, the values for $\alpha^{13}C/^{12}C$, αD/H, $\alpha^{13}CH_3D/CH_4$, and $\alpha^{12}CH_2D_2/CH_4$ of methane oxidation by OH radical in the atmosphere are 0.994, 0.758, 0.752, and 0.521, respectively (Haghnegahdar et al., 2017), which by inspection are seen to be closer to expectations from reduced masses along a C-H reaction coordinate. We suggest that larger fractionation nearer to unity, and resembling plausible ratios of energies of methane transition states, reflect significant binding of methane to the catalyzing enzymes (e.g., Mcr), in the case of AOM, leading to a more dispersed dependence of bond rupture on overall rotational/vibrational energy for the different isotopologues.

The model formulated to accommodate the measured fractionation factors comprises the set of rate constants, with branching ratios, and fractionation factors shown in Table 2. Several assumptions are needed based on theoretical consideration because some inputs are not readily available from the experiments. Taking reactions 2 and 3 as an example, the breakage of a ^{12}C-D bond in $^{12}CH_3D$ (primary kinetic isotope effect for D/H, α_2) is associated with a larger kinetic isotope effect than breaking a ^{12}C-H bond in $^{12}CH_3D$ (secondary kinetic isotope effect, α_3). Thus, we set α_2 to be 0.5, which is close to the primary KIE (0.41 ± 0.04) observed in the methane

activation experiment using the Mcr enzyme (Scheller et al., 2013). The primary KIEs for doubly substituted species are derived following the rule of the geometric mean with measured γ values (Eqs. 8–9). The branching ratios are set to be ¼ for reactions 2 and 7, ¾ for reactions 3 and 8, and ½ for reactions 4 and 5, as only ¼ of the time the D is removed from $^{12}CH_3D$ or $^{13}CH_3D$ in its destruction while ¾ of the time an H is removed. Accordingly, the secondary KIEs are calculated from the measured fractionation factor, $^{D}\alpha$, and the branching ratios such that $^{D}\alpha = ¼\ \alpha_2 + ¾\ \alpha_3$. We further consider bulk and clumped isotope equilibrium in the reversible reactions. At equilibrium, the ratio of the reverse and forward KIEs is equal to the EIE of the reaction. Thus, the KIEs for the reverse reactions are derived using the forward KIEs above and the EIEs calculated by Gropp et al. (2021). When the reaction is irreversible, only the forward KIEs are expressed, whereas the EIEs are expected to be more dominant when the reaction is highly reversible. In the latter case, we have allowed for exchange equilibrium among methane molecules to result from methane formation. This is done by including $^{D2}\gamma_{eq}$ and $^{13D}\gamma_{eq}$, the fractionation factors representing equilibrium abundances of $^{12}CH_2D_2$ and $^{13}CH_3D$ in thermodynamic equilibrium. In what follows we use an equilibration temperature for AOM of 20 °C. We verified the branching ratios in Table 2 using the full 280 reactions involving 50 isotopomer species and simple rate constants composed of square roots of inverse ratios of reduced masses (see below).

Reversibility is determined by the ratio $\Phi = k_r/k_f$. Where $\Phi = 0$, oxidation is "irreversible", corresponding to Rayleigh fractionation with purely kinetic fractionation factors. We assume that the high-sulfate Svalbard incubation represents this irreversible end-member. Where $\Phi > 0$, the influences of reversibility become immediately evident for even small values (and being mindful that k_r refers to a 2nd order reaction while k_f is for a first-order reaction, with the commensurate change in units for the rate constants). As $\Phi \rightarrow 1$, the oxidation at the Mcr step approaches full

reversibility and equilibrium relative abundances of methane isotopologues result from the reaction with only negligible decreases in methane abundance. In all cases, the systems reach steady-state, given sufficient time, with the steady state abundance of methane, and its isotopologue composition, determined by the value for Φ.

Table 2-2 Rate constants (k) and isotope fractionation factors (α) for the simplified reaction network of isotopologues. $^{D}\alpha_{eq\text{-}P}$ and $^{D}\alpha_{eq\text{-}S}$ are the equilibrium fractionation factors for primary and secondary fractionations, respectively. $^{D2}\gamma_{eq(\text{-}P/S)}$ and $^{13D}\gamma_{eq(\text{-}P/S)}$ are the fractionation factors representing equilibrium abundances of $^{12}CH_2D_2$ and $^{13}CH_3D$ in thermodynamic equilibrium. The reader is referred to the text for interpretation of the table.

Reaction	k	α
1. $CH_4 \rightarrow CH_3 + H$	k_f	$\alpha_1 = 1.000$
2. $CH_3D \rightarrow CH_3 + D$	$k_2 = \frac{1}{4}\, k_f\, \alpha_2$	$\alpha_2 = 0.500$
3. $CH_3D \rightarrow CH_2D + H$	$k_3 = \frac{3}{4}\, k_f\, \alpha_3$	$\alpha_3 = 0.968$
4. $CH_2D_2 \rightarrow CH_2D + D$	$k_4 = \frac{1}{2}\, k_f\, \alpha_4$	$\alpha_4 = 0.441$
5. $CH_2D_2 \rightarrow CHD_2 + H$	$k_5 = \frac{1}{2}\, k_f\, \alpha_5$	$\alpha_5 = 0.879$
6. $^{13}CH_4 \rightarrow {}^{13}CH_3 + H$	$k_6 = k_f\, \alpha_6$	$\alpha_6 = 0.995$
7. $^{13}CH_3D \rightarrow {}^{13}CH_3 + D$	$k_7 = \frac{1}{4}\, k_f\, \alpha_7$	$\alpha_7 = 0.490$
8. $^{13}CH_3D \rightarrow {}^{13}CH_2D + H$	$k_8 = \frac{3}{4}\, k_f\, \alpha_8$	$\alpha_8 = 0.949$
9. $CH_3 + H \rightarrow CH_4$	$k_9 = \frac{1}{2}\, k_r\, \alpha_9$	$\alpha_9 = \alpha_1$
10. $CH_3 + D \rightarrow CH_3D$	$k_{10} = \frac{1}{2}\, k_r\, \alpha_{10}$	$\alpha_{10} = \alpha_2 \cdot {}^{D}\alpha_{eq\text{-}P}$
11. $CH_2D + H \rightarrow CH_3D$	$k_{11} = \frac{1}{2}\, k_r\, \alpha_{11}$	$\alpha_{11} = \alpha_3 \cdot {}^{D}\alpha_{eq\text{-}S}$
12. $CH_2D + D \rightarrow CH_2D_2$	$k_{12} = \frac{1}{2}\, k_r\, \alpha_{12}$	$\alpha_{12} = \alpha_4 \cdot {}^{D2}\gamma_{eq\text{-}P} \cdot {}^{D}\alpha_{eq\text{-}P} \cdot {}^{D}\alpha_{eq\text{-}S}$
13. $CHD_2 + H \rightarrow CH_2D_2$	$k_{13} = k_r\, \alpha_{13}$	$\alpha_{13} = \alpha_5 \cdot {}^{D2}\gamma_{eq\text{-}S} \cdot {}^{D}\alpha_{eq\text{-}S} \cdot {}^{D}\alpha_{eq\text{-}S}$
14. $^{13}CH_3 + H \rightarrow {}^{13}CH_4$	$k_{14} = \frac{1}{2}\, k_r\, \alpha_{14}$	$\alpha_{14} = \alpha_6 \cdot {}^{13}\alpha_{eq}$
15. $^{13}CH_3 + D \rightarrow {}^{13}CH_3D$	$k_{15} = \frac{1}{2}\, k_r\, \alpha_{15}$	$\alpha_{15} = \alpha_7 \cdot {}^{13D}\gamma_{eq\text{-}P} \cdot {}^{13}\alpha_{eq} \cdot {}^{D}\alpha_{eq\text{-}P}$
16. $^{13}CH_2D + H \rightarrow {}^{13}CH_3D$	$k_{16} = k_r\, \alpha_{16}$	$\alpha_{16} = \alpha_8 \cdot {}^{13D}\gamma_{eq\text{-}S} \cdot {}^{13}\alpha_{eq} \cdot {}^{D}\alpha_{eq\text{-}S}$

4.3.2 Example applications

Irreversible Rayleigh fractionation: This example application of the model is trivial in so far as it is the model assumed to derive the fractionation factors. Nonetheless, it is useful to

illustrate that the Svalbard sediment incubation data are properly accounted for using the model. Figure 7A shows the path in $\Delta^{13}CH_3D$ vs. $\Delta^{12}CH_2D_2$ space predicted by the model compared with the calibration data for the case of Rayleigh fractionation where $\Phi = 0$. The model also fits the bulk isotope data well for similar values of F, the fraction of methane remaining (Fig. 8A).

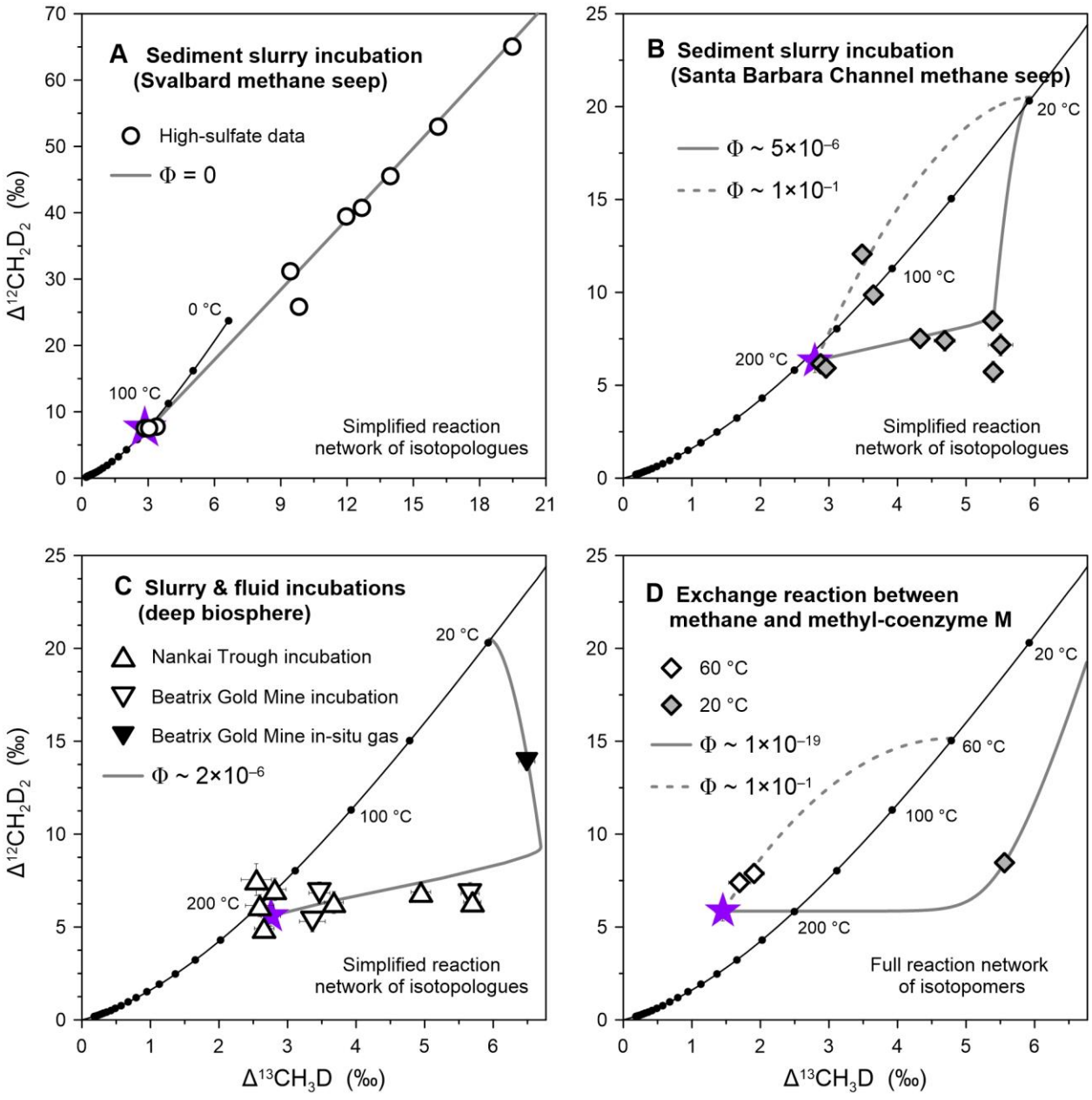

Fig. 2-7 Methane clumped isotope data and model outputs of the general model for methane isotopologue fractionation due to AOM. (A) Comparison of our simplified model with incubations of Svalbard methane seep sediment slurry showing the model fits the data. (B) Comparison between Santa Barbara Channel methane seep incubations and our simplified model with inclusion of low turnover from CH_4 to CH_3 of about 1%, defined as $[CH_3]/[CH_4]$ at steady state. (C) Comparison between deep biosphere incubations and our simplified model. The *in-situ* methane gas from the Beatrix Gold Mine is shown for comparison (Young et al., 2017). The model in panels A–C uses 16 reactions involving 12 isotopologues and measured fractionation factors of the Svalbard incubation (Table 2). (D) Comparison of enzymatically-mediated exchange of methane molecules with our model prediction using the full 280 reactions involving 50 isotopomer species and simple rate constants composed of square roots of inverse ratios of reduced masses. Reversibility (Φ) is determined by the ratio of the reverse rate constant to the forward rate constant (k_r/k_f). Where Φ is closer to one, oxidation is more reversible, and vice versa. The solid black line depicts theoretical thermodynamic equilibrium abundances of methane isotopologues, along with corresponding temperatures. Error bars are one standard error.

Reversibility: Some data for methane known to have been processed by AOM exhibit significant variations in $\Delta^{13}CH_3D$ at roughly constant $\Delta^{12}CH_2D_2$ and minimal variations in bulk isotope ratios. Our model explains these data as being the result of more reversibility in the Mcr-mediated transformation between CH_4 and CH_3+H. We illustrate this here by comparing our results with the sediment slurry incubation data from the Santa Barbara Channel.

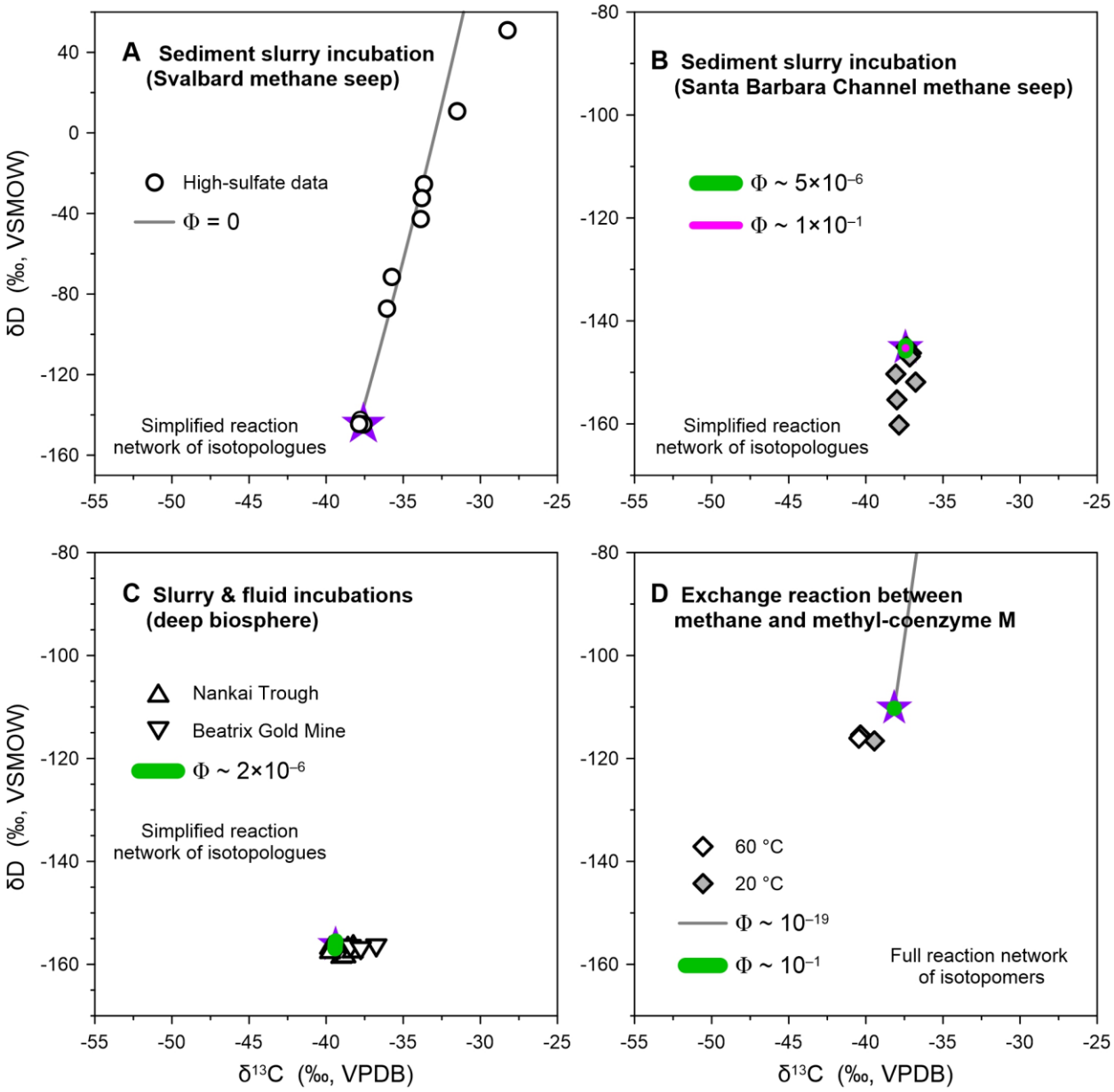

Fig. 2-8 Methane bulk isotope data and model outputs of the general model for methane isotopologue fractionation due to AOM. (A) Comparison of our simplified model with incubations of Svalbard methane seep sediment slurry showing the model fits the data. (B) Comparison between Santa Barbara Channel methane seep incubations and our simplified model. (C) Comparison between deep biosphere incubations and our simplified model. The model in panels A–C uses 16 reactions involving 12 isotopologues and measured fractionation factors of

the Svalbard incubation (Table 2). (D) Comparison of enzymatically-mediated exchange of methane molecules with our model prediction using the full 280 reactions involving 50 isotopomer species and simple rate constants composed of square roots of inverse ratios of reduced masses. Reversibility (Φ) is determined by the ratio of the reverse rate constant to the forward rate constant (k_r/k_f).

Most of the data exhibit a "horizontal" trend in the mass-18 isotopologue diagram that can be reproduced with our model using $k_r/k_f \sim 5\times10^{-6}$, resulting in a predicted steady-state concentration of methane that is about 99% of the initial value, and with negligible changes in δD and $\delta^{13}C$, in broad agreement with the data (Figs. 7B, 8B). As the k_r/k_f increases to 10^{-1}, the model leads to increases in both $\Delta^{13}CH_3D$ and $\Delta^{12}CH_2D_2$ (Fig. 7B). This at least qualitative agreement between the AOM data from the Santa Barbara Channel and the model for significant reversibility in the first AOM step mediated by Mcr raises the specter of a potential monitor of Mcr-catalyzed intracellular isotope exchange operating at near-threshold free energy geochemical settings, such as the deep biosphere (Fig. 7B–C).

Indeed, near-equilibrium methane isotopologue ratio of *in-situ* methane was found in the Beatrix Gold Mine with minor negative excursion in $\Delta^{12}CH_2D_2$ relative to equilibrium (Fig. 7C; Young et al., 2017). Here, methane was produced abiotically with negative $\Delta^{12}CH_2D_2$ values that are progressively erased by the incursion of biological activity that drives the isotopic bond ordering in methane towards equilibrium (Young et al., 2017). The board consistency in isotopologue ratios between the *in-situ* gas and laboratory incubations of the Beatrix samples further confirms the modeled trajectory (Fig. 7C).

We checked that the modeled trajectories are robust, and can be derived using kinetic rate constants defined by reduced masses alone combined with the full 280 reactions for all isomers (see below). We used the measured fractionation factors from the Svalbard incubation as model input for the Santa Barbara Channel and deep biosphere incubations as well. However, this may not be the case. To test whether the model is sensitive to the input fractionation factors, all KIEs and EIEs are set to 1.0 with the $^{D2}\gamma_{eq}$ and $^{13D}\gamma_{eq}$ unchanged. This sensitivity test indicates that the modeled trajectory remains the same and is not sensitive to the input fractionation factors when the reversibility is relatively high (Fig. S7).

Exchange mediated by Mcr: In the last example we make use of a related but different model to illustrate the path in $\Delta^{13}CH_3D$ vs. $\Delta^{12}CH_2D_2$ space due to enzymatically-mediated exchange of isotopes among methane molecules. The Mcr experiments provide the data against which to test this model. We do not use precisely the model shown in Table 2 in this case. The reason is that pure exchange is likely to be dominated by symmetry effects, and the fractionation factors obtained from the Svalbard experiments are an unresolvable convolution of these effects with other factors. To overcome this issue, this model is analogous to the simple model above, but in this case all isomers are included, producing 50 species related by 280 reactions, to explain the kinetics. Rather than the measured fractionation factors, we here use generic kinetic fractionation factors corresponding to square roots of the inverse ratios of relevant reduced masses (^{12}C-H, ^{13}C-H, ^{12}C-D, etc.).

We impose a value for Φ of > 0.1, making the result dependent only on the relative number of isomers for each species and the two equilibrium fractionation factors $^{D2}\gamma_{eq}$ and $^{13D}\gamma_{eq}$. Figure 7D shows our prediction dominated by symmetry with the 60 ºC exchange experiments in which the Mcr enzyme operates at its optimal condition. Here again, the agreement is reasonably good,

suggesting that the inferences about the trajectory in $\Delta^{13}CH_3D$ vs. $\Delta^{12}CH_2D_2$ space due to nearly complete reversibility are correct. However, at 20 ºC, below the optimal condition for the Mcr enzyme, a much lower Φ is needed to reproduce the data.

Limitation: Due to the complexity of isotopomer species involved in the reactions, the models presented here only focus on the first and, arguably, the most important step of AOM but do not include other intracellular pathways. As demonstrated by Wegener et al. (2021), a multistep isotope model for AOM including KIEs and EIEs is useful to explain the opposing bulk isotope effects (cf. Northrop, 1981). Such multistep isotopologue models have also been used to simulate clumped isotope effects of microbial methanogenesis (Cao et al., 2019; Young, 2019; Gropp et al., 2022; Ono et al., 2022). Indeed, this one-step model fails to yield inter-species isotope equilibrium for bulk isotopes with high reversibility, though equilibrium fractionation factors for both bulk and clumped isotopes are parameterized in the model. Therefore, we stress that the inputs and outputs of our model should be considered as illustrative approximations. Furthermore, the rate of AOM itself was not directly measured in our experiments other than the Svalbard slurry incubations. The lack of rate information limits the ability to quantify the degree of reversibility on the isotopologue ratios in our study. Nonetheless, the models presented here allow multiple scenarios to be tested and suggest that high reversibility and low reversibility have characteristic trajectories in $\Delta^{13}CH_3D$ vs. $\Delta^{12}CH_2D_2$ space that are exhibited by the data.

4.4. Kinetically-driven AOM *versus* equilibrium-driven AOM

Taking all of our results together, we find that the $\Delta^{13}CH_3D$ and $\Delta^{12}CH_2D_2$ signatures of AOM can be understood in terms of reversibility at the Mcr step. The degree of reversibility is

presumably controlled by the tenets of disequilibrium thermodynamics in which rates of reaction are proportional to reaction affinity (deviations in chemical potentials from equilibrium). Kinetic clumped isotope fractionation is found in the Svalbard slurry in which large amounts of methane are provided to the active ANME community. This kinetic signature is also seen in natural fluids from the South Chamorro Seamount, indicating that the kinetic isotopologue fractionation does not differ substantially between laboratory incubations and natural environments (Fig. 6). When less methane is provided, $\Delta^{13}CH_3D$ tends to increase towards thermodynamic near-equilibrium values with minimal increase in $\Delta^{12}CH_2D_2$ (Fig. 3E). For example, there is a striking difference in the isotopologue evolution of residual methane between the Svalbard slurry, in which kinetics drives $\Delta^{13}CH_3D$ and $\Delta^{12}CH_2D_2$ to extreme values, and the Santa Barbara slurry incubations in which changes occur mainly in $\Delta^{13}CH_3D$ and appear to approach equilibrium, even though the sediments are both from methane seeps (Fig. 3). The simple kinetic model shown here reproduces the salient features of this behavior as being the result of reversibility (Fig. 7). Another reason for this discrepancy is the biomass of ANME archaea under different conditions, such that in slurry that experienced high methane concentrations over a longer period of time, the biomass may be higher and vice-versa. We therefore infer that AOM with high sulfate concentrations may show either kinetic or equilibrium behavior depending on the local ANME community, the availability of methane, and thus the overall thermodynamic drive.

We conclude that both $\Delta^{13}CH_3D$ and $\Delta^{12}CH_2D_2$ values reflect kinetic isotope fractionation and increase beyond intra-methane thermodynamic equilibrium when the net AOM reaction has low reversibility due to high rates, whereas largely reversible exchange between methane isotopologues facilitated by the Mcr enzyme under a lower thermodynamic drive leads to methane isotopic bond re-ordering, driving the abundances of methane isotopologues ultimately to

thermodynamic quasi-equilibrium values. This observation is consistent with reaction affinity as a primary determinant for the behavior of the system. These departures from equilibrium, or reaction affinities, are controlled by environmental factors, including but not limited to, temperature, concentrations of methane and electron acceptors, and perhaps the type of electron acceptors. Although it seems that $^{13}CH_3D$ and $^{12}CH_2D_2$ equilibration are ultimately controlled by the reversibility of AOM, the driver for different trajectories in $\Delta^{13}CH_3D$ vs. $\Delta^{12}CH_2D_2$ space is still elusive. Future efforts should explicitly focus on the environmental controls of the enzymatic activity of intracellular pathways and the reversibility of AOM, and their intrinsic link to methane isotopologue ratios.

4.5. Implications

A schematic representation of methane clumped isotope signatures of diverse methane sources, as well as kinetically- and equilibrium-driven AOM, is shown in Figure 9. Extremely low $\Delta^{12}CH_2D_2$ values down to ca. −40‰ have been observed for microbial methane under experimental and natural conditions, as well as thermogenic and abiotic methane generated by laboratory experiments (e.g., Young et al., 2017; Young, 2019; Taenzer et al., 2020; Dong et al., 2021). Besides equilibrium-driven AOM, isotopologue data near thermodynamic equilibrium have been attributed to high-maturity thermogenic or high-temperature abiotic methane, as well as low-rate methanogenesis (Stolper et al., 2015; Wang et al., 2015; Young et al., 2017; Ash et al., 2019; Giunta et al., 2019; Labidi et al., 2020; Warr et al., 2021; Xie et al., 2021; Gropp et al., 2022; Ono et al., 2022). Recently, Ono et al. (2022) demonstrated that methanogenesis does not occur or only proceeds at extremely slow rates at low pH_2 in energy-limited deep sedimentary environments using an isotopologue flow network model, and therefore inferred that near-equilibrium methane

isotopologue signals in deep marine sediments are produced by the catalytic reversibility of the Mcr enzyme, likely from ANME archaea performing either AOM or net methanogenesis. This inference is consistent with our incubation experiments in which Mcr-catalyzed isotope exchange occurs.

To date, extremely positive $\Delta^{13}CH_3D$ and $\Delta^{12}CH_2D_2$ values have been observed, as demonstrated here, only under conditions where AOM occurs with a low degree of reversibility. This observation raises an intriguing question whether methane clumped isotope signature of AOM could have the potential to be diagnostic of AOM on Earth and perhaps throughout the solar system where methane has been detected (Webster et al., 2015; Waite et al., 2017; Yung et al., 2018; Thompson et al., 2022). For example, the *in-situ* discovery of isotopically depleted methane gas on Mars by Curiosity (Webster et al., 2015; House et al., 2022) indicates that methane is produced either biogenically or abiogenically (Atreya et al., 2007; Yung et al., 2018), and its emission results in the presence of methane in the atmosphere of Mars (Formisano et al., 2004). On the other hand, although the atmospheric methane sink on Mars has been quantified (Atreya et al., 2007; Yung et al., 2018), abiotic loss mechanisms would suggest a mean atmospheric residence time of ~300 years – substantially longer than observed methane lifetimes on the order of months to years (Lefèvre, 2019). The conditions for a subsurface microbial sink on Mars are still elusive. Nevertheless, the reaction transport model by Marlow et al. (2014) demonstrated that AOM could be a feasible metabolism on ancient Mars, for example, in sulfate-rich groundwater with methane from serpentinization by-products, and acid-sulfate fluids with methane produced from basalt alteration. The surface of Mars also includes deposits of iron oxides and manganese oxides, Fe- and Mn-dependent AOM therefore has also been proposed as a possible metabolism for recent and ancient Mars (House et al., 2011). Applying these inferences to our understanding of methane

cycling on Mars is speculative. Nonetheless, a robust *in-situ* approach is needed to trace processes of methane cycling on future missions such as Mars Life Explorer (National Academies of Sciences, Engineering, and Medicine, 2022).

Mars is one of the most promising candidates for the application of methane isotope clumping. The reason is that doubly substituted isotopologues of methane remove the difficulties associated with using bulk $^{13}C/^{12}C$ and D/H elsewhere in the solar system, where the geochemical context necessary for interpreting these ratios is hampered by incompletely characterized chemical cycles (Lefèvre, 2019; Young, 2019; House et al., 2022). In $\Delta^{13}CH_3D$ vs. $\Delta^{12}CH_2D_2$ space, microbial, thermogenic, and abiotic methane gases are either below or near the thermodynamic equilibrium predictions (Fig. 9). Once formed, methane could be oxidized photochemically or by microbial oxidation. These sinks have different $\Delta^{13}CH_3D$ vs. $\Delta^{12}CH_2D_2$ signatures, depending upon whether a steady state is achieved or not. The details depend on the precise γ values, but in general, by analogy with Earth's atmosphere, oxidation in the atmosphere (e.g., by OH radicals) should ultimately lead to either high $\Delta^{12}CH_2D_2$ of order tens to hundreds of per mil at less variable $\Delta^{13}CH_3D$ values in residual methane at steady state, or extremely low values for both where a steady state between methane formation and oxidation has not been achieved (Fig. 9) (Haghnegahdar et al., 2017). The trajectories for microbial aerobic oxidation of methane are like those of the $CH_4 + \cdot OH$ reaction (Krause et al., 2022). AOM, on the other hand, can lead to extremely high $\Delta^{12}CH_2D_2$ and $\Delta^{13}CH_3D$ values up to 65.1‰ and 19.5‰, respectively, as shown here. Indeed, these signatures are essentially orthogonal. Although mixing scenarios could mimic the extreme signatures from AOM, those mixing scenarios require extremely large differences in bulk carbon and hydrogen isotopic values of the two endmembers of methane (e.g., some 80‰ and 300‰ differences in endmember $\delta^{13}C$ and δD values, respectively), possibly allowing

kinetically-driven AOM to be distinguished from mixing with concurrent measurement of bulk isotopes.

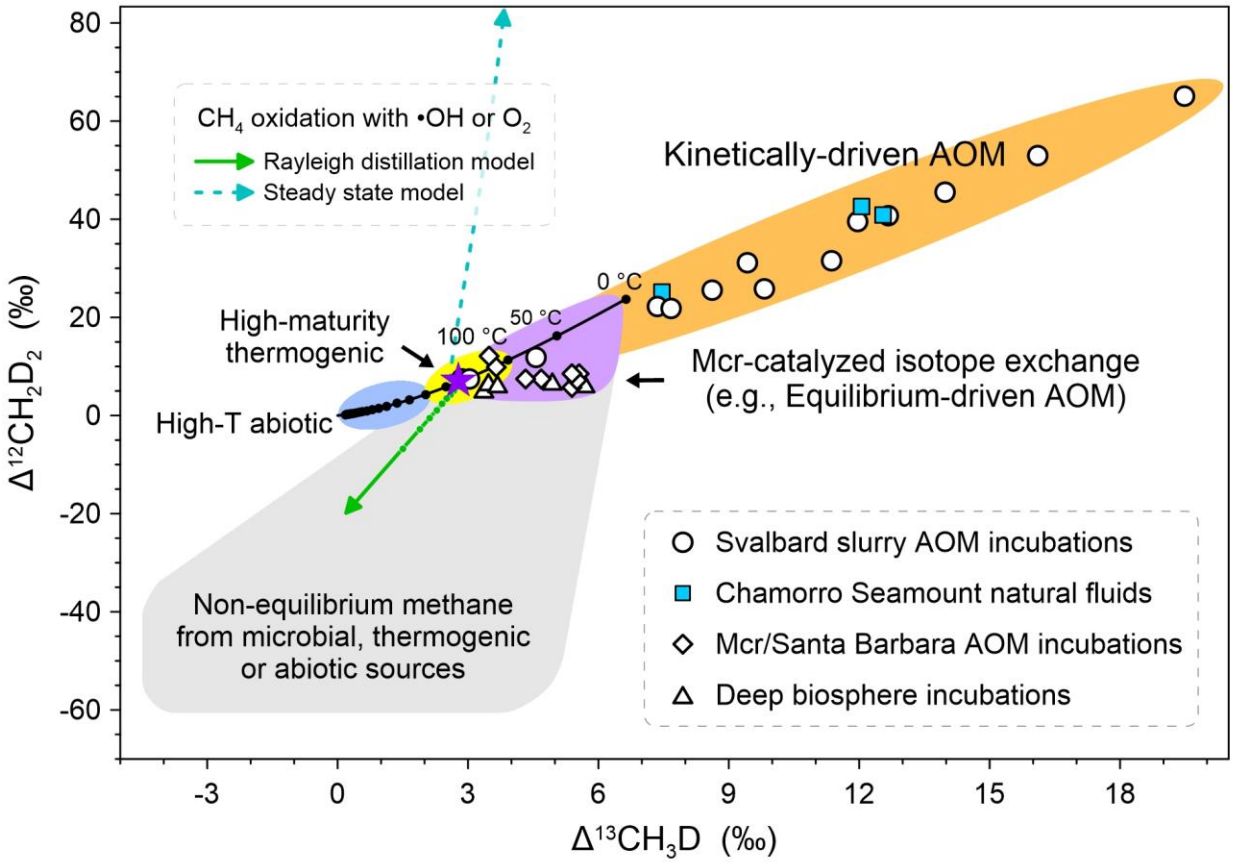

Fig. 2-9 A schematic representation of methane clumped isotope signatures of diverse methane sources and sinks, as well as kinetically- and equilibrium-driven AOM. Circle symbols depict residual methane during incubations of the Svalbard methane seep sediment slurry, while methane data of natural fluids from the South Chamorro Seamount are shown as square symbols. Rhombus symbols illustrate residual methane from the Mcr exchange experiment and incubations of the Santa Barbara Channel sediment slurry. Deep biosphere incubations are shown as triangle symbols. The solid black line depicts theoretical thermodynamic equilibrium

abundances of methane isotopologues, along with corresponding temperatures. The purple star represents the tank gas used in the slurry incubation experiments, and the zone of equilibrium-driven AOM is based on an initial gas of thermogenic origin. For comparison, two modeled trajectories for methane oxidation with OH radical (γ for $^{13}CH_3D$ = 0.999, γ for $^{12}CH_2D_2$ = 0.907; Haghnegahdar et al., 2017), the major methane sink in air, are shown: the solid line is the Rayleigh distillation model (cf. Fig. 6A), the dashed line is the steady-state closed-system model ($(E/k)/n_0$ = 1; cf. Fig. 6E). The trajectories for aerobic oxidation of methane are similar to those of CH_4 + ·OH reaction (Krause et al., 2022). The zonation of methane sources is adopted from Young et al. (2017), Young (2019), Dong et al. (2021), etc. All the plotted data are from this study. The reader is referred to the text for interpretation of the figure.

While intriguing, we presently point out that clumped isotopes for methane would be an approach with a high potential for false negatives, as only anaerobic oxidation of methane, and only under conditions of low reversibility, would reasonably produce a sufficiently diagnostic signal. Another caveat here is that significant technical development would be necessary to measure methane that has an atmospheric mixing ratio on the order of a few ppb. Nonetheless, along with previous isotopologue studies on microbial methanogenesis (Stolper et al., 2015; Wang et al., 2015; Young et al., 2017; Taenzer et al., 2020), our work on the effects of AOM on doubly substituted isotopologues of methane suggests that future missions could benefit from additional research and technique development for *in-situ* mission measurements of methane clumped isotopes on Mars, Enceladus, and other solar system bodies where the methane cycling is a key (bio)geochemical tracer.

5. Conclusions

We performed clumped isotopologue analysis on methane samples from laboratory microbial incubations and natural environments to elucidate the range of clumped isotope effects caused by AOM under different conditions. We found extremely high $\Delta^{13}CH_3D$ and $\Delta^{12}CH_2D_2$ values up to 19.5‰ and 65.1‰, respectively, in microbial incubations of sediment slurries from the Svalbard methane seep and in natural fluids from the South Chamorro Seamount. We found near-equilibrium methane clumped isotope compositions in the Mcr exchange experiment and microbial incubations of sediment slurries and/or fracture fluids from the Santa Barbara Channel and deep biosphere. Thermodynamic drive and the reversibility of AOM intracellular reactions are invoked to interpret the observed differences in $\Delta^{13}CH_3D$ and $\Delta^{12}CH_2D_2$ signatures and the interpretations are consistent with results from a simple, one-step isotopologue fractionation model. Low reversibility of the AOM reaction means a pronounced expression of kinetic fractionation of clumped isotopologues, whereas the Mcr-catalyzed intracellular isotope exchange may be more prominent with higher reversibility. The latter drives the isotopic bond ordering in methane towards equilibrium and may be responsible for the widely observed near-equilibrium clumped isotope signatures in substrate-limited anoxic natural environments where microbial methane production and/or oxidation occur.

Declaration of Competing Interest

The authors declare that they have no known competing financial interests or personal relationships that could have appeared to influence the work reported in this paper.

Acknowledgments

We acknowledge C. Geoffrey Wheat and Jeffrey S. Seewald for providing methane samples from the Chamorro Seamount. Haolan Tang is acknowledged for Panorama Mass Spectrometer training, assistance, and consultation. We are grateful to Evert Duin for the gift of Mcr. We acknowledge Carolynn M. Harris for assistance with water hydrogen isotope analysis and David Yousavich for assistance with sulfate analysis. Formative discussions with Edwin A. Schauble, Jiawen Li, William D. Leavitt, Shuhei Ono, Ao Zhang, and Jingdong Gao helped shape this manuscript. We thank two anonymous reviewers for their helpful and constructive reviews of this paper. The research was funded by the NASA FINESST Fellowship 80NSSC21K1529 (to J. Liu and T. Treude) and the Alfred P. Sloan Foundation under the auspices of the Deep Carbon Observatory (to E.D. Young and R.L. Harris). We acknowledge additional funding for U. Toronto from the NSERC Discovery grant (to B. Sherwood Lollar) and the CIFAR Earth 4D program. R.L. Harris acknowledges financial support from the NASA Award 80NSSC19K1427. J.L. Ash was funded by a C-DEBI Postdoctoral Fellowship during this work.

Appendix A. Supplementary Material

The supplementary material includes supplementary figures S1–S7 and supplementary methods for the $^{13}CH_4$ tracer microcosm experiment at high hydrostatic pressure.

References

Alperin M.J., Reeburgh W.S. and Whiticar M.J. (1988) Carbon and hydrogen isotope fractionation resulting from anaerobic methane oxidation. *Global Biogeochem. Cycles* **2**, 279-288.

Ash J.L., Egger M., Treude T., Kohl I., Cragg B., Parkes R.J., Slomp C.P., Sherwood Lollar B. and Young E.D. (2019) Exchange catalysis during anaerobic methanotrophy revealed by $^{12}CH_2D_2$ and $^{13}CH_3D$ in methane. *Geochem. Persp. Let.* **10**, 26-30.

Atekwana E.A. and Krishnamurthy R.V. (1998) Seasonal variations of dissolved inorganic carbon and $\delta^{13}C$ of surface waters: application of a modified gas evolution technique. *Journal of Hydrology* **205**, 265-278.

Atreya S.K., Mahaffy P.R. and Wong A.-S. (2007) Methane and related trace species on Mars: Origin, loss, implications for life, and habitability. *Planetary and Space Science* **55**, 358-369.

Beulig F., Røy H., McGlynn S.E. and Jørgensen B.B. (2019) Cryptic CH_4 cycling in the sulfate–methane transition of marine sediments apparently mediated by ANME-1 archaea. *The ISME Journal* **13**, 250-262.

Beulig F., Schubert F., Adhikari R.R., Glombitza C., Heuer V.B., Hinrichs K.U., Homola K.L., Inagaki F., Jørgensen B.B., Kallmeyer J., Krause S.J.E., Morono Y., Sauvage J., Spivack A.J. and Treude T. (2022) Rapid metabolism fosters microbial survival in the deep, hot subseafloor biosphere. *Nat. commun.* **13**, 312.

Bigeleisen J. (1952) The Effects of Isotopic Substitution on the rates of Chemical Reactions. *The Journal of Physical Chemistry* **56**, 823-828.

Bigeleisen J. (1955) Statistical Mechanics of Isotopic Systems with Small Quantum Corrections. I. General Considerations and the Rule of the Geometric Mean. *The Journal of Chemical Physics* **23**, 2264-2267.

Bigeleisen J. and Mayer M.G. (1947) Calculation of Equilibrium Constants for Isotopic Exchange Reactions. *The Journal of Chemical Physics* **15**, 261-267.

Cao X., Bao H. and Peng Y. (2019) A kinetic model for isotopologue signatures of methane generated by biotic and abiotic CO2 methanation. *Geochim. Cosmochim. Acta* **249**, 59-75.

Chuang P.-C., Yang T.F., Wallmann K., Matsumoto R., Hu C.-Y., Chen H.-W., Lin S., Sun C.-H., Li H.-C., Wang Y. and Dale A.W. (2019) Carbon isotope exchange during anaerobic oxidation of methane (AOM) in sediments of the northeastern South China Sea. *Geochim. Cosmochim. Acta* **246**, 138-155.

Cord-Ruwisch R. (1985) A quick method for the determination of dissolved and precipitated sulfides in cultures of sulfate-reducing bacteria. *J. Microbiol. Methods* **4**, 33-36.

Curtis A.C., Wheat C.G., Fryer P. and Moyer C.L. (2013) Mariana Forearc Serpentinite Mud Volcanoes Harbor Novel Communities of Extremophilic Archaea. *Geomicrobiol. J.* **30**, 430-441.

Dale A.W., Sommer S., Lomnitz U., Montes I., Treude T., Liebetrau V., Gier J., Hensen C., Dengler M., Stolpovsky K., Bryant L.D. and Wallmann K. (2015) Organic carbon production, mineralisation and preservation on the Peruvian margin. *Biogeosciences* **12**, 1537-1559.

Dong G., Xie H., Formolo M., Lawson M., Sessions A. and Eiler J. (2021) Clumped isotope effects of thermogenic methane formation: Insights from pyrolysis of hydrocarbons. *Geochim. Cosmochim. Acta* **303**, 159-183.

Douglas P.M.J., Stolper D.A., Eiler J.M., Sessions A.L., Lawson M., Shuai Y., Bishop A., Podlaha O.G., Ferreira A.A., Santos Neto E.V., Niemann M., Steen A.S., Huang L., Chimiak L., Valentine D.L., Fiebig J., Luhmann A.J., Seyfried W.E., Etiope G., Schoell M., Inskeep W.P., Moran J.J. and Kitchen N. (2017) Methane clumped isotopes: Progress and potential for a new isotopic tracer. *Org. Geochem.* **113**, 262-282.

Douglas P.M.J., Stolper D.A., Smith D.A., Walter Anthony K.M., Paull C.K., Dallimore S., Wik M., Crill P.M., Winterdahl M., Eiler J.M. and Sessions A.L. (2016) Diverse origins of Arctic and Subarctic methane point source emissions identified with multiply-substituted isotopologues. *Geochim. Cosmochim. Acta* **188**, 163-188.

Eldridge D.L., Korol R., Lloyd M.K., Turner A.C., Webb M.A., Miller T.F., III and Stolper D.A. (2019) Comparison of Experimental vs Theoretical Abundances of $^{13}CH_3D$ and $^{12}CH_2D_2$ for Isotopically Equilibrated Systems from 1 to 500 °C. *ACS Earth and Space Chemistry* **3**, 2747-2764.

Etiope G. and Sherwood Lollar B. (2013) ABIOTIC METHANE ON EARTH. *Rev. Geophys.* **51**, 276-299.

Formisano V., Atreya S., Encrenaz T., Ignatiev N. and Giuranna M. (2004) Detection of Methane in the Atmosphere of Mars. *Science* **306**, 1758-1761.

Fryer P.B. and Salisbury M.H. (2006) Leg 195 synthesis: Site 1200-Serpentinite seamounts of the Izu-Bonin/Mariana convergent plate margin (ODP Leg 125 and 195 drilling results). *Proc. ODP Sci. Res.* **195**, 1-30.

Giunta T., Young E.D., Warr O., Kohl I., Ash J.L., Martini A., Mundle S.O.C., Rumble D., Pérez-Rodríguez I., Wasley M., LaRowe D.E., Gilbert A. and Sherwood Lollar B. (2019) Methane sources and sinks in continental sedimentary systems: New insights from paired clumped isotopologues $^{13}CH_3D$ and $^{12}CH_2D_2$. *Geochim. Cosmochim. Acta* **245**, 327-351.

Gonzalez Y., Nelson D.D., Shorter J.H., McManus J.B., Dyroff C., Formolo M., Wang D.T., Western C.M. and Ono S. (2019) Precise Measurements of $^{12}CH_2D_2$ by Tunable Infrared Laser Direct Absorption Spectroscopy. *Anal. Chem.* **91**, 14967-14974.

Gropp J., Iron M.A. and Halevy I. (2021) Theoretical estimates of equilibrium carbon and hydrogen isotope effects in microbial methane production and anaerobic oxidation of methane. *Geochim. Cosmochim. Acta* **295**, 237-264.

Gropp J., Jin Q. and Halevy I. (2022) Controls on the isotopic composition of microbial methane. *Sci. Adv.* **8**, eabm5713.

Haghnegahdar M.A., Schauble E.A. and Young E.D. (2017) A model for $^{12}CH_2D_2$ and $^{13}CH_3D$ as complementary tracers for the budget of atmospheric CH_4. *Global Biogeochem. Cycles* **31**, 1387-1407.

Harris R.L., Lau M.C.Y., Cadar A., Bartlett D.H., Cason E., Heerden E.v., Onstott T.C. and Hotopp J.C.D. (2018) Draft Genome Sequence of “Candidatus Bathyarchaeota” Archaeon BE326-BA-RLH, an Uncultured Denitrifier and Putative Anaerobic Methanotroph from South Africa's Deep Continental Biosphere. *Microbiology Resource Announcements* **7**, e01295-01218.

Harris R.L., Vetter M.C.Y.L., van Heerden E., Cason E., Vermeulen J.-G., Taneja A., Kieft T.L., DeCoste C.J., Laevsky G.S. and Onstott T.C. (2021) FISH-TAMB, a Fixation-Free

mRNA Fluorescent Labeling Technique to Target Transcriptionally Active Members in Microbial Communities. *Microb. Ecol.*

Hayes J.M. (2001) Fractionation of Carbon and Hydrogen Isotopes in Biosynthetic Processes. *Rev. Mineral Geochem.* **43**, 225-277.

Heuer V.B., Inagaki F., Morono Y., Kubo Y., Maeda L. and the Expedition 370 Scientists (2017) Temperature Limit of the Deep Biosphere off Muroto. *Proceedings of the International Ocean Discovery Program*, Volume 370.

Heuer V.B., Inagaki F., Morono Y., Kubo Y., Spivack A.J., Viehweger B., Treude T., Beulig F., Schubotz F., Tonai S., Bowden S.A., Cramm M., Henkel S., Hirose T., Homola K., Hoshino T., Ijiri A., Imachi H., Kamiya N., Kaneko M., Lagostina L., Manners H., McClelland H.-L., Metcalfe K., Okutsu N., Pan D., Raudsepp M.J., Sauvage J., Tsang M.-Y., Wang D.T., Whitaker E., Yamamoto Y., Yang K., Maeda L., Adhikari R.R., Glombitza C., Hamada Y., Kallmeyer J., Wendt J., Wörmer L., Yamada Y., Kinoshita M. and Hinrichs K.-U. (2020) Temperature limits to deep subseafloor life in the Nankai Trough subduction zone. *Science* **370**, 1230-1234.

Hoehler T.M., Borowski W.S., Alperin M.J., Rodriguez N.M. and Paull C.K. (2000) Model, stable isotope, and radiotracer characterization of anaerobic methane oxidation in gas hydrate-bearing sediments of the Blake Ridge. *Proceedings of the Ocean Drilling Program, Scientific Results* **164**, 79-85.

Hoehler T.M. and Jørgensen B.B. (2013) Microbial life under extreme energy limitation. *Nature Reviews Microbiology* **11**, 83-94.

Holler T., Wegener G., Knittel K., Boetius A., Brunner B., Kuypers M.M.M. and Widdel F. (2009) Substantial $^{13}C/^{12}C$ and D/H fractionation during anaerobic oxidation of methane by marine consortia enriched in vitro. *Environmental Microbiology Reports* **1**, 370-376.

Holler T., Wegener G., Niemann H., Deusner C., Ferdelman T.G., Boetius A., Brunner B. and Widdel F. (2011) Carbon and sulfur back flux during anaerobic microbial oxidation of methane and coupled sulfate reduction. *P. Natl. Acad. Sci. USA* **108**, E1484-E1490.

House C.H., Beal E.J. and Orphan V.J. (2011) The Apparent Involvement of ANMEs in Mineral Dependent Methane Oxidation, as an Analog for Possible Martian Methanotrophy. *Life* **1**, 19-33.

House C.H., Wong G.M., Webster C.R., Flesch G.J., Franz H.B., Stern J.C., Pavlov A., Atreya S.K., Eigenbrode J.L., Gilbert A., Hofmann A.E., Millan M., Steele A., Glavin D.P., Malespin C.A. and Mahaffy P.R. (2022) Depleted carbon isotope compositions observed at Gale crater, Mars. *P. Natl. Acad. Sci. USA* **119**, e2115651119.

IPCC (2021) Climate Change 2021: The Physical Science Basis. Contribution of Working Group I to the Sixth Assessment Report of the Intergovernmental Panel on Climate Change. IPCC, Geneva, Switzerland.

Jordan S.F.A., Treude T., Leifer I., Janßen R., Werner J., Schulz-Vogt H. and Schmale O. (2020) Bubble-mediated transport of benthic microorganisms into the water column: Identification of methanotrophs and implication of seepage intensity on transport efficiency. *Scientific Reports* **10**, 4682.

Joye S.B., Boetius A., Orcutt B.N., Montoya J.P., Schulz H.N., Erickson M.J. and Lugo S.K. (2004) The anaerobic oxidation of methane and sulfate reduction in sediments from Gulf of Mexico cold seeps. *Chem. Geol.* **205**, 219-238.

Kallmeyer J., Ferdelman T.G., Weber A., Fossing H. and Jørgensen B.B. (2004) A cold chromium distillation procedure for radiolabeled sulfide applied to sulfate reduction measurements. *Limnol. Oceanogr. Methods* **2**, 171-180.

Kawagucci S., Miyazaki J., Morono Y., Seewald J.S., Wheat C.G. and Takai K. (2018) Cool, alkaline serpentinite formation fluid regime with scarce microbial habitability and possible abiotic synthesis beneath the South Chamorro Seamount. *Progress in Earth and Planetary Science* **5**, 74.

Kevorkian R.T., Callahan S., Winstead R. and Lloyd K.G. (2021) ANME-1 archaea may drive methane accumulation and removal in estuarine sediments. *Environmental Microbiology Reports* **13**, 185-194.

Kopec B.G., Feng X., Posmentier E.S. and Sonder L.J. (2019) Seasonal Deuterium Excess Variations of Precipitation at Summit, Greenland, and their Climatological Significance. *Journal of Geophysical Research: Atmospheres* **124**, 72-91.

Krause S.J.E., Liu J., Young E.D. and Treude T. (2022) $\Delta^{13}CH_3D$ and $\Delta^{12}CH_2D_2$ signatures of methane aerobically oxidized by Methylosinus trichosporium with implications for deciphering the provenance of methane gases. *Earth Planet. Sci. Lett.* **593**, 117681.

Krause S.J.E. and Treude T. (2021) Deciphering cryptic methane cycling: Coupling of methylotrophic methanogenesis and anaerobic oxidation of methane in hypersaline coastal wetland sediment. *Geochim. Cosmochim. Acta* **302**, 160-174.

Labidi J., Young E.D., Giunta T., Kohl I.E., Seewald J., Tang H., Lilley M.D. and Früh-Green G.L. (2020) Methane thermometry in deep-sea hydrothermal systems: Evidence for re-ordering of doubly-substituted isotopologues during fluid cooling. *Geochim. Cosmochim. Acta* **288**, 248-261.

Lalk E., Pape T., Gruen D.S., Kaul N., Karolewski J.S., Bohrmann G. and Ono S. (2022) Clumped methane isotopologue-based temperature estimates for sources of methane in marine gas hydrates and associated vent gases. *Geochim. Cosmochim. Acta* **327**, 276-297.

Laso-Pérez R., Krukenberg V., Musat F. and Wegener G. (2018) Establishing anaerobic hydrocarbon-degrading enrichment cultures of microorganisms under strictly anoxic conditions. *Nature Protocols* **13**, 1310-1330.

Lau M.C.Y., Kieft T.L., Kuloyo O., Linage-Alvarez B., van Heerden E., Lindsay M.R., Magnabosco C., Wang W., Wiggins J.B., Guo L., Perlman D.H., Kyin S., Shwe H.H., Harris R.L., Oh Y., Yi M.J., Purtschert R., Slater G.F., Ono S., Wei S., Li L., Sherwood Lollar B. and Onstott T.C. (2016) An oligotrophic deep-subsurface community dependent on syntrophy is dominated by sulfur-driven autotrophic denitrifiers. *P. Natl. Acad. Sci. USA* **113**, E7927-E7936.

Lee T.J., Martin J.M.L. and Taylor P.R. (1995) An accurate ab initio quartic force field and vibrational frequencies for CH_4 and isotopomers. *The Journal of Chemical Physics* **102**, 254-261.

Lefèvre F. (2019) The Enigma of Methane on Mars, in: Cavalazzi B., Westall F. (Eds.), Biosignatures for Astrobiology. Springer International Publishing, Cham, pp. 253-266.

Liu Q. and Liu Y. (2016) Clumped-isotope signatures at equilibrium of CH_4, NH_3, H_2O, H_2S and SO_2. *Geochim. Cosmochim. Acta* **175**, 252-270.

Ma Q., Wu S. and Tang Y. (2008) Formation and abundance of doubly-substituted methane isotopologues ($^{13}CH_3D$) in natural gas systems. *Geochim. Cosmochim. Acta* **72**, 5446-5456.

Mahlert F., Grabarse W., Kahnt J., Thauer R.K. and Duin E.C. (2002) The nickel enzyme methyl-coenzyme M reductase from methanogenic archaea: in vitro interconversions among the EPR detectable MCR-red1 and MCR-red2 states. *JBIC Journal of Biological Inorganic Chemistry* **7**, 101-112.

Mariotti A., Germon J.C., Hubert P., Kaiser P., Letolle R., Tardieux A. and Tardieux P. (1981) Experimental determination of nitrogen kinetic isotope fractionation: Some principles; illustration for the denitrification and nitrification processes. *Plant Soil* **62**, 413-430.

Marlow J.J., LaRowe D.E., Ehlmann B.L., Amend J.P. and Orphan V.J. (2014) The Potential for Biologically Catalyzed Anaerobic Methane Oxidation on Ancient Mars. *Astrobiology* **14**, 292-307.

Melaniuk K., Sztybor K., Treude T., Sommer S. and Rasmussen T.L. (2022) Influence of methane seepage on isotopic signatures in living deep-sea benthic foraminifera, 79° N. *Scientific Reports* **12**, 1169.

National Academies of Sciences, Engineering, and Medicine (2022) Origins, Worlds, and Life: A Decadal Strategy for Planetary Science and Astrobiology 2023-2032. The National Academies Press, Washington, DC.

Northrop D.B. (1981) The Expression of Isotope Effects on Enzyme-Catalyzed Reactions. *Annu. Rev. Biochem.* **50**, 103-131.

Ono S., Rhim J.H., Gruen D.S., Taubner H., Kölling M. and Wegener G. (2021) Clumped isotopologue fractionation by microbial cultures performing the anaerobic oxidation of methane. *Geochim. Cosmochim. Acta* **293**, 70-85.

Ono S., Rhim J.H. and Ryberg E.C. (2022) Rate limits and isotopologue fractionations for microbial methanogenesis examined with combined pathway protein cost and isotopologue flow network models. *Geochim. Cosmochim. Acta* **325**, 296-315.

Ono S., Wang D.T., Gruen D.S., Sherwood Lollar B., Zahniser M.S., McManus B.J. and Nelson D.D. (2014) Measurement of a Doubly Substituted Methane Isotopologue, $^{13}CH_3D$, by Tunable Infrared Laser Direct Absorption Spectroscopy. *Anal. Chem.* **86**, 6487-6494.

Reeburgh W.S. (2007) Global Methane Biogeochemistry, in: Holland H.D., Turekian K.K. (Eds.), Treatise on Geochemistry. Pergamon, Oxford, pp. 1-32.

Repeta D.J., Ferrón S., Sosa O.A., Johnson C.G., Repeta L.D., Acker M., DeLong E.F. and Karl D.M. (2016) Marine methane paradox explained by bacterial degradation of dissolved organic matter. *Nat. Geosci.* **9**, 884-887.

Röckmann T., Popa M.E., Krol M.C. and Hofmann M.E.G. (2016) Statistical clumped isotope signatures. *Scientific Reports* **6**, 31947.

Scheller S., Goenrich M., Boecher R., Thauer R.K. and Jaun B. (2010) The key nickel enzyme of methanogenesis catalyses the anaerobic oxidation of methane. *Nature* **465**, 606-608.

Scheller S., Goenrich M., Thauer R.K. and Jaun B. (2013) Methyl-Coenzyme M Reductase from Methanogenic Archaea: Isotope Effects on the Formation and Anaerobic Oxidation of Methane. *J. Am. Chem. Soc.* **135**, 14975-14984.

Schoell M. (1983) Genetic Characterization of Natural Gases. *AAPG Bulletin* **67**, 2225-2238.

Seewald J.S., Doherty K.W., Hammar T.R. and Liberatore S.P. (2002) A new gas-tight isobaric sampler for hydrothermal fluids. *Deep-Sea Res. Pt. I* **49**, 189-196.

Sherwood Lollar B., Lacrampe-Couloume G., Slater G.F., Ward J., Moser D.P., Gihring T.M., Lin L.H. and Onstott T.C. (2006) Unravelling abiogenic and biogenic sources of methane in the Earth's deep subsurface. *Chem. Geol.* **226**, 328-339.

Stolper D.A., Lawson M., Davis C.L., Ferreira A.A., Neto E.V.S., Ellis G.S., Lewan M.D., Martini A.M., Tang Y., Schoell M., Sessions A.L. and Eiler J.M. (2014a) Formation temperatures of thermogenic and biogenic methane. *Science* **344**, 1500-1503.

Stolper D.A., Martini A.M., Clog M., Douglas P.M., Shusta S.S., Valentine D.L., Sessions A.L. and Eiler J.M. (2015) Distinguishing and understanding thermogenic and biogenic sources of methane using multiply substituted isotopologues. *Geochim. Cosmochim. Acta* **161**, 219-247.

Stolper D.A., Sessions A.L., Ferreira A.A., Santos Neto E.V., Schimmelmann A., Shusta S.S., Valentine D.L. and Eiler J.M. (2014b) Combined ^{13}C–D and D–D clumping in methane: Methods and preliminary results. *Geochim. Cosmochim. Acta* **126**, 169-191.

Taenzer L., Labidi J., Masterson A.L., Feng X., Rumble D., Young E.D. and Leavitt W.D. (2020) Low $\Delta^{12}CH_2D_2$ values in microbialgenic methane result from combinatorial isotope effects. *Geochim. Cosmochim. Acta* **285**, 225-236.

Takai K., Moyer C.L., Miyazaki M., Nogi Y., Hirayama H., Nealson K.H. and Horikoshi K. (2005) Marinobacter alkaliphilus sp. nov., a novel alkaliphilic bacterium isolated from subseafloor alkaline serpentine mud from Ocean Drilling Program Site 1200 at South Chamorro Seamount, Mariana Forearc. *Extremophiles* **9**, 17-27.

Thiagarajan N., Kitchen N., Xie H., Ponton C., Lawson M., Formolo M. and Eiler J. (2020) Identifying thermogenic and microbial methane in deep water Gulf of Mexico Reservoirs. *Geochim. Cosmochim. Acta* **275**, 188-208.

Thompson M.A., Krissansen-Totton J., Wogan N., Telus M. and Fortney J.J. (2022) The case and context for atmospheric methane as an exoplanet biosignature. *P. Natl. Acad. Sci. USA* **119**, e2117933119.

Timmers P.H.A., Welte C.U., Koehorst J.J., Plugge C.M., Jetten M.S.M. and Stams A.J.M. (2017) Reverse Methanogenesis and Respiration in Methanotrophic Archaea. *Archaea* **2017**, 22.

Treude T., Krüger M., Boetius A. and Jørgensen B.B. (2005) Environmental control on anaerobic oxidation of methane in the gassy sediments of Eckernförde Bay (German Baltic). *Limnol. Oceanogr.* **50**, 1771-1786.

Treude T., Orphan V., Knittel K., Gieseke A., House C.H. and Boetius A. (2007) Consumption of Methane and CO2 by Methanotrophic Microbial Mats from Gas Seeps of the Anoxic Black Sea. *Appl. Environ. Microbiol.* **73**, 2271-2283.

Treude T. and Ziebis W. (2010) Methane oxidation in permeable sediments at hydrocarbon seeps in the Santa Barbara Channel, California. *Biogeosciences* **7**, 3095-3108.

Turner A.C., Korol R., Eldridge D.L., Bill M., Conrad M.E., Miller T.F. and Stolper D.A. (2021) Experimental and theoretical determinations of hydrogen isotopic equilibrium in the system CH_4–H_2–H_2O from 3 to 200 °C. *Geochim. Cosmochim. Acta* **314**, 223-269.

Tyne R.L., Barry P.H., Lawson M., Byrne D.J., Warr O., Xie H., Hillegonds D.J., Formolo M., Summers Z.M., Skinner B., Eiler J.M. and Ballentine C.J. (2021) Rapid microbial methanogenesis during CO2 storage in hydrocarbon reservoirs. *Nature* **600**, 670-674.

Urey H.C. (1947) The thermodynamic properties of isotopic substances. *Journal of the Chemical Society (Resumed)*, 562-581.

Waite J.H., Glein C.R., Perryman R.S., Teolis B.D., Magee B.A., Miller G., Grimes J., Perry M.E., Miller K.E., Bouquet A., Lunine J.I., Brockwell T. and Bolton S.J. (2017) Cassini finds molecular hydrogen in the Enceladus plume: Evidence for hydrothermal processes. *Science* **356**, 155-159.

Wang D.T., Gruen D.S., Lollar B.S., Hinrichs K.-U., Stewart L.C., Holden J.F., Hristov A.N., Pohlman J.W., Morrill P.L., Könneke M., Delwiche K.B., Reeves E.P., Sutcliffe C.N., Ritter D.J., Seewald J.S., McIntosh J.C., Hemond H.F., Kubo M.D., Cardace D., Hoehler T.M. and Ono S. (2015) Nonequilibrium clumped isotope signals in microbial methane. *Science* **348**, 428-431.

Wang D.T., Welander P.V. and Ono S. (2016) Fractionation of the methane isotopologues $^{13}CH_4$, $^{12}CH_3D$, and $^{13}CH_3D$ during aerobic oxidation of methane by Methylococcus capsulatus (Bath). *Geochim. Cosmochim. Acta* **192**, 186-202.

Warr O., Young E.D., Giunta T., Kohl I.E., Ash J.L. and Sherwood Lollar B. (2021) High-resolution, long-term isotopic and isotopologue variation identifies the sources and sinks of methane in a deep subsurface carbon cycle. *Geochim. Cosmochim. Acta* **294**, 315-334.

Webb M.A. and Miller T.F. (2014) Position-Specific and Clumped Stable Isotope Studies: Comparison of the Urey and Path-Integral Approaches for Carbon Dioxide, Nitrous Oxide, Methane, and Propane. *The Journal of Physical Chemistry A* **118**, 467-474.

Webster C.R., Mahaffy P.R., Atreya S.K., Flesch G.J., Mischna M.A., Meslin P.-Y., Farley K.A., Conrad P.G., Christensen L.E., Pavlov A.A., Martín-Torres J., Zorzano M.-P., McConnochie T.H., Owen T., Eigenbrode J.L., Glavin D.P., Steele A., Malespin C.A., Archer P.D., Sutter B., Coll P., Freissinet C., McKay C.P., Moores J.E., Schwenzer S.P.,

Bridges J.C., Navarro-Gonzalez R., Gellert R. and Lemmon M.T. (2015) Mars methane detection and variability at Gale crater. *Science* **347**, 415-417.

Wegener G., Gropp J., Taubner H., Halevy I. and Elvert M. (2021) Sulfate-dependent reversibility of intracellular reactions explains the opposing isotope effects in the anaerobic oxidation of methane. *Sci. Adv.* **7**, eabe4939.

Wheat C.G., Fryer P., Fisher A.T., Hulme S., Jannasch H., Mottl M.J. and Becker K. (2008) Borehole observations of fluid flow from South Chamorro Seamount, an active serpentinite mud volcano in the Mariana forearc. *Earth Planet. Sci. Lett.* **267**, 401-409.

Wheat C.G., Seewald J.S. and Takai K. (2020) Fluid transport and reaction processes within a serpentinite mud volcano: South Chamorro Seamount. *Geochim. Cosmochim. Acta* **269**, 413-428.

Whitehill A.R., Joelsson L.M.T., Schmidt J.A., Wang D.T., Johnson M.S. and Ono S. (2017) Clumped isotope effects during OH and Cl oxidation of methane. *Geochim. Cosmochim. Acta* **196**, 307-325.

Whiticar M.J. (1999) Carbon and hydrogen isotope systematics of bacterial formation and oxidation of methane. *Chem. Geol.* **161**, 291-314.

Widdel F. and Bak F. (1992) Gram-Negative Mesophilic Sulfate-Reducing Bacteria, in: Balows A., Trüper H.G., Dworkin M., Harder W., Schleifer K.-H. (Eds.), The Prokaryotes: A Handbook on the Biology of Bacteria: Ecophysiology, Isolation, Identification, Applications. Springer New York, New York, NY, pp. 3352-3378.

Xiao K.-Q., Beulig F., Kjeldsen K.U., Jørgensen B.B. and Risgaard-Petersen N. (2017) Concurrent Methane Production and Oxidation in Surface Sediment from Aarhus Bay, Denmark. *Front. Microbiol.* **8**.

Xie H., Dong G., Formolo M., Lawson M., Liu J., Cong F., Mangenot X., Shuai Y., Ponton C. and Eiler J. (2021) The evolution of intra- and inter-molecular isotope equilibria in natural gases with thermal maturation. *Geochim. Cosmochim. Acta* **307**, 22-41.

Yamamoto S., Alcauskas J.B. and Crozier T.E. (1976) Solubility of methane in distilled water and seawater. *Journal of Chemical & Engineering Data* **21**, 78-80.

Yan Z., Joshi P., Gorski C.A. and Ferry J.G. (2018) A biochemical framework for anaerobic oxidation of methane driven by Fe (III)-dependent respiration. *Nat. commun.* **9**.

Yeung L.Y. (2016) Combinatorial effects on clumped isotopes and their significance in biogeochemistry. *Geochim. Cosmochim. Acta* **172**, 22-38.

York D., Evensen N.M., Martínez M.L. and Delgado J.D.B. (2004) Unified equations for the slope, intercept, and standard errors of the best straight line. *American Journal of Physics* **72**, 367-375.

Yoshinaga M.Y., Holler T., Goldhammer T., Wegener G., Pohlman J.W., Brunner B., Kuypers M.M.M., Hinrichs K.-U. and Elvert M. (2014) Carbon isotope equilibration during sulphate-limited anaerobic oxidation of methane. *Nat. Geosci.* **7**, 190-194.

Young E.D. (2019) A Two-Dimensional Perspective on CH_4 Isotope Clumping: Distinguishing Process from Source, in: Orcutt B.N., Daniel I., Dasgupta R. (Eds.), Deep Carbon: Past to Present. Cambridge University Press, Cambridge, pp. 388-414.

Young E.D., Kohl I.E., Lollar B.S., Etiope G., Rumble D., Li S., Haghnegahdar M.A., Schauble E.A., McCain K.A., Foustoukos D.I., Sutclife C., Warr O., Ballentine C.J., Onstott T.C., Hosgormez H., Neubeck A., Marques J.M., Pérez-Rodríguez I., Rowe A.R., LaRowe D.E., Magnabosco C., Yeung L.Y., Ash J.L. and Bryndzia L.T. (2017) The relative

abundances of resolved $^{12}CH_2D_2$ and $^{13}CH_3D$ and mechanisms controlling isotopic bond ordering in abiotic and biotic methane gases. *Geochim. Cosmochim. Acta* **203**, 235-264.

Young E.D., Rumble D., Freedman P. and Mills M. (2016) A large-radius high-mass-resolution multiple-collector isotope ratio mass spectrometer for analysis of rare isotopologues of O_2, N_2, CH_4 and other gases. *Int. J. Mass spectrom.* **401**, 1-10.

Yu L., He D., Yang L., Rensing C., Zeng R.J. and Zhou S. (2022) Anaerobic methane oxidation coupled to ferrihydrite reduction by Methanosarcina barkeri. *Sci. Total Environ.* **844**, 157235.

Yung Y.L., Chen P., Nealson K., Atreya S., Beckett P., Blank J.G., Ehlmann B., Eiler J., Etiope G., Ferry J.G., Forget F., Gao P., Hu R., Kleinböhl A., Klusman R., Lefèvre F., Miller C., Mischna M., Mumma M., Newman S., Oehler D., Okumura M., Oremland R., Orphan V., Popa R., Russell M., Shen L., Sherwood Lollar B., Staehle R., Stamenković V., Stolper D., Templeton A., Vandaele A.C., Viscardy S., Webster C.R., Wennberg P.O., Wong M.L. and Worden J. (2018) Methane on Mars and Habitability: Challenges and Responses. *Astrobiology* **18**, 1221-1242.

Zhang J., Quay P.D. and Wilbur D.O. (1995) Carbon isotope fractionation during gas-water exchange and dissolution of CO_2. *Geochim. Cosmochim. Acta* **59**, 107-114.

Zhang N., Snyder G.T., Lin M., Nakagawa M., Gilbert A., Yoshida N., Matsumoto R. and Sekine Y. (2021) Doubly substituted isotopologues of methane hydrate ($^{13}CH_3D$ and $^{12}CH_2D_2$): Implications for methane clumped isotope effects, source apportionments and global hydrate reservoirs. *Geochim. Cosmochim. Acta* **315**, 127-151.

Supplementary Material: Liu et al. Reversibility controls on extreme methane clumped isotope signatures from anaerobic oxidation of methane

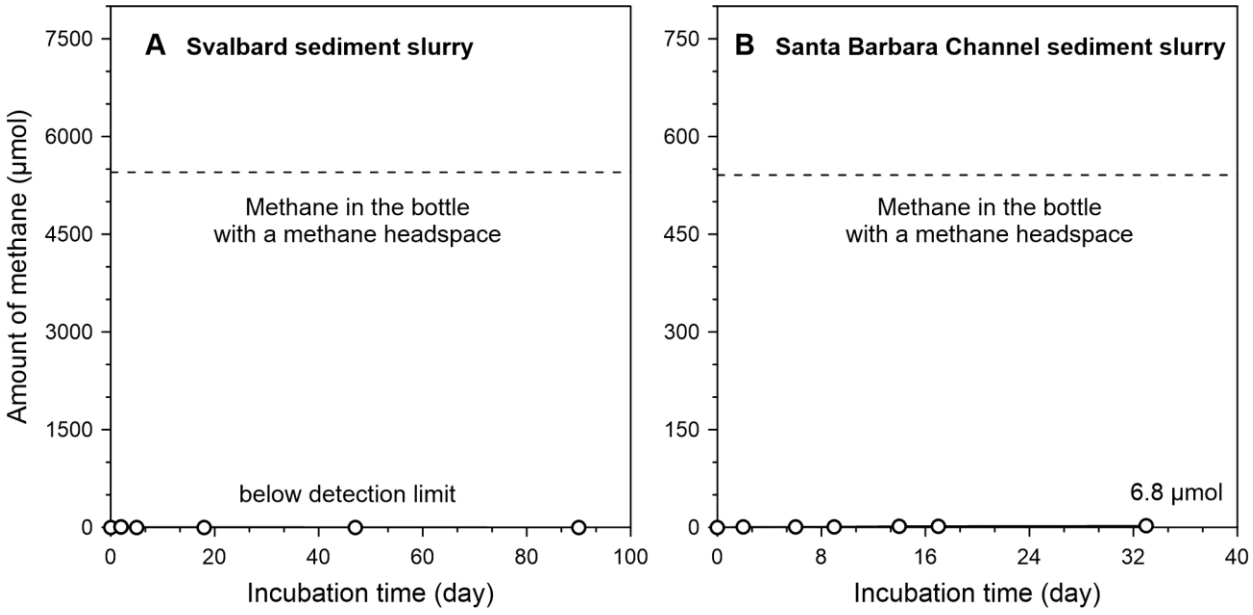

Fig. 2-S1 Methane production (amount of methane over time) in the methane-free control experiment: (A) Svalbard sediment slurry, (B) Santa Barbara Channel sediment slurry. For reference, dashed lines represent the amount of methane in the bottle with a pure methane headspace. The control incubation of Santa Barbara slurry showed a small amount of methane build-up in the headspace of the sediment slurry over the 33 days. We interpret this methane increase as the result of equilibration between the slurry and gaseous phases rather than microbial methanogenesis, because unlike the Svalbard sediment slurry (flushed three times), the Santa Barbara Channel sediment slurry was flushed only one time following previous experiments with a pure methane headspace. However, if the methane build-up was the result of microbial methanogenesis, it would represent a very small fraction (ca. 1%) of the methane that is normally added during our experiments, resulting in a negligible isotope effect.

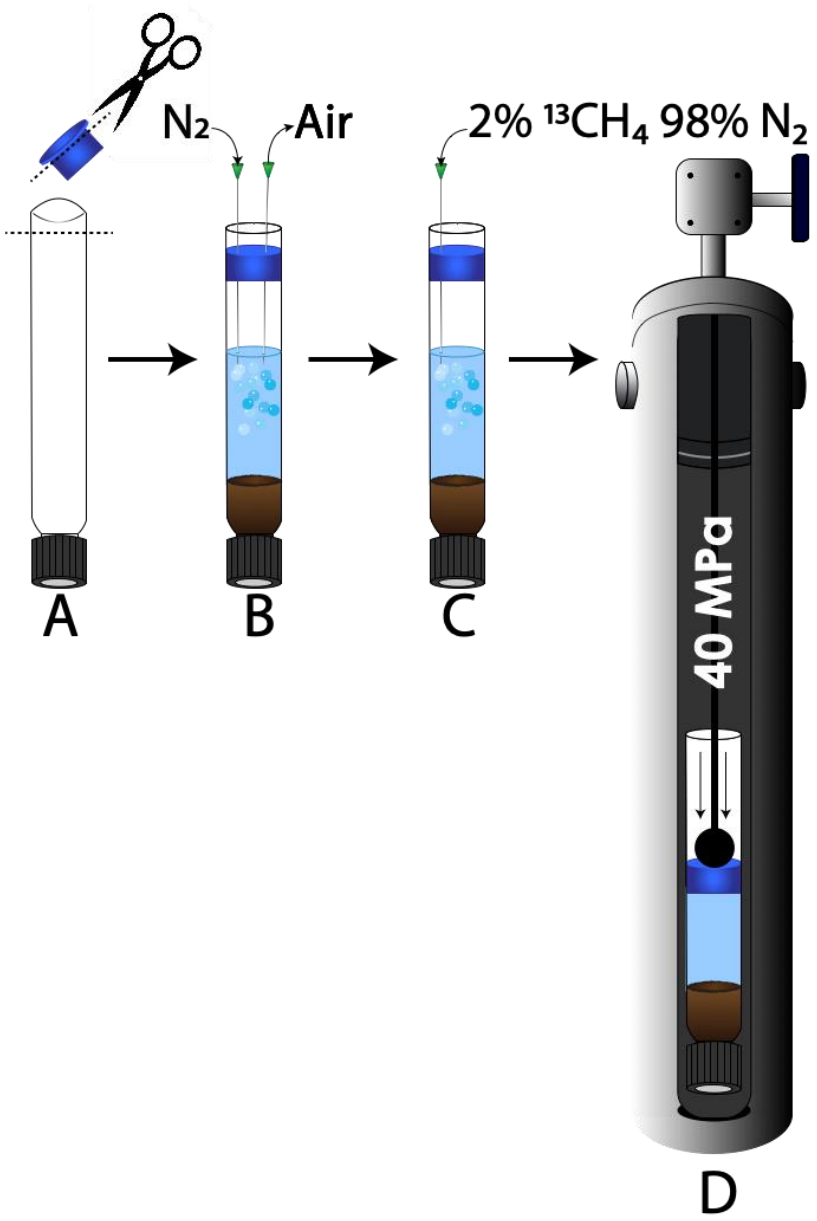

Fig. 2-S2 High pressure cultivation scheme. (A) The bottoms of Hungate tubes are removed using a glass cutter and replaced with a hand-made piston prepared from a butyl rubber stopper. (B) Headspace is sparged with N_2 gas to remove lab air following anaerobic addition of sediment and media. (C) Headspace is replaced with N_2 atmosphere with ^{13}C-labeled CH_4. (D) Cross-section of stainless-steel hydrostatic pressure vessel containing inverted Hungate tubes. Pressurization to 40 MPa pushes the $^{13}CH_4$ headspace into solution by way of the butyl rubber piston.

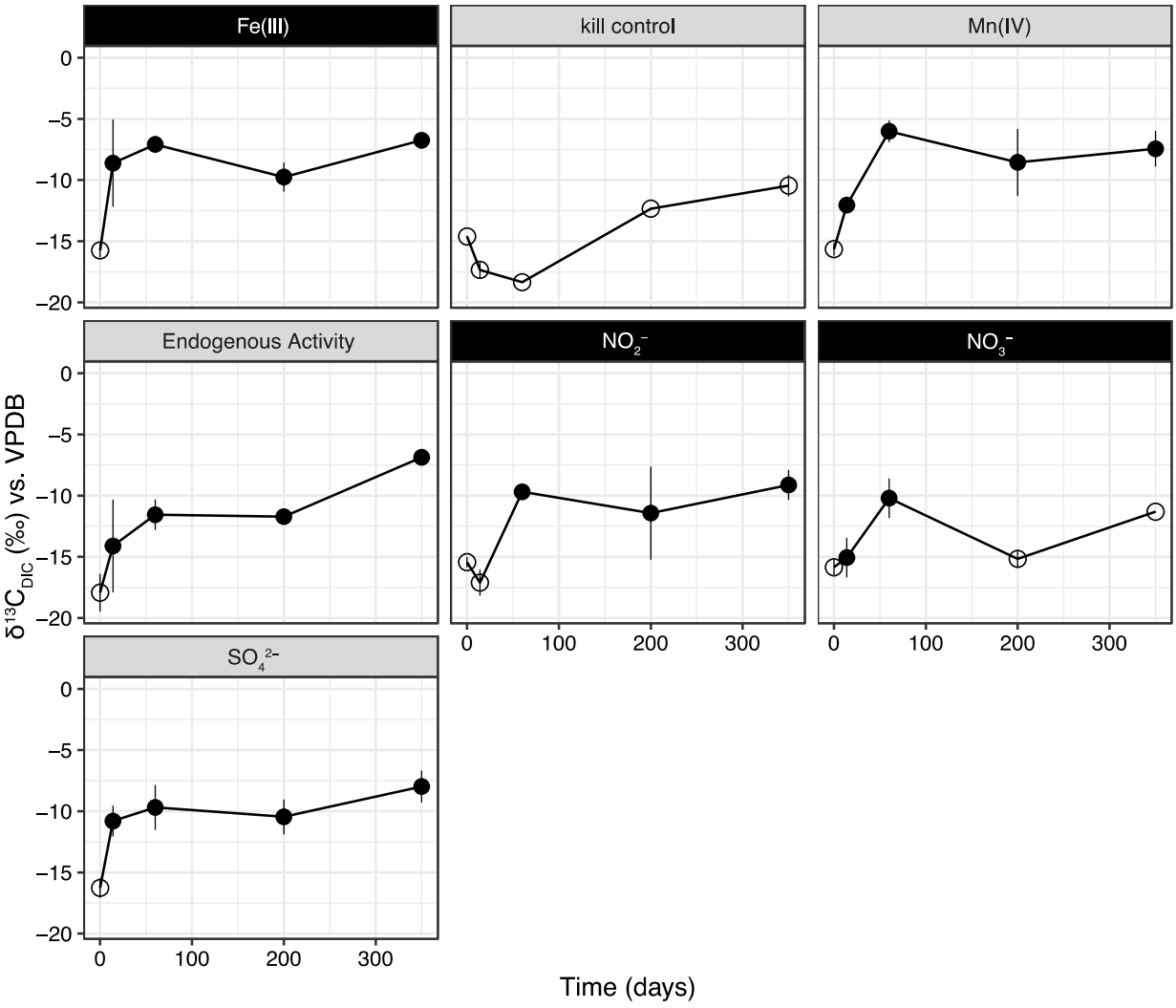

Fig. 2-S3 $\delta^{13}C_{DIC}$ in high pressure (40 MPa) Nankai deep biosphere sediments incubated with $^{13}CH_4$. Rates were calculated relative to an autoclaved kill control according to Eq. S1. Black facets indicate electron acceptor conditions where $\Delta^{13}CH_3D$ and $\Delta^{12}CH_2D_2$ were measured in parallel experiments incubated at ambient pressure (ca. 150 kPa) and with 100% natural abundance methane. Significance (closed circles) was determined at each time point if $\delta^{13}C_{DIC\_sample} > (\delta^{13}C_{DIC\_kill} + 3*SD_{kill})$. $\delta^{13}C_{DIC}$ was calculated according to Eq. S1.

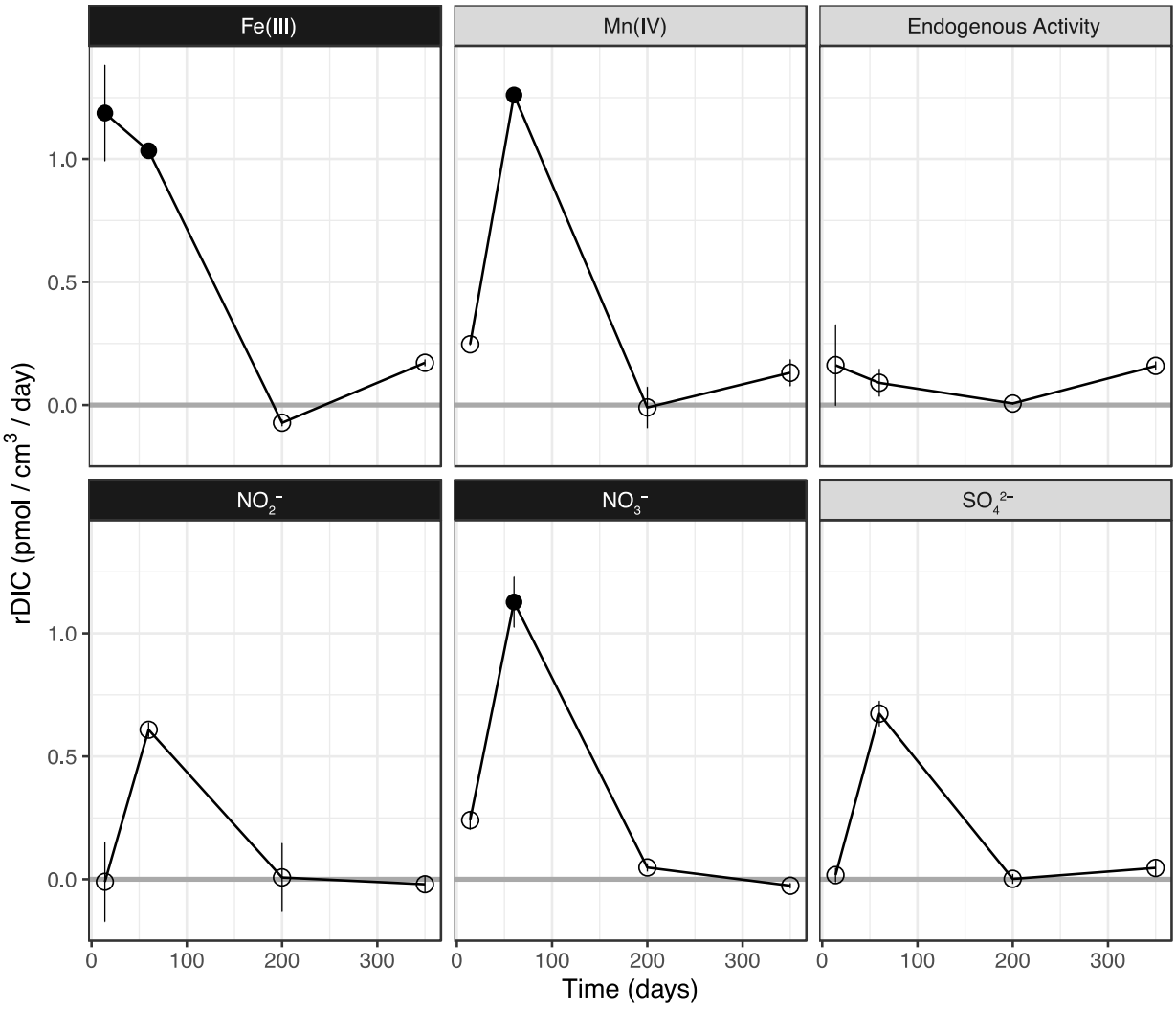

Fig. 2-S4 Rates of AOM $^{13}C_{DIC}$ production (r_{DIC}) in high pressure (40 MPa) Nankai deep biosphere sediments incubated with $^{13}CH_4$. Rates were calculated relative to an autoclaved kill control (normalized here as $r_{DIC} = 0$) according to Eq. S2. Black facets indicate electron acceptor conditions where $\Delta^{12}CH_2D_2$ and $\Delta^{13}CH_3D$ were measured in parallel experiments incubated at ambient pressure (ca. 150 kPa) and with 100% natural abundance methane. Closed circles indicate statistically significant r_{DIC} relative to the kill control (one-tailed test, $P < 0.05$).

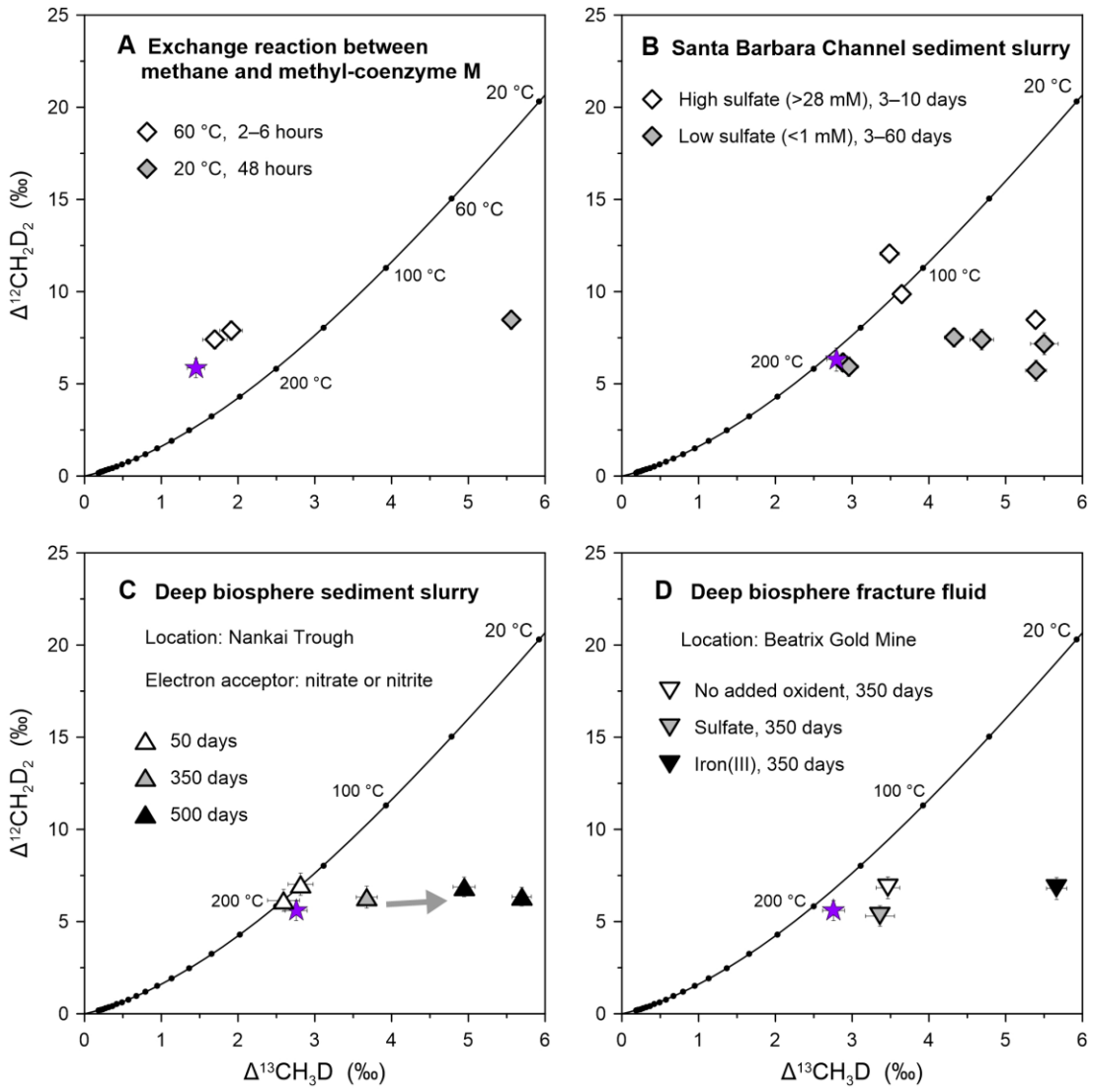

Fig. 2-S5 Equilibrium-driven methane isotopologue data with detailed description for residual methane in incubation experiments. (A) Exchange reaction between methane and methyl-coenzyme M. (B) Santa Barbara Channel sediment incubation with sulfate. (C) Nankai Trough sediment incubation with nitrate or nitrite. (D) Beatrix Gold Mine fracture fluid incubation with sulfate or iron (III). Electron acceptor, incubation time and temperature are shown in the legend of each panel. The purple stars represent the initial tank gas. The solid black line depicts theoretical thermodynamic equilibrium abundances of methane isotopologues, along with corresponding temperatures. Error bars are one standard error.

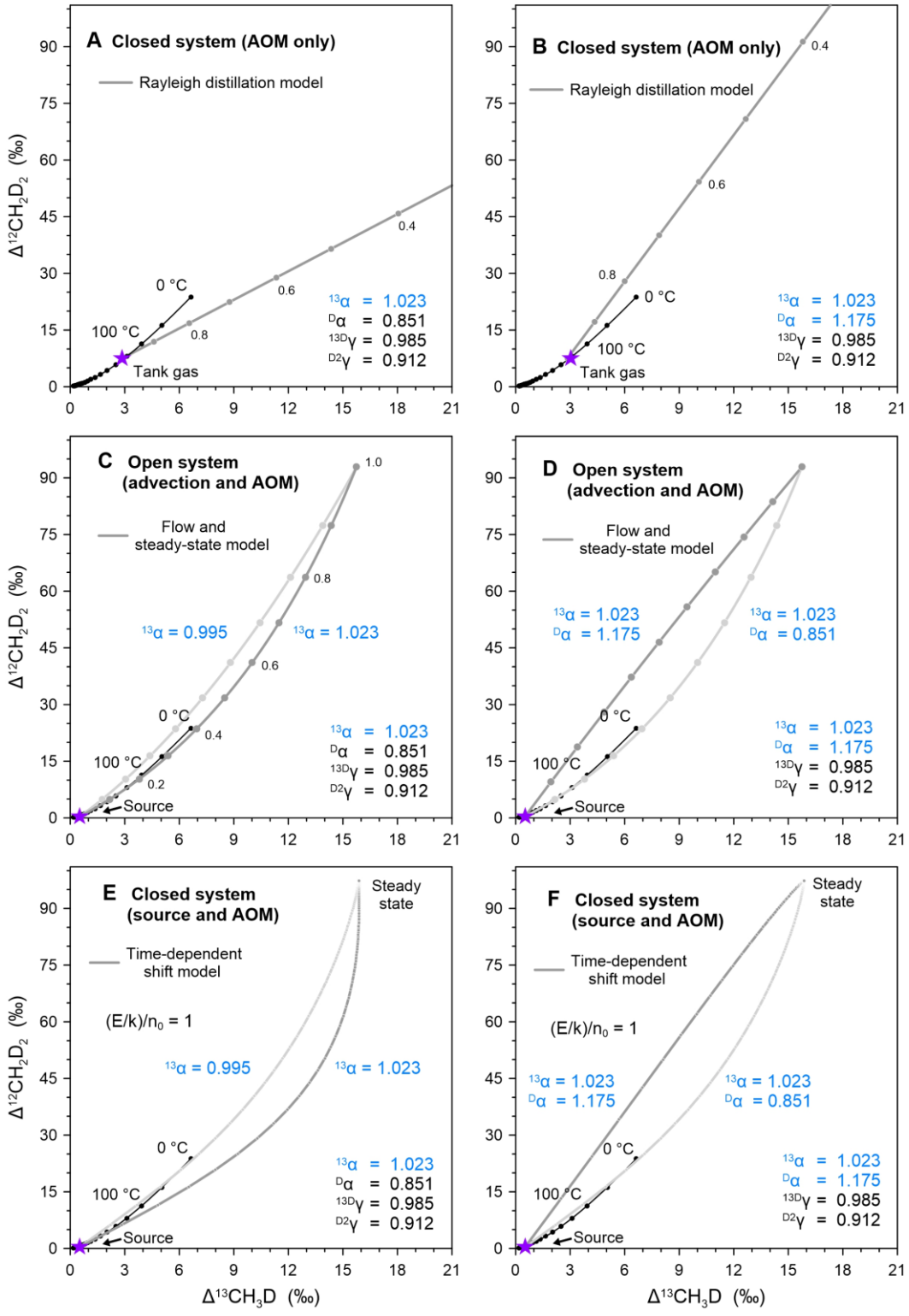

Fig. 2-S6 Sensitivity test of the Rayleigh fractionation model (A–B), open-system flow and steady-state model (C–D) and closed-system time-dependent shift model (E–F). Bulk isotope

fractionation factors in blue are changed from the original values shown in Fig. 6. The carbon isotope fractionation factor (1.023) is adopted from the low sulfate experiment of Wegener et al. (2021). A higher hydrogen isotope fractionation factor of 1.175 is used here as a maximum estimation. Lines and markers follow Fig. 6.

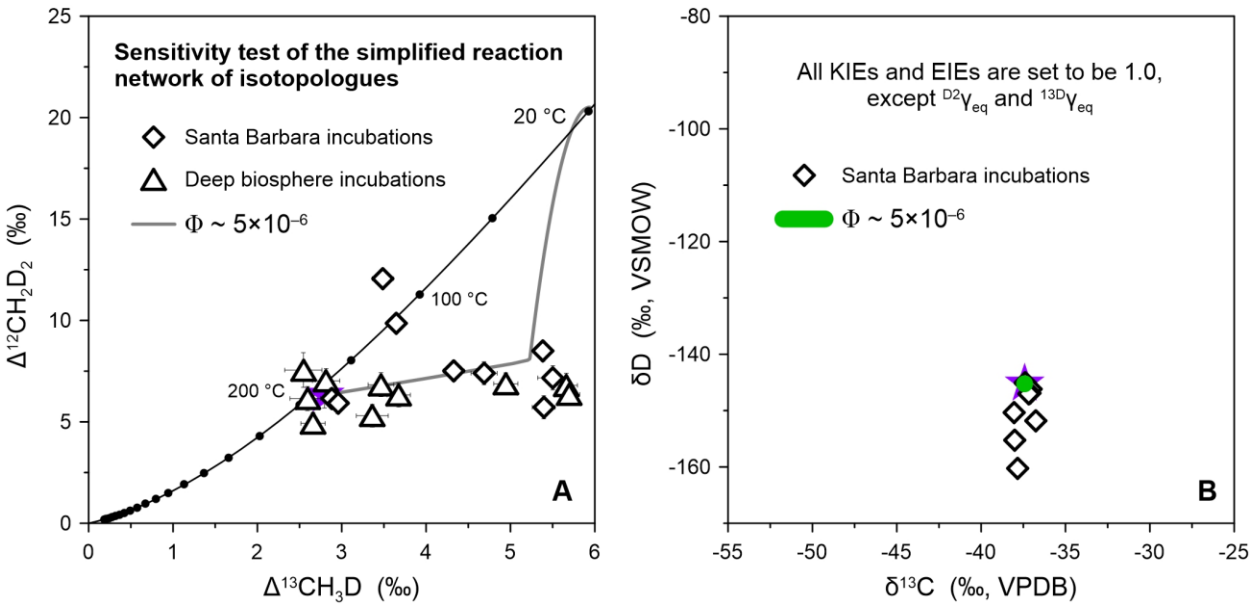

Fig. 2-S7 Sensitivity test of the general model for methane isotopologue fractionation due to AOM. Instead of using the fractionation factors in Table 2, all KIEs and EIEs are set to 1.0 with the exception of $^{D2}\gamma_{eq}$ and $^{13D}\gamma_{eq}$. Lines and markers follow Figs. 7 and 8.

SUPPLEMENTARY METHODS

$^{13}CH_4$ tracer microcosm experiment at high hydrostatic pressure – Nankai Trough

Microcosms were set up inside an anaerobic glove bag (Coy Laboratory Products, Grass Lake, MI USA) under a 5:95 H_2:N_2 atmosphere. Fresh aluminum foil was placed on the working surface of the glove bag and ethanol-sterilized nitrile gloves were worn over the glove bag's neoprene gloves to minimize potential contamination of low-biomass samples. The surface of each C0023A whole round core (WRC) was scraped using an ethanol-sterilized scalpel to remove sediment exposed to Kochi Core Center's anaerobic packaging. For each WCR, ~ 1 g (wet weight) of freshly exhumed interior sediment was transferred into high-pressure modified Hungate tubes (Fig. S2; Bowles et al., 2011) containing 5 mL anoxic sulfate-free artificial seawater medium at pH 8.0 (Widdel and Bak, 1992; Holler et al., 2011) and supplemented with 10 mM (final concentration) of one of the following electron acceptors: SO_4^{2-}, NO_2^-, NO_3^- , Mn^{4+} (in the form of MnO_2), or Fe^{3+} (in the form of Fe_2O_3•H_2O), in addition to a no-added oxidant control (i.e., "endogenous activity). Fe_2O_3•H_2O and MnO_2 were synthesized as previously described (Cornell and Schwertmann, 2003; Händel et al., 2013). The headspace of each microcosm was replaced with 2:98 $^{13}CH_4$:N_2 (100 kPa), prepared by mixing via gas-tight syringes (Trajan Scientific and Medical, Melbourne, Australia) in sealed Tedlar® bags (DuPont, Wilmington, DE USA). An autoclaved kill control was included as a reference for determining significant biological AOM. All treatments were assessed in biological triplicate.

Microcosms were inverted and placed inside stainless-steel hydrostatic vessels with a pin-retained piston closure pre-heated in gravity ovens to an approximate *in-situ* temperature of 40˚C (Fig. S2). Vessels were sealed and pressurized to 40 ± 0.5 MPa using a hydrostatic pump as previously described (Yayanos, 1995) and subsequently returned to gravity ovens for incubation.

Subsamples of the enrichments were collected at 0, 14, 60, 200, and 350 days to monitor CH_4 concentrations and the evolution of $\delta^{13}C_{DIC}$. Briefly, hydrostatic vessels were removed from ovens and depressurized for retrieval of Hungate tube microcosms. From each sample, a 500 µl aliquot of the slurry was anaerobically transferred using Ar-sparged syringes and needles into combusted borosilicate serum vials pre-treated with saturated $HgCl_2$ to kill any microbes contained in the sample (Sherwood Lollar et al., 1993a; Sherwood Lollar et al., 1993b). Vials were sealed under a 100% N_2 atmosphere with crimped 0.1 NaOH-treated butyl rubber stoppers (Bellco Glass, Inc., Vineland, NJ USA). Following sample transfer, serum vials were over-pressurized with N_2 gas to minimize the risk of mixing with atmospheric CO_2. To exsolve all DIC out of solution, vials were supplemented with 100 µL of 0.5 N H_3PO_4, and heated overnight in a water bath at 70˚C. CH_4 concentrations and $\delta^{13}C_{DIC}$ were analyzed from the headspace using a Picarro cavity ringdown spectrometer equipped with a G2101-I Isotopic CO_2 analyzer (Picarro, Inc., Sunnyvale, CA USA). Resulting isotopic values were calculated according to

$$\delta^{13}C_{DIC} = \left(\frac{\left(\frac{^{13}C_{DIC}}{^{12}C_{DIC}}\right)_{sample}}{\left(\frac{^{13}C_{DIC}}{^{12}C_{DIC}}\right)_{standard}} - 1 \right) \times 1000\ ‰ \quad \text{(S1)}$$

with respect to the [$^{13}C/^{12}C$] ratio of the Vienna Pee Dee Belemnite standard. AOM was determined to have a significant influence on $\delta^{13}C_{DIC}$ if its average $\delta^{13}C_{DIC} \pm$ standard deviation (SD) was greater than the average $\delta^{13}C_{DIC}$ + 3 × SD of the kill control ($\delta^{13}C_{DIC_{d.kill}}$) (Fig. S3).

DIC production rates (r_{DIC}) for each sample are shown in Figure S4 and were calculated according to

$$r_{DIC}\ \left(\text{pmol cm}^{-3}\text{day}^{-1}\right) = \frac{\left(\frac{\delta^{13}C_{DIC_d} - \delta^{13}C_{DIC_{d.kill}}}{\delta^{13}C_{^{13}CH_4} - \delta^{13}C_{DIC_{d.kill}}}\right) DIC_d \left(\frac{\rho_d}{g_d}\right)}{t} \quad \text{(S2)}$$

where DIC_d is the sum of $^{13}C_{DIC}$ and $^{12}C_{DIC}$ in pmol at depth d, ρ_d is the bulk density of the sediment at depth d in grams cm^{-3} (http://sio7.jamstec.go.jp/j-cores.data/370/C0023A/), and g_d is the grams of sediment incubated from depth d, and t is the number of days of incubation. Data were assumed to follow a normal distribution and r_{DIC} values were assigned z-scores according to

$$z = (r_{DIC\_sample} - \mu_{kill})/\sigma_{kill} \quad \text{(S3)}$$

from which P values were subsequently calculated using a 1-tailed test.

SUPPLEMENTARY REFERENCES

Bowles M. W., Samarkin V. A. and Joye S. B. (2011) Improved measurement of microbial activity in deep-sea sediments at in situ pressure and methane concentration. *Limnol. Oceanogr. Methods* **9**, 499–506.

Cornell R. M. and Schwertmann U. (2003) Introduction to the Iron Oxides. In *The Iron Oxides* Wiley. pp. 1–7.

Händel M., Rennert T. and Totsche K. U. (2013) A simple method to synthesize birnessite at ambient pressure and temperature. *Geoderma* **193**–**194**, 117–121.

Holler T., Widdel F., Knittel K., Amann R., Kellermann M. Y., Hinrichs K.-U., Teske A., Boetius A. and Wegener G. (2011) Thermophilic anaerobic oxidation of methane by marine microbial consortia. *ISME J.* **5**, 1946–1956.

Sherwood Lollar B., Frape S. K., Fritz P., Macko S. A., Welhan J. A., Blomqvist R. and Lahermo P. W. (1993a) Evidence for bacterially generated hydrocarbon gas in Canadian shield and fennoscandian shield rocks. *Geochim. Cosmochim. Acta* **57**, 5073–5085.

Sherwood Lollar B., Frape S. K., Weise S. M., Fritz P., Macko S. A. and Welhan J. A. (1993b) Abiogenic methanogenesis in crystalline rocks. *Geochim. Cosmochim. Acta* **57**, 5087–5097.

Wegener G., Gropp J., Taubner H., Halevy I. and Elvert M. (2021) Sulfate-dependent reversibility of intracellular reactions explains the opposing isotope effects in the anaerobic oxidation of methane. *Sci. Adv.* **7**, eabe4939.

Widdel F. and Bak F. (1992) *The Prokaryotes*. eds. A. Balows, H. G. Trüper, M. Dworkin, W. Harder, and K.-H. Schleifer, Springer New York, New York, NY.

Yayanos A. A. (1995) Microbiology to 10,500 Meters in the Deep Sea. *Annu. Rev. Microbiol.* **49**, 777–805.

Chapter 3

Clumped isotope evidence for microbial alteration of thermogenic methane in terrestrial mud volcanoes

Jiarui Liu[1*], Tina Treude[1,2], Orhan R. Abbasov[3], Elnur E. Baloglanov[3], Adil A. Aliyev[3], Carolynn M. Harris[4], William D. Leavitt[4,5], Edward D. Young[1]

[1]Department of Earth, Planetary and Space Sciences, University of California, Los Angeles, CA, USA

[2]Department of Atmospheric and Oceanic Sciences, University of California, Los Angeles, CA, USA

[3]Institute of Geology and Geophysics, Azerbaijan National Academy of Sciences, Baku, Azerbaijan

[4]Department of Earth Sciences, Dartmouth College, Hanover, NH, USA

[5]Department of Chemistry, Dartmouth College, Hanover, NH, USA

[*]E-mail: jiaruiliu@ucla.edu

ABSTRACT

Methane in oil reservoirs originates mostly from thermogenic sources, yet secondary microbial methane production from petroleum biodegradation is known to be pervasive. The conventional approach for identifying this secondary microbial methane commonly relies on geochemical characteristics of other gas molecules such as the carbon isotopic composition of carbon dioxide and propane. This information is sometimes obscured by isotopic variations in source material and may not be available in certain geological reservoirs. To better constrain the presence of secondary microbial methane, we studied the clumped isotopologue compositions of methane in terrestrial Azerbaijanian mud volcanoes, which support the occurrence of secondary microbial gas. Here, a deficit in $\Delta^{12}CH_2D_2$ of thermogenic methane occurs due to different δD of hydrogen sources that contribute to the formation of methane molecules (i.e., combinatorial effect). The $\Delta^{12}CH_2D_2$ is expected to move towards equilibrium as thermal maturity increases. More importantly, both $\Delta^{13}CH_3D$ and $\Delta^{12}CH_2D_2$ values of methane approach low-temperature thermodynamic equilibrium in most gases, suggesting that the original thermogenic methane has been altered by newly formed microbial methane in addition to isotope exchange among methane molecules catalyzed by the methyl-coenzyme M reductase enzyme. We conclude that methane clumped isotopes provide a unique proxy for identifying secondary microbial methane and understanding the exact evolution stages for natural gases.

INTRODUCTION

Methane is the simplest of all hydrocarbons and the main constituent of natural gas. Naturally occurring methane derives from three main sources: microbial, thermogenic, and abiotic. Microbial and thermogenic methane are formed by microbial degradation and thermocatalytic decomposition of organic matter, respectively (e.g., Reeburgh, 2007). Primary microbial gas forms from dispersed organic matter in relatively shallow sediments, whereas secondary microbial gas is produced from petroleum accumulations during biodegradation (e.g., Milkov, 2011). Abiotic methane is generated by magmatic and gas-water-rock reactions such as serpentinization and Sabatier reaction (e.g., Etiope and Sherwood Lollar, 2013).

The origins of methane are commonly inferred using diagrams plotting molecular ratios of alkanes against the bulk carbon and hydrogen isotopic composition of methane (Bernard et al., 1977; Whiticar, 1999). The fields indicating the methane sources in these empirical bivariate diagrams may overlap because bulk isotopic ratios reflect a combination of formation and alteration processes coupled with mixing and migration. For example, secondary microbial gas is commonly mixed with the original thermogenic gas in natural gas reservoirs, whereas their bulk isotopic compositions are almost indistinguishable (e.g., Milkov and Etiope, 2018). Given the complexity of bulk isotopic systematics of methane, an integrated geochemical–geological approach including geochemical characteristics of associated gas molecules, is commonly used to recognize the presence of secondary microbial gas (Milkov, 2011, and references therein).

During petroleum biodegradation, both short- and long-chain alkanes can be converted to methane. This methanogenic degradation can proceed either through syntrophic partnerships of hydrocarbon-degrading bacteria and methanogenic archaea (e.g., Zengler et al., 1999) or by alkylotrophic methanogenic archaea (Zhou et al., 2022). As biodegradation continues, the gas

becomes more methane dominated with high $C_1/(C_2+C_3)$ ratios, where C_1 is methane, C_2 is ethane, and C_3 is propane. In addition, as CO_2 derived from biodegraded petroleum is progressively converted into methane through the syntrophic pathway, the residual CO_2 becomes more enriched in ^{13}C, with $\delta^{13}C$ values commonly exceeding +2‰ and as high as +36‰ (Milkov and Etiope, 2018). This ^{13}C enrichment of CO_2 is considered to be one of the best geochemical indicators of secondary microbial gas (Etiope et al., 2009b; Milkov, 2011). As Etiope et al. (2009b) also pointed out, however, $\delta^{13}C_{CO2}$ variability can be more than 50‰ within the same seepage system, both in space and time, suggesting that the $\delta^{13}C$ of CO_2 may be affected by environmental conditions such as isotopic variations in source material and/or extent of CO_2 conversion to methane. Similarly, ^{13}C-enriched propane has been used as a tracer of anaerobic biodegradation, but propane concentrations are commonly below detection limits in many natural gas reservoirs (Etiope et al., 2009b; Milkov, 2011).

To better identify the presence of secondary microbial methane, we focus on the multiply substituted, a.k.a. "clumped," isotopologue compositions of methane. In general, isotope clumping, or isotopic bond ordering, traces the processes controlling the formation of the molecules independent of source material (Stolper et al., 2014; Wang et al., 2015; Young et al., 2017). The combination of two mass-18 methane isotopologues ($^{13}CH_3D$ and $^{12}CH_2D_2$) of thermogenic methane commonly records equilibrium at its formation temperature of ~100–250 °C (e.g., Stolper et al., 2014; Young et al., 2017; Xie et al., 2021). Microbially produced methane, on the other hand, shows disequilibrium signatures or approaches equilibrium at an ambient temperature of ~0–80 °C (e.g., Wang et al., 2015; Young et al., 2017; Taenzer et al., 2020). Therefore, we would expect distinct clumped isotope signatures of secondary microbial methane different from those of the original thermogenic gas (cf. Giunta et al., 2019; Thiagarajan et al., 2020; Jautzy et al., 2021;

Zhang et al., 2021; Lalk et al., 2022). To further our understanding of natural gas evolution, we analyzed the isotopologue ratios of methane from terrestrial mud volcanoes in Azerbaijan, where methanogenic biodegradation has been proposed based on simulated petroleum seepage experiments and the presence of ^{13}C-enriched CO_2 and propane (Etiope et al., 2009b; Mishra et al., 2017).

STUDY AREA AND METHODOLOGY

Mud volcanoes are constructional features from which sediments and fluids flow or erupt, acting as an important source of methane to the atmosphere and to the ocean (e.g., Etiope et al., 2004). The most active terrestrial area with the highest number of mud volcanoes is located in eastern Azerbaijan (Aliyev et al., 2015). We sampled gas and liquid mud separately from 13 mud volcanoes across different tectonic blocks in eastern Azerbaijan (Fig. 1; Figs. S1–S2 in the Supplemental Material). Their geochemical characteristics were analyzed using standard methods (see the Supplemental Material), including gas compositions, isotopologue ratios of methane, $\delta^{13}C$ of CO_2, and δD of water. The relative abundances of the two mass-18 isotopologues are presented in standard Δ notation (Fig. 2A), representing deviations from a stochastic standard in which distributions of isotopes across all isotopologues are effectively random (Young et al., 2017).

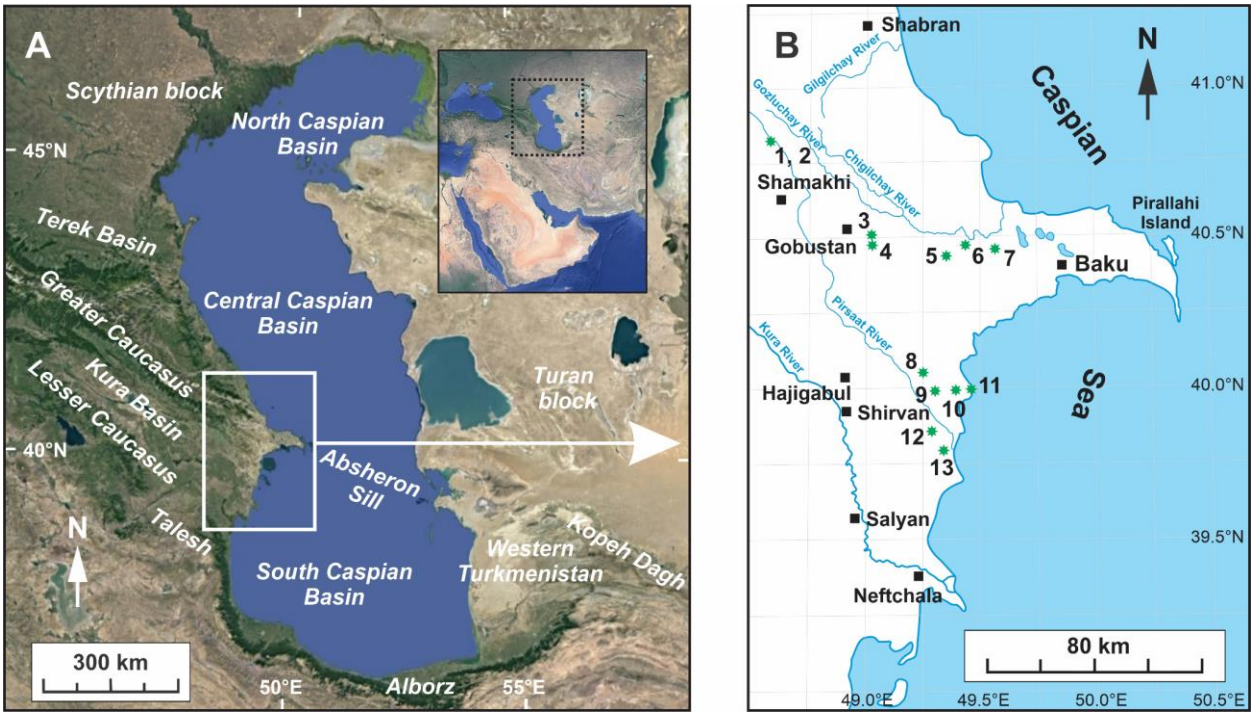

Fig. 3-1 Location map of sampled mud volcanoes. (A) Satellite maps of the Caspian Sea and surrounding geological features (Google Earth). Insert places the enlargement within the wider West and Central Asia. (B) Map of sampled mud volcanoes in eastern Azerbaijan (Aliyev et al., 2015). Green asterisks represent sampled mud volcanoes 1–13 as detailed in Table 1. White box in map A shows location of map B.

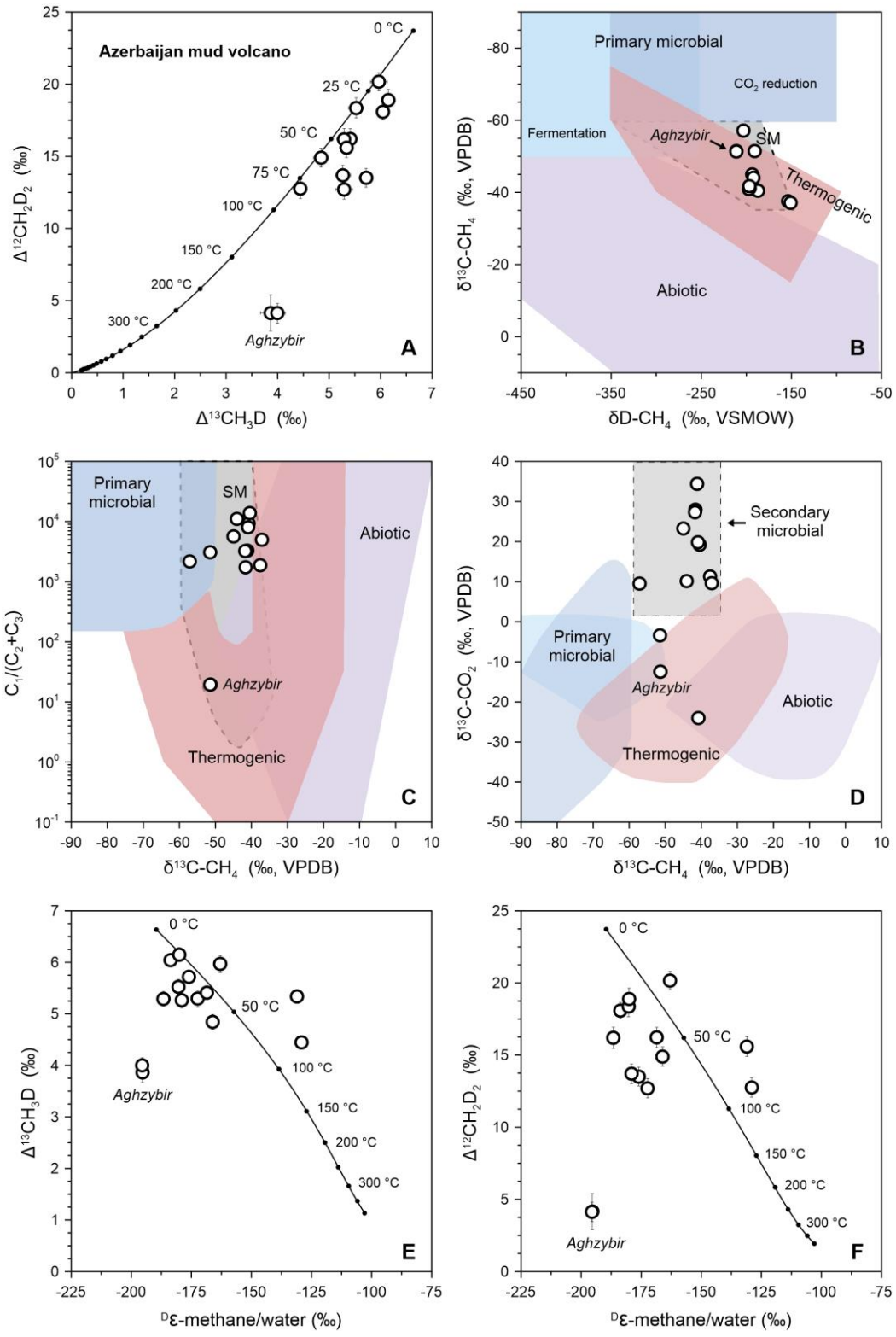

Fig. 3-2 Genetic diagrams of mud volcano gases from Azerbaijan. (A) Clumped isotope data of methane. Solid black line depicts theoretical thermodynamic equilibrium abundances of

methane isotopologues, along with corresponding temperatures. (B) Bulk isotope data of methane. (C) $\delta^{13}C_{CH4}$ versus $C_1/(C_2+C_3)$. (D) $\delta^{13}C_{CH4}$ versus $\delta^{13}C_{CO2}$. Genetic fields in panels B–D follow Bernard et al. (1977), Whiticar (1999), and Milkov and Etiope (2018). Secondary microbial (SM) field is shown in gray with dashed line. (E–F) $\Delta^{13}CH_3D$ and $\Delta^{12}CH_2D_2$ versus hydrogen isotope fractionation ($^{D}\varepsilon$) between methane and associated environmental water (cf. Wang et al., 2015). Solid black curve represents thermodynamic isotopic equilibrium, with the $\varepsilon_{methane/water}$ calibration given by Turner et al. (2022). Aghzybir mud volcano is the only one releasing typical thermogenic methane. Error bars are one standard error. VPDB—Vienna Peedee belemnite; VSMOW—Vienna standard mean ocean water.

CLUMPED ISOTOPE SIGNATURE OF THERMOGENIC METHANE FROM MUD VOLCANOES

Methane gas from mud volcanoes mostly originates from thermogenic sources in the deep subsurface (Etiope et al., 2009a). However, only one out of the 13 sampled mud volcanoes in the study area released typical thermogenic methane as inferred using diagrams shown in Figures 2B–D and S3. This thermogenic gas, sampled from the Aghzybir mud volcano (location 13 in Fig. 1), has a low $C_1/(C_2+C_3)$ ratio of 19 as a result of high abundances of ethane and propane, though its bulk $\delta^{13}C$ and δD are indistinguishable from those of the rest of the gases (Table 1). The clumped isotope composition of this methane sample exhibits a pronounced disequilibrium isotopologue signature with a low $\Delta^{12}CH_2D_2$ value (Fig. 2A). Recent studies demonstrate that $\Delta^{13}CH_3D$ values of thermogenic methane gases are consistent with thermodynamic equilibrium at their formation temperatures (Dong et al., 2021; Xie et al., 2021). The authors of these studies found that, however, a deficit in $\Delta^{12}CH_2D_2$ in thermogenic methane can occur due to significantly different δD of hydrogen sources that contribute to the formation of methane molecules (i.e., combinatorial effect). The departure from equilibrium is most pronounced at low thermal maturities, and the $\Delta^{12}CH_2D_2$ moves towards equilibrium as maturity increases (Xie et al., 2021). This deficit in $\Delta^{12}CH_2D_2$ is observed in the Aghzybir gas, while its $\Delta^{13}CH_3D$ value (3.9 ± 0.2‰) corresponds to an apparent formation temperature of 100 ± 8 °C. This temperature is lower than the peak thermogenic gas window (170–180 °C) but still within the nominal gas window (e.g., Stolper et al., 2014). In addition, the δD offset between methane and water is 192‰ in the Aghzybir mud volcano, significantly higher than the equilibrium prediction of 136 ± 2‰ at 100 ± 8 °C (Turner et al., 2022), which further confirms hydrogen isotope disequilibrium between methane and groundwater (Fig. 2E–F).

Table 3-1 Isotopic ratio, gas composition, and in situ temperature of liquid mud (T_{liquid}) of samples from Azerbaijan mud volcanoes.

Location	$\delta^{13}C_{CH4}$ (‰, VPDB)	δD_{CH4} (‰, VSMOW)	$\Delta^{13}CH_3D$ (‰)	$\Delta^{12}CH_2D_2$ (‰)	$C_1/(C_2+C_3)$	C_3 (ppm)	i-C_4 (ppm)	*n*-C_4 (ppm)	$\delta^{13}C_{CO2}$ (‰, VPDB)	δD_{H2O} (‰, VSMOW)	T_{liquid} (°C)
1. Demirchi (gray)	-37.1	-150.7	4.4	12.8	4948	5	35	0	9.6	-24.8	14
2. Demirchi (brown)	-37.5	-153.9	5.3	15.6	1874	18	33	0	11.3	-26.3	12
3. Kichik Mereze	-40.9	-197.2	6.1	18.9	8052	0	37	0	19.8	-21.0	23
4. Shikhzarli	-40.5	-186.8	5.4	16.2	13831	0	25	0	19.2	-22.0	25
5. Garyja	-41.8	-196.7	5.3	13.7	3219	14	38	4	27.3	-21.6	18
6. Pirekeshkul	-41.6	-197.0	5.3	16.2	1729	5	24	0	28.0	-12.7	21
7. Uchtepe	-41.1	-196.1	5.5	18.4	3302	0	34	0	34.4	-19.3	22
8. Solakhay	-57.1	-203.1	6.0	18.1	2176	41	46	0	9.6	-23.8	22
9. Ayrantoken	-45.0	-193.7	5.7	13.5	5683	7	38	0	23.3	-21.5	21
10. Dashgil	-40.8	-190.1	4.8	14.9	9279	5	18	0	-24.0	-28.8	22
11. Bahar	-44.0	-192.3	5.3	12.7	11043	0	5	0	10.2	-24.2	25
12. Khydyrly	-51.4	-190.8	6.0	20.2	3096	0	19	0	-3.4	-33.3	26
13. Aghzybir	-51.4	-211.3	4.0	4.1	19	14865	3240	3063	-12.5	-19.7	25
	-51.4	-211.2	3.9	4.1	19	14993	3271	3207			

Note: C_1—methane; C_2—ethane; C_3—propane; i-C_4—iso-butane; *n*-C_4—n-butane. Note that two mud volcanoes were sampled near Demirchi village, one with gray liquid mud, the other with brown liquid mud. Two subsamples from the Aghzybir mud volcano were measured for methane isotopologue ratio and alkane composition, as shown in the bottom two rows. VPDB—Vienna Peedee belemnite; VSMOW—Vienna standard mean ocean water.

MICROBIAL ALTERATION OF THERMOGENIC METHANE

Except for the Aghzybir mud volcano, all the remaining sampled mud volcanoes release methane-dominated gas with high $C_1/(C_2+C_3)$ ratios on the order of 10^3 to 10^4 (Fig. 2C). In particular, the propane (C_3) and *n*-butane (*n*-C_4) concentrations in these gases are near or below detection limits (7.9 ± 11.9 and 0.3 ± 1.2 ppm, respectively), whereas the average iso-butane (i-C_4) concentration is 29.3 ± 11.5 ppm (Table 1). These gas compositions are consistent with anaerobic degradation of propane and *n*-butane by microorganisms. Microbial ecosystems documented in marine hydrocarbon seeps can oxidize propane and *n*-butane simultaneously, but not iso-butane (e.g., Kniemeyer et al., 2007). Furthermore, most of these gases are associated with ^{13}C-enriched CO_2 (Fig. 2D), supporting the hypothesis of coupled hydrocarbon degradation and secondary methanogenesis (Etiope et al., 2009b). In addition to biodegradation, molecular fractionation during migration further leads to systematic loss of heavy hydrocarbons from reservoir to surface in mud volcanoes where gas migration is dominated by advection but not diffusion (Etiope et al., 2009a). Accordingly, isotope fractionation may occur during transportation but is generally not significant (Etiope et al., 2009a, b).

The $\Delta^{13}CH_3D$ and $\Delta^{12}CH_2D_2$ values of biodegraded gases range from 4.4 to 6.1‰ and from 12.7 to 20.2‰, respectively, corresponding to apparent temperatures of 13–75 °C and 21–83 °C, respectively (Fig. 2A). In plots of $\Delta^{13}CH_3D$ versus $\Delta^{12}CH_2D_2$, methane from four samples plot on the thermodynamic equilibrium curve, yielding equilibrium temperatures of ~20, 33, 59, and 79 °C. The lowest temperature of 20 °C inferred from the Khydyrly gas is consistent with the measured *in-situ* liquid temperature of 21 ± 4 °C at the surface (Table 1). The clumped isotopologue ratios, therefore, suggest that isotopic bond ordering in the original higher-temperature thermogenic methane has been modified by microbial activity at lower temperatures, resulting in methane

equilibrated at the low ambient temperatures. Therefore, methane seeping from these mud volcanoes is a mixture of thermogenic and its equivalent biodegraded methane, the latter being the result of low-temperature microbial methanogenesis. With burial, the evolution of isotopic bond ordering in thermogenic gas from low to high maturity occurs at temperatures >100 °C (e.g., 175 °C; Xie et al., 2021). Accordingly, we assume that the $\Delta^{12}CH_2D_2$ increases from negative values (e.g., −25‰ at early thermal maturity) to equilibrium values (e.g., +7‰) for the thermogenic end member. Subsequently, uplift and/or migration allow biodegradation to occur at lower temperatures. The microbial end-member corresponds to thermodynamic equilibrium at 12 °C, the lowest measured *in situ* liquid temperature (Table 1). Mixing between these end-members, therefore, encompasses all the mud volcano data (Fig. 3).

The isotopologue signature of microbial methane found here is different from that from laboratory culture studies and many terrestrial settings where significant clumped isotope disequilibrium is observed (Wang et al., 2015; Young et al., 2017). Recent studies demonstrate that the kinetic isotope effects and associated combinatorial effects are expressed when the reversibility of intracellular reactions is low (e.g., laboratory culture), leading to disequilibrium isotopologue signals (Cao et al., 2019; Young, 2019; Gropp et al., 2022; Ono et al., 2022). In energy-limited deep sedimentary environments with higher reaction reversibility (e.g., mud volcano), however, enzymatically mediated exchange of isotopes among methane molecules is evidently more pronounced, translating into near-equilibrium isotopologue signatures (Gropp et al., 2022; Ono et al., 2022). Thus, the observed isotopologue values (Fig. 2A) are consistent with these model predictions. Among all the intracellular pathways, the last step of microbial methanogenesis catalyzed by the methyl-coenzyme M reductase (Mcr) enzyme is evidently central to the mechanism for isotopologue equilibration. Recent experiments demonstrated that the headspace

methane approaches isotopologue equilibration during isotope exchange solely with the Mcr enzyme (Liu et al., 2023). Accordingly, in addition to the generation of newly formed secondary microbial methane, this Mcr-catalyzed isotope exchange promotes isotopic bond reordering within the original thermogenic methane, both contributing to the observed low-temperature thermodynamic equilibrium (Fig. 2A). Indeed, the microbially altered methane appears to approach hydrogen isotope equilibrium with associated waters at or near the temperatures indicated by the $\Delta^{13}CH_3D$ and $\Delta^{12}CH_2D_2$ data (Figs. 2E–2F), suggesting the occurrence of both intra- and inter-species isotope equilibrium.

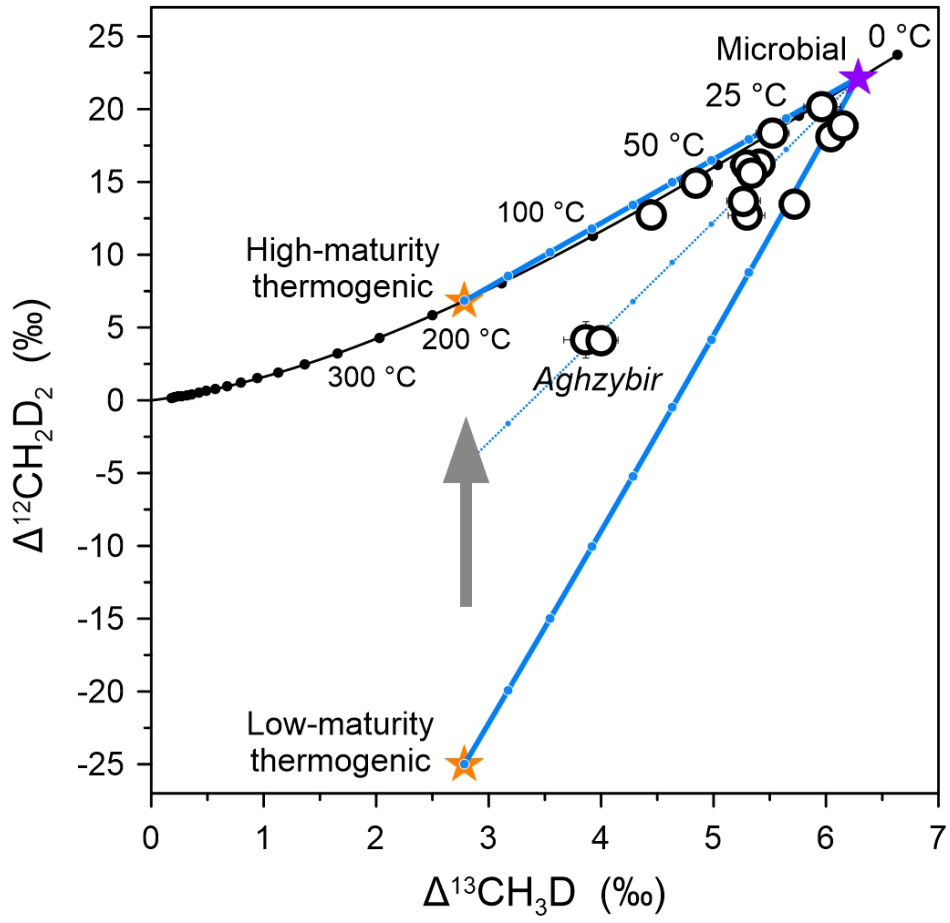

Fig. 3-3 Schematic illustration of clumped isotope evolution of methane in natural gas reservoirs. Two orange stars and gray arrow depict evolution of thermogenic methane from low

to high maturity with formation temperature of 175 °C (Dong et al., 2021; Xie et al., 2021). Purple star represents a microbial end member at 12 °C (Table 1). Blue lines demonstrate three scenarios of mixing between thermogenic and low-temperature microbial end members with blue points marking 10% intervals of mixing. Measured bulk isotopic data are used for the calculation. In principle, mixing is nonlinear for multiply substituted isotopologues, whereas the mixing lines here are quasi-linear because the bulk isotopic compositions of the two end members are similar (Young et al., 2017). The solid black line depicts theoretical thermodynamic equilibrium abundances of methane isotopologues along with corresponding temperatures.

Once formed, methane could be oxidized by anaerobic methanotrophic (ANME) archaea in the subsurface. Indeed, ANME archaea have been reported in terrestrial mud volcanoes and nearby sediment across the globe, including the ones studied here (Alain et al., 2006; Stagars et al., 2017; Lin et al., 2018). Because anaerobic oxidation of methane (AOM) is the enzymatic reversal of major methanogenic pathways, the principle of the clumped isotopologue effect during AOM is broadly similar to that of methanogenesis, meaning isotopologue equilibration under energy-limited conditions (Young et al., 2017; Ash et al., 2019; Ono et al., 2022; Liu et al., 2023). Given the potential occurrence of simultaneous methane production and consumption, we generalized the near-equilibrium methane isotopologue signatures as a result of the Mcr-catalyzed intracellular isotope exchange operating under near-threshold free-energy conditions in the deep biosphere.

CONCLUSIONS

Using terrestrial Azerbaijanian mud volcanoes as an example, we demonstrate that the original thermogenic methane gas is augmented by methane formed during methanogenic hydrocarbon biodegradation. The clumped isotopic ratios of this secondary microbial methane ultimately approach low-temperature thermodynamic equilibrium, whereas primary microbial methane emissions exhibit notable clumped isotope disequilibrium (e.g., Young, 2019). Given that secondary methanogenesis significantly increases methane emissions into the atmosphere (Milkov, 2011), it is crucial to consider the role of secondary microbial methane in biological contributions to global isotopologue budgets. Overall, this independent approach offers a unique perspective for identifying secondary microbial gas and tracking the fate of methane in oil and gas reservoirs.

ACKNOWLEDGMENTS

The research was funded by the NASA FINESST Fellowship 80NSSC21K1529 and the Alfred P. Sloan Foundation under the auspices of the Deep Carbon Observatory. We acknowledge Xiahong Feng for access to water H-isotope analysis and Jiawen Li for discussion. We thank Hao Xie and two anonymous reviewers for their helpful and constructive reviews of this paper.

References

Alain, K., Holler, T., Musat, F., Elvert, M., Treude, T., and Krüger, M., 2006, Microbiological investigation of methane- and hydrocarbon-discharging mud volcanoes in the Carpathian Mountains, Romania: Environmental Microbiology, v. 8, p. 574-590, https://doi.org/10.1111/j.1462-2920.2005.00922.x.

Aliyev, A. A., Guliyev, I. S., Dadashev, F. G., and Rahmanov, R. R., 2015, Atlas of the world mud volcanoes: Baku, Nafta-Press Publishing House, Sandro Teti Editore, 361 p.

Ash, J. L., Egger, M., Treude, T., Kohl, I., Cragg, B., Parkes, R. J., Slomp, C. P., Sherwood Lollar, B., and Young, E. D., 2019, Exchange catalysis during anaerobic methanotrophy revealed by $^{12}CH_2D_2$ and $^{13}CH_3D$ in methane: Geochemical Perspectives Letters, v. 10, p. 26-30, https://doi.org/10.7185/geochemlet.1910.

Bernard, B., Brooks, J. M., and Sackett, W. M., 1977, A Geochemical Model For Characterization Of Hydrocarbon Gas Sources In Marine Sediments: Paper OTC 2934, presented at 9th Annual Offshore Technology Conference, Houston, Texas, 2–5 May, p. 435-438, https://doi.org/10.4043/2934-MS.

Cao, X., Bao, H., and Peng, Y., 2019, A kinetic model for isotopologue signatures of methane generated by biotic and abiotic CO_2 methanation: Geochimica et Cosmochimica Acta, v. 249, p. 59-75, https://doi.org/10.1016/j.gca.2019.01.021.

Dong, G., Xie, H., Formolo, M., Lawson, M., Sessions, A., and Eiler, J., 2021, Clumped isotope effects of thermogenic methane formation: Insights from pyrolysis of hydrocarbons: Geochimica et Cosmochimica Acta, v. 303, p. 159-183, https://doi.org/10.1016/j.gca.2021.03.009.

Etiope, G., Feyzullayev, A., and Baciu, C. L., 2009a, Terrestrial methane seeps and mud volcanoes: A global perspective of gas origin: Marine and Petroleum Geology, v. 26, p. 333-344, https://doi.org/10.1016/j.marpetgeo.2008.03.001.

Etiope, G., Feyzullayev, A., Baciu, C. L., and Milkov, A. V., 2004, Methane emission from mud volcanoes in eastern Azerbaijan: Geology, v. 32, p. 465-468, https://doi.org/10.1130/g20320.1.

Etiope, G., Feyzullayev, A., Milkov, A. V., Waseda, A., Mizobe, K., and Sun, C. H., 2009b, Evidence of subsurface anaerobic biodegradation of hydrocarbons and potential secondary methanogenesis in terrestrial mud volcanoes: Marine and Petroleum Geology, v. 26, p. 1692-1703, https://doi.org/10.1016/j.marpetgeo.2008.12.002.

Etiope, G., and Sherwood Lollar, B., 2013, ABIOTIC METHANE ON EARTH: Reviews of Geophysics, v. 51, p. 276-299, https://doi.org/10.1002/rog.20011.

Giunta, T., Young, E. D., Warr, O., Kohl, I., Ash, J. L., Martini, A., Mundle, S. O. C., Rumble, D., Pérez-Rodríguez, I., Wasley, M., LaRowe, D. E., Gilbert, A., and Sherwood Lollar, B., 2019, Methane sources and sinks in continental sedimentary systems: New insights from paired clumped isotopologues $^{13}CH_3D$ and $^{12}CH_2D_2$: Geochimica et Cosmochimica Acta, v. 245, p. 327-351, https://doi.org/10.1016/j.gca.2018.10.030.

Gropp, J., Jin, Q., and Halevy, I., 2022, Controls on the isotopic composition of microbial methane: Science Advances, v. 8, p. eabm5713, https://doi.org/10.1126/sciadv.abm5713.

Jautzy, J. J., Douglas, P. M. J., Xie, H., Eiler, J. M., and Clark, I. D., 2021, CH_4 isotopic ordering records ultra-slow hydrocarbon biodegradation in the deep subsurface: Earth and Planetary Science Letters, v. 562, p. 116841, https://doi.org/10.1016/j.epsl.2021.116841.

Kniemeyer, O., Musat, F., Sievert, S. M., Knittel, K., Wilkes, H., Blumenberg, M., Michaelis, W., Classen, A., Bolm, C., Joye, S. B., and Widdel, F., 2007, Anaerobic oxidation of short-chain hydrocarbons by marine sulphate-reducing bacteria: Nature, v. 449, p. 898-901, https://doi.org/10.1038/nature06200.

Lalk, E., Pape, T., Gruen, D. S., Kaul, N., Karolewski, J. S., Bohrmann, G., and Ono, S., 2022, Clumped methane isotopologue-based temperature estimates for sources of methane in marine gas hydrates and associated vent gases: Geochimica et Cosmochimica Acta, v. 327, p. 276-297, https://doi.org/10.1016/j.gca.2022.04.013.

Lin, Y.-T., Tu, T.-H., Wei, C.-L., Rumble, D., Lin, L.-H., and Wang, P.-L., 2018, Steep redox gradient and biogeochemical cycling driven by deeply sourced fluids and gases in a terrestrial mud volcano: FEMS Microbiology Ecology, v. 94, p. fiy171, https://doi.org/10.1093/femsec/fiy171.

Liu, J., Harris, R. L., Ash, J. L., Ferry, J. G., Krause, S. J. E., Labidi, J., Prakash, D., Sherwood Lollar, B., Treude, T., Warr, O., and Young, E. D., 2023, Reversibility controls on extreme methane clumped isotope signatures from anaerobic oxidation of methane: Geochimica et Cosmochimica Acta, v. 348, p. 165-186, https://doi.org/10.1016/j.gca.2023.02.022.

Milkov, A. V., 2011, Worldwide distribution and significance of secondary microbial methane formed during petroleum biodegradation in conventional reservoirs: Organic Geochemistry, v. 42, p. 184-207, https://doi.org/10.1016/j.orggeochem.2010.12.003.

Milkov, A. V., and Etiope, G., 2018, Revised genetic diagrams for natural gases based on a global dataset of >20,000 samples: Organic Geochemistry, v. 125, p. 109-120, https://doi.org/10.1016/j.orggeochem.2018.09.002.

Mishra, S., Wefers, P., Schmidt, M., Knittel, K., Krüger, M., Stagars, M. H., and Treude, T., 2017, Hydrocarbon Degradation in Caspian Sea Sediment Cores Subjected to Simulated Petroleum Seepage in a Newly Designed Sediment-Oil-Flow-Through System: Frontiers in Microbiology, v. 8, https://doi.org/10.3389/fmicb.2017.00763.

Ono, S., Rhim, J. H., and Ryberg, E. C., 2022, Rate limits and isotopologue fractionations for microbial methanogenesis examined with combined pathway protein cost and isotopologue flow network models: Geochimica et Cosmochimica Acta, v. 325, p. 296-315, https://doi.org/10.1016/j.gca.2022.03.017.

Reeburgh, W. S., 2007, Global Methane Biogeochemistry, *in* Keeling, R.F., ed., Treatise on Geochemistry, Volume 4: The Atmosphere: Oxford, Pergamon, 32 p., https://doi.org/10.1016/B0-08-043751-6/04036-6.

Stagars, M. H., Mishra, S., Treude, T., Amann, R., and Knittel, K., 2017, Microbial Community Response to Simulated Petroleum Seepage in Caspian Sea Sediments: Frontiers in Microbiology, v. 8, https://doi.org/10.3389/fmicb.2017.00764.

Stolper, D. A., Lawson, M., Davis, C. L., Ferreira, A. A., Neto, E. V. S., Ellis, G. S., Lewan, M. D., Martini, A. M., Tang, Y., Schoell, M., Sessions, A. L., and Eiler, J. M., 2014, Formation temperatures of thermogenic and biogenic methane: Science, v. 344, p. 1500-1503, https://doi.org/10.1126/science.1254509.

Taenzer, L., Labidi, J., Masterson, A. L., Feng, X., Rumble, D., Young, E. D., and Leavitt, W. D., 2020, Low $\Delta^{12}CH_2D_2$ values in microbialgenic methane result from combinatorial isotope effects: Geochimica et Cosmochimica Acta, v. 285, p. 225-236, https://doi.org/10.1016/j.gca.2020.06.026.

Thiagarajan, N., Kitchen, N., Xie, H., Ponton, C., Lawson, M., Formolo, M., and Eiler, J., 2020, Identifying thermogenic and microbial methane in deep water Gulf of Mexico Reservoirs: Geochimica et Cosmochimica Acta, v. 275, p. 188-208, https://doi.org/10.1016/j.gca.2020.02.016.

Turner, A. C., Pester, N. J., Bill, M., Conrad, M. E., Knauss, K. G., and Stolper, D. A., 2022, Experimental determination of hydrogen isotope exchange rates between methane and water under hydrothermal conditions: Geochimica et Cosmochimica Acta, v. 329, p. 231-255, https://doi.org/10.1016/j.gca.2022.04.029.

Wang, D. T., Gruen, D. S., Lollar, B. S., Hinrichs, K.-U., Stewart, L. C., Holden, J. F., Hristov, A. N., Pohlman, J. W., Morrill, P. L., Könneke, M., Delwiche, K. B., Reeves, E. P., Sutcliffe, C. N., Ritter, D. J., Seewald, J. S., McIntosh, J. C., Hemond, H. F., Kubo, M. D., Cardace, D., Hoehler, T. M., and Ono, S., 2015, Nonequilibrium clumped isotope signals in microbial methane: Science, v. 348, p. 428-431, https://doi.org/10.1126/science.aaa4326.

Whiticar, M. J., 1999, Carbon and hydrogen isotope systematics of bacterial formation and oxidation of methane: Chemical Geology, v. 161, p. 291-314, https://doi.org/10.1016/S0009-2541(99)00092-3.

Xie, H., Dong, G., Formolo, M., Lawson, M., Liu, J., Cong, F., Mangenot, X., Shuai, Y., Ponton, C., and Eiler, J., 2021, The evolution of intra- and inter-molecular isotope equilibria in natural gases with thermal maturation: Geochimica et Cosmochimica Acta, v. 307, p. 22-41, https://doi.org/10.1016/j.gca.2021.05.012.

Young, E. D., 2019, A Two-Dimensional Perspective on CH_4 Isotope Clumping: Distinguishing Process from Source, *in* Orcutt, B. N., Daniel, I., and Dasgupta, R., eds., Deep Carbon:

Past to Present: Cambridge, Cambridge University Press, p. 388-414, https://doi.org/10.1016/j.gca.2016.12.041.

Young, E. D., Kohl, I. E., Lollar, B. S., Etiope, G., Rumble, D., Li, S., Haghnegahdar, M. A., Schauble, E. A., McCain, K. A., Foustoukos, D. I., Sutclife, C., Warr, O., Ballentine, C. J., Onstott, T. C., Hosgormez, H., Neubeck, A., Marques, J. M., Pérez-Rodríguez, I., Rowe, A. R., LaRowe, D. E., Magnabosco, C., Yeung, L. Y., Ash, J. L., and Bryndzia, L. T., 2017, The relative abundances of resolved $^{12}CH_2D_2$ and $^{13}CH_3D$ and mechanisms controlling isotopic bond ordering in abiotic and biotic methane gases: Geochimica et Cosmochimica Acta, v. 203, p. 235-264, https://doi.org/10.1016/j.gca.2016.12.041.

Zengler, K., Richnow, H. H., Rosselló-Mora, R., Michaelis, W., and Widdel, F., 1999, Methane formation from long-chain alkanes by anaerobic microorganisms: Nature, v. 401, p. 266-269, https://doi.org/10.1038/45777.

Zhang, N., Snyder, G. T., Lin, M., Nakagawa, M., Gilbert, A., Yoshida, N., Matsumoto, R., and Sekine, Y., 2021, Doubly substituted isotopologues of methane hydrate ($^{13}CH_3D$ and $^{12}CH_2D_2$): Implications for methane clumped isotope effects, source apportionments and global hydrate reservoirs: Geochimica et Cosmochimica Acta, v. 315, p. 127-151, https://doi.org/10.1016/j.gca.2021.08.027.

Zhou, Z., Zhang, C.-j., Liu, P.-f., Fu, L., Laso-Pérez, R., Yang, L., Bai, L.-p., Li, J., Yang, M., Lin, J.-z., Wang, W.-d., Wegener, G., Li, M., and Cheng, L., 2022, Non-syntrophic methanogenic hydrocarbon degradation by an archaeal species: Nature, v. 601, p. 257-262, https://doi.org/10.1038/s41586-021-04235-2.

SUPPLEMENTAL MATERIAL: Liu et al. Clumped isotope evidence for microbial alteration of thermogenic methane in terrestrial mud volcanoes.

GEOLOGICAL BACKGROUND

General features of the formation of mud volcanoes in Azerbaijan

On a global scale, mud volcanoes usually occur in groups over large areas. One of the reasons for this arrangement is the provision of geological and chemical factors that create the necessary conditions for the formation and accumulation of hydrocarbon gases in the geological sections of those areas that mainly consist of Cenozoic deposits. Another reason is the presence of plastic clays and tectonic disturbances in geological sections.

Many mud volcanoes around the world arose in the eastern part of the Caucasian segment of the Mediterranean (Alpine-Himalayan) belt, and in the western parts of the South Caspian Megabasin (both together are called East Azerbaijan) (Baloglanov et al., 2018). Here, mud volcanoes are located to the east of the West Caspian deep fault, cutting through the entire sedimentary stratum. From a structural point of view, most of the volcanoes are located in the periclinal parts of the folds, sometimes in their highest parts (especially in cryptodiapirs) or on the limbs of the folds subject to tectonic disturbances (Aliyev and Rahmanov, 2018).

East Azerbaijan, located in the collision zone of the African-Arabian plate, was characterized by rapid and large-scale sediment accumulation, regional compression with anomalous high pressure, and rich oil and gas formation processes (Guliyev and Feizullayev, 1997; Aliyev and Abbasov, 2019; Odonne et al., 2020). In this regard, the formation of mud volcanoes in the region is promoted by a series of factors, including the accumulation of thick Cenozoic sediments rich in clay minerals in the tectonically descending areas, the formation of anomalous

high pressures, the intensive accumulation of hydrocarbon gases in sandy reservoirs, as well as the development of fractures in geological sections (Planke et al., 2003; Aliyev et al., 2015).

Basins/Megabasin associated with mud volcanoes and their geological and geotectonic characteristics

The zones where mud volcanoes are recorded in the territory of Azerbaijan are related to local basins such as Gusar-Devechi, Shahdagh-Khyzy, Vendam-Gobustan, Absheron, Lower Kura and South Caspian, which cover the northern, eastern, and southern areas of the south-eastern plunge of the Great Caucasus (Babayev et al., 2015). The depth of the consolidated surface of such basins affects the number of mud volcanoes, their morphological (conical and flat-topped) characteristics and their sizes. In the Lower Kura-Gobustan-Absheron regional subsidence area, the consolidated surface of the earth's crust lies at a depth of about 12 km. However, in the southeast, that surface descends to about 20 km. In connection with this, the maximum number of mud volcanoes is found in the South Caspian Basin, which is located at the southeast tip of the Greater Caucasus (Aliyev and Rahmanov, 2018).

The Gusar-Devechi Basin is the southeastern extension of the Terek-Caspian Foothill Depression. Due to frequent stratigraphic breaks in the Cenozoic section (continental origin) of the basin located on the north-eastern slopes of the Azerbaijani part of the Greater Caucasus Folded Structure (Fig. S1), mud volcanoes are weakly developed here (eruptions are not typical). As for the Shahdag-Khizi Basin, which is also located in the northern part of Eastern Azerbaijan and where few mud volcanoes are weakly developed, it is the most lowered zone between the uplift in the southeastern extension of the Great Caucasus (Lateral Ridge Megazone) and the Tangi-

Beshbarmag Uplift. The eastern border of that zone continues to the coast of the Caspian Sea. Here it is buried under modern molasses sediments (Aliyev et al., 2005).

The Jeyrankechmez-South Caspian Megabasin, which connects local basins such as Vandam-Gobustan, Absheron, Lower Kura and South Caspian, differs in comparison with local depressions located in the north (Gusar-Devechi and Shahdagh-Khyzy). Thus, the mud volcanoes recorded in the megabasin have a denser location, more intense activity, and larger sizes. The Shamakhy-Gobustan oil and gas region is located in the north-west, the Absheron oil and gas region in the north and the Lower Kura oil and gas region in the west of the megabasin (Aliyev et al., 2015).

The southeastern part of the Vandam-Gobustan Basin, which is a part of the Jeyrankechmez-South Caspian Megabasin including the South Gobustan zone (Toraghay microblock; Figs. 1, S2), has undergone the most subsidence (the top of the Upper Cretaceous has decreased to a depth of 8–11.5 km). Here, stratigraphic breaks in the thicker section of the Cenozoic are rare. The listed factors have led to mud volcanoes being more densely distributed and having higher hypsometric dimensions (up to 400 m) (Aliyev and Abbasov, 2019). Compared to flat-topped mud volcanoes, cone-shaped mud volcanoes are thought to have deeper underlying mud chambers. Industrially important hydrocarbon deposits have also been discovered in the Toraghay microblock. In South Gobustan, the thickness of Pliocene sediments, which have more favorable conditions for the accumulation of hydrocarbons in Azerbaijan, reaches 5 km in some areas (Aliyev and Rahmanov, 2018).

The thickness of Eocene-Miocene sediments, which play a crucial role in the formation of Azerbaijani mud volcanoes, does not exceed 4.5 km in the Bayanata microblock, located north of the Gujur-Gyzyldash Thrust (Figs. 1, S2). In general, the distribution of Paleogene-Miocene

sediments is characteristic for the surface geological structure of Central Gobustan, which covers the Bayanata microblock. In some areas, the top of the Upper Cretaceous lies at a lower depth (2.5 km). Although no significant reserves of hydrocarbons were found here at the Paleogene-Miocene intersection, the presence of oil shales rich in organic matter (3–42%) is noteworthy (Baldermann et al., 2020). Compared to South Gobustan, the presence of Eocene and Maykop sediments in shallower intervals, which are in contact with the roots of Azerbaijani mud volcanoes, can be explained as the reason for the absence of cone-shaped high volcanoes in the Bayanata microblock. The flat-topped mud volcanoes found in central Gobustan are smaller in size (Aliyev et al., 2015).

In the northern and northwestern parts of the Shamakhy region, the Paleogene-Miocene sediments are buried under the Basgal cover, which is composed of carbonate rocks belonging to the Upper Cretaceous. In this allochthonous zone of North Gobustan, which is separated from the Bayanta microblock by the Goredil-Masazyr Convergence Zone (Figs. 1, S2), the smaller mud volcano manifestations (Bizlan, Sarsura, Demirchi, etc.) are recorded. There is also information about the Paleogene and Miocene sediments covering the Pliocene sediments in the south of the Shamakhy region. The faults and mud volcanoes (Charhan, Malikchobanly) appear in the crests of the folds. Most of the mud volcanoes found in the North Gobustan allochthon are characterized by gryphon-salsa activity. The dimensions of such flat-topped mud volcanoes are also smaller (Aliyev and Rahmanov, 2018).

The Lower-Kura Basin is the lowest tectonic block recorded in the dry parts of the Jeyrankechmez-South Caspian Megabasin. Here, the thickness of sedimentary rocks reaches 16–20 km, and more than half of them belong to Pliocene-Quaternary sediments. The largest mud volcanoes (conical) are located in the southeast of the depression. The western border of the basin is separated from the Transcaucasian Island Arc System, which is mainly composed of Mesozoic

volcanic rocks, but without any signs of mud volcanism, by means of the Shamakhy-Neftchala right-lateral strike-slip fault (Figs. 1, S2). Mud volcanoes are spread along the fault zone. Unlike the Absheron Peninsula and partially Gobustan volcanoes, the mud volcanoes of the Lower Kura oil-gas region are localized not in the axis of the anticlines, but in the flanks (especially in the west).

The Absheron Basin corresponds to the seaward continuation of the southeastern dip of the Great Caucasus, including the Mesozoic fold (Aliyev et al., 2005). In the southern part of the Absheron peninsula, the top of the Upper Cretaceous descends sharply, and the structure of the uplifts is dominated by almost continuously deposited thick Cenozoic sediments (10–20 km and more). As mentioned above, the largest (conical) and strongly erupting mud volcanoes in Eastern Azerbaijan are found in such modern depressions, where the molasse sedimentary complex (of the Pliocene-Quaternary period) is involved.

Collectively, the geochemical characteristics of mud volcanoes presented in the main text seem to not have an obvious relationship with the geological zonation discussed above. On the other hand, the geochemical feature of the Aghzybir gas was very different from the gases of neighboring mud volcanoes (Figs. 1, S2), whereas they are located within the same geological province. We do notice that the liquid in the Aghzybir mud volcano seems to have more oil-like substances (Fig. S4), consistent with its low degree of petroleum biodegradation. In addition, sulfate concentrations at the Aghzybir mud volcano, without evidence of biodegradation, are below the detection limit of 30 μM (see supplemental research data). At the other studied mud volcanoes, sulfate concentrations range between 0.1 and 31.5 mM. Sulfate-reducing bacteria may directly oxidize short-chain hydrocarbons anaerobically or act as syntrophic partners to receive reducing equivalents from archaea (Kniemeyer et al., 2007; Laso-Pérez et al., 2016). Therefore, we

hypothesize that the availability of sulfate may limit the occurrence of biodegradation, implying that the role of other electron acceptors is minor.

SUPPLEMENTAL MATERIALS AND METHODS

Sampling and geochemical analyses

One mud volcano was sampled for both gas and liquid at each location as the color of the liquid mud was identical among individual mud volcanoes, whereas two mud volcanoes were sampled near Demirchi village, one with grey liquid mud, the other with brown liquid mud. Gas samples were collected in 50 ml glass vials by liquid mud displacement method in summer 2019. The vials were dipped into the liquid mud pool and filled. The vials were then held upside down and free gas bubbles were funneled into the vials that were filled with liquid mud. Once most of the liquid mud was displaced by gas, the vials were sealed with rubber septa within the liquid mud pool. Immediately after the fieldwork, NaOH solution was injected into glass vials for methane analysis with a final concentration of 2.5%, to inhibit microbial activity. A few drops of liquid were withdrawn by syringes from the glass vials and pH strips were used to check and ensure that the pH was higher than 13. At each mud volcano where gas samples were sampled, liquid mud was also collected into 500 ml sterile plastic bottles without headspace. The *in-situ* temperature of liquid mud was measured by submerging a mercury thermometer into the liquid mud pool. Both gas and liquid samples were then shipped to home laboratory and stored at 4 °C until analysis.

Alkane concentrations (C1–C4) in gas samples were determined using a Shimadzu gas chromatograph (GC-2014) with a packed HayeSep-D column and a flame ionization detector. Helium was used as the carrier gas at a flow rate of 35 ml/min. The column temperature was set at 120 °C and held for 6 min, then increased up to 160 °C at 20°C/min and held for 4 min. C1–C4

alkane concentrations were calibrated against calibration standards (GASCO Precision Calibration Gas). The relative standard deviation (RSD) was better than 5% and the detection limit was about 1 ppm. For isotopologue analysis, gas was sampled from glass vials using a gas-tight syringe and injected on a vacuum line for purification (see section below).

Liquid mud samples were centrifuged at 4300g for 20 min and the supernatant was collected. Sulfate and chloride concentrations were analyzed by ion chromatography (Metrohm 761). Alkalinity was determined by acid titration with a Metrohm 876 Dosimat Plus (Dale et al., 2015). The concentrations were calibrated against the IAPSO standard seawater with RSD of sulfate and alkalinity analyses better than 2%. The detection limit for sulfate was about 30 μM with dilution. Note that the liquid samples were preserved at 4 °C for two years before analysis. Minor alteration may occur for alkalinity and sulfate concentration during storage.

Analysis of hydrogen isotopic composition of water in liquid mud samples was conducted at the Stable Isotope Laboratory at Dartmouth College (Kopec et al., 2019; Taenzer et al., 2020). Water hydrogen isotopic ratios (δD) were measured using an H-Device, in which water was reduced by hot chromium (850 °C), and the resulting hydrogen gas was measured by a Thermo Delta Plus XL isotope-ratio mass spectrometer (IRMS). Isotopic ratios (D/H) are reported in δ-notation relative to the Standard Mean Ocean Water (VSMOW) standard. Analytical precision for δD is <0.5‰ (1σ) based on replicate analyses of laboratory standards.

Analysis of carbon isotopic composition of CO_2 gas was performed in 12 ml Labco Exetainer vials on a Thermo Scientific GasBench II coupled to a Thermo Finnigan Delta Plus XL IRMS at the UC Davis Stable Isotope Facility. An autosampler with a 2-hole sampling needle used a helium carrier stream (2.0 mL/min) to push CO_2 out of the vial and into a 100 μL sample loop. Once the loop was adequately flushed, pulses of sample gas were injected into the IRMS for

isotopic measurement. Isotopic values are reported in δ-notation relative to the Vienna Pee Dee Belemnite (VPDB) standard. Analytical precision for $\delta^{13}C$ is <0.1‰ (1σ) based on replicate analyses of laboratory standards.

Doubly substituted isotopologue measurements and isotope notation

Methane isotopologue abundances of methane gas samples were measured using the Panorama (Nu Instruments) high-mass-resolution gas-source IRMS housed at UCLA. Details surrounding the purification and measurement of methane gas were previously published (Young et al., 2016; Young et al., 2017) and are briefly summarized here. Methane sample gases were purified on a vacuum line interfaced with a gas chromatograph (GC). Three to four ml of gas were delivered to the vacuum line through a septum by a gas-tight syringe and trapped on silica gel at liquid nitrogen temperature. The helium carrier gas was then used to flush the sample to the GC. Separation was accomplished with a 3-meter 1/8-inch OD stainless steel column packed with 5 Å molecular sieve, followed in series by a 2-meter 1/8-inch OD stainless steel column packed with HayeSep D porous polymer. Peaks were identified using an in-line, passive thermal conductivity detector (TCD). Once methane collection was complete, the sample was transferred to an evacuated sample tube filled with silica gel at liquid nitrogen temperature. Methane in this tube was introduced to the inlet of the mass spectrometer where it was warmed to 40 °C and expanded into the bellow of the instrument.

The Panorama mass spectrometer was set to a mass resolving power of ~40,000 or greater, allowing the measurement of ion currents for resolved $^{12}CH_4^+$, $^{13}CH_4^+$, $^{12}CH_3D^+$, $^{13}CH_3D^+$, and $^{12}CH_2D_2^+$. Isotopologues of masses 16 and 17 were measured using Faraday collectors with amplifier resistors of 10^{11} Ω. Both doubly substituted mass-18 isotopologues, $^{13}CH_3D^+$ and

$^{12}CH_2D_2^+$, were measured with an electron multiplier as the axial collector. The measured ratios of these ion currents yield values for bulk $^{13}C/^{12}C$ and D/H as well as for both $\Delta^{13}CH_3D$ and $\Delta^{12}CH_2D_2$. The isotopic compositions of carbon and hydrogen are reported as deviations from the carbon and hydrogen reference materials VPDB and VSMOW. Standard delta notation is used to express the fractional differences in per mil units:

$$\delta^{13}C = [(^{13}C/^{12}C)_{sample}/(^{13}C/^{12}C)_{VPDB} - 1] \times 1000 \quad (1)$$

$$\delta D = [(D/H)_{sample}/(D/H)_{VSMOW} - 1] \times 1000 \quad (2)$$

The relative abundances of the two mass-18 isotopologues of methane are reported relative to the stochastic reference frame expressed in per mil using the capital delta notation:

$$\Delta^{13}CH_3D = [(^{13}CH_3D\ /^{12}CH_4)_{sample}/(^{13}CH_3D\ /^{12}CH_4)_{stochastic} - 1] \times 1000 \quad (3)$$

$$\Delta^{12}CH_2D_2 = [(^{12}CH_2D_2/^{12}CH_4)_{sample}/(^{12}CH_2D_2/^{12}CH_4)_{stochastic} - 1] \times 1000 \quad (4)$$

External precision for $\delta^{13}C$, δD, $\Delta^{13}CH_3D$, and $\Delta^{12}CH_2D_2$ is approximately 0.1‰, 0.3‰, 0.3‰ and 0.7‰, respectively (1σ), based on replicate samples. The relationship between temperature and both $\Delta^{13}CH_3D$ and $\Delta^{12}CH_2D_2$ has been predicted through *ab initio* calculations and can be expressed by the following equations (Young et al., 2017):

$$\Delta^{13}CH_3D\ (T) \approx 1000\ \ln(1 + 0.0355502/T - 433.038/T^2 + 1270210.0/T^3 - 5.94804 \times 10^8/T^4 + 1.196630 \times 10^{11}/T^5 - 9.07230 \times 10^{12}/T^6) \quad (5)$$

$$\Delta^{12}CH_2D_2\ (T) \approx 1000\ \ln(1 + 0.183798/T - 785.483/T^2 + 1056280.0/T^3 + 9.37307 \times 10^7/T^4 - 8.919480 \times 10^{10}/T^5 + 9.901730 \times 10^{12}/T^6) \quad (6)$$

where T is in Kelvin. Eqs. (5) and (6) show that $\Delta^{13}CH_3D$ and $\Delta^{12}CH_2D_2$ values are both positive when methane is formed at thermodynamic equilibrium, and approach 0‰ at high temperatures (>1000 K).

SUPPLEMENTAL FIGURES

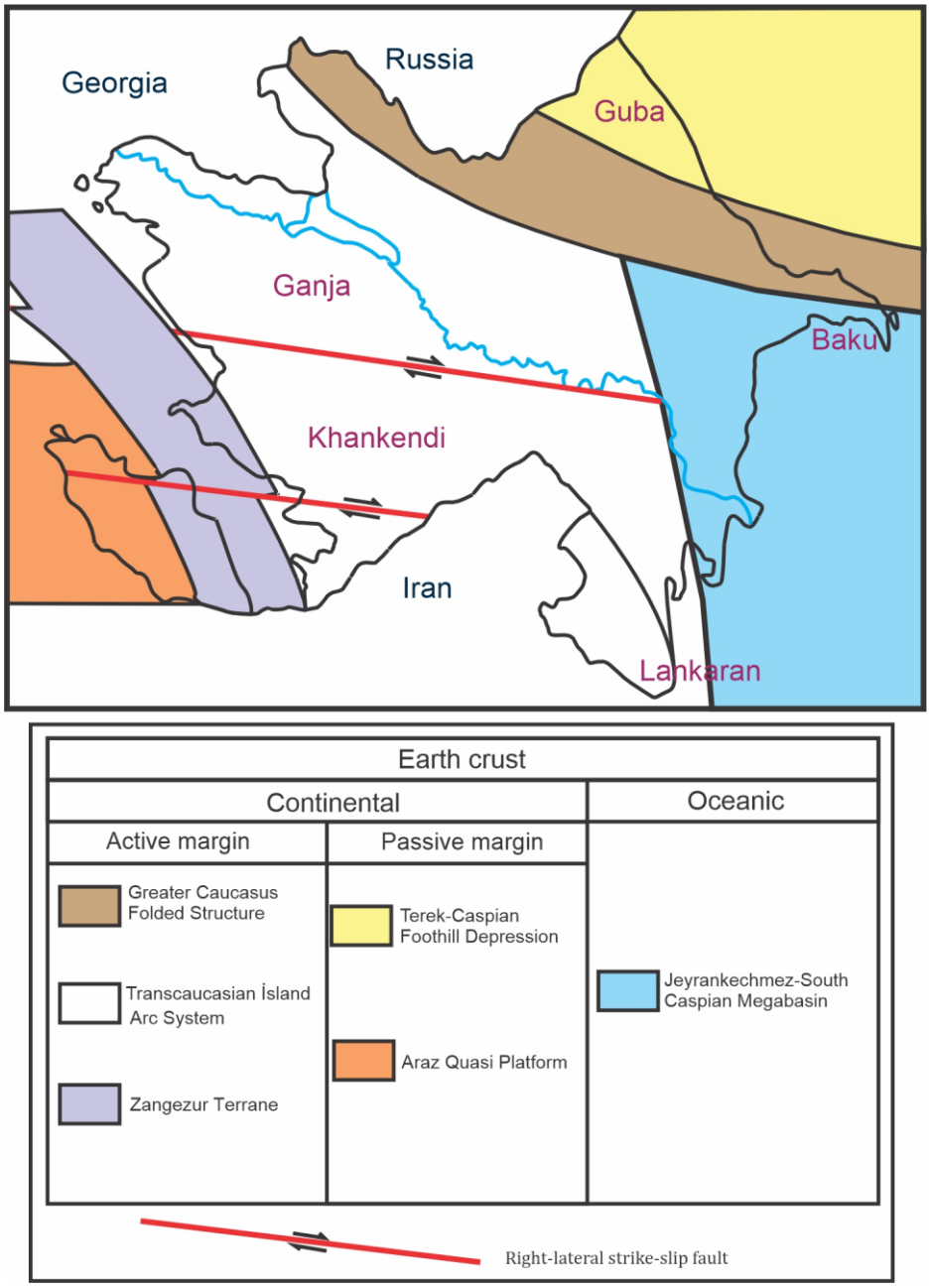

Figure 3-S1. Geodynamic zones in Azerbaijan (Aliyev and Rahmanov, 2018).

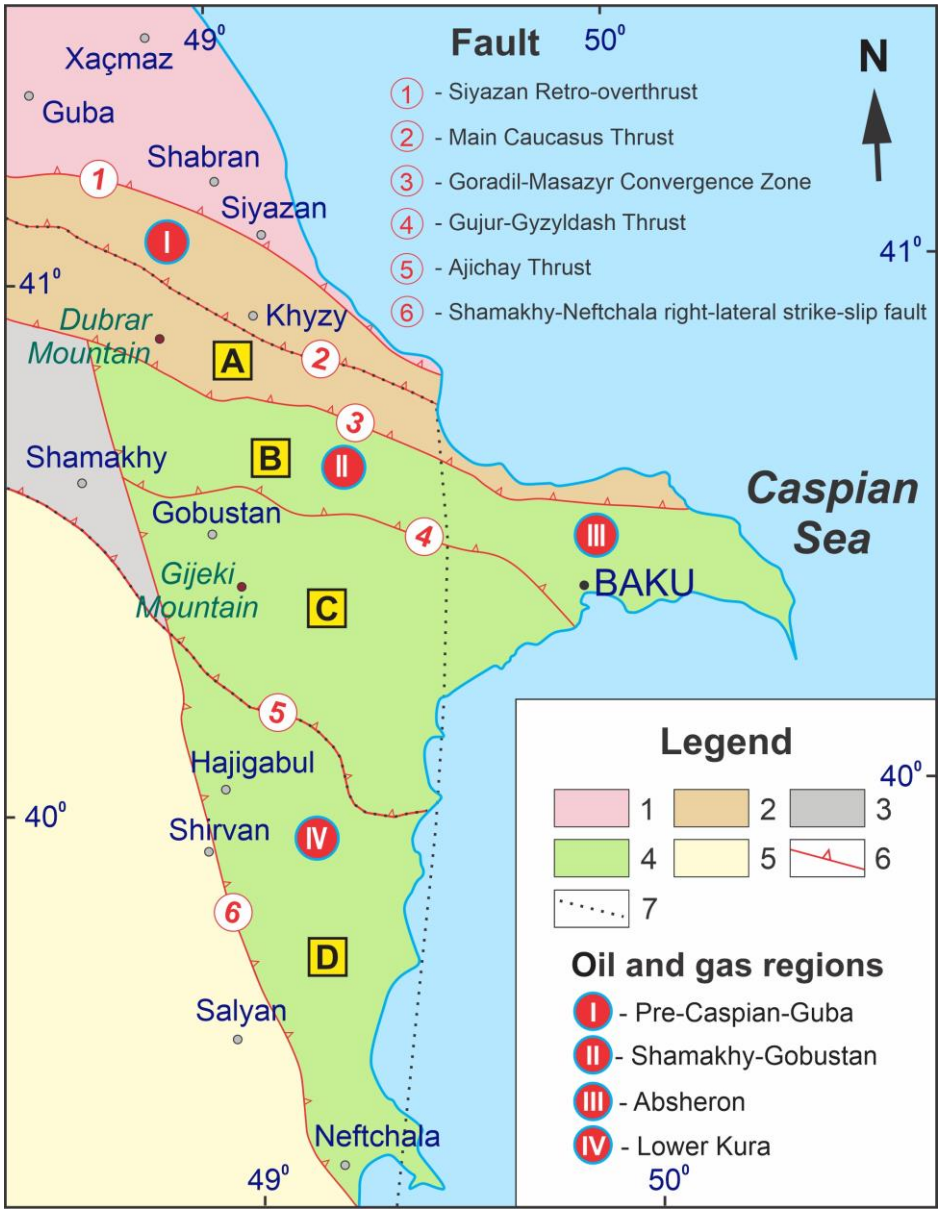

Figure 3-S2. Geological map of eastern Azerbaijan (Aliyev et al., 2015). Map legends 1–7 are shown in the bottom right and their explanation is as follows: (1) Gusar-Devechi Basin; (2) Greater Caucasus Folded Structure; (3) Shamakhy Region; (4) Jeirankechmez-South Caspian Megabasin; (5) Transcaucasian Island Arc System; (6) fault; (7) boundary of oil and gas regions. Boxed A–D represents (A) North Gobustan (allochthonous), (B) Bayanata Microblock (parautochtonous), (C) Toragay Microblock (autochtonous) and (D) South-Eastern Shirvan. The names of faults 1–6 and oil and gas regions I–IV are shown on the map.

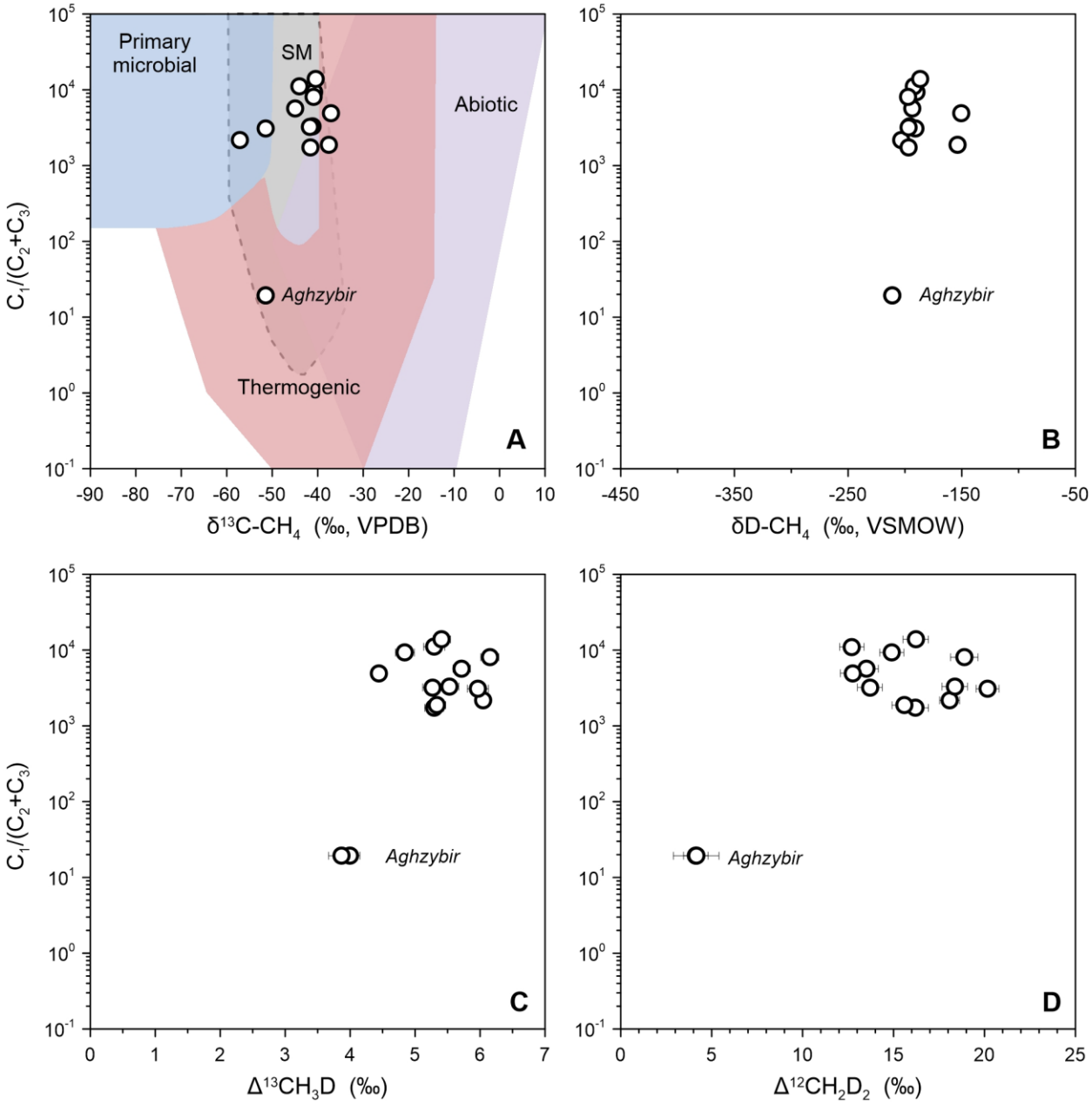

Figure 3-S3. Isotope data versus $C_1/(C_2+C_3)$ of mud volcano gases from Azerbaijan. Panel A is also plotted in Figure 2C. Error bars are one standard error.

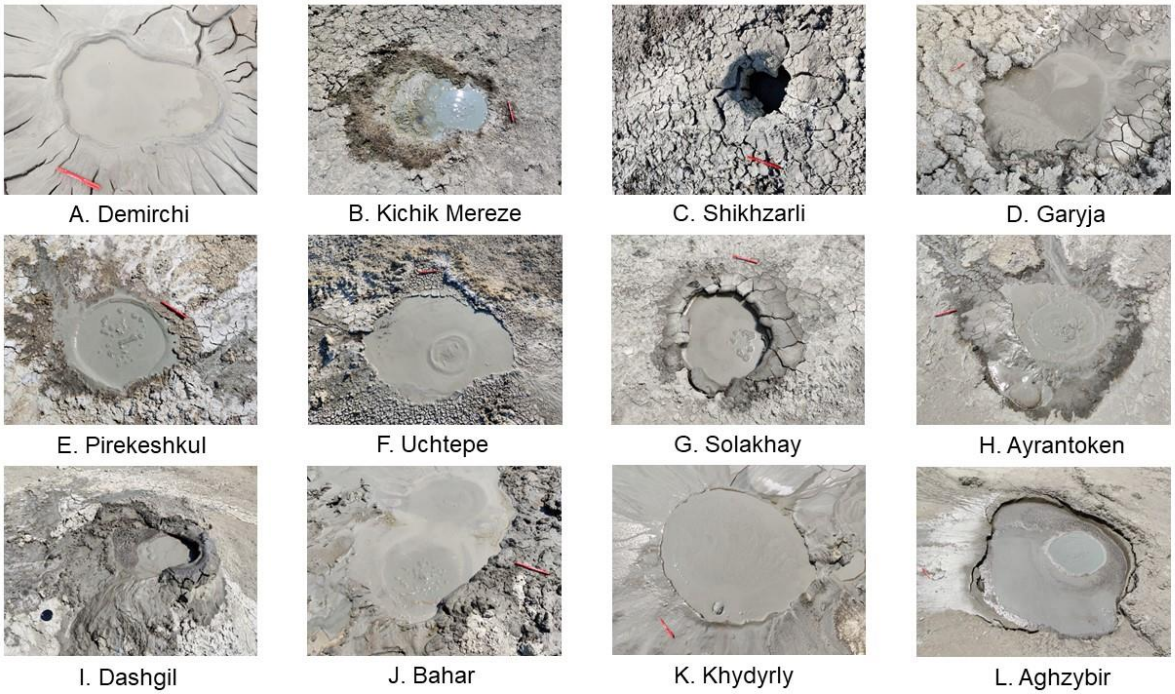

Figure 3-S4. Images of the sampled mud volcanoes in eastern Azerbaijan. The red marker pen is 14 cm in scale.

REFERENCES CITED

Aliyev, A. A., and Abbasov, O., 2019, Nature of the provenance and tectonic setting of oil shale (Middle Eocene) in the Greater Caucasus southeastern plunge: Journal of Geodynamics, v. 2019, p. 43-59, https://doi.org/10.23939/jgd2019.01.043.

Aliyev, A. A., Guliyev, I. S., Dadashev, F. G., and Rahmanov, R. R., 2015, Atlas of the world mud volcanoes: Baku, Nafta-Press Publishing House, Sandro Teti Editore.

Aliyev, A. A., and Rahmanov, R. R., 2018, Mud volcanism: Baku, Nafta-Press Publishing House.

Aliyev, A. H., Ahmedbeyli, F. S., Ismailzade, A. J., Kengerli, T. N., and Rustamov, M. I., 2005, Geology of Azerbaijan, Vol. IV: Tectonics: Baku, Nafta-Press Publishing House.

Babayev, S. E., Baghmanov, M. A., Aliyeva, E. H.-M., Alizadeh, K. A., Kengerli, T. N., Letifova, Y. N., and Zohrabova, V. R., 2015, Geology of Azerbaijan, Vol. I: Baku, Nafta-Press Publishing House.

Baldermann, A., Abbasov, O. R., Bayramova, A., Abdullayev, E., and Dietzel, M., 2020, New insights into fluid-rock interaction mechanisms at mud volcanoes: Implications for fluid origin and mud provenance at Bahar and Zenbil (Azerbaijan): Chemical Geology, v. 537, p. 119479, https://doi.org/10.1016/j.chemgeo.2020.119479.

Baloglanov, E., Abbasov, O., and Akhundov, R., 2018, Mud volcanoes of the world: Classifications, activities and environmental hazard (informational-analytical review): European Journal of Natural History, v. 5, p. 12-26.

Dale, A. W., Sommer, S., Lomnitz, U., Montes, I., Treude, T., Liebetrau, V., Gier, J., Hensen, C., Dengler, M., Stolpovsky, K., Bryant, L. D., and Wallmann, K., 2015, Organic carbon production, mineralisation and preservation on the Peruvian margin: Biogeosciences, v. 12, p. 1537-1559, https://doi.org/10.5194/bg-12-1537-2015.

Guliyev, I. S., and Feizullayev, A. A., 1997, All about mud volcanoes: Baku, Nafta-Press Publishing House, 120 p.

Kniemeyer, O., Musat, F., Sievert, S. M., Knittel, K., Wilkes, H., Blumenberg, M., Michaelis, W., Classen, A., Bolm, C., Joye, S. B., and Widdel, F., 2007, Anaerobic oxidation of short-chain hydrocarbons by marine sulphate-reducing bacteria: Nature, v. 449, p. 898-901, https://doi.org/10.1038/nature06200.

Kopec, B. G., Feng, X., Posmentier, E. S., and Sonder, L. J., 2019, Seasonal Deuterium Excess Variations of Precipitation at Summit, Greenland, and their Climatological Significance: Journal of Geophysical Research: Atmospheres, v. 124, p. 72-91, https://doi.org/10.1029/2018JD028750.

Laso-Pérez, R., Wegener, G., Knittel, K., Widdel, F., Harding, K. J., Krukenberg, V., Meier, D. V., Richter, M., Tegetmeyer, H. E., Riedel, D., Richnow, H.-H., Adrian, L., Reemtsma, T., Lechtenfeld, O. J., and Musat, F., 2016, Thermophilic archaea activate butane via alkyl-coenzyme M formation: Nature, v. 539, p. 396-401, https://doi.org/10.1038/nature20152.

Odonne, F., Imbert, P., Dupuis, M., Aliyev, A. A., Abbasov, O. R., Baloglanov, E. E., Vendeville, B. C., Gabalda, G., Remy, D., Bichaud, V., Juste, R., Pain, M., Blouin, A., Dofal, A., and Gertauda, M., 2020, Mud volcano growth by radial expansion: Examples from onshore Azerbaijan: Marine and Petroleum Geology, v. 112, p. 104051, https://doi.org/10.1016/j.marpetgeo.2019.104051.

Planke, S., Svensen, H., Hovland, M., Banks, D. A., and Jamtveit, B., 2003, Mud and fluid migration in active mud volcanoes in Azerbaijan: Geo-Marine Letters, v. 23, p. 258-268, https://doi.org/10.1007/s00367-003-0152-z.

Taenzer, L., Labidi, J., Masterson, A. L., Feng, X., Rumble, D., Young, E. D., and Leavitt, W. D., 2020, Low $\Delta^{12}CH_2D_2$ values in microbialgenic methane result from combinatorial isotope effects: Geochimica et Cosmochimica Acta, v. 285, p. 225-236, https://doi.org/10.1016/j.gca.2020.06.026.

Young, E. D., Kohl, I. E., Lollar, B. S., Etiope, G., Rumble, D., Li, S., Haghnegahdar, M. A., Schauble, E. A., McCain, K. A., Foustoukos, D. I., Sutclife, C., Warr, O., Ballentine, C. J., Onstott, T. C., Hosgormez, H., Neubeck, A., Marques, J. M., Pérez-Rodríguez, I., Rowe, A. R., LaRowe, D. E., Magnabosco, C., Yeung, L. Y., Ash, J. L., and Bryndzia, L. T., 2017, The relative abundances of resolved $^{12}CH_2D_2$ and $^{13}CH_3D$ and mechanisms controlling isotopic bond ordering in abiotic and biotic methane gases: Geochimica et Cosmochimica Acta, v. 203, p. 235-264, https://doi.org/10.1016/j.gca.2016.12.041.

Young, E. D., Rumble, D., Freedman, P., and Mills, M., 2016, A large-radius high-mass-resolution multiple-collector isotope ratio mass spectrometer for analysis of rare isotopologues of O_2, N_2, CH_4 and other gases: International Journal of Mass Spectrometry, v. 401, p. 1-10, https://doi.org/10.1016/j.ijms.2016.01.006.

Chapter 4

Clumped isotopes of methane trace bioenergetics in the environment

Jiarui Liu[1]*, Edward D. Young[1]*, André Pellerin[2], Jeanine L. Ash[3], Gerard T. Barrett[4], Xiahong Feng[5], Peter R. Girguis[6], Sebastian J.E. Krause[7], William D. Leavitt[5, 8], Kyla Murphy[9], Qianhui Qin[10], Andreas Teske[12], David L. Valentine[9, 13], Katey Walter Anthony[14], Tina Treude[1]*

[1]Department of Earth, Planetary and Space Sciences, University of California, Los Angeles, CA 90095, USA.

[2]Institut des sciences de la mer, Université du Québec à Rimouski, Rimouski, Québec G5L 3A1, Canada.

[3]Department of Earth, Environmental and Planetary Sciences, Rice University, Houston, TX 77005, USA.

[4]CHRONO Centre for Climate, the Environment and Chronology, School of Natural and Built Environment, Queen's University Belfast, Belfast BT9 6AX, UK.

[5]Department of Earth Sciences, Dartmouth College, Hanover, NH 03755, USA.

[6]Department of Organismic and Evolutionary Biology, Harvard University, Cambridge, MA 02138, USA.

[7]Earth Research Institute, University of California, Santa Barbara, CA 93106, USA.

[8]Department of Chemistry, Dartmouth College, Hanover, NH 03755, USA.

[9]Department of Earth Science, University of California, Santa Barbara, CA 93106, USA.

[10]Interdepartmental Graduate Program in Marine Science, University of California, Santa Barbara, CA 93106, USA.

[11]Department of Earth, Marine, and Environmental Sciences, University of North Carolina, Chapel Hill, NC 27599, USA.

[12]Marine Science Institute, University of California, Santa Barbara, CA 93106, USA.

[13]Water and Environmental Research Center, University of Alaska Fairbanks, Fairbanks, AK 99775, USA.

*Corresponding author. Email: jiaruiliu@ucla.edu, eyoung@epss.ucla.edu, ttreude@g.ucla.edu

Abstract:

Methane is a major greenhouse gas and a key component of global biogeochemical cycles. Microbial methane often deviates from isotope and isotopologue equilibrium in shallow terrestrial environments but approaches equilibrium in deep marine sediments. The origin of this near-equilibrium methane, whether directly produced by methanogens or achieved through anaerobic oxidation of methane (AOM), remains uncertain. Here, we show that, in the absence of AOM, microbial methane produced from deep-sea sediments exhibits isotopologue compositions approaching thermodynamic equilibrium due to energy limitation. In contrast, microbial methane from salt marsh and thermokarst lakes exhibits significant hydrogen and clumped isotope disequilibrium due to high free-energy availability. We propose that clumped isotopes of methane provide a proxy for characterizing the bioenergetics of environments for methane production, where substrate concentrations are not readily available to calculate the Gibbs free energy. Furthermore, we suggest that the near-equilibrium methane isotopologue signatures result from intracellular isotope exchange operating under conditions of near-threshold free-energy. When the thermodynamic driving force is elevated, methanogenesis and AOM can generate more negative and positive isotopologue signatures, respectively. Together these observations demonstrate clumped isotopes of methane as a powerful tool to better understand the relation between methane metabolisms and the energy landscape in natural environments.

Introduction

Methane is a potent greenhouse gas emitted from both anthropogenic and natural sources (Dlugokencky et al., 2011; Saunois et al., 2020). Microbial methanogenesis contributes more than half of annual emissions to the atmosphere (Conrad, 2009; Schwietzke et al., 2016). The strong isotopic discrimination imparted by methanogenesis has driven the widespread application of conventional stable carbon ($^{13}C/^{12}C$) and hydrogen (D/H) isotope ratios for distinguishing the origins of methane (Whiticar, 1999). Conventional stable isotope measurements of methane have become a cornerstone of global methane budgets and the assessment of its climatic impacts (Nisbet et al., 2016; Schwietzke et al., 2016). Yet, a significant limitation of this conventional isotope approach is the overlapping isotope signals from distinct sources of methane (Milkov and Etiope, 2018). The recent development and application of doubly substituted "clumped" isotopologues (i.e., $^{13}CH_3D$ and $^{12}CH_2D_2$) has emerged as a powerful tool for characterizing sources and sinks of methane (Stolper et al., 2014; Wang et al., 2015; Young et al., 2017; Haghnegahdar et al., 2023; Sivan et al., 2024). When the distribution of carbon and hydrogen isotopes among methane molecules is consistent with thermodynamic equilibrium, clumped isotopologues record the formation temperatures of thermogenic methane in natural gas reservoirs (Stolper et al., 2014; Young et al., 2017; Xie et al., 2021). In microbial ecosystems, methane clumped isotopologues often exhibit departures from equilibrium (i.e., disequilibrium) in shallow terrestrial environments but near-equilibrium signals in deep marine sediments (Wang et al., 2015; Young et al., 2017; Ash et al., 2019; Young, 2019; Douglas et al., 2020). However, the near-equilibrium isotopologue signature imparted by microbial metabolisms is not well-understood. In deep subsurface sediments, limited substrates, and thereby limitations of free energy availability during methanogenesis may lead to isotopologue ratios approaching equilibrium (Wang et al., 2015; Douglas et al., 2020;

Turner et al., 2021). Yet, additional processes, such as anaerobic oxidation of methane, may explain the generation of methane at isotopic equilibrium (Yoshinaga et al., 2014; Ash et al., 2019; Giunta et al., 2019).

To test whether methane near thermodynamic equilibrium (i) can be produced by methanogens, (ii) is influenced by energy landscape (i.e., substrate availability), and (iii) is produced in the absence of anaerobic oxidation, we examined methane sampled from diverse systems, including freshwater lakes, brackish wetlands, and marine basins (Table S1 and Fig. S1). We collected on-site methane gas in the field where methanogenesis rates were shown to significantly exceed the anaerobic oxidation of methane (AOM), and we performed incubation experiments to study methanogenesis in these sediments (see materials and methods). As a precaution we amended these samples with AOM inhibitors, doing so in a manner that did not alter natural substrate concentrations. We quantified the abundance of the two most common methane clumped isotopologues $\Delta^{13}CH_3D$ and $\Delta^{12}CH_2D_2$ relative to a random isotopic distribution (Young et al., 2017). This enables us to link methane clumped isotope signatures to formation processes.

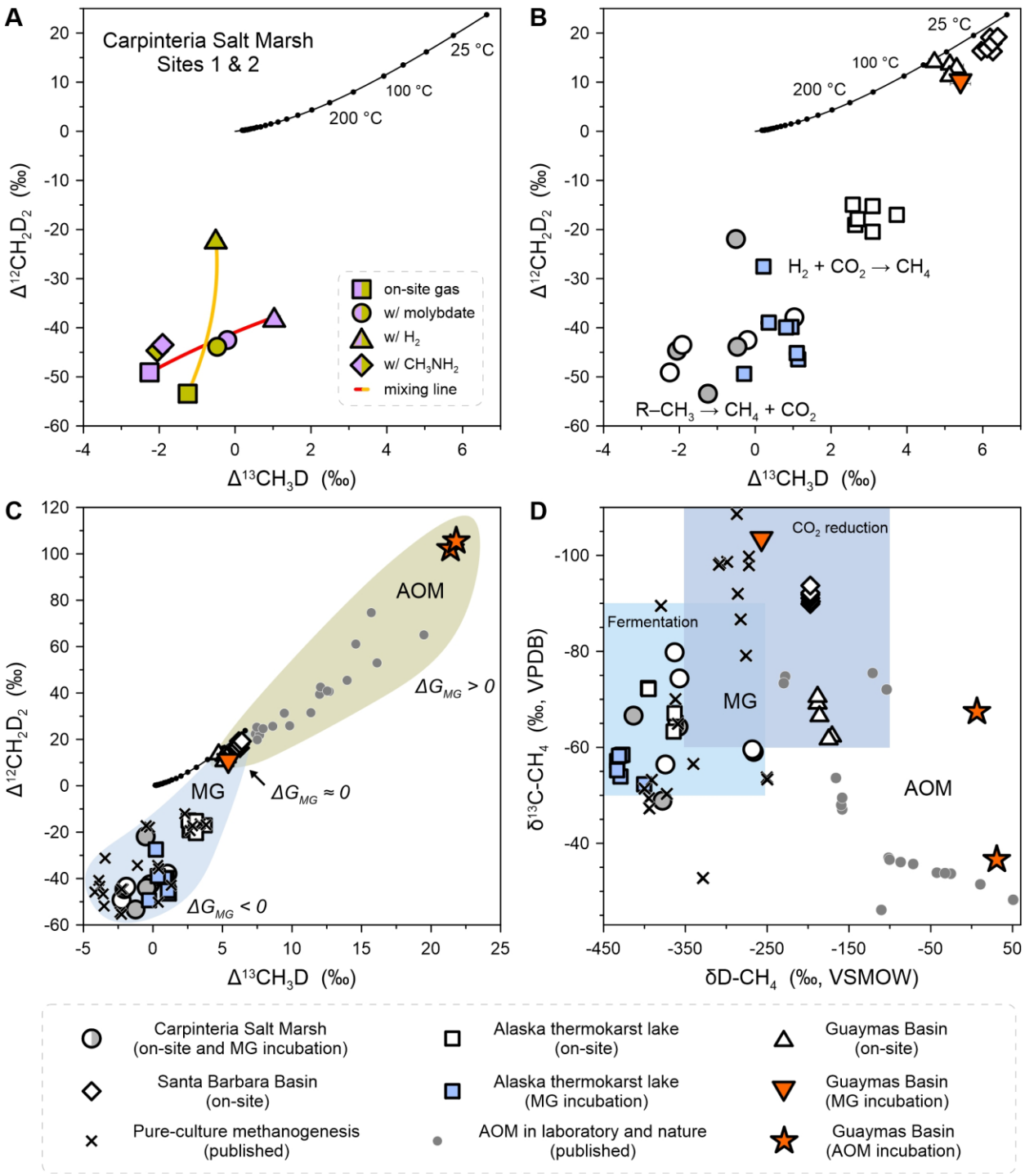

Fig. 4-1 **Isotopologue compositions of methane samples.** (**A–B**) $\Delta^{13}CH_3D$ plotted against $\Delta^{12}CH_2D_2$ for methanogenesis samples from the Carpinteria salt marsh (**A**) and all study sites (**B**). In panel A, light purple and dark yellow symbols depict samples from sites 1 and 2, respectively.

The red and orange curves represent mixing lines between the two methanogenic end-members, the methylotrophic and hydrogenotrophic pathways. The solid black curve depicts theoretical thermodynamic equilibrium abundances of methane isotopologues, along with corresponding temperatures. (**C**) Illustration outlining clumped isotope signatures of methanogenesis and anaerobic oxidation of methane (AOM). The orange stars represent Guaymas Basin slurry incubations involving simultaneous methanogenesis and AOM. The cross symbols represent published methanogenesis data from pure culture incubations, while the grey dots depict published kinetically-driven AOM data from slurry incubations and natural samples (Young et al., 2017; Young, 2019; Giunta et al., 2022; Liu et al., 2023). The light blue and dark yellow fields, characterized by negative and positive ΔG values with respect to methanogenesis, encompass all the methanogenesis (MG) and AOM data, respectively. (**D**) $\delta^{13}C$ plotted against δD. The genetic fields for methane sources follow Whiticar (1999); Milkov and Etiope (2018). The legend for panels B–D is displayed below the plots. Error bars of one standard error are mostly encompassed by individual data points.

Departures from equilibrium reflecting kinetics

Methanogens from laboratory pure cultures have so far exclusively produced methane with pronounced kinetic isotope and isotopologue signals (Wang et al., 2015; Young et al., 2017). Similarly, methane from the Carpinteria salt marsh (California) and thermokarst lakes (Alaska) yielded disequilibrium isotopologue compositions with low $\Delta^{13}CH_3D$ and $\Delta^{12}CH_2D_2$ values, down to −2.3‰ and −53.4‰, respectively (Fig. 1, A and B). Control incubations with a tracer eliminated the possibility of concurrent AOM (Figs. S2 to S3, and Table S2). Therefore, these values reflect kinetic isotope effects and associated combinatorial effects during methanogenesis (Young et al.,

2017; Gruen et al., 2018; Cao et al., 2019; Young, 2019; Taenzer et al., 2020; Gropp et al., 2022; Ono et al., 2022). Using the Carpinteria salt marsh as an example, we investigated the isotopologue effects of different methanogenic pathways (Fig. 1A and Fig. S4). Firstly, the on-site methane primarily originates from methylotrophic methanogenesis within sulfate-rich sediments (Oremland and Polcin, 1982; Krause and Treude, 2021) (see supplementary text). This is further confirmed by minor differences in methane isotopologue compositions observed between methylamine (CH_3NH_2) incubations and on-site methane (Fig. 1A). These differences likely arise from distinct clumping signals of the precursor methyl groups in natural and synthetic methyl compounds (Lloyd et al., 2021). Methylotrophic methanogenesis yields substantial free energy, with the molar Gibbs free energy of the reaction ($\Delta\hat{G}_{rxn}$, hereafter termed ΔG) in the range of approximately −60 kJ mol^{-1} per carbon transferred (Table S3). The extremely low $\Delta^{12}CH_2D_2$ values, approximately −45‰, result from significantly different δD between water and methyl groups, which serve as hydrogen sources contributing to the formation of methane molecules (i.e., an exogenous combinatorial effect) (Taenzer et al., 2020). In Carpinteria salt marsh sediments where we introduced excess H_2, we observe a greater fraction of methane from hydrogenotrophic methanogenesis. This leads to less negative $\Delta^{12}CH_2D_2$ values because the four hydrogen atoms that form methane are derived from water during hydrogenotrophic methanogenesis (Gruen et al., 2018), confining the combinatorial isotopologue effect to endogenous processes within the cells (Cao et al., 2019; Young, 2019). Lastly, we employed molybdate and H_2S to inhibit the reduction of sulfate and iron(III) associated with AOM, respectively, allowing in-situ H_2 to be consumed by methanogens instead of sulfate and iron reducers. The outcome is the simultaneous occurrence of methylotrophic and hydrogenotrophic methanogenesis in sediment incubations, as evidenced by

their methane isotopologue compositions falling along a mixing trajectory between the two methanogenic pathways (Fig. 1A).

Methane isotopologue data obtained from Alaska thermokarst lakes revealed two distinct groups: in vitro incubations of surface sediment exhibiting more negative $\Delta^{13}CH_3D$ and $\Delta^{12}CH_2D_2$ values, and on-site deep subsurface gas with less negative values (Fig. 1B). Methane production in sulfate-free lake sediments is typically dominated by acetoclastic methanogenesis, especially at low in-situ temperatures (Schulz and Conrad, 1996; Conrad, 2020). Near-surface sediment incubations highly favored this pathway at the study site (Pellerin et al., 2022), producing strongly negative $\Delta^{12}CH_2D_2$ values reflecting combinatorial effects from hydrogen sources in acetate and water. Deeper in the sediments, where the buried organic matter becomes less degradable and the microbial communities face increased energy limitations, hydrogenotrophic methanogenesis assumes a more significant role (Hornibrook et al., 1997; Chan et al., 2005). This shift is evident in the less negative $\Delta^{12}CH_2D_2$ values observed in deeper incubation and on-site subsurface methane (Fig. 1B and Fig. S5). Diminished availability of labile organic matter and the resultant reduction in free energy availability downcore may have fostered metabolic reversibility (i.e., the ratio of the reverse to forward rates of reaction) in methanogenesis, thereby contributing to less negative isotopologue compositions (Douglas et al., 2020). We suggest that methanogenesis evolution in $\Delta^{13}CH_3D$ vs. $\Delta^{12}CH_2D_2$ space is governed by the changing organic matter dynamics with depth within lake sediments, reflecting a convolution of pathway transition from acetoclastic to hydrogenotrophic methanogenesis and possibly an increase in metabolic reversibility attributable to limitations of free energy.

Methane approaching thermodynamic equilibrium under energy-limited conditions

Deep-sea marine sediments, where methane is predominantly produced through hydrogenotrophic methanogenesis (Oremland and Taylor, 1978; Beulig et al., 2018), lend additional support to our proposition. For instance, methane collected below the sulfate-methane transition zone (SMTZ) in the Santa Barbara Basin exhibits apparent formation temperatures of 7–19 °C and 27–49 °C based on $\Delta^{13}CH_3D$ and $\Delta^{12}CH_2D_2$ values, respectively (Fig. 1B). These apparent formation temperatures approach the in-situ temperature of 6 °C, though some disequilibrium persists. Porewater methane modeling indicates the presence of active methanogenesis (Fig. S6). Sulfate reduction, if occurring, proceeds at an exceptionally slow rate below the SMTZ (Pellerin et al., 2018). The elevated concentrations of aqueous sulfide, coupled with the absence of dissolved Fe^{2+}, preclude the possibility of microbial iron(III) reduction (Canfield et al., 1992) (Fig. S6). With negligible electron-accepting processes to accommodate AOM, we conclude that the near-equilibrium methane isotopologue values of the Santa Barbara samples result from a slow rate of methanogenesis (0.2 nmol cm^{-3} d^{-1}) under energy-limited conditions (ΔG ranging from −22.6 to −14.7 kJ mol^{-1} C), characterized by an extremely low hydrogen availability (4.7±0.7 nM; Fig. S6 and Table S3).

In addition to the Santa Barbara Basin, the Guaymas Basin offers a unique perspective for comparing surface and deep subsurface methanogenesis. To completely rule out AOM, we conducted slurry incubations of surface sediment from the Guaymas Basin with molybdate and H_2S at 20 °C. Notably, the AOM rate, as determined by ^{14}C-radiotracer, was below the detection limit (Table S2). The data fall near the equilibrium curve in this case, with apparent formation temperatures of the produced methane being 37±10 °C and 122±14 °C implied by $\Delta^{13}CH_3D$ and $\Delta^{12}CH_2D_2$ values, respectively (Fig. 1B). To our knowledge, this result marks the first clear demonstration that natural methanogens can produce methane approaching isotopologue

equilibrium independently of AOM. Additionally, on-site methane collected below the SMTZ from a drilling core in the Guaymas Basin exhibits clumped isotopologue abundances near equilibrium at relatively low temperatures, with apparent $\Delta^{13}CH_3D$ and $\Delta^{12}CH_2D_2$ formation temperatures being 40–62 °C and 64–95 °C, respectively, compared with measured in-situ temperatures of 18–31 °C (Fig. 1B). While the potential role of AOM in this drilling core cannot be entirely discounted, AOM rates were either near or below the detection limit in analogous deep biosphere sediments (Beulig et al., 2022). The close agreement between AOM-free incubations and the on-site data suggests that AOM does not influence $\Delta^{13}CH_3D$ and $\Delta^{12}CH_2D_2$ values in this setting (Fig. 1B).

Taken together, we applied metabolic-isotopic and isotopologue flow network models of hydrogenotrophic methanogenesis to our dataset (Gropp et al., 2022; Ono et al., 2022). We find our data are largely consistent with these model predictions (Fig. S7). We extend our analysis to compare the degree of D/H fractionation between methane and environmental water ($^{D}\varepsilon$-methane/water) with the isotopologue data. The notable positive correlation between $^{D}\varepsilon$-methane/water and methane isotopologue compositions underscores a strong connection between hydrogen isotope and clumped isotopologue disequilibrium (Wang et al., 2015) (Fig. 2, A and B). On the other hand, microbial methane in deep-sea environments tends to approach hydrogen isotope equilibrium with associated waters at or near the temperatures indicated by the $\Delta^{13}CH_3D$ and $\Delta^{12}CH_2D_2$ data, suggesting the occurrence of both intra- and inter-species isotope equilibrium (Fig. 2, A and B).

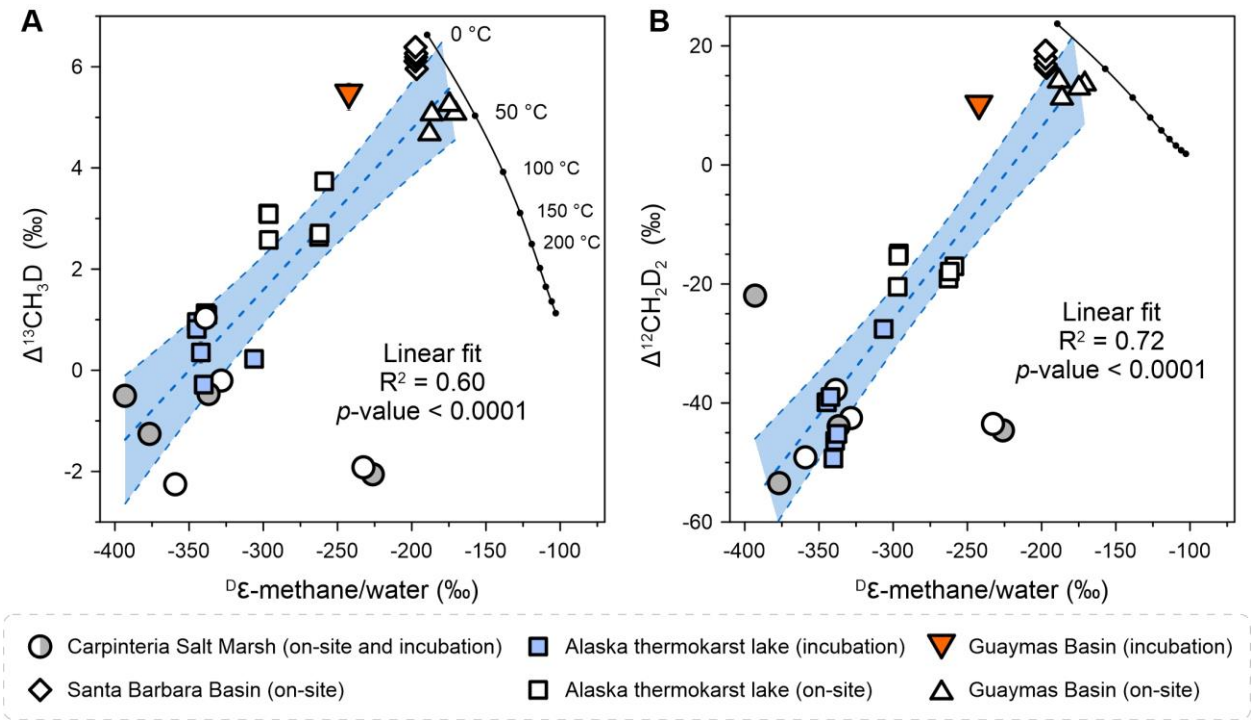

Fig. 4-2 The degree of hydrogen and clumped isotopic disequilibria in methane. Hydrogen isotope fractionation between methane and associated water is plotted against $\Delta^{13}CH_3D$ (**A**) and $\Delta^{12}CH_2D_2$ (**B**). The solid black curve depicts thermodynamic isotopic equilibrium, with the $^{D}\varepsilon$-methane/water calibration given by Turner et al. (2022). Linear regressions are presented with 95% confidence intervals. R-squared and p-values are provided in each panel. Error bars of one standard error are mostly encompassed by individual data points.

Linking methane metabolisms to the energy landscape

In the SMTZ of marine sediments, methane is oxidized by anaerobic methanotrophic archaea (Boetius et al., 2000). To explore the isotopologue effects of concurrent methanogenesis and AOM, we initiated two parallel incubations using separate aliquots of sediment slurries sampled from an active methane seep in the Guaymas Basin. The first was under an argon

headspace, while the second was under a methane headspace. Combining methane concentration analysis and ^{14}C-radiotracer techniques, net methanogenesis with simultaneous AOM was identified in the slurry with an argon headspace (Table S2 and Fig. S8A). The produced methane displays remarkably high $\Delta^{13}CH_3D$ and $\Delta^{12}CH_2D_2$ values, reaching up to 21.8‰ and 105.4‰, respectively—representing, we believe, the highest methane isotopologue compositions yet reported (Fig. 1C). In the slurry containing a methane headspace, net AOM with simultaneous methanogenesis resulted in nearly identical, elevated $\Delta^{13}CH_3D$ and $\Delta^{12}CH_2D_2$ values (Fig. 1C). Similar trajectories in $\Delta^{13}CH_3D$ vs. $\Delta^{12}CH_2D_2$ space have been observed in both laboratory incubations and natural samples associated with kinetically-driven AOM (Giunta et al., 2022; Liu et al., 2023). A steady-state model reproduced these exceptionally high values by incorporating the clumped isotopologue fractionation factors reported in previous AOM incubations (Liu et al., 2023) (Fig. S8). Conversely, recent investigations have demonstrated that AOM leads methane isotopologues towards thermodynamic equilibrium under energy-limited conditions (Ash et al., 2019; Liu et al., 2023). Given that the initial step of AOM and the final step of methanogenesis are catalyzed by the same enzyme, methyl-coenzyme M reductase (Mcr) (Scheller et al., 2010), we suggest that the near-equilibrium methane isotopologue signatures result from the Mcr-catalyzed intracellular isotope exchange operating under conditions of near-threshold free-energy, allowing for either net methanogenesis or AOM (Ono et al., 2022; Liu et al., 2023). When the thermodynamic driving force is elevated, methanogenesis and AOM can generate more negative and positive isotopologue signatures, respectively, in comparison to thermodynamic equilibrium (Fig. 1C). By amalgamating isotope data from prior studies, we illustrate that methane isotopologues are able to provide additional information on anaerobic microbial metabolisms than conventional isotope measurements (Fig. 1, C and D).

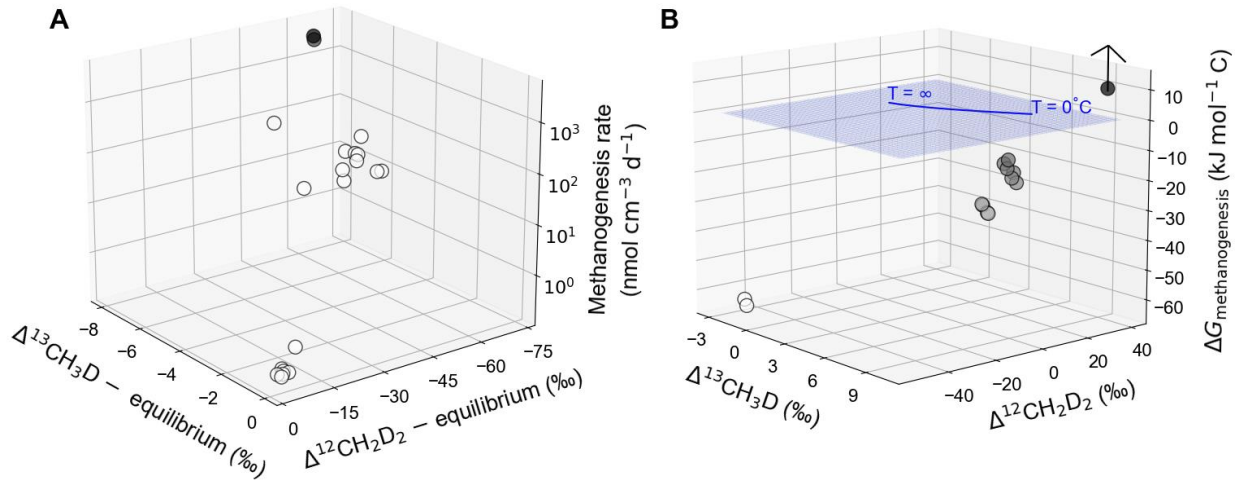

Fig. 4-3 Methanogenesis rate and Gibbs free energy plotted against isotopologue data. The departures from isotopologue equilibrium in panel A are defined as the difference between measured isotopologue compositions and equilibrium isotopologue compositions at in-situ or incubation temperatures. In panel B, the published AOM isotopologue data are averaged (Giunta et al., 2022; Liu et al., 2023) and presented with a published ΔG value of 11 kJ mol^{-1} C with respect to hydrogenotrophic methanogenesis (Dale et al., 2008), offering a conservative estimate. The solid blue curve depicts theoretical thermodynamic equilibrium abundances of methane isotopologues, along with corresponding temperatures. The blue plane represents the surface at which Gibbs free energy equals zero. The symbols are shown in grayscale to reflect variations along the z-axis. This figure is also shown in Fig. S9 with more details.

We extend our analysis to evaluate the fundamental mechanisms that dictate the degree of isotopologue disequilibrium. Notably, a significant positive correlation is observed between

methanogenesis rate and departures from isotopologue equilibrium (Fig. 3A and Fig. S9). This finding aligns with the notion that a high rate of methanogenesis exhibits pronounced kinetic and combinatorial imprints, whereas a low rate of methanogenesis results in a near-equilibrium signature on the methane (Douglas et al., 2020). The difference in departures from isotopologue equilibrium caused by high and low rates of methanogenesis is inherently driven by the reactivity of substrates in the environment. Ramped pyrolysis analysis confirmed a higher proportion of refractory organic carbon in deep-sea sediments (Fig. S10), leading to reduced substrate reactivity (Middelburg, 1989). Therefore, the low availability and high recalcitrance of metabolizable substrates in deep-sea sediments maintain low rates of methanogenesis.

Departures from isotopologue equilibrium can be related to the bioenergetics of a site using the principles of disequilibrium thermodynamics, in which rates of reaction are proportional to reaction affinity (Pekař, 2009). Reaction affinity can be related to the forward and reverse reaction rates, r_f and r_{rev}, respectively, using $A = RT\ln(r_f/r_{rev})$. Reaction affinity is defined as $A = -\sum v_i \mu_i$ where v_i are stoichiometric coefficients for species i in a reaction and μ_i are the chemical potentials. From the definition of chemical potential, we have $A = RT\ln(K_{Eq}/Q) = -\Delta G$ where Q is the measured activity quotient for the reaction and K_{Eq} is the equilibrium constant, and thus $\Delta G = -RT\ln(r_f/r_{rev})$. The measured activity quotients, and thus free energies, are indicators of net reaction rates (although often applicable, deviations from these simple relationships can be expected for non-elementary reactions (Beard and Qian, 2007)). We include AOM data in our analysis here by expressing the ΔG of the environment in terms of that available for hydrogenotrophic methanogenesis (Fig. 3B). Where AOM is dominant, a positive ΔG for methanogenesis occurs, as expected. Taking the data in combination, we observe a positive correlation between isotopologue compositions and ΔG values for methanogenesis, with near-equilibrium methane isotopologue

compositions aligning with ΔG values close to zero (blue plane in Fig. 3B). Therefore, we propose that the relative abundances of clumped isotopologues of methane provide a proxy for the bioenergetics of a site with respect to methanogenesis. This provides a useful tool for characterizing the bioenergetics of environments for methane production, where estimates of hydrogen concentrations are not readily available to calculate ΔG.

On a global scale, microbial methane emissions mainly stem from shallow terrestrial environments (Saunois et al., 2020). Despite Earth's largest methane reservoir residing in deep-sea sediments as gas hydrates, current assessments reveal that only a small fraction of atmospheric methane originates from the marine realm (Conrad, 2009; Dlugokencky et al., 2011). Recent measurements of methane isotopologues in the atmosphere validate that significant isotopologue disequilibrium in global microbial methane emissions indicates the dominance of terrestrial sources over marine ones (Haghnegahdar et al., 2023; Sivan et al., 2024), thereby introducing an additional constraint to the global methane budgets. Clumped isotopes of methane have the potential to be a powerful tool for characterizing the energy landscape of microbial metabolisms in the environment, serving as interplanetary biosignatures, and providing new insights into methane emissions.

Materials and Methods

Four study sites were chosen to investigate the clumped isotopologue effects of natural methanogenesis, including freshwater lakes, brackish wetlands, and marine basins (Fig. S1 and Table S1). Rates of methanogenesis and anaerobic oxidation of methane (AOM) were determined under ex-situ and in vitro conditions. The goal was to sample on-site methane gas where methanogenesis rates significantly exceeded AOM rates, and to incubate sediments for methanogenesis with the addition of AOM inhibitors. Site descriptions, sampling and geochemical analyses are provided in the supporting information. Methane isotopologue abundances of methane gas samples were measured using the Panorama (Nu Instruments) high-mass-resolution gas-source isotope-ratio mass spectrometer (Young et al., 2017).

Sediment slurry incubation

We conducted sediment slurry incubation experiments to collect methane produced by indigenous methanogens, amended with AOM inhibitors but without alteration of the natural substrate concentration. To date, there is no inhibitor that specifically targets AOM without inhibiting methanogenesis simultaneously (Oremland and Capone, 1988). However, AOM is coupled to the reduction of electron acceptors (Boetius et al., 2000; Beal et al., 2009). Sulfate reduction is readily inhibited by the addition of molybdate (Oremland and Capone, 1988). Iron reduction can be prevented by the addition of sulfide because aqueous sulfide reacts with iron oxides, resulting in the absence of microbially reducible Fe(III) in the system (Laufer et al., 2020).

For salt marsh and Guaymas Basin sediment, artificial seawater medium was prepared without sulfate following the method by Widdel and Bak (1992). Sediment slurries were made by

mixing sediment with seawater medium. Molybdate was introduced to reach a final concentration of 20 mM. These slurries were used to study methanogenesis under the simultaneous inhibition of iron and sulfate reduction and without amendment of methanogenic substrates. Furthermore, we set up three additional sets of slurries for each site following the procedure above but with the addition of methanogenic substrates to access the isotopologue signatures of common methanogenic pathways. These substrates included 150 kPa hydrogen gas in the headspace, 40 mM acetate, and 100 mM monomethylamine, respectively (Gruen et al., 2018).

Alaska lake sediments were flushed with argon and incubated at 4 °C without the addition of liquid medium and inhibitors, as porewater sulfate concentrations (< 30 μM) were near or below the detection limit (Pellerin et al., 2022).

The sediment from the Guaymas Basin, collected from an active methane seep, was an excellent candidate for accessing the isotopologue effect of concurrent methanogenesis and AOM. Following the same procedure as above but without molybdate and sulfide addition, we established another two sets of Guaymas Basin slurries. We aim to investigate the isotopologue effects of net methanogenesis and net AOM when methanogenesis and AOM were occurring simultaneously. One set was flushed with argon to remove methane in the slurry, whereas the headspace of the other set was replenished with ca. 200 kPa of tank methane.

Rate measurements of sediment slurries

Methane concentrations in the headspace of slurry incubations were monitored by gas chromatography throughout the incubation period. The amounts of dissolved methane were calculated using Henry's law and the Bunsen solubility coefficient. Methanogenesis rates were

determined by combining the total amounts of methane in the headspace and the liquid phase. In addition, the activity of AOM was determined using ^{14}C-methane tracer.

Thermodynamic calculations

Molar Gibbs free energies (ΔG) of methanogenic reactions were computed utilizing in-situ physicochemical data collected down the sampling interval where methane isotopologue composition was analyzed. The SUPCRT92 software package was employed to compute the standard state Gibbs free energy (ΔG^0) under in-situ temperature and pressure conditions, with the consideration that all species are assumed to be in aqueous (aq) form. Based on previous studies in similar environments, we assume that the sulfate-free deep-sea sediments were dominated by hydrogenotrophic methanogenesis (Oremland and Taylor, 1978; Beulig et al., 2018), whereas methylotrophic methanogenesis is the primary pathway in the sulfate-rich salt marsh (Oremland and Polcin, 1982; Krause and Treude, 2021). Activities were determined by multiplying the concentrations of reactants and products by their respective activity coefficients. The values of ΔG, where $\Delta G = \Delta G^0 + RT \ln Q$, are presented in units of kJ/mol-carbon-transferred, or kJ mol^{-1} C, facilitating standardized energetic comparisons.

Acknowledgments: We gratefully acknowledge the crews and shipboard scientists aboard the R/Vs *JOIDES Resolution*, *Atlantis*, and *Roger Revelle*, in addition to sampling assistance from colleagues of the Treude laboratory at UCLA. We thank Xingqian Cui, Huiyuan Yang, Orit Sivan, and Jiawen Li for their contribution and support. The research was funded by the NASA FINESST Fellowship 80NSSC21K1529 (JL, TT), National Science Foundation grants EAR-1852912 and OCE-1829981 (TT), NASA grant 80NSSC21K0477 (EDY, WDL), Alfred P. Sloan Foundation via the Deep Carbon Observatory (EDY), National Science Foundation grant OCE-2321651 (PRG), and NASA grants 80NSSC18K1140 and 80NSSC19K1427 (PRG).

References

Ash J.L., Egger M., Treude T., Kohl I., Cragg B., Parkes R.J., Slomp C.P., Sherwood Lollar B. and Young E.D. (2019) Exchange catalysis during anaerobic methanotrophy revealed by 12CH2D2 and 13CH3D in methane. *Geochemical Perspectives Letters* **10**, 26-30.

Beal E.J., House C.H. and Orphan V.J. (2009) Manganese-and iron-dependent marine methane oxidation. *Science* **325**, 184-187.

Beard D.A. and Qian H. (2007) Relationship between Thermodynamic Driving Force and One-Way Fluxes in Reversible Processes. *PLOS ONE* **2**, e144.

Beulig F., Røy H., Glombitza C. and Jørgensen B.B. (2018) Control on rate and pathway of anaerobic organic carbon degradation in the seabed. *P. Natl. Acad. Sci. USA* **115**, 367-372.

Beulig F., Schubert F., Adhikari R.R., Glombitza C., Heuer V.B., Hinrichs K.U., Homola K.L., Inagaki F., Jørgensen B.B., Kallmeyer J., Krause S.J.E., Morono Y., Sauvage J., Spivack A.J. and Treude T. (2022) Rapid metabolism fosters microbial survival in the deep, hot subseafloor biosphere. *Nat. commun.* **13**, 312.

Boetius A., Ravenschlag K., Schubert C.J., Rickert D., Widdel F., Gieseke A., Amann R., Jørgensen B.B., Witte U. and Pfannkuche O. (2000) A marine microbial consortium apparently mediating anaerobic oxidation of methane. *Nature* **407**, 623-626.

Canfield D.E., Raiswell R. and Bottrell S.H. (1992) The reactivity of sedimentary iron minerals toward sulfide. *Am. J. Sci.* **292**, 659-683.

Cao X., Bao H. and Peng Y. (2019) A kinetic model for isotopologue signatures of methane generated by biotic and abiotic CO2 methanation. *Geochim. Cosmochim. Acta* **249**, 59-75.

Chan O.C., Claus P., Casper P., Ulrich A., Lueders T. and Conrad R. (2005) Vertical distribution of structure and function of the methanogenic archaeal community in Lake Dagow sediment. *Environ. Microbiol.* **7**, 1139-1149.

Conrad R. (2009) The global methane cycle: recent advances in understanding the microbial processes involved. *Environmental Microbiology Reports* **1**, 285-292.

Conrad R. (2020) Importance of hydrogenotrophic, aceticlastic and methylotrophic methanogenesis for methane production in terrestrial, aquatic and other anoxic environments: A mini review. *Pedosphere* **30**, 25-39.

Dale A.W., Regnier P., Knab N.J., Jørgensen B.B. and Van Cappellen P. (2008) Anaerobic oxidation of methane (AOM) in marine sediments from the Skagerrak (Denmark): II. Reaction-transport modeling. *Geochim. Cosmochim. Acta* **72**, 2880-2894.

Dlugokencky E.J., Nisbet E.G., Fisher R. and Lowry D. (2011) Global atmospheric methane: budget, changes and dangers. *Philosophical Transactions of the Royal Society A: Mathematical, Physical and Engineering Sciences* **369**, 2058-2072.

Douglas P.M.J., Gonzalez Moguel R., Walter Anthony K.M., Wik M., Crill P.M., Dawson K.S., Smith D.A., Yanay E., Lloyd M.K., Stolper D.A., Eiler J.M. and Sessions A.L. (2020) Clumped Isotopes Link Older Carbon Substrates With Slower Rates of Methanogenesis in Northern Lakes. *Geophys. Res. Lett.* **47**, e2019GL086756.

Giunta T., Young E.D., Labidi J., Sansjofre P., Jézéquel D., Donval J.-P., Brandily C. and Ruffine L. (2022) Extreme methane clumped isotopologue bio-signatures of aerobic and anaerobic methanotrophy: Insights from the Lake Pavin and the Black Sea sediments. *Geochim. Cosmochim. Acta* **338**, 34-53.

Giunta T., Young E.D., Warr O., Kohl I., Ash J.L., Martini A., Mundle S.O.C., Rumble D., Pérez-Rodríguez I., Wasley M., LaRowe D.E., Gilbert A. and Sherwood Lollar B. (2019) Methane sources and sinks in continental sedimentary systems: New insights from paired clumped isotopologues 13CH3D and 12CH2D2. *Geochim. Cosmochim. Acta* **245**, 327-351.

Gropp J., Jin Q. and Halevy I. (2022) Controls on the isotopic composition of microbial methane. *Sci. Adv.* **8**, eabm5713.

Gruen D.S., Wang D.T., Könneke M., Topçuoğlu B.D., Stewart L.C., Goldhammer T., Holden J.F., Hinrichs K.-U. and Ono S. (2018) Experimental investigation on the controls of clumped isotopologue and hydrogen isotope ratios in microbial methane. *Geochim. Cosmochim. Acta* **237**, 339-356.

Haghnegahdar M.A., Sun J., Hultquist N., Hamovit N.D., Kitchen N., Eiler J., Ono S., Yarwood S.A., Kaufman A.J., Dickerson R.R., Bouyon A., Magen C. and Farquhar J. (2023) Tracing sources of atmospheric methane using clumped isotopes. *P. Natl. Acad. Sci. USA* **120**, e2305574120.

Hornibrook E.R.C., Longstaffe F.J. and Fyfe W.S. (1997) Spatial distribution of microbial methane production pathways in temperate zone wetland soils: Stable carbon and hydrogen isotope evidence. *Geochim. Cosmochim. Acta* **61**, 745-753.

Krause S.J.E. and Treude T. (2021) Deciphering cryptic methane cycling: Coupling of methylotrophic methanogenesis and anaerobic oxidation of methane in hypersaline coastal wetland sediment. *Geochim. Cosmochim. Acta* **302**, 160-174.

Laufer K., Michaud A.B., Røy H. and Jørgensen B.B. (2020) Reactivity of Iron Minerals in the Seabed Toward Microbial Reduction – A Comparison of Different Extraction Techniques. *Geomicrobiol. J.* **37**, 170-189.

Liu J., Harris R.L., Ash J.L., Ferry J.G., Krause S.J.E., Labidi J., Prakash D., Sherwood Lollar B., Treude T., Warr O. and Young E.D. (2023) Reversibility controls on extreme methane clumped isotope signatures from anaerobic oxidation of methane. *Geochim. Cosmochim. Acta* **348**, 165-186.

Lloyd M.K., Eldridge D.L. and Stolper D.A. (2021) Clumped 13CH2D and 12CHD2 compositions of methyl groups from wood and synthetic monomers: Methods, experimental and theoretical calibrations, and initial results. *Geochim. Cosmochim. Acta* **297**, 233-275.

Middelburg J.J. (1989) A simple rate model for organic matter decomposition in marine sediments. *Geochim. Cosmochim. Acta* **53**, 1577-1581.

Milkov A.V. and Etiope G. (2018) Revised genetic diagrams for natural gases based on a global dataset of >20,000 samples. *Org. Geochem.* **125**, 109-120.

Nisbet E.G., Dlugokencky E.J., Manning M.R., Lowry D., Fisher R.E., France J.L., Michel S.E., Miller J.B., White J.W.C., Vaughn B., Bousquet P., Pyle J.A., Warwick N.J., Cain M., Brownlow R., Zazzeri G., Lanoisellé M., Manning A.C., Gloor E., Worthy D.E.J., Brunke E.-G., Labuschagne C., Wolff E.W. and Ganesan A.L. (2016) Rising atmospheric methane: 2007–2014 growth and isotopic shift. *Global Biogeochem. Cycles* **30**, 1356-1370.

Ono S., Rhim J.H. and Ryberg E.C. (2022) Rate limits and isotopologue fractionations for microbial methanogenesis examined with combined pathway protein cost and isotopologue flow network models. *Geochim. Cosmochim. Acta* **325**, 296-315.

Oremland R.S. and Capone D.G. (1988) Use of “Specific” Inhibitors in Biogeochemistry and Microbial Ecology, in: Marshall K.C. (Ed.), Advances in Microbial Ecology. Springer US, Boston, MA, pp. 285-383.

Oremland R.S. and Polcin S. (1982) Methanogenesis and Sulfate Reduction: Competitive and Noncompetitive Substrates in Estuarine Sediments. *Appl. Environ. Microbiol.* **44**, 1270-1276.

Oremland R.S. and Taylor B.F. (1978) Sulfate reduction and methanogenesis in marine sediments. *Geochim. Cosmochim. Acta* **42**, 209-214.

Pekař M. (2009) Affinity and Reaction Rates: Reconsideration of Theoretical Background and Modelling Results. *Zeitschrift für Naturforschung A* **64**, 289-299.

Pellerin A., Antler G., Røy H., Findlay A., Beulig F., Scholze C., Turchyn A.V. and Jørgensen B.B. (2018) The sulfur cycle below the sulfate-methane transition of marine sediments. *Geochim. Cosmochim. Acta* **239**, 74-89.

Pellerin A., Lotem N., Walter Anthony K., Eliani Russak E., Hasson N., Røy H., Chanton J.P. and Sivan O. (2022) Methane production controls in a young thermokarst lake formed by abrupt permafrost thaw. *Global Change Biol.* **28**, 3206-3221.

Saunois M., Stavert A.R., Poulter B., Bousquet P., Canadell J.G., Jackson R.B., Raymond P.A., Dlugokencky E.J., Houweling S., Patra P.K., Ciais P., Arora V.K., Bastviken D., Bergamaschi P., Blake D.R., Brailsford G., Bruhwiler L., Carlson K.M., Carrol M., Castaldi S., Chandra N., Crevoisier C., Crill P.M., Covey K., Curry C.L., Etiope G., Frankenberg C., Gedney N., Hegglin M.I., Höglund-Isaksson L., Hugelius G., Ishizawa M., Ito A., Janssens-Maenhout G., Jensen K.M., Joos F., Kleinen T., Krummel P.B., Langenfelds R.L., Laruelle G.G., Liu L., Machida T., Maksyutov S., McDonald K.C., McNorton J., Miller P.A., Melton J.R., Morino I., Müller J., Murguia-Flores F., Naik V., Niwa Y., Noce S., O'Doherty S., Parker R.J., Peng C., Peng S., Peters G.P., Prigent C., Prinn R., Ramonet M., Regnier P., Riley W.J., Rosentreter J.A., Segers A., Simpson I.J.,

Shi H., Smith S.J., Steele L.P., Thornton B.F., Tian H., Tohjima Y., Tubiello F.N., Tsuruta A., Viovy N., Voulgarakis A., Weber T.S., van Weele M., van der Werf G.R., Weiss R.F., Worthy D., Wunch D., Yin Y., Yoshida Y., Zhang W., Zhang Z., Zhao Y., Zheng B., Zhu Q., Zhu Q. and Zhuang Q. (2020) The Global Methane Budget 2000–2017. *Earth Syst. Sci. Data* **12**, 1561-1623.

Scheller S., Goenrich M., Boecher R., Thauer R.K. and Jaun B. (2010) The key nickel enzyme of methanogenesis catalyses the anaerobic oxidation of methane. *Nature* **465**, 606-608.

Schulz S. and Conrad R. (1996) Influence of temperature on pathways to methane production in the permanently cold profundal sediment of Lake Constance. *FEMS Microbiol. Ecol.* **20**, 1-14.

Schwietzke S., Sherwood O.A., Bruhwiler L.M.P., Miller J.B., Etiope G., Dlugokencky E.J., Michel S.E., Arling V.A., Vaughn B.H., White J.W.C. and Tans P.P. (2016) Upward revision of global fossil fuel methane emissions based on isotope database. *Nature* **538**, 88-91.

Sivan M., Röckmann T., van der Veen C. and Popa M.E. (2024) Extraction, purification, and clumped isotope analysis of methane (Δ13CDH3 and Δ12CD2H2) from sources and the atmosphere. *Atmos. Meas. Tech.* **17**, 2687-2705.

Stolper D.A., Lawson M., Davis C.L., Ferreira A.A., Neto E.V.S., Ellis G.S., Lewan M.D., Martini A.M., Tang Y., Schoell M., Sessions A.L. and Eiler J.M. (2014) Formation temperatures of thermogenic and biogenic methane. *Science* **344**, 1500-1503.

Taenzer L., Labidi J., Masterson A.L., Feng X., Rumble D., Young E.D. and Leavitt W.D. (2020) Low Δ12CH2D2 values in microbialgenic methane result from combinatorial isotope effects. *Geochim. Cosmochim. Acta* **285**, 225-236.

Turner A.C., Korol R., Eldridge D.L., Bill M., Conrad M.E., Miller T.F. and Stolper D.A. (2021) Experimental and theoretical determinations of hydrogen isotopic equilibrium in the system CH4–H2–H2O from 3 to 200 °C. *Geochim. Cosmochim. Acta* **314**, 223-269.

Turner A.C., Pester N.J., Bill M., Conrad M.E., Knauss K.G. and Stolper D.A. (2022) Experimental determination of hydrogen isotope exchange rates between methane and water under hydrothermal conditions. *Geochim. Cosmochim. Acta* **329**, 231-255.

Wang D.T., Gruen D.S., Lollar B.S., Hinrichs K.-U., Stewart L.C., Holden J.F., Hristov A.N., Pohlman J.W., Morrill P.L., Könneke M., Delwiche K.B., Reeves E.P., Sutcliffe C.N., Ritter D.J., Seewald J.S., McIntosh J.C., Hemond H.F., Kubo M.D., Cardace D., Hoehler T.M. and Ono S. (2015) Nonequilibrium clumped isotope signals in microbial methane. *Science* **348**, 428-431.

Whiticar M.J. (1999) Carbon and hydrogen isotope systematics of bacterial formation and oxidation of methane. *Chem. Geol.* **161**, 291-314.

Widdel F. and Bak F. (1992) Gram-Negative Mesophilic Sulfate-Reducing Bacteria, in: Balows A., Trüper H.G., Dworkin M., Harder W., Schleifer K.-H. (Eds.), The Prokaryotes: A Handbook on the Biology of Bacteria: Ecophysiology, Isolation, Identification, Applications. Springer New York, New York, NY, pp. 3352-3378.

Xie H., Dong G., Formolo M., Lawson M., Liu J., Cong F., Mangenot X., Shuai Y., Ponton C. and Eiler J. (2021) The evolution of intra- and inter-molecular isotope equilibria in natural gases with thermal maturation. *Geochim. Cosmochim. Acta* **307**, 22-41.

Yoshinaga M.Y., Holler T., Goldhammer T., Wegener G., Pohlman J.W., Brunner B., Kuypers M.M.M., Hinrichs K.-U. and Elvert M. (2014) Carbon isotope equilibration during sulphate-limited anaerobic oxidation of methane. *Nat. Geosci.* **7**, 190-194.

Young E.D. (2019) A Two-Dimensional Perspective on CH4 Isotope Clumping: Distinguishing Process from Source, in: Orcutt B.N., Daniel I., Dasgupta R. (Eds.), Deep Carbon: Past to Present. Cambridge University Press, Cambridge, pp. 388-414.

Young E.D., Kohl I.E., Lollar B.S., Etiope G., Rumble D., Li S., Haghnegahdar M.A., Schauble E.A., McCain K.A., Foustoukos D.I., Sutclife C., Warr O., Ballentine C.J., Onstott T.C., Hosgormez H., Neubeck A., Marques J.M., Pérez-Rodríguez I., Rowe A.R., LaRowe D.E., Magnabosco C., Yeung L.Y., Ash J.L. and Bryndzia L.T. (2017) The relative abundances of resolved 12CH2D2 and 13CH3D and mechanisms controlling isotopic bond ordering in abiotic and biotic methane gases. *Geochim. Cosmochim. Acta* **203**, 235-264.

Supplementary Material: Liu et al. Clumped isotopes of methane trace bioenergetics in the environment

Materials and Methods

Materials

Four study sites were chosen to investigate the clumped isotopologue effects of natural methanogenesis, including freshwater lakes, brackish wetlands, and marine basins (Fig. S1 and Table S1). Rates of methanogenesis and anaerobic oxidation of methane (AOM) were determined under ex-situ and in vitro conditions. The goal was to sample on-site methane gas where methanogenesis rates significantly exceeded AOM rates, and to incubate sediments for methanogenesis with the addition of AOM inhibitors.

Carpinteria Salt Marsh Reserve

The Carpinteria Salt Marsh Reserve (CSMR) is an estuarine wetland located on the south coast of Santa Barbara County in southern California, United States. Freshwater runoff flows into the marsh through six drainage channels along the northern boundary, while tidal waters enter via an inlet that is open to the Santa Barbara Channel at the southern boundary (Page et al., 1995). Krause et al. (2024) collected sediment cores across the main channel along the service road and measured rates of methylotrophic methanogenesis and AOM using ^{14}C-radiotracers. Guided by these results, we selected two brackish sites located in close proximity to freshwater runoff (Table S1), where AOM rates were found to be less than 5% of the rates of methylotrophic

methanogenesis in the upper 5 cm (Fig. S2). Sediment in the upper 5 cm of brackish sites 1 and 2 was characterized by a slightly lower and higher sulfate concentration (ca. 20 and 26 mM), respectively. We collected sediment from the upper 5 cm at each site in 2022. The sediment was transferred to borosilicate bottles without headspace, sealed with black butyl rubber stoppers, and stored at 4 °C for in vitro slurry incubation. We also collected on-site methane dissolved in sediments for isotopologue analysis. Due to the low methane concentrations (12–20 μM) at the two sites, we modified 3.8-L glass Mason jars with screw plastic lids and airtight silicone gaskets. A hole was drilled through the plastic lid to install a blue butyl rubber stopper for gas sampling. In the field, we transferred ~2500 cm^3 of sediments to each jar. Subsequently, we introduced ~500 g of solid NaCl and ~800 ml of saturated NaCl solution immediately before sealing the lid, ensuring an air headspace of ~250 ml. The jars were vigorously shaken and stored at 20 ºC for one week before transferring the headspace to evacuated 160-ml crimp vials.

Alaska thermokarst lake

Big Trail Lake is located 8 km north of Fairbanks, Alaska, in the Goldstream Valley (Table S1). It sits at the confluence of Goldstream Creek and Big Eldorado Creek, approximately 4 km west of Goldstream Mine in Fox. Big Trail Lake is an actively expanding thermokarst lake, currently covering an area of about 40,000 m^2, with average and maximum depths of 1.2 m and 4.1 m, respectively. The lake is notable for its history of thermokarst activity, including vigorous methane seeps (Walter Anthony et al., 2021). Aerial photographic records suggest that the lake formed from a wetland between 1949 and 1967 (Walter Anthony et al., 2018). Sediment cores were extracted from two sites by percussion coring in March 2020; specifically, Sites D and S were situated in the western and northern portion of the lake, respectively. The lithology between the

two sites was identical (Pellerin et al., 2022). Sediment from a slit layer (unit 1), a peat layer (unit 2), and a dark mud layer (unit 4) at Site S was transferred to glass vials and sealed with blue butyl rubber stoppers for incubation (Fig. S3). The vials were immediately flushed with pure nitrogen gas for 3 intervals of 5 minutes, and vigorously shaken between the intervals to remove all traces of methane and oxygen. Porewater and sediment geochemistry and microbial activity have been previously published (Pellerin et al., 2022; Lotem et al., 2023). AOM rates were determined using ^{13}C-CH_4 and were found to be only around 1% of the methanogenesis rates in the sediments (Lotem et al., 2023) (Fig. S3B).

Sediment coring established a conduit for the upward migration and ebullition of subsurface methane gas. At Site S in Big Trail Lake, after vibracore coring down to 4 m, three gas samples were obtained from three boreholes using the water displacement method, where glass vials were immersed in the lake water and filled. Subsequently, the vials were inverted, allowing free gas bubbles to be directed into the vials already filled with lake water. Upon displacement of all the lake water by gas, the vials were sealed with blue butyl rubber stoppers while submerged in the water. Similarly, three gas samples were collected from Goldstream Lake, located 1.3 km west of Big Trail Lake (Table S1).

Santa Barbara Basin

Located in the California Borderlands, Santa Barbara Basin (SBB) is a coastal basin with a seasonal anoxic water column, reaching a maximum depth of around 600 meters (Sholkovitz and Gieskes, 1971). The average sedimentation rate at the center of the SBB was estimated to be 4.2 ± 0.4 mm per year (Reimers et al., 1996). A gravity core was taken from the depocenter Site NDRO

in November 2019 during an expedition aboard R/V *Atlantis* (AT42-19; Table S1) (Krause et al., 2023). For methane concentration analysis, sediment samples of 2 cm^3 were immediately collected using cut-off syringes and transferred to 12 ml crimp vials containing 5 ml of 2.5% NaOH solution. The vials were then crimp sealed, shaken vigorously and stored upside down at 4 °C. Around 25 cm^3 sediment was transferred to argon-flushed 50 ml centrifuge tubes and centrifuged at 4300g for 20 min for porewater analysis. The remaining sediment was transferred to 1-L glass Mason jars for on-site methane isotopologue analysis, utilizing the same sampling procedure as outlined in the salt marsh section. In July 2023, we returned to the same site aboard R/V *Atlantis* (AT50-11) to acquire a higher-resolution geochemical profile, employing the same methodology used in 2019. Furthermore, 6 cm^3 of sediments were transferred to 12 ml glass vials for the analysis of hydrogen concentration. We note that part of the soft surface sediment was lost during both gravity core retrievals. To identify the original sediment depths, we aligned our porewater sulfate data with previously published sulfate profiles from multi- and gravity cores in the depocenter of the Basin (Li et al., 2009).

Guaymas Basin

Guaymas Basin, located in the Gulf of California, is a young marginal rift basin between the western margin of mainland Mexico and the Baja California Peninsula. It is characterized by active seafloor spreading, steep geothermal gradients, and rapid deposition of organic-rich sediments (Calvert, 1966; Lonsdale and Becker, 1985). During the International Ocean Discovery Program (IODP) Expedition 385 in fall 2019, drilling activities targeted organic-rich sediments and intruded sills, covering an extensive area within the Basin (Teske et al., 2021). We focused on two sites with relatively low and high geothermal gradients (Table S1 and Fig. S11). Site U1550

is situated in the axial graben of the northern spreading segment of the Guaymas Basin. It is characterized by a relatively low geothermal gradient of 135 °C/km and an average sedimentation rate greater than 69.2 cm/ka. Site U1547 is located about 27 km northwest of the axial graben in the northern Guaymas Basin, within a circular, bowl-shaped hydrothermal mound called Ringvent, that rises approximately 20 m above the seafloor and exhibits a maximum diameter of around 800 m (Teske et al., 2019). It is characterized by a notably high geothermal gradient of 529 °C/km (measured at Hole U1547B) and an average sedimentation rate exceeding 52.4 cm/ka. Additional details about the two drilling sites and their geochemistry have been previously published (Teske et al., 2021).

Three types of methane gas were collected from sediment. Firstly, headspace samples were collected immediately upon retrieval of sediment cores on the core receiving platform. Two replicates of ~5 cm^3 wet sediment were placed in 20 ml glass vials containing 5 ml of 1 M NaOH solution. The vials were capped with a polytetrafluoroethylene/silicone septum and crimp sealed. Following vortexing, the sealed vials were stored upside down at 4 °C. Secondly, the expansion of entrapped gases can create voids in the sediments. To collect void gas samples, a specialized piercing tool was used to puncture the core liner, enabling the gas to expand into a gas-tight syringe connected to the tool. The obtained sample was then transferred to crimp-capped headspace vials pre-filled with a saturated NaCl solution. Thirdly, during hard rock coring, a small (5–15 cm long) whole-round sample of subsurface igneous rock was placed into a trilaminated foil barrier bag and immediately sealed. These samples were incubated for at least 24 h at 70 °C to stimulate degassing. Bags were then sampled using a gas-tight syringe through a polytetrafluoroethylene/silicone septum to quantitatively extract gas. This gas, termed rock incubation, was subsampled into crimped septa vials pre-filled with saturated NaCl solution.

In addition to the drilling samples, we obtained surface sediments from a neighboring site characterized by active methane bubbling (Table S1). Push cores were collected by the remotely operated vehicle *Jason* aboard R/V *Roger Revelle* (RR2107) in November 2021. The top 20 cm sediments were transferred to 500 ml borosilicate bottles without headspace, sealed with black butyl rubber stoppers, and stored at 4 °C for in vitro slurry incubation.

Methods

Sediment slurry incubation

While methane gases collected in the field were chosen from natural settings characterized by low rates of AOM, the AOM rates were still on the order of tens to hundreds of pmol cm^{-3} d^{-1} in the salt marsh and thermokarst lake (Figs. S2 and S3). Simultaneous AOM activity, even if low, complicates the interpretation of isotopologue data when studying the signatures of methanogenesis. Accordingly, we conducted sediment slurry incubation experiments to collect methane produced by indigenous methanogens, amended with AOM inhibitors but without alteration of the natural substrate concentration. To date, there is no inhibitor that specifically targets AOM without inhibiting methanogenesis simultaneously (e.g., 2-bromoethanesulfonate; BES) (Oremland and Capone, 1988). However, AOM is coupled to the reduction of electron acceptors, including but not limited to sulfate, nitrate, and iron oxides (Boetius et al., 2000; Beal et al., 2009; Haroon et al., 2013). In anoxic sediments, nitrate is the first electron acceptor to be depleted, driven by the high energy yield of denitrification, occurring before the accumulation of methane begins (Froelich et al., 1979). We anticipate the absence of nitrate in our sediment slurries. Sulfate reduction is readily inhibited by the addition of molybdate (Oremland and Capone, 1988).

Iron reduction can be prevented by the addition of sulfide because aqueous sulfide reacts with iron oxides, resulting in the absence of microbially reducible Fe(III) in the system (Laufer et al., 2020). However, sulfide toxicity at sulfide levels greater than 3 mM may substantially inhibit methanogenic activity (Koster et al., 1986). Therefore, we introduced an initial sulfide concentration of 1 mM or less and ensured the presence of aqueous sulfide at the end of the incubation period.

For salt marsh and Guaymas Basin sediment, artificial seawater medium was prepared without sulfate following the method by Widdel and Bak (1992). Sediment slurries were made by mixing sediment with seawater medium at a 1:1 to 1:2 (v:v) ratio in 500 ml borosilicate bottles, leaving a 20–60 ml headspace. Concurrently, molybdate was introduced to reach a final concentration of 20 mM. The headspace was immediately flushed with pure argon gas for 3 intervals of 5 minutes, and vigorously shaken between the intervals to remove all traces of methane and oxygen. The bottles were kept in the dark and shaken on a weekly basis. The incubation temperature was 20 °C for the salt marsh and Guaymas Basin slurries, which closely approximated the in-situ condition. These slurries were used to study methanogenesis under the simultaneous inhibition of iron and sulfate reduction and without amendment of methanogenic substrates. Furthermore, we set up three additional sets of slurries for each site following the procedure above but with the addition of methanogenic substrates to access the isotopologue signatures of common methanogenic pathways. These substrates included 150 kPa hydrogen gas in the headspace, 40 mM acetate, and 100 mM monomethylamine (referred to as methylamine hereafter), respectively, reflecting standard methanogen pure culture incubations (Balch et al., 1979; Gruen et al., 2018). Slurry volumes for these incubations were smaller (40–200 ml) as methane production was much faster compared to slurries without substrate addition.

The sediment from the Guaymas Basin, collected from an active methane seep, was an excellent candidate for accessing the isotopologue effect of concurrent methanogenesis and AOM. Following the same procedure as above but without molybdate and sulfide addition, we established another two sets of Guaymas Basin slurries. We aim to investigate the isotopologue effects of net methanogenesis and net AOM when methanogenesis and AOM were occurring simultaneously. One set was flushed with argon to remove methane in the slurry, whereas the headspace of the other set was replenished with ca. 200 kPa of tank methane (Airgas).

Alaska lake sediments were flushed with argon and incubated at 4 °C without the addition of liquid medium and inhibitors, as porewater sulfate concentrations (< 30 μM) were near or below the detection limit (Pellerin et al., 2022). Moreover, Lotem et al. (2023) found that the reduction of iron(III) was not coupled to AOM and demonstrated that the AOM signals in the incubation experiments may result from enzymatic reversibility ("back-flux") during methane production, rather than thermodynamically favorable AOM.

Geochemical analyses

Porewater was separated from sediment by centrifugation in argon-flushed centrifuge tubes. Supernatant from sediment slurries was sampled using a long needle through the rubber stopper without opening the bottle. The concentrations of dissolved solutes in sediment porewater (ex-situ) and sediment slurry incubations (in vitro) were immediately measured after sampling, with the exception of sulfate, which was preserved at −20 °C. For dissolved sulfide and iron analyses, porewater was immediately fixed with 5% zinc acetate solution (1:1 v:v) and 1% ascorbic acid solution (100:1 v:v), respectively. Dissolved sulfide and ferrous iron concentrations were

determined by the methylene blue method (Cline, 1969) and the ferrozine assay (Stookey, 1970), respectively, using a spectrophotometer (Shimadzu UV-1800). The detection limits for sulfide and ferrous iron were 1 μM, exhibiting relative standard deviations (RSD) of less than 5%. Alkalinity was determined by acid titration with a Metrohm 876 Dosimat Plus (Dale et al., 2015). Sulfate concentrations were analyzed by ion chromatography (Metrohm 761). Alkalinity and sulfate concentrations were calibrated against the IAPSO standard seawater with RSD better than 2%. The detection limit for sulfate was about 30 μM with dilution. Furthermore, pH was determined by a pH meter (VWR sympHony B10P).

Alkane concentrations (C_1–C_4) in gas samples were determined using a Shimadzu gas chromatograph (GC-2014) with a packed HayeSep-D column and a flame ionization detector. Helium was used as the carrier gas at a flow rate of 35 ml/min. The column temperature was set at 120 °C and held for 6 min, then increased up to 160 °C at 20 °C/min and held for 4 min. Alternatively, when only C_1 was analyzed, the column temperature was set at 80 °C with a helium flow of 15 ml/min. C_1–C_4 alkane concentrations were calibrated against calibration standards (GASCO Precision Calibration Gas). The RSD was better than 5% and the detection limit was about 1 ppm.

Porewater hydrogen concentrations were determined in triplicates for gravity core sediments from the Santa Barbara Basin following a headspace equilibration technique (Hoehler et al., 1998). Sediment samples (6 cm^3) were enclosed in 12 ml serum vials with an O_2-free nitrogen headspace. The samples underwent a 54-hour incubation in the dark at 6 °C for equilibration. Following this incubation period, the H_2 concentration in the headspace was determined using Peak Performer 1 gas chromatography with a reducing compound photometer on board. Measurements on replicate standards typically exhibited a precision of less than 5%. The

partial pressure values of the gas phase obtained through chromatographic analysis were converted to porewater concentrations using solubility constants corrected for temperature and salinity (Crozier and Yamamoto, 1974).

Analysis of hydrogen isotopic composition of water from slurry incubations and sediment porewater was conducted at the Stable Isotope Laboratory at Dartmouth College (Kopec et al., 2019). Water hydrogen isotopic ratios (δD) were measured using an H-Device, in which water was reduced by hot chromium (850 °C), and the resulting hydrogen gas was measured by a Thermo Delta Plus XL isotope-ratio mass spectrometer (IRMS). Isotopic ratios (D/H) are reported in δ-notation relative to the Standard Mean Ocean Water (VSMOW) standard. Analytical precision for δD is <0.5‰ (1σ) based on replicate analyses of laboratory standards.

To determine the thermochemical stability of organic matter, we performed ramped pyrolysis/oxidation analysis on sediment samples (Cui et al., 2022). The system is made up of a carrier gas supply unit, pyrolysis furnaces and an infrared CO_2 analyzer. Defrosted sediment was acidified overnight using 0.5N HCl to remove carbonates, washed three times using Milli-Q water, and dried at 40 °C prior to analysis. Acid rinsed sediments containing 0.8–1.1 mg of organic carbon were loaded into the inner quartz reactor and operated in sub-oxidation mode. In this mode, the gas supply to the inner tube consisted of 27 ml min^{-1} helium and 3 ml min^{-1} diluted oxygen (5% oxygen / 95% nitrogen). An additional 5 ml min^{-1} of oxygen was introduced directly to the outer quartz tube, oxidizing pyrolytic products from the inner quartz reactor to CO_2 downstream. Samples underwent pyrolysis of the upper furnace, with temperatures ramping from 70 °C to 1050 °C at a constant ramping rate of 5 °C min^{-1}, while the lower furnace was maintained at 800 °C. The carrier gas with evolved CO_2 then passed through the CO_2 analyzer (Sable CA-10), and instantaneous CO_2 concentrations were recorded. CO_2 concentrations were plotted against

temperatures to generate thermograms, displaying the temperature-dependent decomposition of organic carbon. The precision of the oven ramping rate and CO_2 concentration measurements were better than 1% and 5 ppm, respectively.

To quantitatively compare organic carbon bond strengths between samples, observed thermograms were converted to activation energy (*E*) distributions using a Python package (Hemingway et al., 2017). A regularized inverse method was utilized to estimate the distribution of organic carbon activation energy using serial oxidation. *E* distributions were calculated by finding the inverse solution to a set of parallel, non-isothermal, first-order kinetic decay reactions. *E* reflects the energy required to fully oxidize each carbon atom when exposed to a particular oxidation reaction pathway and is a suitable quantitative proxy for bond strength (Hemingway et al., 2017). The mean value of *E* (μ_E) and the fraction of organic carbon within *E* values higher than 190 kJ mol^{-1} ($f_{E>190}$) were calculated accordingly. Higher μ_E and $f_{E>190}$ values mean the sediment contains more refractory, or less labile organic carbon (Cui et al., 2022).

Rate measurements and modeling of methanogenesis and anaerobic oxidation of methane

Methane concentrations in the headspace of slurry incubations were monitored by gas chromatography throughout the incubation period. Using the known volume and porosity of the slurry, the amounts of dissolved methane were calculated using Henry's law and the Bunsen solubility coefficient (Yamamoto et al., 1976). Methanogenesis rates were then determined by combining the total amounts of methane in the headspace and the liquid phase. After extracting the headspace gas for isotopologue analysis using a gas-tight syringe, the activity of AOM was determined in the remaining slurry.

Each slurry was subsampled into duplicate 12 ml glass crimp vial without headspace. AOM rates were determined by injecting 20 µL of ^{14}C-methane tracer (dissolved in MilliQ water, activity 0.7 kBq, specific activity 185 MBq mmol^{-1}) to each vial. The vials were incubated in the dark for two days at the same temperatures applied to the stock slurries (20 °C). To terminate AOM activity, samples were transferred to 50 ml glass vials filled with 20 ml 5% NaOH. The vials were sealed with rubber stoppers immediately and shaken thoroughly. AOM rates were determined by oven combustion (Treude et al., 2005) and acidification (Joye et al., 2004). Samples were considered active only if the sample value exceeded the control mean + (3 × standard deviation). If a sample value surpassed this threshold, the killed control mean was subtracted from the sample value. Taking into account the dilution factor of the slurry, rates of both methanogenesis and AOM in slurry incubations were normalized to nmol methane per cm^3 undiluted sediment per day, facilitating comparisons with the rates obtained through ex-situ measurements and modeling.

Ex-situ rates of methanogenesis and AOM in sediment cores from the salt marsh and thermokarst lake have been previously published (Pellerin et al., 2022; Lotem et al., 2023; Krause et al., 2024). In brief, rates of methanogenesis, AOM and sulfate reduction in salt marsh sediments were tracked using ^{14}C-labeled methylamine, ^{14}C-labeled methane, and ^{35}S-labeled sulfate, respectively (Krause et al., 2024). Note that the methylamine-based methanogenesis rate should be considered as the hypothetical minimum rate of methane production since methanogenesis rates of other pathways and other methylated compounds were not determined. In thermokarst lake sediments, methanogenesis rates were quantified through ^{14}C-labeled bicarbonate and acetate in short-term incubation, and methane concentration in long-term incubation, while AOM rates were determined by ^{13}C-labeled methane (Pellerin et al., 2022; Lotem et al., 2023).

Ex-situ rates of methanogenesis were not measured for the Santa Barbara and Guaymas Basins. To determine net rates of methane production and consumption, we utilized one-dimensional reaction-transport modeling with the software PROFILE (Berg et al., 1998). Assuming that the depth profiles of methane concentration represent a quasi-steady state, the PROFILE model partitioned the sediment pile into discrete depth intervals (e.g., 1–4 zones), each assigned a constant process rate that best replicated the observed concentration profiles. In this context, transport is exclusively assumed to occur through molecular diffusion—a condition we consider realistic in the deep Santa Barbara Basin where the bottom water is generally hypoxic–anoxic, limiting bioirrigation and bioturbation, and the sediments lack gas bubbles (Sholkovitz and Gieskes, 1971; Li et al., 2009). Porewater methane concentrations at the top and bottom of the modeled depth interval served as boundary conditions. Both measured and modeled volumetric rates are expressed in units of nmol cm^{-3} d^{-1}. The same modeling approach cannot be applied to the deep subsurface sediments from the Guaymas Basin because the methane concentration data become unreliable at methane partial pressure greater than 3–5 bar, and they are affected by outgassing when the drilling cores were retrieved and subsampled (Jørgensen, 2021; Teske et al., 2021). The methane concentrations in the sulfate-rich Carpinteria Salt Marsh sediments, which exhibit little variation, do not allow for the effective determination of a net methanogenesis rate (Fig. S2).

Thermodynamic and kinetic calculations

Molar Gibbs free energies (ΔG) of the three methanogenic catabolisms (reactions 1–3) listed below were computed utilizing in-situ physicochemical data collected down the sampling interval where methane isotopologue composition was analyzed. The reactions are:

$$4H_{2(aq)} + CO_{2(aq)} \rightarrow CH_{4(aq)} + 2H_2O_{(l)} \quad (1)$$

$$4CH_3OH_{(aq)} \rightarrow 3CH_{4(aq)} + CO_{2(aq)} + 2H_2O_{(l)} \quad (2)$$

$$4(CH_3)NH_{2(aq)} + 4H^+_{(aq)} + 2H_2O_{(l)} \rightarrow 3CH_{4(aq)} + CO_{2(aq)} + 4NH_4^+{}_{(aq)} \quad (3)$$

The SUPCRT92 software package was employed to compute the standard state Gibbs free energy (ΔG^0) under in-situ temperature and pressure conditions, with the consideration that all species are assumed to be in aqueous (aq) form (Johnson et al., 1992). Based on previous studies in similar environments, we assume that the sulfate-free deep-sea sediments were dominated by hydrogenotrophic methanogenesis (Oremland and Taylor, 1978; Beulig et al., 2018), whereas methylotrophic methanogenesis is the primary pathway in the sulfate-rich salt marsh (Oremland and Polcin, 1982; Krause and Treude, 2021). For hydrogenotrophic methanogenesis, our calculations utilized measured concentrations of CO_2 derived from alkalinity and pH data (Lewis and Wallace, 1998). For methylotrophic methanogenesis, we used methanol and methylamine as examples. The concentrations of methanol and methylamine at the Carpinteria Salt Marsh were found to be detectable (>3 μM) but fell below quantification limit (10 μM) (Krause et al., 2024). Consequently, a range of 3–10 μM for methanol and methylamine was employed in the calculations, along with the measured concentrations of other species (CH_4, CO_2, NH_4^+, and pH). Activities were determined by multiplying the concentrations of reactants and products by their respective activity coefficients (Amend and LaRowe, 2019). Given our assessment of two disproportionation reactions, the values of ΔG, where $\Delta G = \Delta G^0 + RT \ln Q$, are presented in units of kJ/mol-carbon-transferred, or kJ mol^{-1} C, facilitating standardized energetic comparisons (Bojanova et al., 2023). Note that we did not attempt to calculate ΔG values for incubation experiments due to the potential concurrent production of methane through multiple methanogenic pathways. To compare the methanogenic data in this study with published AOM data, the published

AOM isotopologue data were averaged (Giunta et al., 2022; Liu et al., 2023) and presented with a published ΔG value of 11 kJ mol^{-1} C with respect to hydrogenotrophic methanogenesis (Dale et al., 2008). In reality, anaerobic methanotrophic archaea oxidize methane through direct electron transfer rather than hydrogen gas (McGlynn et al., 2015; Wegener et al., 2015). Therefore, we consider the ΔG value of 11 kJ mol^{-1} C as a rough estimate, which should be regarded as the hypothetical minimum ΔG value.

We calculated the kinetic driving force of AOM ($F_{K,AOM}$) to further constrain the depth of potential AOM activity in the Santa Barbara Basin. The $F_{K,AOM}$ for both sulfate and methane was computed using the general Michaelis–Menten model, governing substrate uptake by microorganisms, with the following equation (Jin and Bethke, 2002):

$$F_{K,AOM} = ([CH_4] / (K_{CH4} + [CH_4])) \times ([SO_4^{2-}] / (K_{SO42-} + [SO_4^{2-}])). \quad (4)$$

Here, $[CH_4]$ represents the methane concentration, $[SO_4^{2-}]$ is the sulfate concentration, and K_{CH4} and K_{SO42-} are half-saturation constants (K_M) for methane and sulfate, respectively. Laboratory experiments suggest that K_M values for methane during sulfate-dependent AOM are in the mM range, while those for sulfate are in the sub-mM range (Nauhaus et al., 2002; Wegener and Boetius, 2009). Therefore, we adopted a K_{CH4} of 10 mM and a K_{SO42-} of 0.1 mM for our calculations (Beulig et al., 2019). The $F_{K,AOM}$ values were normalized to the highest $F_{K,AOM}$ in a given core, yielding dimensionless values ranging from 0 (complete kinetic inhibition) to 1 (no inhibition).

Doubly substituted isotopologue measurements and isotope notation

Methane isotopologue abundances of methane gas samples were measured using the Panorama (Nu Instruments) high-mass-resolution gas-source IRMS housed at University of

California, Los Angeles. Details surrounding the purification and measurement of methane gas were previously published (Young et al., 2016; Young et al., 2017) and are briefly summarized here. Methane sample gases were purified on a vacuum line interfaced with a gas chromatograph (GC). Samples were delivered to the vacuum line through a septum by a gas-tight syringe and trapped on silica gel at liquid nitrogen temperature. The helium carrier gas was then used to flush the sample to the GC. Separation was accomplished with a 3-meter 1/8-inch OD stainless steel column packed with 5 Å molecular sieve, followed in series by a 2-meter 1/8-inch OD stainless steel column packed with HayeSep D porous polymer. Peaks were identified using an in-line, passive thermal conductivity detector (TCD). Once methane collection was complete, the sample was transferred to an evacuated sample tube filled with silica gel at liquid nitrogen temperature. Methane in this tube was introduced to the inlet of the mass spectrometer where it was warmed to 40 °C and expanded into the bellow of the instrument.

The Panorama mass spectrometer was set to a mass resolving power of ~40,000 or greater, allowing the measurement of ion currents for resolved $^{12}CH_4^+$, $^{13}CH_4^+$, $^{12}CH_3D^+$, $^{13}CH_3D^+$, and $^{12}CH_2D_2^+$. Isotopologues of masses 16 and 17 were measured using Faraday collectors with amplifier resistors of 10^{11} Ω. Both doubly substituted mass-18 isotopologues, $^{13}CH_3D^+$ and $^{12}CH_2D_2^+$, were measured with an electron multiplier as the axial collector. The measured ratios of these ion currents yield values for bulk $^{13}C/^{12}C$ and D/H as well as for both $\Delta^{13}CH_3D$ and $\Delta^{12}CH_2D_2$. The isotopic compositions of carbon and hydrogen are reported as deviations from the carbon and hydrogen reference materials Vienna Pee Dee Belemnite (VPDB) and VSMOW. Standard delta notation is used to express the fractional differences in per mil units:

$$\delta^{13}C = [(^{13}C/^{12}C)_{sample}/(^{13}C/^{12}C)_{VPDB} - 1] \times 1000 \quad (5)$$

$$\delta D = [(D/H)_{sample}/(D/H)_{VSMOW} - 1] \times 1000. \quad (6)$$

The relative abundances of the two mass-18 isotopologues of methane are reported relative to the stochastic reference frame expressed in per mil using the capital delta notation:

$$\Delta^{13}CH_3D = [(^{13}CH_3D\ /^{12}CH_4)_{sample}/(^{13}CH_3D\ /^{12}CH_4)_{stochastic} - 1] \times 1000 \quad (7)$$

$$\Delta^{12}CH_2D_2 = [(^{12}CH_2D_2/^{12}CH_4)_{sample}/(^{12}CH_2D_2/^{12}CH_4)_{stochastic} - 1] \times 1000. \quad (8)$$

External precision for $\delta^{13}C$, δD, $\Delta^{13}CH_3D$, and $\Delta^{12}CH_2D_2$ is approximately 0.1‰, 0.3‰, 0.3‰ and 0.7‰, respectively (1σ), based on replicate samples. The relationship between temperature and both $\Delta^{13}CH_3D$ and $\Delta^{12}CH_2D_2$ has been predicted through *ab initio* calculations and can be expressed by the following equations (Young et al., 2017):

$$\Delta^{13}CH_3D\ (T) \approx 1000\ \ln(1 + 0.0355502/T - 433.038/T^2 + 1270210.0/T^3 - 5.94804 \times 10^8/T^4 + 1.196630 \times 10^{11}/T^5 - 9.07230 \times 10^{12}/T^6) \quad (9)$$

$$\Delta^{12}CH_2D_2\ (T) \approx 1000\ \ln(1 + 0.183798/T - 785.483/T^2 + 1056280.0/T^3 + 9.37307 \times 10^7/T^4 - 8.919480 \times 10^{10}/T^5 + 9.901730 \times 10^{12}/T^6) \quad (10)$$

where T is in Kelvin. Eqs. (9) and (10) show that $\Delta^{13}CH_3D$ and $\Delta^{12}CH_2D_2$ values are both positive when methane is formed at thermodynamic equilibrium, and approach 0‰ at high temperatures (>1000 K).

Modeling of methanogenesis and anaerobic oxidation of methane

As of now, modeling efforts in methanogenesis have predominantly concentrated on the hydrogenotrophic pathway. This focus arises from the fact that methane generated through acetoclastic and methylotrophic methanogenesis inherits clumping signals from precursor organic substrates, the analysis of which has only recently been developed (Lloyd et al., 2021). We

incorporated metabolic-isotopic and isotopologue flow network models from two recent studies on hydrogenotrophic methanogenesis into our dataset without modification (Gropp et al., 2022; Ono et al., 2022). Therefore, the modeling output is intended solely to depict a subset of our dataset, encompassing Santa Barbara and Guaymas Basin samples, on-site methane from the subsurface of Alaska thermokarst lakes, and Carpinteria salt marsh incubations with an H_2 headspace.

Further, we utilized a closed-system steady-state model to comprehend the concurrent methanogenesis and AOM in the incubation of Guaymas Basin slurry (Haghnegahdar et al., 2017; Liu et al., 2023). In this model, the time-dependent evolution of the moles of an isotopologue of methane can be described in terms of a constant rate of production and a rate of oxidation that behaves as a first-order reaction with an invariable rate constant. In this simplest model, where the balance is only between production and consumption, the system can be described as:

$$\frac{dn_i}{dt} = E_i - k_i n_i , \tag{11}$$

where n_i is the moles of the isotopic species of interest, E_i is the source term for i (e.g., rate of methanogenesis), and k_i is the rate constant for the sink i (i.e., the rate constant for oxidation). The solution to Eq. (11) yields:

$$n_i(t) = n_i^0 \mathrm{e}^{-k_i t} + \frac{E_i}{k_i}\left(1 - \mathrm{e}^{-k_i t}\right) , \tag{12}$$

where n_i^0 is the initial moles of i. The moles of species i at steady state is obtained by evaluation Eq. (12) where $t \to \infty$, and thus $e^{-k_i t} \to 0$, yielding:

$$n_i(t \sim \infty) = \frac{E_i}{k_i} . \tag{13}$$

Considering *i* to be the major isotopologue, the steady-state amount of methane is controlled by the ratio of the production rate and the rate constant for oxidation. The steady-state ratio of two isotopologues can therefore be expressed as:

$$\frac{n_j(t \sim \infty)}{n_i(t \sim \infty)} = \frac{E_j}{E_i}\frac{k_i}{k_j} \tag{14}$$

where n is the moles of the two isotopologues i and j. The steady-state isotopologue ratio depends on the isotopologue ratio of the methane produced (E_j/E_i) and the reciprocal of the fractionation due to oxidation (k_i/k_j), independent of the absolute rates. The ratio of the steady-state moles to initial moles of methane, $(E/k)/n_0$, was determined by assessing the changes in methane concentrations within the bottles. Methane accumulation was observed in the Guaymas Basin slurry without initial methane, while methane consumption was noted in the slurry containing a methane headspace. These observations indicate net methanogenesis and net AOM occurring in the respective incubations. The ratio $(E/k)/n_0$ was set to 500 and 0.2, respectively, based on measured methane concentrations. We set the clumped isotopologue fractionation factors ${}^{13D}\gamma$ and ${}^{D2}\gamma$ to be 0.985 and 0.912, respectively, as defined and reported in Liu et al. (2023). The bulk isotope fractionation factors, ${}^{13}\alpha$ and ${}^{D}\alpha$, were set to be 0.962 and 0.738, respectively, through the fitting of measured data. These values fall within the range established by previous studies (Holler et al., 2009). The steady-state clumped isotopologue compositions are solely controlled by ${}^{13D}\gamma$ and ${}^{D2}\gamma$, while ${}^{13}\alpha$, ${}^{D}\alpha$ and $(E/k)/n_0$ only contribute to shaping the curvature of the trajectory toward the steady state (Liu et al., 2023). We note that in the slurry containing a methane headspace, the source term includes both the tank methane added at the beginning of the incubation and the newly produced methane by methanogens throughout the incubation. We simplify the system with

a single effective source term, *E*, characterized by isotopologue compositions predominantly from the tank methane, albeit with caveats.

Supplementary Text

Methanogenic pathways in Carpinteria Salt Marsh sediments

In sulfate-depleted marine sediments, methane is generated through two primary pathways: the reduction of CO_2 with H_2 as the electron donor (hydrogenotrophic methanogenesis) and the disproportionation of acetate (acetoclastic methanogenesis) (Rudd and Taylor, 1980; Conrad, 1999). Methanogens are not able to effectively compete with sulfate-reducing bacteria for common substrates, especially H_2 and acetate (Oremland and Taylor, 1978). The free energy available from sulfate reduction exceeds that of methane production in the sulfate zone (Froelich et al., 1979). While hydrogenotrophic and acetoclastic methanogenesis are largely inhibited in the sulfate-reducing zone, methylotrophic methanogenesis is known to occur in this zone. It is well established that methylated compounds, such as methylamine and methanol, are important non-competitive substrates for methanogenesis in the presence of sulfate reduction (Oremland and Polcin, 1982; Maltby et al., 2016; Zhuang et al., 2018).

As a result, methylotrophic methanogenesis was suggested to be the predominant pathway for methane production in the sulfate-reducing sediments within the Carpinteria Salt Marsh (Krause and Treude, 2021; Krause et al., 2024). Indeed, elevated methanogenesis rates, determined using ^{14}C-methylamine radiotracer, were observed in the upper 5 cm of sediments, coinciding with the peak in sulfate reduction rates (Fig. S2). We suggest that the contributions of hydrogenotrophic and acetoclastic methanogenesis are negligible (Xiao et al., 2018; Zhuang et al., 2018). It is

important to acknowledge that the methanogenesis rates derived from ^{14}C-methylamine only represent a fraction of the methylotrophic methanogenesis rates, likely underestimating the gross methanogenesis rates since methanogenesis from other methylated compounds is not taken into account.

In investigating the isotopologue effects of the three methanogenic pathways, we introduced H_2, acetate and methylamine to slurries incubations of the salt marsh sediments. Incubations with methylamine exhibited the highest methanogenesis rates, reaching approximately 3000 nmol cm^{-3} d^{-1}, consistent with the ongoing natural methylotrophic methanogenesis. Methanogenesis rates in H_2 incubations varied from 37 to 197 nmol cm^{-3} d^{-1}, while rates in acetate incubations were two orders of magnitude lower than those in H_2 incubations, indicating the minor significance of acetoclastic methanogenesis in the investigated salt marsh sediments. This suggests that either the sediments lack the requisite microorganisms capable of utilizing acetate for methanogenesis, or the acetate was used for other processes. Therefore, we argue that introducing molybdate and H_2S to sediment slurries mostly stimulates hydrogenotrophic but not acetoclastic methanogenesis, complementing the concurrently occurring methylotrophic methanogenesis. Methane produced in molybdate incubations aligns with the mixing lines between the methylotrophic and hydrogenotrophic end-members (Fig. S4), providing additional support for our interpretation.

Methanogenesis evolution in $\Delta^{13}CH_3D$ vs. $\Delta^{12}CH_2D_2$ space for Alaska lake incubations

In addition to the depth-dependent evolution of isotopologue compositions discussed in the main text, we explored time-dependent changes in the same sediment incubations in $\Delta^{13}CH_3D$ vs.

$\Delta^{12}CH_2D_2$ space. The sediments from units 2 and 4 of the Big Trail Lake were incubated from 2020 to 2022, and the headspace was collected before purging it with argon. Subsequently, the same sediments underwent another two years of incubation under identical conditions. The newly generated methane exhibited $\Delta^{12}CH_2D_2$ values less negative than those in the initial incubation, indicating a trajectory towards equilibrium (Fig. S5). We propose that this shift reflects the aging of organic matter, resulting in a diminished availability of the labile fraction over time. The four-year time scale is comparable to the age of this thermokarst lake (50–70 years) (Walter Anthony et al., 2018). Before the lake formed between 1949 and 1967, the sediments existed as permafrost, retarding the degradation of organic matter under frozen conditions until the sediments eventually thawed (Pellerin et al., 2022).

Based on short-term radiotracer incubations, approximately 43% of methanogenesis in unit 2 occurred through the hydrogenotrophic pathway, with the remaining portion occurring via the acetoclastic pathway (Fig. S3C). In unit 4 at the sediment surface, all methanogenesis followed the acetoclastic pathway (Fig. S3C). However, the isotopologue compositions of methane from the two units exhibit only minor differences (Fig. S5). Two possible explanations arise: first, isotopologue values may not be entirely indicative of the metabolic pathways of methanogenesis in certain natural environments (Gruen et al., 2018). Second, the occurrence of methylotrophic methanogenesis in the lake sediments cannot be ruled out, as the short-term incubation did not consider the role of methyl compounds (Pellerin et al., 2022). Collectively, the thermokarst lake sediments demonstrate a transition from acetoclastic to hydrogenotrophic methanogenesis downcore, with potential involvement of methylotrophic methanogenesis. Due to the intricate biogeochemical cycling of methane at this site, calculations for Gibbs free energy were not pursued.

Evaluation of Gibbs free energies at the marine sites

In marine sediments, methanogenesis starts in the absence of sulfate at a subsurface depth where the buried organic matter has become notably recalcitrant to microbial degradation. As a result, it is well established that hydrogenotrophic methanogenesis predominates in marine sediments (Oremland and Taylor, 1978; Crill and Martens, 1986; Whiticar et al., 1986; Beulig et al., 2018). To assess the Gibbs free energies at the two marine settings, porewater H_2 concentrations were determined using two distinct methods. H_2 concentrations were measured using a headspace equilibration technique for the Santa Barbara Basin sediments (Hoehler et al., 1998), whereas an extraction method was applied to the Guaymas Basin sediments (Lin et al., 2012; Teske et al., 2021). Each method has its advantages and drawbacks, but the extraction method was found to yield higher H_2 concentrations compared to the headspace equilibration technique (Lin et al., 2012). Therefore, the ΔG values at the two sites are observed in distinct ranges (Table S3). Recognizing that this variation could stem from technique-related challenges, we propose considering the higher range, ranging from −22.6 to −14.7 kJ mol^{-1} C, as hypothetical maximum values. This implies that hydrogenotrophic methanogenesis was exergonic beneath the SMTZ and was close to the suggested energetic limit of methanogenic archaea, which falls between −10 to −20 kJ mol^{-1} C (Hoehler et al., 1998). Using the lower range from −36.2 to −25.1 kJ mol^{-1} C as hypothetical minimum values, they are half of the ΔG values calculated for the salt marsh sediments (Table S3). This indicates a notable difference in the thermodynamic driving force between salt marsh and deep-sea sediments.

Comparison of microbial versus non-microbial methane in the Guaymas Basin

Guaymas Basin is characterized by high heat flow and magmatism, along with rapid deposition of organic-rich sediments (Calvert, 1966; Lonsdale and Becker, 1985). Magmatism, in the form of sill intrusions into sediments, provides transient heat sources that mobilize buried sedimentary organic material, leading to the formation of thermogenic methane and other hydrocarbons (Einsele et al., 1980). The sedimentary carbon also serves as potential microbial substrates, fostering the production of microbial methane in sediments with lower temperatures (Teske et al., 2014). To investigate the formation mechanism of methane under varying geothermal gradients, we analyzed the isotopologue compositions of methane collected from two drilling cores within the Basin.

At Site U1550, the in-situ temperatures varied from 16 to 31 °C across the sampling depths for methane clumping analysis (Fig. S11C). The notably high $C_1/(C_2+C_3)$ ratios, ranging from 630–4022, along with low apparent temperatures derived from $\Delta^{13}CH_3D$ (40–62 °C), suggest that microbial methanogenesis predominantly contributes to methane formation at relatively low temperatures (Figs. S11 and S12). The negative ΔG values, approximately −30 kJ mol^{-1} C, further support the occurrence of hydrogenotrophic methanogenesis (Table S3). Functional gene sequencing has detected functionally and phylogenetically diverse methanogens at Site 1550, including members of the *Methanosaetaceae*, *Methanosarcinaceae*, *Methanobacteraceae*, and uncultured lineages (Hinkle et al., 2023). Essential genes for methanogenic archaea are expressed in sediments from this site (Mara et al., 2023). Site U1550, along with other microbial gases characterized by elevated $C_1/(C_2+C_3)$ ratios (Fig. S12), is discussed in detail in the main text.

On the contrary, Site U1547 displayed notably higher in-situ temperatures, ranging from 55 to 100 °C (Fig. S11F). The $C_1/(C_2+C_3)$ ratios fell within the range of 80 to 142 (Fig. S12), below the typical microbial methane threshold of ~200 (Milkov and Etiope, 2018). Positive values for

ΔG in hydrogenotrophic methanogenesis further exclude microbial contributions from this pathway (Table S3). Recent studies highlight that $\Delta^{13}CH_3D$ values of thermogenic methane gases align with thermodynamic equilibrium at their formation temperatures, whereas a deficit in $\Delta^{12}CH_2D_2$ can occur due to a combinatorial effect (Dong et al., 2021; Xie et al., 2021; Liu et al., 2024). Indeed, clumped isotope analysis of methane unveiled varying levels of disequilibrium in $\Delta^{12}CH_2D_2$ values (Fig. S13). This departure from equilibrium is most prominent at low thermal maturities, and $\Delta^{12}CH_2D_2$ tends to approach equilibrium with increasing maturity (Xie et al., 2021). The apparent temperatures, based on $\Delta^{13}CH_3D$ values, varied between 141 and 239 °C, falling within the thermogenic gas window (Xie et al., 2021). Notably, these temperatures were higher than the in-situ temperatures at the gas sampling location. This suggests that the gases likely originated at greater depths, where methane reached isotopologue equilibrium with the ambient temperature, and subsequently migrated upward to sediments with lower temperatures, where isotope exchange proceeds at a slower rate (Lalk et al., 2023). In summary, methane collected below 80 mbsf at Site U1547 is consistent with a thermogenic origin, although we cannot entirely rule out the possibility of minor mixing with microbial methane at shallower depths (Bojanova et al., 2023). At shallower depths above 74 mbsf, functional gene sequencing at Site 1547 detected members of the *Methanosarcinaceae*, *Methanomicrobiaceae*, and the hyperthermophilic *Methanocaldococcaceae* (Hinkle et al., 2023). Within the same depth horizon, essential genes for methanogenesis remain expressed in Site 1547 sediments (Mara et al., 2023).

Supplementary Figures S1–S13

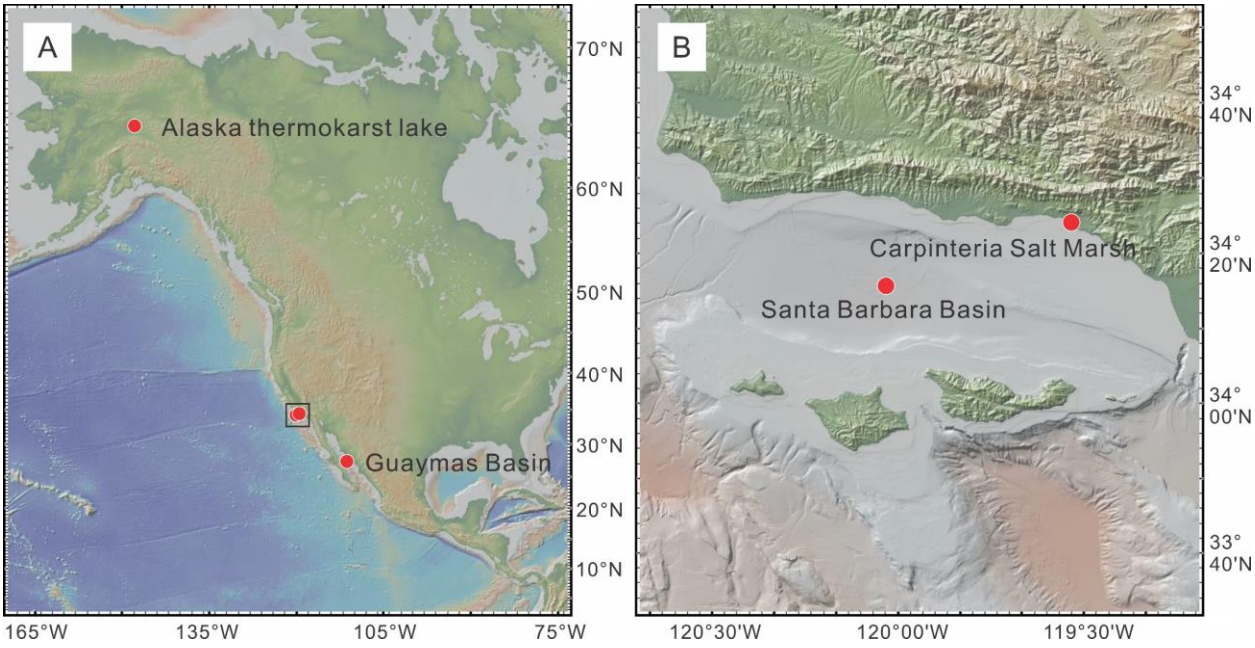

Fig. 4-S1.

Maps with sampling sites. Black box in map A shows location of map B. The maps were generated via GeoMapApp.

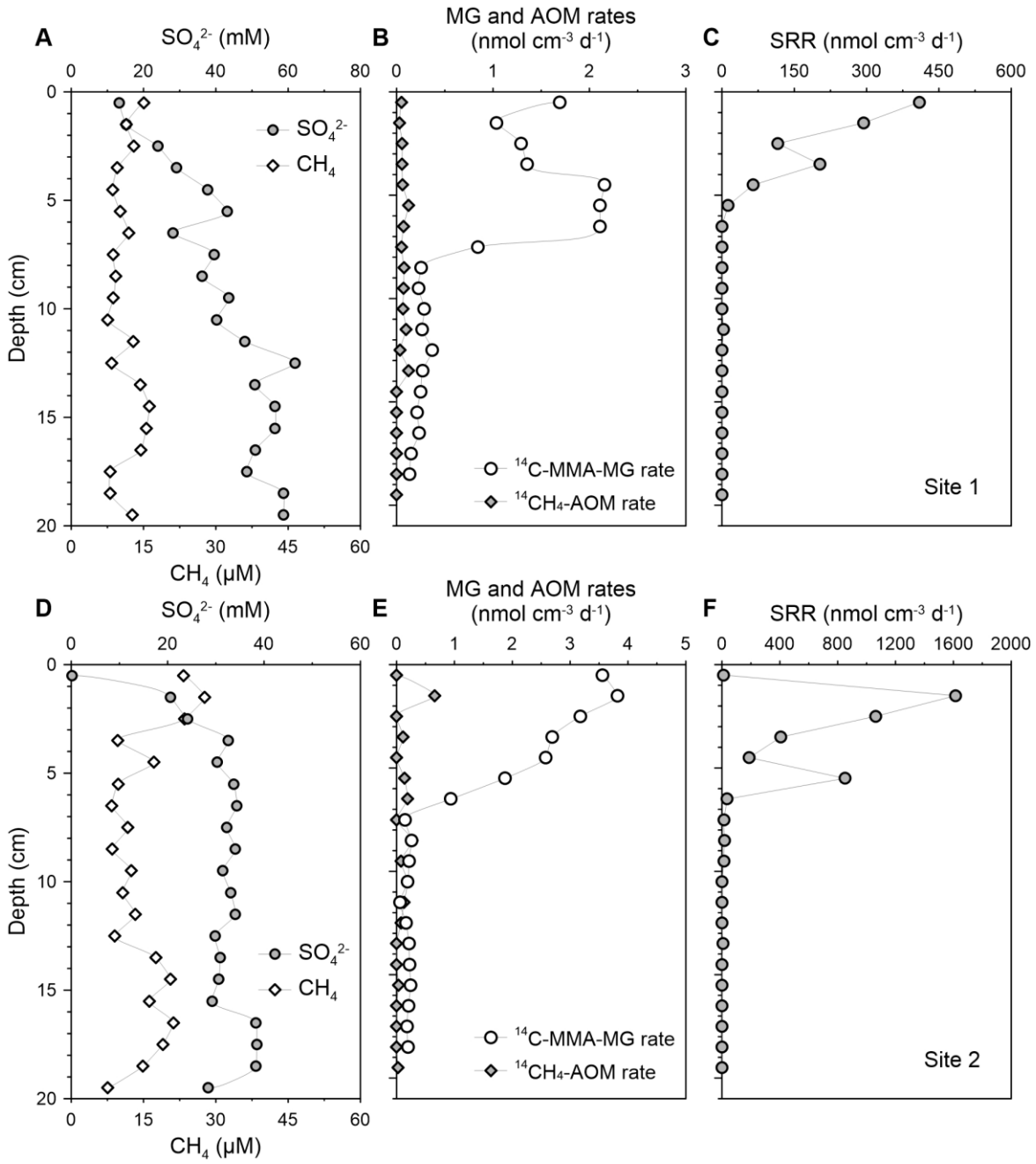

Fig. 4-S2.

Depth profiles of biogeochemical parameters in sediments of two sites within the Carpinteria Salt Marsh. (A, D) Porewater sulfate and methane concentrations. (B, E) Rates of monomethylamine-based methanogenesis (MMA-MG) and AOM determined from direct injection of ^{14}C-MMA and ^{14}C-CH_4, respectively. (C, F) Sulfate reduction rates (SRR) determined from direct injection of

^{35}S-sulfate. The top and bottom panels depict Sites 1 and 2, respectively. Data were adopted from Krause et al. (2024).

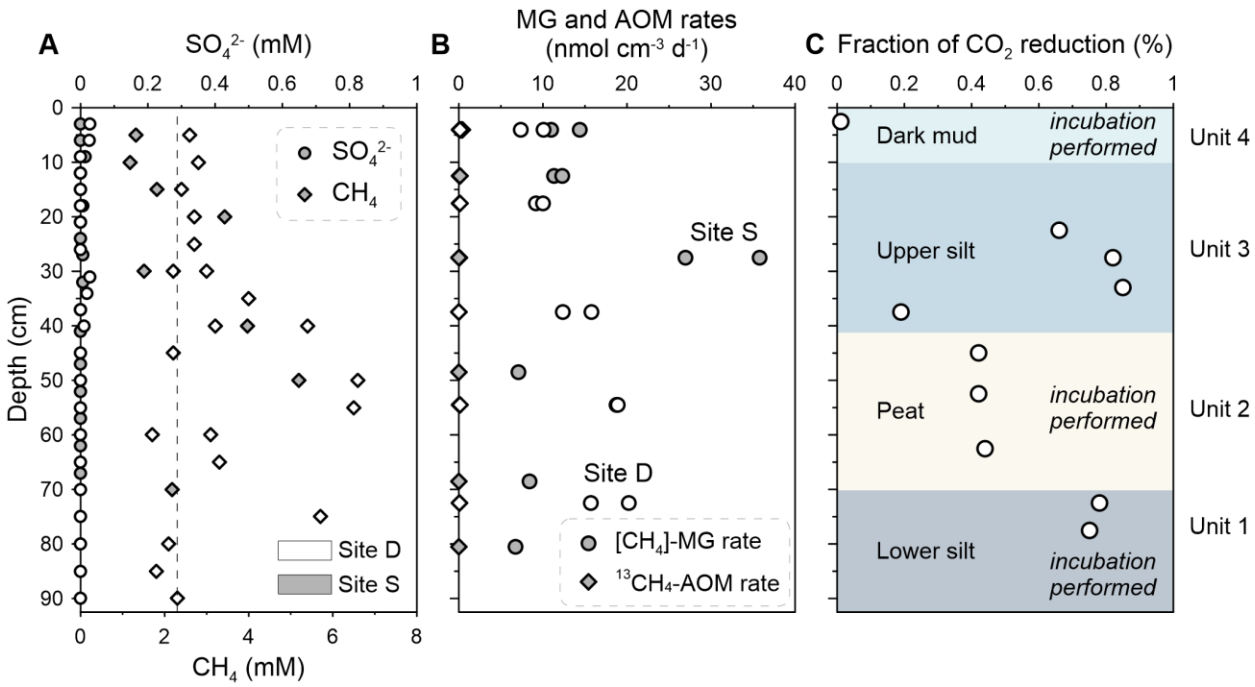

Fig. 4-S3.

Depth profiles of biogeochemical parameters in sediments of two sites within the Big Trail Lake, a thermokarst lake located in Alaska. (A) Porewater sulfate and methane concentrations. The dashed line denotes the concentration of methane saturation at ~4 °C. (B) Rates of methanogenesis and AOM determined from long-term methane concentration analysis and incubation using ^{13}C-CH_4, respectively. (C) The fraction of hydrogenotrophic methanogenesis relative to the total methane production (hydrogenotrophic and acetoclastic methanogenesis) determined from short-term incubation using ^{14}C-labeled bicarbonate and acetate. Data were adopted from Pellerin et al. (2022); Lotem et al. (2023), in which lithological units shown in the background were described.

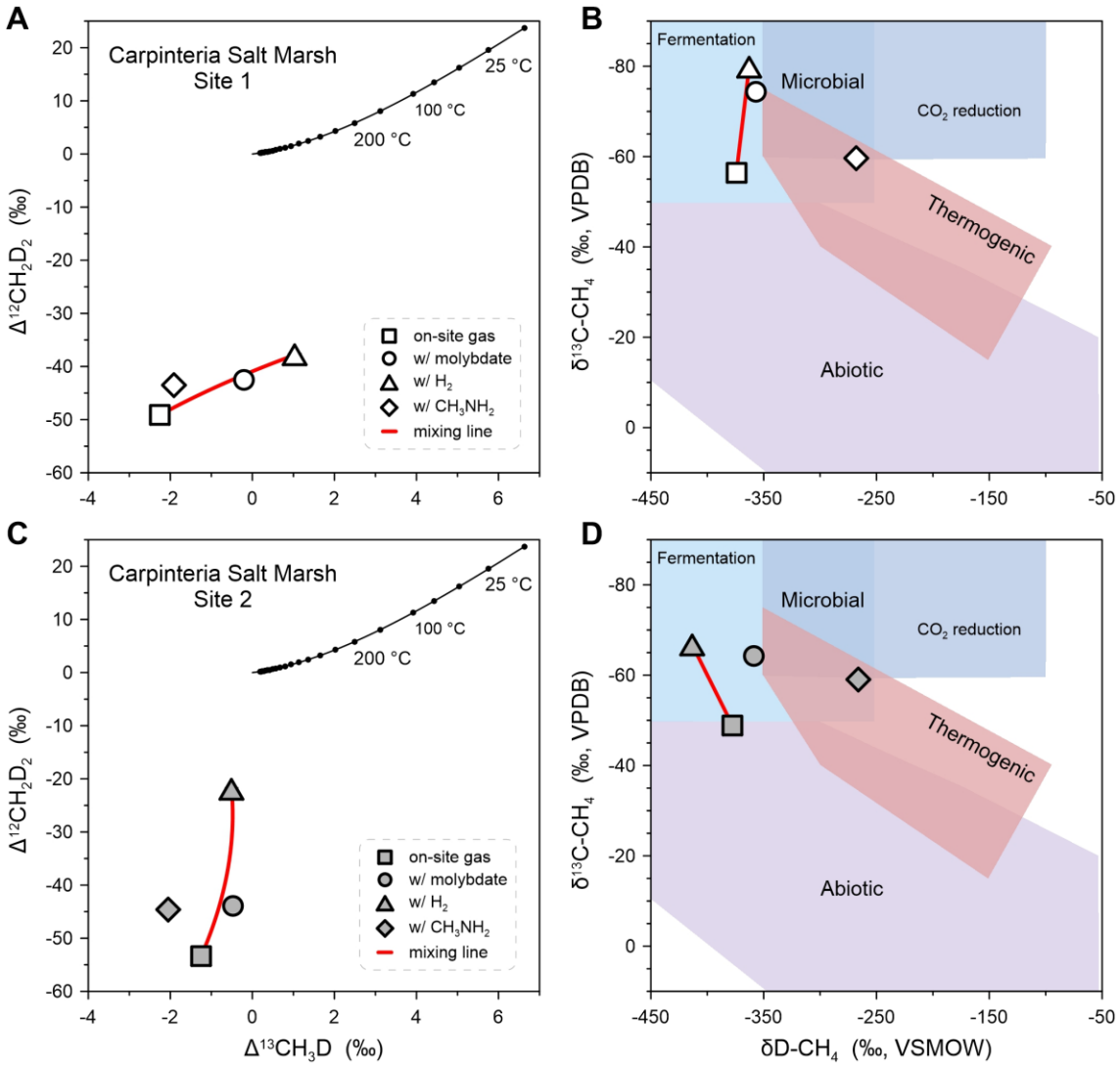

Fig. 4-S4.

Isotopologue compositions of methane samples from the Carpinteria Salt Marsh. (A, C) $\Delta^{13}CH_3D$ plotted against $\Delta^{12}CH_2D_2$. The solid black curve depicts theoretical thermodynamic equilibrium abundances of methane isotopologues, along with corresponding temperatures. The red curves represent mixing lines between the two methanogenic end-members, the methylotrophic and hydrogenotrophic pathways. (B, D) $\delta^{13}C$ plotted against δD. The genetic fields for methane sources follow Whiticar (1999); Milkov and Etiope (2018). The top and bottom panels depict Sites 1 and 2, respectively.

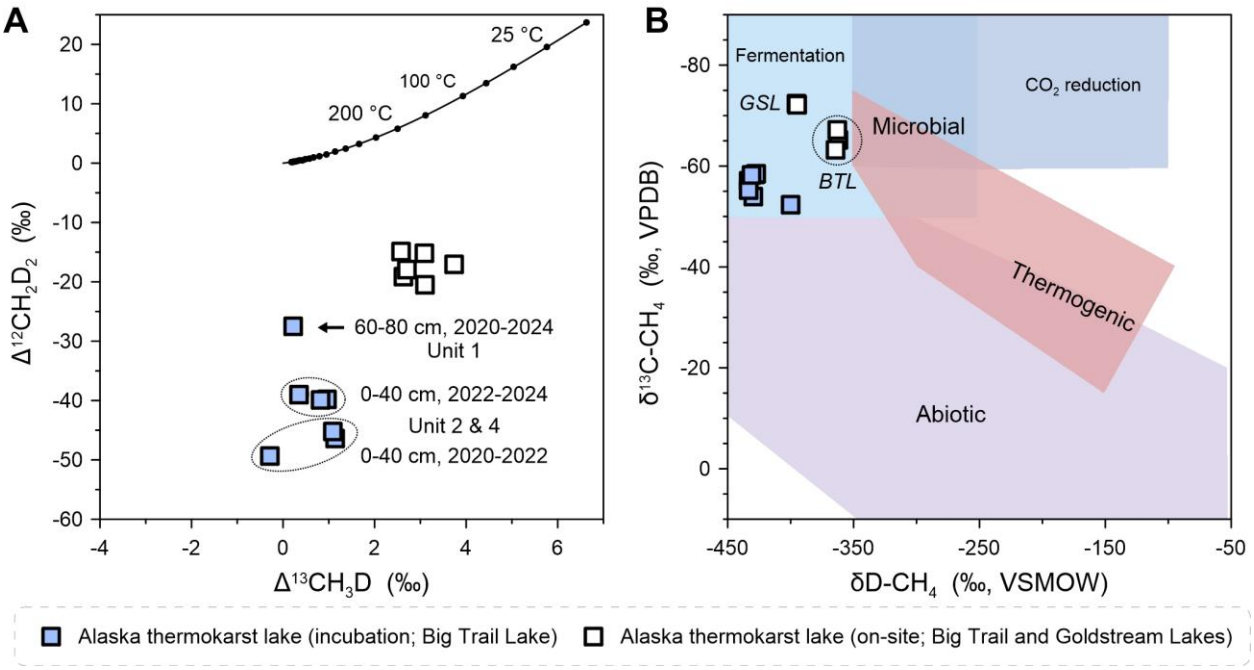

Fig. 4-S5.

Isotopologue compositions of methane samples from the Alaska thermokarst Lakes. Lithological units are shown in Figure S3. The initial incubations for units 2 and 4 extended from 2020 to 2022. The samples from these units underwent argon reflushing in 2022 and were subsequently incubated for another two years. BTL and GSL denote Big Trail Lake and Goldstream Lake, respectively.

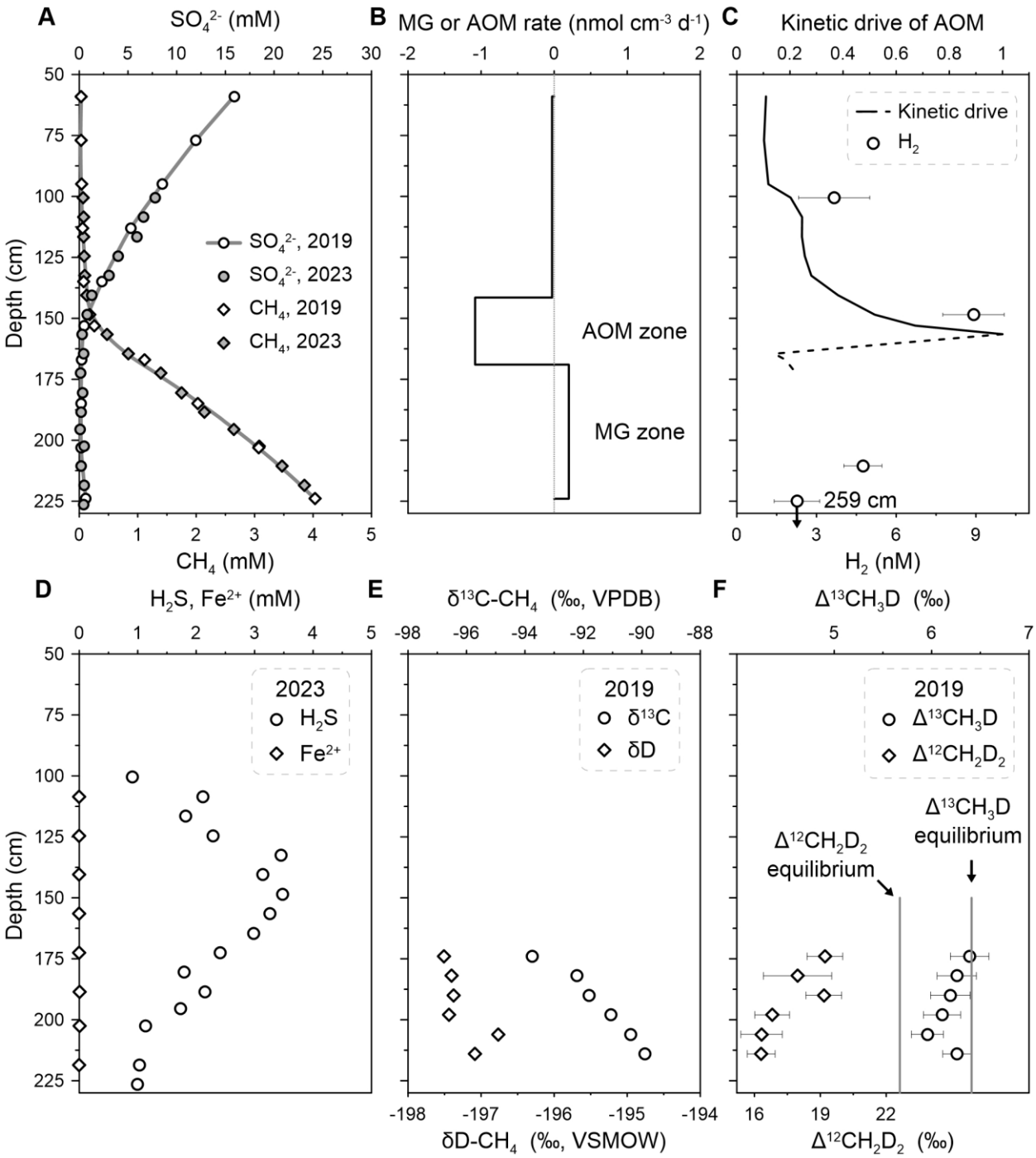

Fig. 4-S6.

Depth profiles of biogeochemical parameters in sediments of Site NDRO within the Santa Barbarba Basin. (A) Porewater sulfate and methane concentrations. The grey line through methane

data represents the model fit to the methane concentration data. (B) Modeled rates of net methanogenesis (MG) and AOM. (C) Kinetic drive of AOM and porewater hydrogen concentration. The solid line was derived from measured sulfate and methane concentrations, while the dashed line was calculated by assuming sulfate concentrations of 0.01 mM below the SMTZ (Pellerin et al., 2018). (D) Porewater aqueous sulfide and dissolved iron(II) concentrations. (E) Bulk isotopic compositions of methane. (F) Clumped isotopologue compositions of methane. The solid grey lines denote equilibrium isotopologue compositions for the in-situ temperature of 6 °C. Error bars are one standard error.

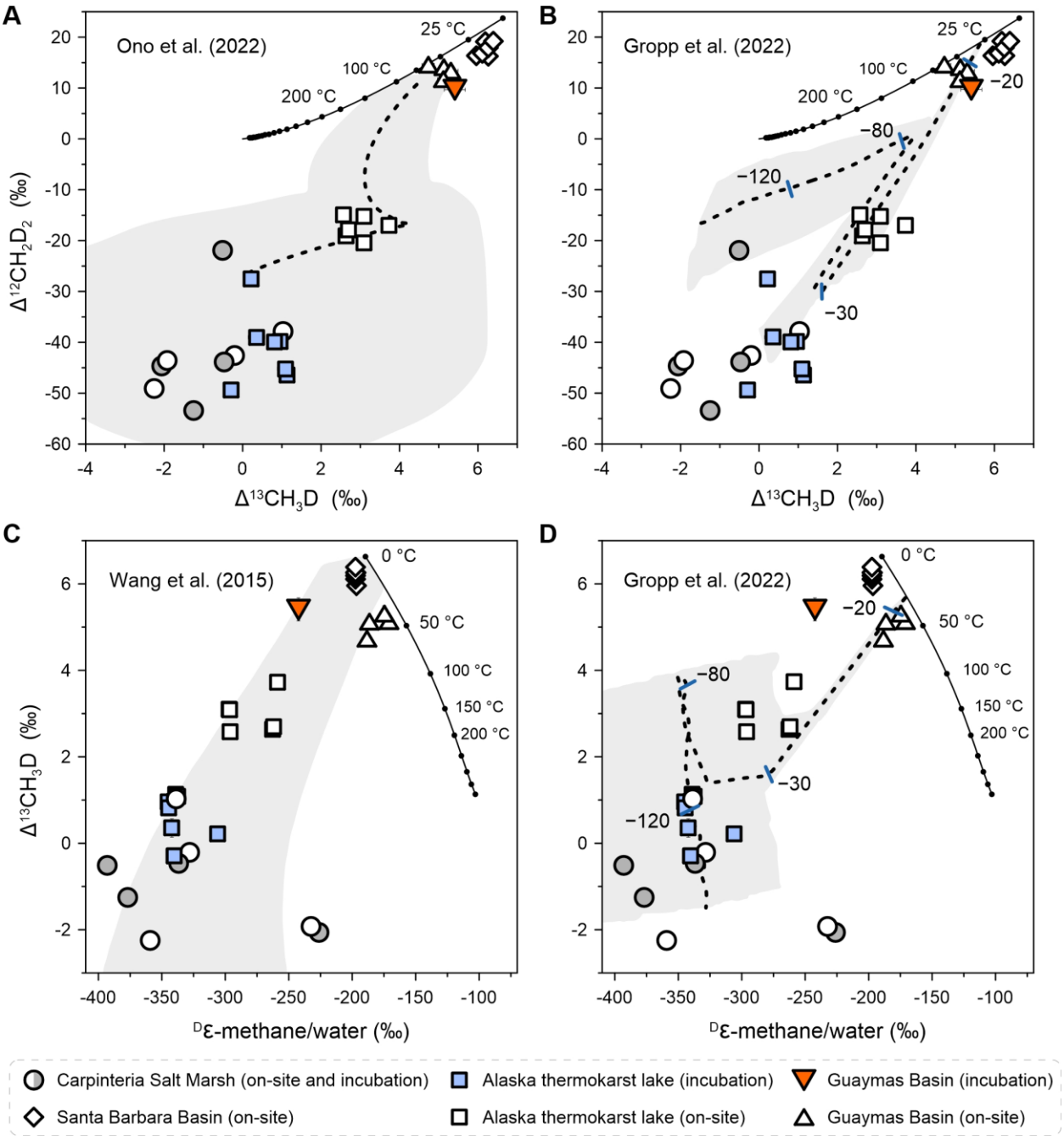

Fig. 4-S7.

Model-observation comparison plotted in $\Delta^{13}CH_3D$ versus $\Delta^{12}CH_2D_2$ (A–B) and $^{D}\varepsilon$-methane/water versus $\Delta^{13}CH_3D$ (C) and $\Delta^{12}CH_2D_2$ (D). The modeling results were redrawn onto the data presented in Figures 1 and 2 (Wang et al., 2015; Gropp et al., 2022; Ono et al., 2022).

Note that the model outputs are only applicable to hydrogenotrophic methanogenesis. The dashed black lines show the median of the simulations. Data from the Carpinteria Salt Marsh are represented by circles, with site 1 shown in white and site 2 in grey. Panels B and D depict simulations without the methylene-H4MPT dehydrogenase enzyme, with tick marks at ΔG_{net} values of −20, −30, −80, and −120 kJ mol^{-1}.

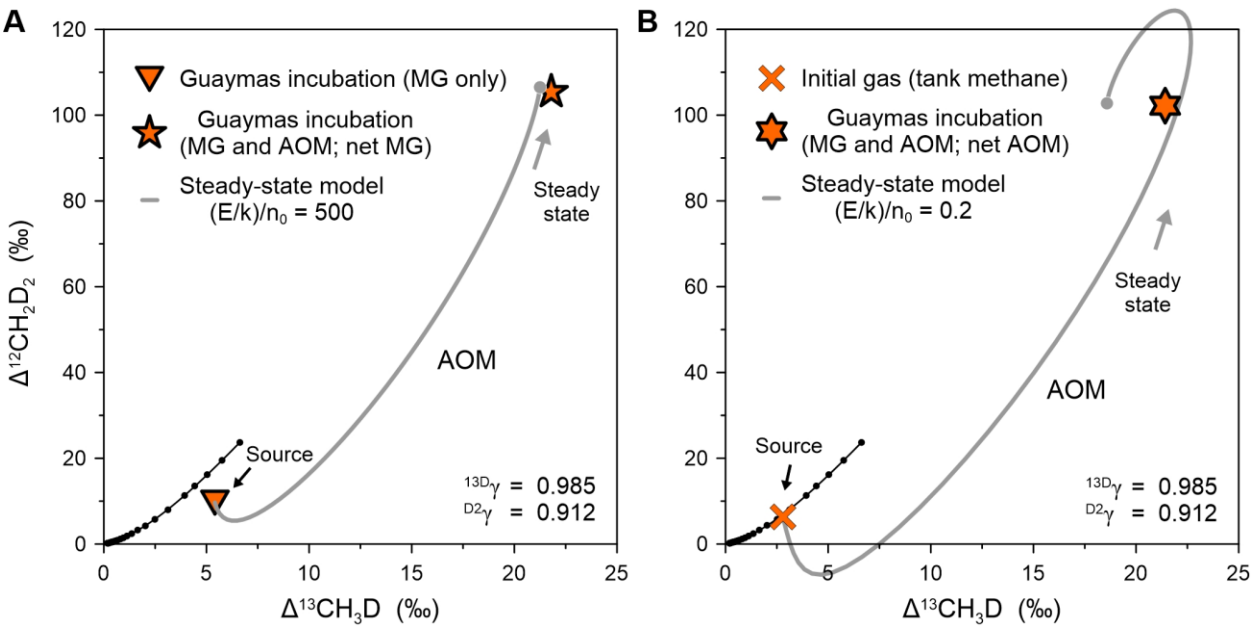

Fig. 4-S8.

Isotopologue compositions of methane samples from the incubations of the Guaymas Basin slurries. In panel A, the orange triangle represents the methane source produced by methanogenesis, while the orange star depicts the resultant methane, reflecting concurrent methanogenesis and AOM leading to net methanogenesis. The incubation began with no methane present in the headspace. In panel B, the cross symbol denotes the methane source of tank methane, while the orange hexagram signifies the resulting methane, reflecting concurrent methanogenesis and AOM leading to net AOM. The incubation started with tank methane (200 kPa) in the headspace. Grey lines depict simulation outputs of the closed-system steady-state model. The clumped isotopologue fractionation factors, adopted from Liu et al. (2023), and the ratio of the steady-state moles to initial moles of methane, $(E/k)/n_0$, used in the model, are shown in each panel.

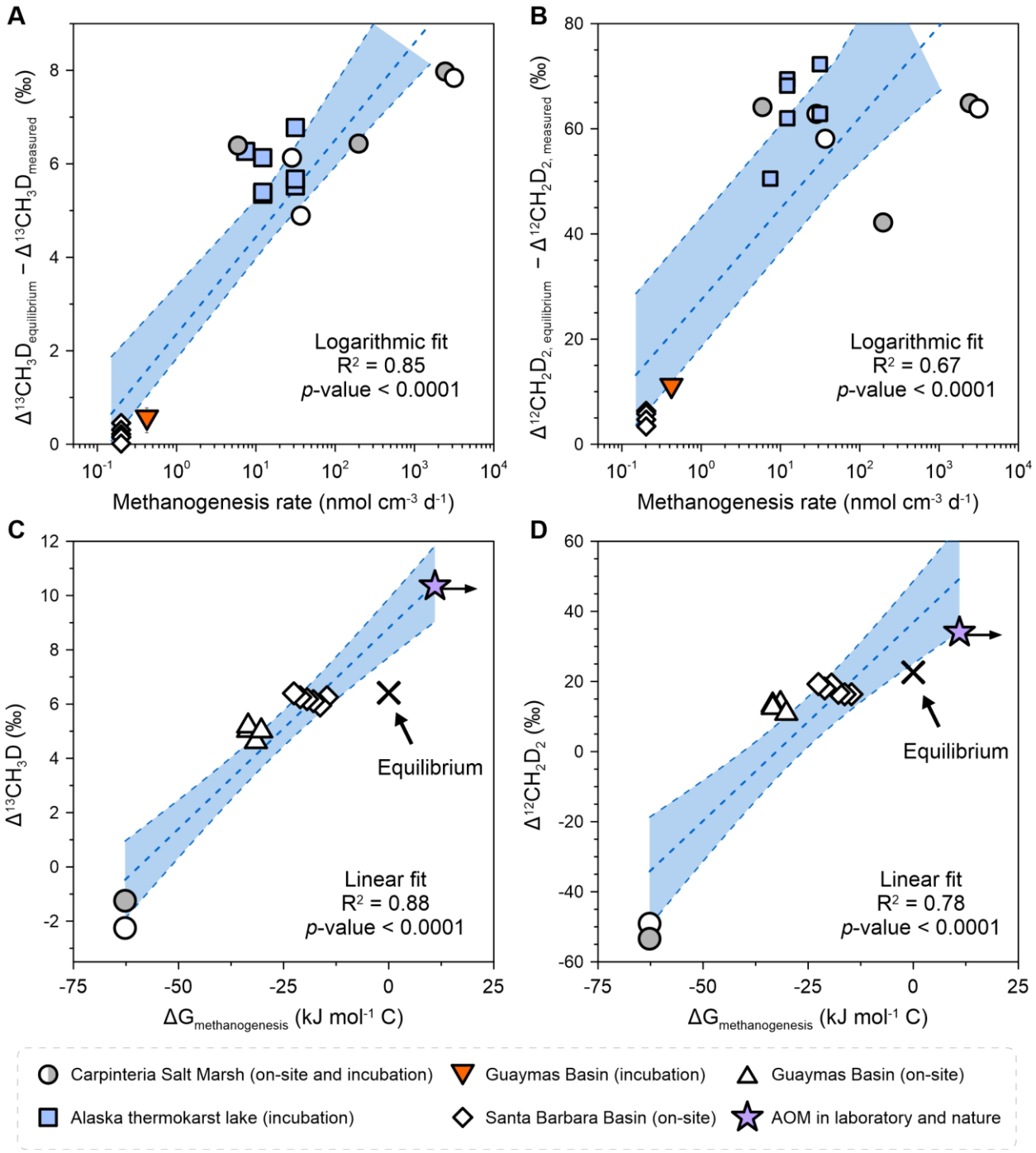

Fig. 4-S9.

Methanogenesis rate (A–B) and Gibbs free energy (C–D) plotted against isotopologue data. Linear regressions are presented with 95% confidence intervals. R-squared and p-values are provided in

each panel. Data from the Carpinteria Salt Marsh are represented by circles, with site 1 shown in white and site 2 in grey. Methanogenesis rates of Alaska thermokarst lake incubations were adopted from Lotem et al. (2023). Methanogenesis rates for on-site methane in the Santa Barbara Basin were determined through modeling based on methane concentration profiles, illustrated in Figure S5B. The departures from isotopologue equilibrium in panels A–B are defined as the difference between equilibrium isotopologue compositions and measured isotopologue compositions at in-situ or incubation temperatures. In panels C–D, the published AOM isotopologue data are averaged (Giunta et al., 2022; Liu et al., 2023) and presented with a published ΔG value of 11 kJ mol^{-1} C with respect to hydrogenotrophic methanogenesis (Dale et al., 2008), offering a conservative estimate. The X markers in panels C–D denote Gibbs free energy of zero and equilibrium isotopologue compositions at 6 °C.

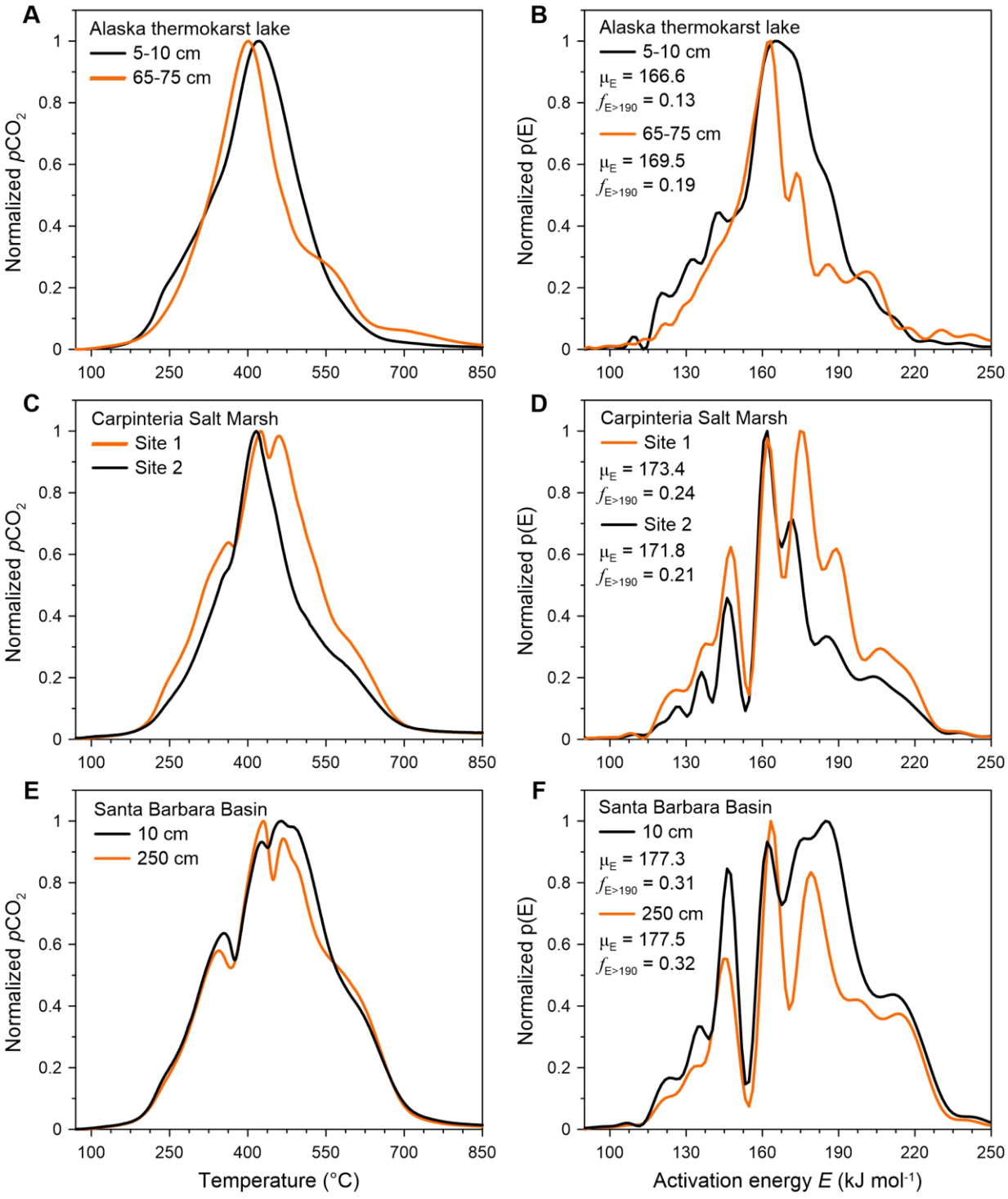

Fig. 4-S10.

Patterns of thermograms and activation energy profiles for the Alaska thermokarst Lake (A–B), the Carpinteria Salt Marsh (C–D), and the Santa Barbarba Basin (E–F) sediments. Mean activation

energy (μ_E) and fractions of organic carbon with activation energy values greater than 190 kJ mol^{-1} (f_E>190; more refractory organic carbon) are shown in panels B, D and F. Ramped pyrolysis/oxidation analysis quantifies the thermochemical stability of organic matter and, therefore, determines the proportion of refractory versus labile organic carbon in sediment.

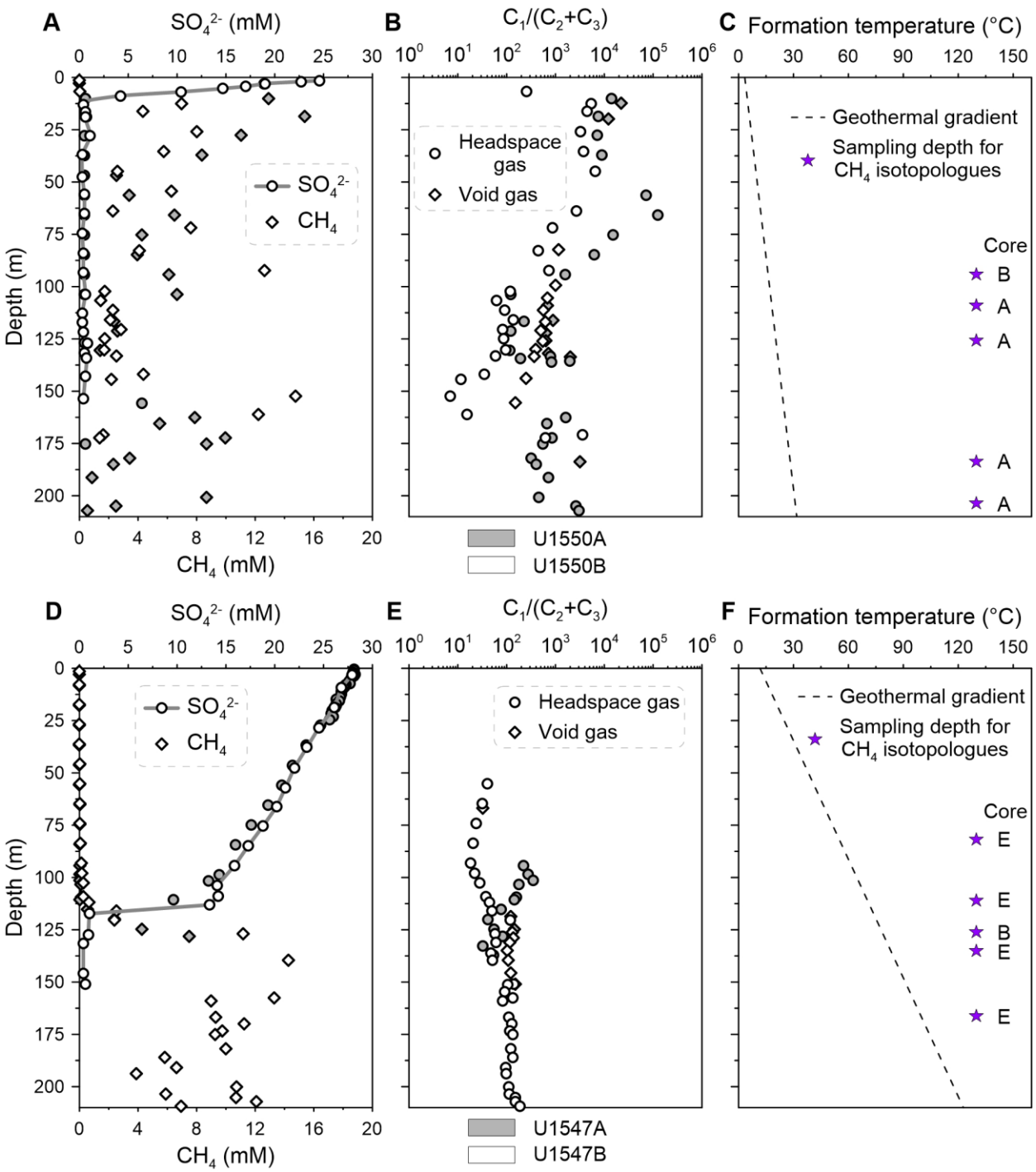

Fig. 4-S11.

Depth profiles of physical and geochemical parameters in sediments of two sites within the Guaymas Basin. (A, D) Porewater sulfate and methane concentrations. (B, E) Ratios of C_1 versus

$C_2 + C_3$. (C, F) Formation temperatures along the drilling cores, accompanied by the depths at which methane samples were analyzed for isotopologue compositions. The top and bottom panels depict Sites U1550 and U1547, respectively. Data were adopted from Teske et al. (2021).

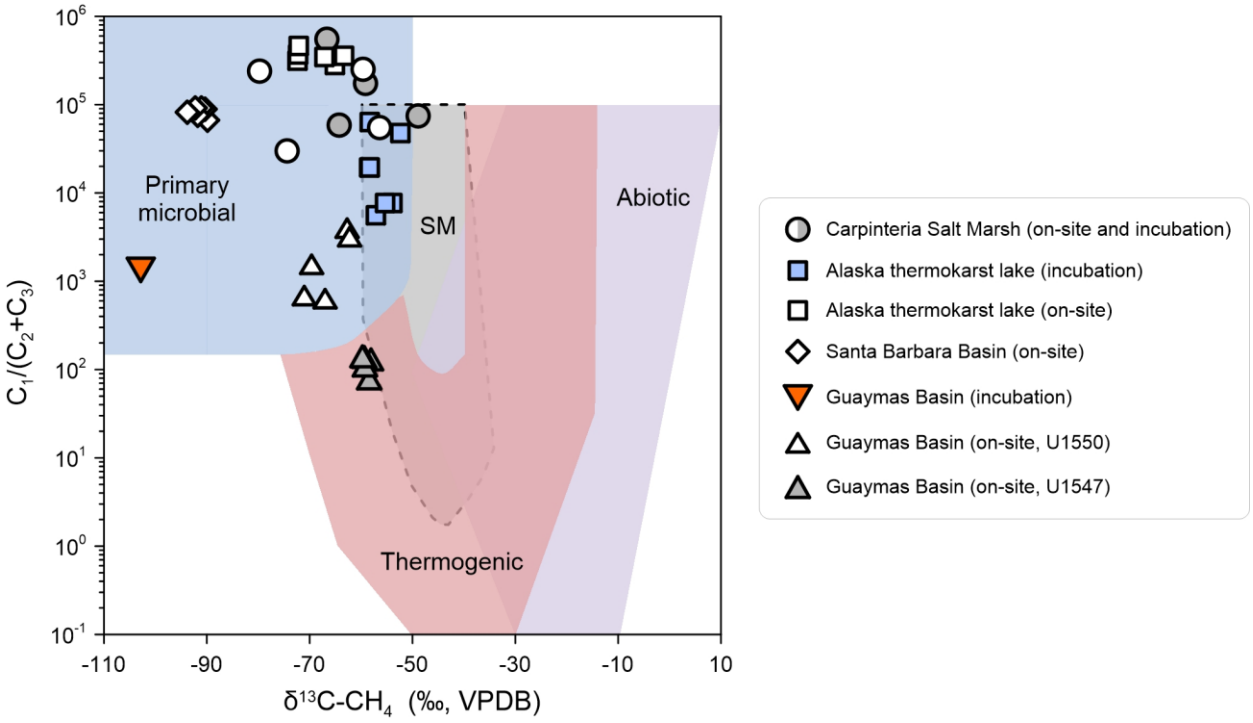

Fig. 4-S12.

$\delta^{13}C_{CH4}$ plotted against $C_1/(C_2 + C_3)$. Genetic fields follow Bernard et al. (1977); Milkov and Etiope (2018). Secondary microbial (SM) field is shown in grey with dashed line. The $C_1/(C_2 + C_3)$ ratios of on-site gas from the Guaymas Basin were adopted from Teske et al. (2021).

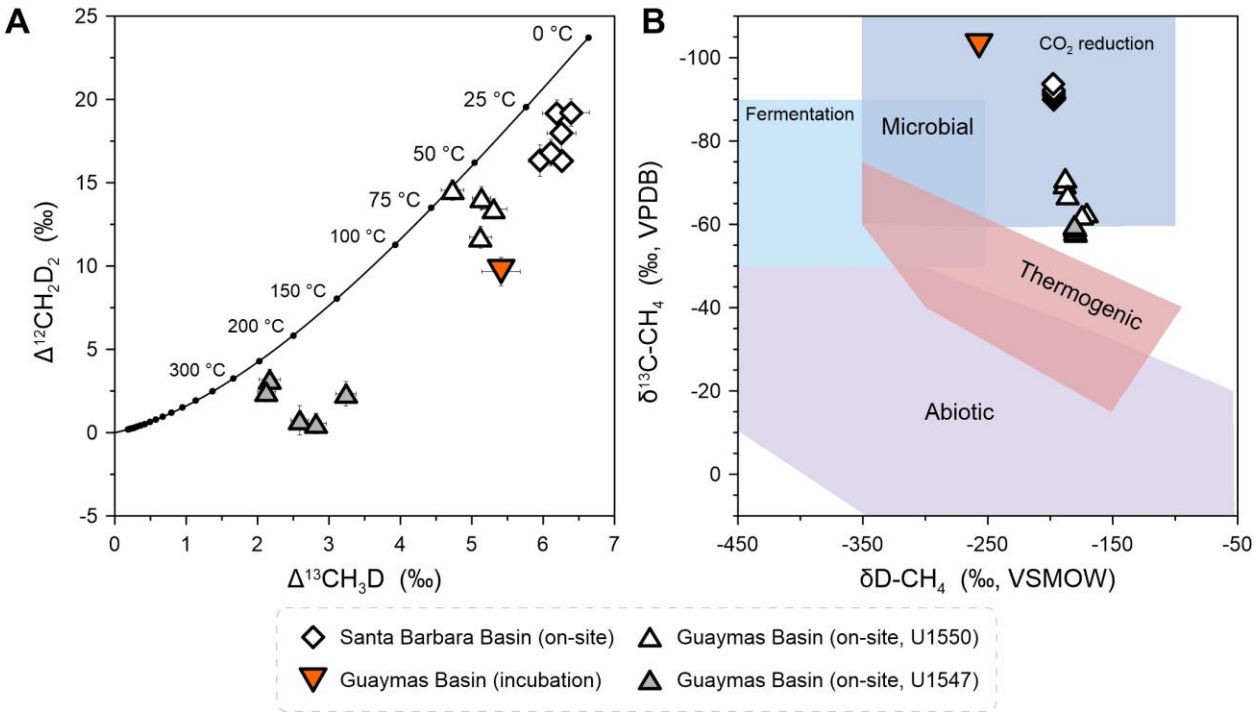

Fig. 4-S13.

Isotopologue compositions of methane samples from deep-sea settings. The same data are presented in Figure 1, alongside non-microbial methane data obtained from Site U1547 in the Guaymas Basin for comparison.

Supplementary Tables S1–S3

Table 4-S1.

Details describing the sampling sites. Data of Alaska Lakes from Walter Anthony et al. (2021); Pellerin et al. (2022). Data of Guaymas Basin Sites U1550 and U1547 from Teske et al. (2021).

Site	Latitude/longitude	Water depth (m)	Temperature (ºC)
Carpinteria Salt Marsh Site 1	34°24'12.8"N/119°32'07.0"W	0.1–0.2*	19†
Carpinteria Salt Marsh Site 2	34°24'10.2"N/119°32'01.6"W	0.1–0.2*	19†
Alaska Big Trail Lake	64°55'09.5"N/147°49'20.1"W	0.6–2.5	4
Alaska Goldstream Lake	64°54'57.6"N/147°50'52.8"W	1.6–3.3	4
Santa Barbara Basin Site NDRO	34°15'43.8"N/120°01'50.0"W	580	6
Guaymas Basin Seep Site	27°24'18.4"N/111°19'17.2"W	1813	20‡
Guaymas Basin Site U1550	27°15'09.6"N/111°30'25.0"W	2001	16–31
Guaymas Basin Site U1547	27°30'24.8"N/111°40'44.1"W	1732	55–100

*Water depth during low tide.

†Sediment temperature during sampling season.

‡Incubation temperature.

Table 4-S2.

Rates of anaerobic oxidation of methane (AOM) in sediment slurry incubations determined by ^{14}C-radiotracer techniques. All these slurries initially had an argon headspace and accumulated methane over time. Mb and H_2S stand for molybdate and aqueous sulfide, respectively.

Site	Amendment	AOM rate (nmol cm^{-3} d^{-1})
Carpinteria Salt Marsh Site 1	with Mb & H_2S	0
Carpinteria Salt Marsh Site 2	with Mb & H_2S	0
Santa Barbara Basin Site NDRO	with Mb & H_2S	0
Guaymas Basin Seep Site	with Mb & H_2S	0
Guaymas Basin Seep Site	no amendment	19

Table 4-S3.

Gibbs free energies (ΔG) of methanogenic catabolic pathways at the study sites. Possible ranges of ΔG were determined for the sampling depth of methane isotopologue analysis.

Site	Depth	Substrate	ΔG (kJ mol^{-1} C)
Carpinteria Salt Marsh Sites 1&2	0–5 cm	Methanol	-64.3 to -58.1
Carpinteria Salt Marsh Sites 1&2	0–5 cm	Methylamine	-69.1 to -59.4
Santa Barbara Basin Site NDRO	174–214 cm	H_2/CO_2	-22.6 to -14.7
Guaymas Basin Site U1550	94–204 m	H_2/CO_2	-36.2 to -25.1
Guaymas Basin Site U1547	82–166 m	H_2/CO_2	-6.1 to 36.5

References

Amend J.P. and LaRowe D.E. (2019) Minireview: demystifying microbial reaction energetics. *Environ. Microbiol.* **21**, 3539-3547.

Balch W.E., Fox G.E., Magrum L.J., Woese C.R. and Wolfe R.S. (1979) Methanogens: reevaluation of a unique biological group. *Microbiological Reviews* **43**, 260-296.

Beal E.J., House C.H. and Orphan V.J. (2009) Manganese-and iron-dependent marine methane oxidation. *Science* **325**, 184-187.

Berg P., Risgaard-Petersen N. and Rysgaard S. (1998) Interpretation of measured concentration profiles in sediment pore water. *Limnol. Oceanogr.* **43**, 1500-1510.

Bernard B., Brooks J.M. and Sackett W.M. (1977) A Geochemical Model For Characterization Of Hydrocarbon Gas Sources In Marine Sediments, Offshore Technology Conference, pp. 435-438.

Beulig F., Røy H., Glombitza C. and Jørgensen B.B. (2018) Control on rate and pathway of anaerobic organic carbon degradation in the seabed. *P. Natl. Acad. Sci. USA* **115**, 367-372.

Beulig F., Røy H., McGlynn S.E. and Jørgensen B.B. (2019) Cryptic CH4 cycling in the sulfate–methane transition of marine sediments apparently mediated by ANME-1 archaea. *The ISME Journal* **13**, 250-262.

Boetius A., Ravenschlag K., Schubert C.J., Rickert D., Widdel F., Gieseke A., Amann R., Jørgensen B.B., Witte U. and Pfannkuche O. (2000) A marine microbial consortium apparently mediating anaerobic oxidation of methane. *Nature* **407**, 623-626.

Bojanova D.P., De Anda V.Y., Haghnegahdar M.A., Teske A.P., Ash J.L., Young E.D., Baker B.J., LaRowe D.E. and Amend J.P. (2023) Well-hidden methanogenesis in deep, organic-rich sediments of Guaymas Basin. *The ISME Journal* **17**, 1828-1838.

Calvert S.E. (1966) Origin of Diatom-Rich, Varved Sediments from the Gulf of California. *The Journal of Geology* **74**, 546-565.

Cline J.D. (1969) Spectrophotometric determination of hydrogen sulfide in natural waters. *Limnol. Oceanogr.* **14**, 454-458.

Conrad R. (1999) Contribution of hydrogen to methane production and control of hydrogen concentrations in methanogenic soils and sediments. *FEMS Microbiol. Ecol.* **28**, 193-202.

Crill P.M. and Martens C.S. (1986) Methane production from bicarbonate and acetate in an anoxic marine sediment. *Geochim. Cosmochim. Acta* **50**, 2089-2097.

Crozier T.E. and Yamamoto S. (1974) Solubility of hydrogen in water, sea water, and sodium chloride solutions. *Journal of Chemical & Engineering Data* **19**, 242-244.

Cui X., Mucci A., Bianchi T.S., He D., Vaughn D., Williams E.K., Wang C., Smeaton C., Koziorowska-Makuch K., Faust J.C., Plante A.F. and Rosenheim B.E. (2022) Global fjords as transitory reservoirs of labile organic carbon modulated by organo-mineral interactions. *Sci. Adv.* **8**, eadd0610.

Dale A.W., Regnier P., Knab N.J., Jørgensen B.B. and Van Cappellen P. (2008) Anaerobic oxidation of methane (AOM) in marine sediments from the Skagerrak (Denmark): II. Reaction-transport modeling. *Geochim. Cosmochim. Acta* **72**, 2880-2894.

Dale A.W., Sommer S., Lomnitz U., Montes I., Treude T., Liebetrau V., Gier J., Hensen C., Dengler M., Stolpovsky K., Bryant L.D. and Wallmann K. (2015) Organic carbon production, mineralisation and preservation on the Peruvian margin. *Biogeosciences* **12**, 1537-1559.

Dong G., Xie H., Formolo M., Lawson M., Sessions A. and Eiler J. (2021) Clumped isotope effects of thermogenic methane formation: Insights from pyrolysis of hydrocarbons. *Geochim. Cosmochim. Acta* **303**, 159-183.

Einsele G., Gieskes J.M., Curray J., Moore D.M., Aguayo E., Aubry M.-P., Fornari D., Guerrero J., Kastner M., Kelts K., Lyle M., Matoba Y., Molina-Cruz A., Niemitz J., Rueda J., Saunders A., Schrader H., Simoneit B. and Vacquier V. (1980) Intrusion of basaltic sills into highly porous sediments, and resulting hydrothermal activity. *Nature* **283**, 441-445.

Froelich P.N., Klinkhammer G.P., Bender M.L., Luedtke N.A., Heath G.R., Cullen D., Dauphin P., Hammond D., Hartman B. and Maynard V. (1979) Early oxidation of organic matter in pelagic sediments of the eastern equatorial Atlantic: suboxic diagenesis. *Geochim. Cosmochim. Acta* **43**, 1075-1090.

Giunta T., Young E.D., Labidi J., Sansjofre P., Jézéquel D., Donval J.-P., Brandily C. and Ruffine L. (2022) Extreme methane clumped isotopologue bio-signatures of aerobic and anaerobic methanotrophy: Insights from the Lake Pavin and the Black Sea sediments. *Geochim. Cosmochim. Acta* **338**, 34-53.

Gropp J., Jin Q. and Halevy I. (2022) Controls on the isotopic composition of microbial methane. *Sci. Adv.* **8**, eabm5713.

Gruen D.S., Wang D.T., Könneke M., Topçuoğlu B.D., Stewart L.C., Goldhammer T., Holden J.F., Hinrichs K.-U. and Ono S. (2018) Experimental investigation on the controls of clumped isotopologue and hydrogen isotope ratios in microbial methane. *Geochim. Cosmochim. Acta* **237**, 339-356.

Haghnegahdar M.A., Schauble E.A. and Young E.D. (2017) A model for 12CH2D2 and 13CH3D as complementary tracers for the budget of atmospheric CH4. *Global Biogeochem. Cycles* **31**, 1387-1407.

Haroon M.F., Hu S., Shi Y., Imelfort M., Keller J., Hugenholtz P., Yuan Z. and Tyson G.W. (2013) Anaerobic oxidation of methane coupled to nitrate reduction in a novel archaeal lineage. *Nature* **500**, 567-570.

Hemingway J.D., Rothman D.H., Rosengard S.Z. and Galy V.V. (2017) Technical note: An inverse method to relate organic carbon reactivity to isotope composition from serial oxidation. *Biogeosciences* **14**, 5099-5114.

Hinkle J.E., Mara P., Beaudoin D.J., Edgcomb V.P. and Teske A.P. (2023) A PCR-Based Survey of Methane-Cycling Archaea in Methane-Soaked Subsurface Sediments of Guaymas Basin, Gulf of California. *Microorganisms* **11**, 2956.

Hoehler T.M., Alperin M.J., Albert D.B. and Martens C.S. (1998) Thermodynamic control on hydrogen concentrations in anoxic sediments. *Geochim. Cosmochim. Acta* **62**, 1745-1756.

Holler T., Wegener G., Knittel K., Boetius A., Brunner B., Kuypers M.M.M. and Widdel F. (2009) Substantial 13C/12C and D/H fractionation during anaerobic oxidation of methane by marine consortia enriched in vitro. *Environmental Microbiology Reports* **1**, 370-376.

Jin Q. and Bethke C.M. (2002) Kinetics of Electron Transfer through the Respiratory Chain. *Biophys. J.* **83**, 1797-1808.

Johnson J.W., Oelkers E.H. and Helgeson H.C. (1992) SUPCRT92: A software package for calculating the standard molal thermodynamic properties of minerals, gases, aqueous species, and reactions from 1 to 5000 bar and 0 to 1000°C. *Computers & Geosciences* **18**, 899-947.

Jørgensen B.B. (2021) Sulfur Biogeochemical Cycle of Marine Sediments. *Geochem. Perspect.* **10**, 145-146.

Joye S.B., Boetius A., Orcutt B.N., Montoya J.P., Schulz H.N., Erickson M.J. and Lugo S.K. (2004) The anaerobic oxidation of methane and sulfate reduction in sediments from Gulf of Mexico cold seeps. *Chem. Geol.* **205**, 219-238.

Kopec B.G., Feng X., Posmentier E.S. and Sonder L.J. (2019) Seasonal Deuterium Excess Variations of Precipitation at Summit, Greenland, and their Climatological Significance. *Journal of Geophysical Research: Atmospheres* **124**, 72-91.

Koster I.W., Rinzema A., de Vegt A.L. and Lettinga G. (1986) Sulfide inhibition of the methanogenic activity of granular sludge at various pH-levels. *Water Res.* **20**, 1561-1567.

Krause S., Wipfler R., Liu J., Yousavich D.J., Robinson D., Hoyt D.W., Orphan V.J. and Treude T. (2024) Spatial evidence of cryptic methane cycling and methylotrophic metabolisms along a land-ocean transect in a California coastal wetland. bioRxiv 603764 [Preprint].

Krause S.J.E., Liu J., Yousavich D.J., Robinson D., Hoyt D.W., Qin Q., Wenzhöfer F., Janssen F., Valentine D.L. and Treude T. (2023) Evidence of cryptic methane cycling and non-methanogenic methylamine consumption in the sulfate-reducing zone of sediment in the Santa Barbara Basin, California. *Biogeosciences* **20**, 4377-4390.

Krause S.J.E. and Treude T. (2021) Deciphering cryptic methane cycling: Coupling of methylotrophic methanogenesis and anaerobic oxidation of methane in hypersaline coastal wetland sediment. *Geochim. Cosmochim. Acta* **302**, 160-174.

Lalk E., Seewald J.S., Bryndzia L.T. and Ono S. (2023) Kilometer-scale Δ13CH3D profiles distinguish end-member mixing from methane production in deep marine sediments. *Org. Geochem.* **181**, 104630.

Laufer K., Michaud A.B., Røy H. and Jørgensen B.B. (2020) Reactivity of Iron Minerals in the Seabed Toward Microbial Reduction – A Comparison of Different Extraction Techniques. *Geomicrobiol. J.* **37**, 170-189.

Lewis E.R. and Wallace D.W.R. (1998) Program Developed for CO2 System Calculations. Carbon Dioxide Information Analysis Center, Oak Ridge National Laboratory, U.S. Department of Energy, Oak Ridge, TN, USA.

Li C., Sessions A.L., Kinnaman F.S. and Valentine D.L. (2009) Hydrogen-isotopic variability in lipids from Santa Barbara Basin sediments. *Geochim. Cosmochim. Acta* **73**, 4803-4823.

Lin Y.-S., Heuer V.B., Goldhammer T., Kellermann M.Y., Zabel M. and Hinrichs K.-U. (2012) Towards constraining H2 concentration in subseafloor sediment: A proposal for combined analysis by two distinct approaches. *Geochim. Cosmochim. Acta* **77**, 186-201.

Liu J., Harris R.L., Ash J.L., Ferry J.G., Krause S.J.E., Labidi J., Prakash D., Sherwood Lollar B., Treude T., Warr O. and Young E.D. (2023) Reversibility controls on extreme methane clumped isotope signatures from anaerobic oxidation of methane. *Geochim. Cosmochim. Acta* **348**, 165-186.

Liu J., Treude T., Abbasov O.R., Baloglanov E.E., Aliyev A.A., Harris C.M., Leavitt W.D. and Young E.D. (2024) Clumped isotope evidence for microbial alteration of thermogenic methane in terrestrial mud volcanoes. *Geology* **52**, 22-26.

Lloyd M.K., Eldridge D.L. and Stolper D.A. (2021) Clumped 13CH2D and 12CHD2 compositions of methyl groups from wood and synthetic monomers: Methods, experimental and theoretical calibrations, and initial results. *Geochim. Cosmochim. Acta* **297**, 233-275.

Lonsdale P. and Becker K. (1985) Hydrothermal plumes, hot springs, and conductive heat flow in the Southern Trough of Guaymas Basin. *Earth Planet. Sci. Lett.* **73**, 211-225.

Lotem N., Pellerin A., Anthony K.W., Gafni A., Boyko V. and Sivan O. (2023) Anaerobic oxidation of methane does not attenuate methane emissions from thermokarst lakes. *Limnol. Oceanogr.* **68**, 1316-1330.

Maltby J., Sommer S., Dale A.W. and Treude T. (2016) Microbial methanogenesis in the sulfate-reducing zone of surface sediments traversing the Peruvian margin. *Biogeosciences* **13**, 283-299.

Mara P., Zhou Y.-L., Teske A., Morono Y., Beaudoin D. and Edgcomb V. (2023) Microbial gene expression in Guaymas Basin subsurface sediments responds to hydrothermal stress and energy limitation. *The ISME Journal* **17**, 1907-1919.

McGlynn S.E., Chadwick G.L., Kempes C.P. and Orphan V.J. (2015) Single cell activity reveals direct electron transfer in methanotrophic consortia. *Nature* **526**, 531.

Milkov A.V. and Etiope G. (2018) Revised genetic diagrams for natural gases based on a global dataset of >20,000 samples. *Org. Geochem.* **125**, 109-120.

Nauhaus K., Boetius A., Krüger M. and Widdel F. (2002) In vitro demonstration of anaerobic oxidation of methane coupled to sulphate reduction in sediment from a marine gas hydrate area. *Environ. Microbiol.* **4**, 296-305.

Ono S., Rhim J.H. and Ryberg E.C. (2022) Rate limits and isotopologue fractionations for microbial methanogenesis examined with combined pathway protein cost and isotopologue flow network models. *Geochim. Cosmochim. Acta* **325**, 296-315.

Oremland R.S. and Capone D.G. (1988) Use of “Specific” Inhibitors in Biogeochemistry and Microbial Ecology, in: Marshall K.C. (Ed.), Advances in Microbial Ecology. Springer US, Boston, MA, pp. 285-383.

Oremland R.S. and Polcin S. (1982) Methanogenesis and Sulfate Reduction: Competitive and Noncompetitive Substrates in Estuarine Sediments. *Appl. Environ. Microbiol.* **44**, 1270-1276.

Oremland R.S. and Taylor B.F. (1978) Sulfate reduction and methanogenesis in marine sediments. *Geochim. Cosmochim. Acta* **42**, 209-214.

Page H.M., Petty R.L. and Meade D.E. (1995) Influence of Watershed Runoff on Nutrient Dynamics in a Southern California Salt Marsh. *Estuar. Coast. Shelf Sci.* **41**, 163-180.

Pellerin A., Antler G., Røy H., Findlay A., Beulig F., Scholze C., Turchyn A.V. and Jørgensen B.B. (2018) The sulfur cycle below the sulfate-methane transition of marine sediments. *Geochim. Cosmochim. Acta* **239**, 74-89.

Pellerin A., Lotem N., Walter Anthony K., Eliani Russak E., Hasson N., Røy H., Chanton J.P. and Sivan O. (2022) Methane production controls in a young thermokarst lake formed by abrupt permafrost thaw. *Global Change Biol.* **28**, 3206-3221.

Reimers C.E., Ruttenberg K.C., Canfield D.E., Christiansen M.B. and Martin J.B. (1996) Porewater pH and authigenic phases formed in the uppermost sediments of the Santa Barbara Basin. *Geochim. Cosmochim. Acta* **60**, 4037-4057.

Rudd J. and Taylor C.D. (1980) Methane cycling in aquatic environments. *Adv. Aquat. Microbiol.* **2**, 77-150.

Sholkovitz E.R. and Gieskes J.M. (1971) A PHYSICAL-CHEMICAL STUDY OF THE FLUSHING OF THE SANTA BARBARA BASIN. *Limnol. Oceanogr.* **16**, 479-489.

Stookey L.L. (1970) Ferrozine---a new spectrophotometric reagent for iron. *Anal. Chem.* **42**, 779-781.

Teske A., Callaghan A.V. and LaRowe D.E. (2014) Biosphere frontiers of subsurface life in the sedimented hydrothermal system of Guaymas Basin. *Front. Microbiol.* **5**.

Teske A., Lizarralde D., Höfig T.W. and the Expedition 385 Scientists (2021) Guaymas Basin Tectonics and Biosphere. Proceedings of the International Ocean Discovery Program. International Ocean Discovery Program, College Station, TX.

Teske A., McKay L.J., Ravelo A.C., Aiello I., Mortera C., Núñez-Useche F., Canet C., Chanton J.P., Brunner B., Hensen C., Ramírez G.A., Sibert R.J., Turner T., White D., Chambers C.R., Buckley A., Joye S.B., Soule S.A. and Lizarralde D. (2019) Characteristics and Evolution of sill-driven off-axis hydrothermalism in Guaymas Basin – the Ringvent site. *Scientific Reports* **9**, 13847.

Treude T., Krüger M., Boetius A. and Jørgensen B.B. (2005) Environmental control on anaerobic oxidation of methane in the gassy sediments of Eckernförde Bay (German Baltic). *Limnol. Oceanogr.* **50**, 1771-1786.

Walter Anthony K., Schneider von Deimling T., Nitze I., Frolking S., Emond A., Daanen R., Anthony P., Lindgren P., Jones B. and Grosse G. (2018) 21st-century modeled permafrost carbon emissions accelerated by abrupt thaw beneath lakes. *Nat. commun.* **9**, 3262.

Walter Anthony K.M., Lindgren P., Hanke P., Engram M., Anthony P., Daanen R.P., Bondurant A., Liljedahl A.K., Lenz J., Grosse G., Jones B.M., Brosius L., James S.R., Minsley B.J., Pastick N.J., Munk J., Chanton J.P., Miller C.E. and Meyer F.J. (2021) Decadal-scale hotspot methane ebullition within lakes following abrupt permafrost thaw. *Environmental Research Letters* **16**, 035010.

Wang D.T., Gruen D.S., Lollar B.S., Hinrichs K.-U., Stewart L.C., Holden J.F., Hristov A.N., Pohlman J.W., Morrill P.L., Könneke M., Delwiche K.B., Reeves E.P., Sutcliffe C.N., Ritter

D.J., Seewald J.S., McIntosh J.C., Hemond H.F., Kubo M.D., Cardace D., Hoehler T.M. and Ono S. (2015) Nonequilibrium clumped isotope signals in microbial methane. *Science* **348**, 428-431.

Wegener G. and Boetius A. (2009) An experimental study on short-term changes in the anaerobic oxidation of methane in response to varying methane and sulfate fluxes. *Biogeosciences* **6**, 867-876.

Wegener G., Krukenberg V., Riedel D., Tegetmeyer H.E. and Boetius A. (2015) Intercellular wiring enables electron transfer between methanotrophic archaea and bacteria. *Nature* **526**, 587.

Whiticar M.J. (1999) Carbon and hydrogen isotope systematics of bacterial formation and oxidation of methane. *Chem. Geol.* **161**, 291-314.

Whiticar M.J., Faber E. and Schoell M. (1986) Biogenic methane formation in marine and freshwater environments: CO2 reduction vs. acetate fermentation—Isotope evidence. *Geochim. Cosmochim. Acta* **50**, 693-709.

Widdel F. and Bak F. (1992) Gram-Negative Mesophilic Sulfate-Reducing Bacteria, in: Balows A., Trüper H.G., Dworkin M., Harder W., Schleifer K.-H. (Eds.), The Prokaryotes: A Handbook on the Biology of Bacteria: Ecophysiology, Isolation, Identification, Applications. Springer New York, New York, NY, pp. 3352-3378.

Xiao K.-Q., Beulig F., Røy H., Jørgensen B.B. and Risgaard-Petersen N. (2018) Methylotrophic methanogenesis fuels cryptic methane cycling in marine surface sediment. *Limnol. Oceanogr.* **63**, 1519-1527.

Xie H., Dong G., Formolo M., Lawson M., Liu J., Cong F., Mangenot X., Shuai Y., Ponton C. and Eiler J. (2021) The evolution of intra- and inter-molecular isotope equilibria in natural gases with thermal maturation. *Geochim. Cosmochim. Acta* **307**, 22-41.

Yamamoto S., Alcauskas J.B. and Crozier T.E. (1976) Solubility of methane in distilled water and seawater. *Journal of Chemical & Engineering Data* **21**, 78-80.

Young E.D., Kohl I.E., Lollar B.S., Etiope G., Rumble D., Li S., Haghnegahdar M.A., Schauble E.A., McCain K.A., Foustoukos D.I., Sutclife C., Warr O., Ballentine C.J., Onstott T.C., Hosgormez H., Neubeck A., Marques J.M., Pérez-Rodríguez I., Rowe A.R., LaRowe D.E., Magnabosco C., Yeung L.Y., Ash J.L. and Bryndzia L.T. (2017) The relative abundances of resolved 12CH2D2 and 13CH3D and mechanisms controlling isotopic bond ordering in abiotic and biotic methane gases. *Geochim. Cosmochim. Acta* **203**, 235-264.

Young E.D., Rumble D., Freedman P. and Mills M. (2016) A large-radius high-mass-resolution multiple-collector isotope ratio mass spectrometer for analysis of rare isotopologues of O2, N2, CH4 and other gases. *Int. J. Mass spectrom.* **401**, 1-10.

Zhuang G.-C., Heuer V.B., Lazar C.S., Goldhammer T., Wendt J., Samarkin V.A., Elvert M., Teske A.P., Joye S.B. and Hinrichs K.-U. (2018) Relative importance of methylotrophic methanogenesis in sediments of the Western Mediterranean Sea. *Geochim. Cosmochim. Acta* **224**, 171-186.

Chapter 5

Iron oxides fuel anaerobic oxidation of methane in the presence of sulfate in hypersaline coastal wetland sediment

Jiarui Liu[1]*, Emily Klonicki-Ference[1], Sebastian J. E. Krause[2], Tina Treude[1]*

[1]Department of Earth, Planetary, and Space Sciences, University of California, Los Angeles, California 90095, USA

[2]Earth Research Institute, University of California, Santa Barbara, California 93106, USA

*Corresponding author: jiaruiliu@ucla.edu, ttreude@g.ucla.edu

ABSTRACT

Wetland methane emissions are the primary natural contributor to the global methane budget, accounting for approximately one third of total emissions from natural and anthropogenic sources. Anaerobic oxidation of methane (AOM) serves as the major sink of methane in anoxic wetland sediments, where electron acceptors are present, thereby effectively mitigating its emissions. Nevertheless, environmental controls on electron acceptors, in particular the ubiquitous iron oxides, involved in AOM are poorly understood. Here, we explored methane sinks within a hypersaline

pool situated in a coastal wetland. The geochemical profiles reveal a tiering, where microbial sulfate reduction dominates in the organic-rich surface sediment, yielding to iron reduction in the deeper organic-poor yet sulfate-rich subsurface sediment. This shift is attributed to the drilling-induced depression and subsequent diagenetic transformation of the surface sediment. Radiotracer incubations demonstrate a strong association of AOM with sulfate in surface sediments and with iron oxides in subsurface sediments. Despite high concentrations of sulfate in coastal wetlands, Fe-dependent AOM may play a significant, yet often under-considered, role as a sink for methane emissions. The substantial production of Fe^{2+} during Fe-dependent AOM could enhance phosphorus sequestration through the formation of Fe(II)-phosphate minerals, potentially limiting coastal eutrophication.

Keywords: iron reduction; methane oxidation; radiotracer incubations; salt marsh; sediment diagenesis; sulfate reduction.

Synopsis statement: Microbial anaerobic oxidation of methane is coupled to iron reduction in iron-oxide-rich sediment of a coastal wetland, thereby serving as a sink for methane.

INTRODUCTION

Methane is a potent greenhouse gas and is the second-largest contributor to global warming after carbon dioxide (Mitchell, 1989; Dlugokencky et al., 2011; Nisbet et al., 2019). It arises from both natural sources and human activities. Approximately 60% of current methane emissions stem from human activities, with the remaining portion originating from natural processes (Saunois et al., 2020). Notably, wetlands stand out as the predominant natural contributor to atmospheric methane globally, making them a significant focal point in addressing climate change concerns (Bridgham et al., 2013). Methane emissions from wetlands are dictated by its microbial production and oxidation. Methanogenic archaea use a range of substrates such as H_2/CO_2, acetate, and methylated compounds to produce methane under anoxic conditions (Reeburgh, 2007), while a group of aerobic bacteria can also generate methane in oxic water bodies (Repeta et al., 2016). Once formed in anoxic sediments, methane can be oxidized by anaerobic oxidation of methane (AOM), depending on the availability of electron acceptors (Knittel and Boetius, 2009; Segarra et al., 2013). Methane entering the water column or surface soil may undergo partial or complete aerobic oxidation before eventually being released into the atmosphere (Le Mer and Roger, 2001; Chowdhury and Dick, 2013).

Common electron acceptors for AOM include sulfate, nitrate, nitrite, humic substances, and metal oxides (Beal et al., 2009; Knittel and Boetius, 2009; Ettwig et al., 2010; Haroon et al., 2013; Scheller et al., 2016). Sulfate-driven AOM is ubiquitous in coastal and marine environments and is typically performed by consortia of anaerobic methanotrophic (ANME) archaea and sulfate-reducing bacteria (Niewöhner et al., 1998; Boetius et al., 2000; McGlynn et al., 2015; Wegener et al., 2015). Nitrate- and nitrite-dependent AOM has been observed in freshwater environments

(Raghoebarsing et al., 2006). Nitrate-dependent AOM is mediated by specific members of the ANME clade (ANME-2d, "*Ca. Methanoperedens*"), operating in a syntrophic relationship with nitrite consumers or performing denitrification independently (Haroon et al., 2013; Yao et al., 2024). Nitrite-dependent AOM, on the other hand, is performed by oxygenic bacteria known as "*Methylomirabilis oxyfera*" from the NC10 group, which reduce nitrite and concurrently produce oxygen as an intermediate, facilitating the oxidation of methane (Ettwig et al., 2010). Humic substances, such as anthraquinone 2,6-disulfonate (AQDS), have been employed as electron sinks for AOM in short-term experiments, whereas their environment significance is yet to be thoroughly investigated (Scheller et al., 2016; Bai et al., 2019; Yu et al., 2022).

AOM can also be coupled to the reduction of various heavy metals, such as Fe(III), Mn(IV), Cr(VI), As(V), and Se(VI) (Beal et al., 2009; He et al., 2018; Shi et al., 2020). Notably, Fe stands out as the most prevalent heavy metal, with its oxides widely distributed in natural environments, particularly in wetlands. Fe-mediated AOM can be performed by methanotrophs, such as ANME-2d archaea ("*Ca. Methanoperedens*"), which oxidize methane nonsyntropically, exploiting soluble, nanophase, or solid-phase ferric Fe as electron acceptors (Ettwig et al., 2016; Scheller et al., 2016; Cai et al., 2018; Yan et al., 2018). In particular, incubation experiments demonstrated that Fe-AOM has the potential to reduce a range of solid-phase ferric Fe, from highly reactive Fe oxides (FeOx) such as ferrihydrite to poorly reactive Fe minerals such as hematite and magnetite (Beal et al., 2009; Bar-Or et al., 2017). By employing tracer incubation of sediment slurries, modeling of porewater profiles and the identification of authigenic minerals, the presence of Fe-AOM has been documented in diverse aquatic settings, encompassing both marine and freshwater environments (Beal et al., 2009; Sivan et al., 2011; Wankel et al., 2012; Norði et al., 2013; Riedinger et al., 2014;

Treude et al., 2014; Egger et al., 2015b; Liu et al., 2018; Aromokeye et al., 2020). For example, in typical marine sediments, Fe-AOM has been identified beneath the sulfate-methane transition zone (SMTZ) where sulfate-driven AOM effectively oxidizes the majority of the upward methane flux, and the high dissolved Fe^{2+} concentration and vivianite authigenesis below the SMTZ have been attributed to the occurrence of Fe-AOM (Riedinger et al., 2014; Egger et al., 2015a; Egger et al., 2015b; Egger et al., 2017; Liu et al., 2018). In freshwater lakes, the role of Fe-AOM can be more predominant due to low sulfate concentrations (Sivan et al., 2011; Norði et al., 2013; Mostovaya et al., 2022; Vigderovich et al., 2022).

Nonetheless, the role of Fe-AOM as a methane sink in wetlands, a significant contributor to methane emissions, has been poorly studied (Segarra et al., 2013; Zhao and Lu, 2023). Given the importance of AOM in mitigating methane emissions, knowledge about Fe-AOM in wetland sediments is essential. Enhancing our comprehension of methane oxidation pathways will enable more accurate predictions of methane emissions from wetlands, especially in the context of eutrophication and climate change. In this study, we investigate the interplay of carbon-sulfur-iron biogeochemical cycles, placing particular emphasis on the dynamic interaction between methane and Fe(III) minerals within the Carpinteria Salt Marsh Reserve. Krause and Treude (2021) inferred the potential occurrence of Fe-AOM at the study site based on ex-situ AOM rates. Combining porewater and solid-phase analyses with the determination of microbial turnover rates, we present compelling geochemical evidence confirming the occurrence of Fe-AOM in the subsurface sediments from a hypersaline pool. In light of the concurrent methane production and oxidation observed at the study site (Krause and Treude, 2021), a comprehensive understanding of AOM

pathways offers novel perspectives on the cryptic methane cycling and its pivotal role in regulating methane emissions from wetlands.

MATERIALS AND METHODS

Study Site and Sampling

The Carpinteria Salt Marsh Reserve (CSMR) is an estuary located on the south coast of Santa Barbara County in southern California, United States (Ferren, 1985). As one of the most well-preserved salt marshes in southern California, the CSMR offers a natural laboratory to explore how AOM mitigates methane emissions from coastal wetlands. Guided by Krause and Treude's previous study (2021), we chose a hypersaline pool within the CSMR to investigate the role of various electron acceptors in AOM. The authors found a decoupled relationship between the rates of AOM and sulfate reduction in the subsurface of this pool, implying that AOM may be linked to the reduction of alternative electron acceptors. The pool is located at latitude 34°23'56.1"N and longitude 119°32'10.2"W with an oval shape, measuring 24 meters in length along its major axis and 13 meters in length along its minor axis (Figure S1) (Krause and Treude, 2021). We tracked variations in the salinity of the pool water from summer 2021 to winter 2023 using a refractometer. The salinity varies significantly annually, from below-seawater salinity (17 PSU) in winter due to rainfall to supersaturation (>200 PSU) in summer and fall due to evaporation (Figure S2). Photosynthesis-based microbial mats develop year-round on the surface of water-covered sediments.

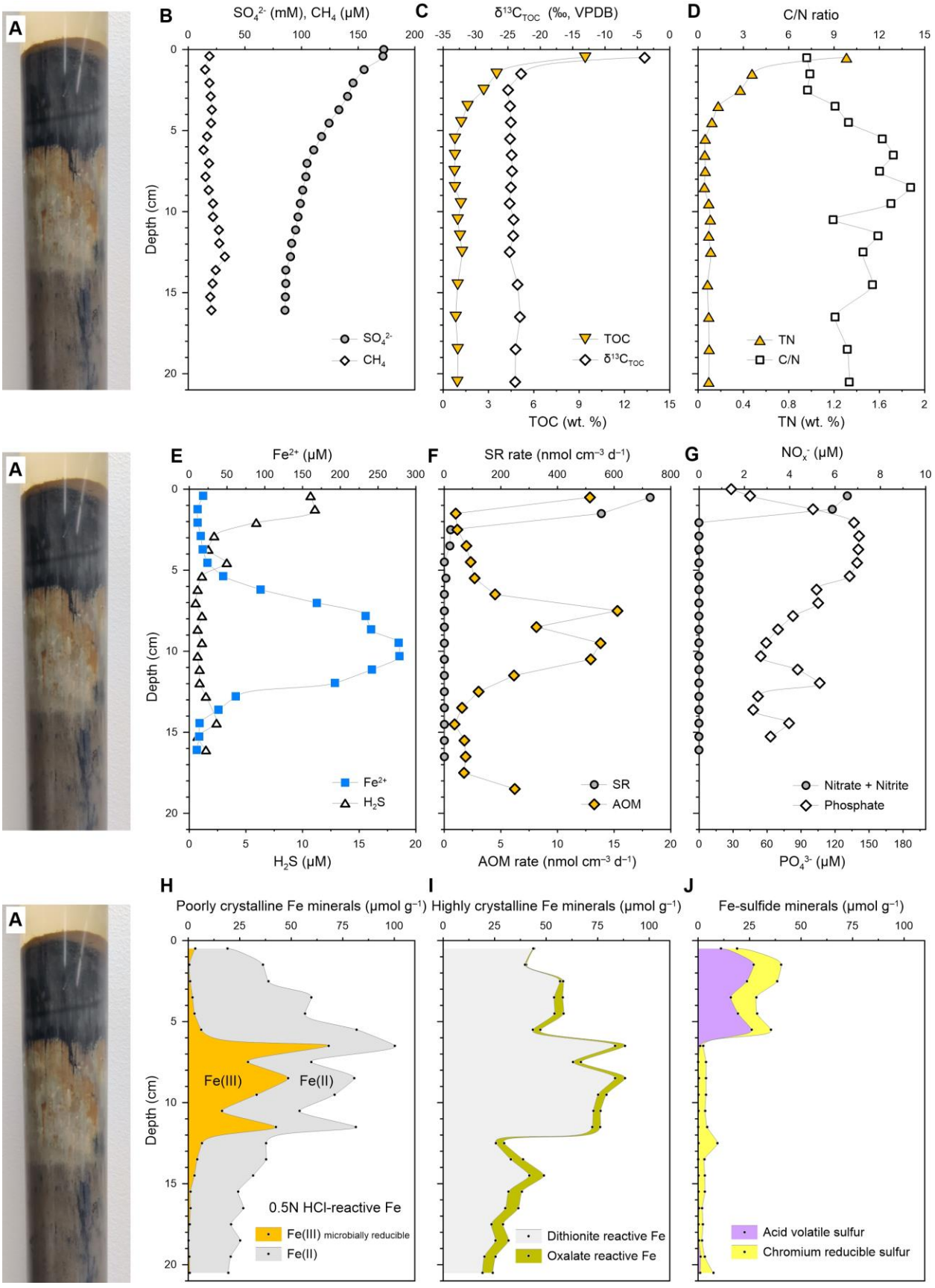
A
B
SO_4^{2-} (mM), CH_4 (μM)
Depth (cm)
SO_4^{2-}
CH_4
C
$\delta^{13}C_{TOC}$ (‰, VPDB)
TOC
$\delta^{13}C_{TOC}$
TOC (wt. %)
D
C/N ratio
TN
C/N
TN (wt. %)
A
E
Fe^{2+} (μM)
Fe^{2+}
H_2S
H_2S (μM)
F
SR rate (nmol cm^{-3} d^{-1})
SR
AOM
AOM rate (nmol cm^{-3} d^{-1})
G
NO_x^- (μM)
Nitrate + Nitrite
Phosphate
PO_4^{3-} (μM)
A
H
Poorly crystalline Fe minerals (μmol g^{-1})
Fe(III)
Fe(II)
0.5N HCl-reactive Fe
Fe(III) microbially reducible
Fe(II)
I
Highly crystalline Fe minerals (μmol g^{-1})
Dithionite reactive Fe
Oxalate reactive Fe
J
Fe-sulfide minerals (μmol g^{-1})
Acid volatile sulfur
Chromium reducible sulfur

Fig. 5-1 Core image and geochemical depth profiles in sediment from the hypersaline pool in the Carpinteria Salt Marsh Reserve. (A) Image of the solid-phase sediment core collected in November 2021. (B, E, G) Data from the porewater core collected in September 2022: (B) Porewater sulfate and methane concentrations; (E) porewater sulfide and ferrous iron concentrations; (G) porewater phosphate and combined nitrate and nitrite concentrations. (F) Rates of sulfate reduction (SR) and anaerobic oxidation of methane (AOM) collected by Krause and Treude (2021) in June 2018. Note that rates were calculated based on methane and sulfate concentrations, respectively, collected during the same sampling campaign (see Figure S2). (C&D, H-J) Data from the solid-phase sediment core collected in November 2021: (C) Total organic carbon (TOC) content and carbon isotopic composition of TOC; (D) total nitrogen (TN) content and C/N ratio; (H) contents of poorly crystalline Fe(III) and Fe(II) minerals; (I) contents of highly crystalline Fe oxide minerals; (J) contents of Fe sulfide minerals. We synchronized the depth axis of the porewater core with the solid-phase and ex-situ rate cores, using the identified lithological transition as our reference point. Details regarding the sampling of sediment cores are provided in the Materials and Methods section.

One sediment core for solid-phase analysis was sampled in November 2021 and two sediment cores for porewater analysis and microbial incubations were sampled in September 2022 (Figure S1). Furthermore, we included data of ex-situ rates collected in 2018 and published by Krause and Treude (2021) in this study. The sediment core for this published dataset was sampled from the same location as the solid-phase core (Figure S1). Visible salt precipitates were observed in the pool during all coring events. The water depth above the sampled sediment measured approximately 5–10 cm during all sampling periods. The top 20 cm of sediment near the center of

the pool was sampled by hand using polycarbonate push core liners. Sediments were characterized by a brown surface (0–1 cm), a distinct black (1–6 cm) and grey/brown (>6 cm) layer as shown by the solid-phase core in Figure 1A. The cores for porewater analysis and slurry incubations were sampled closer to the center of the pool when compared to the solid-phase and ex-situ rate cores, with a distance of 2 meters. The transition from the black layer to the grey/brown layer occurred 2 cm deeper than the solid-phase and ex-situ rate cores due to a higher sedimentation rate towards the center (Figure S1). In Figure 1, we synchronize the depth axis of the porewater core with the solid-phase and ex-situ rate cores, using the identified lithological transition as our reference point. After same-day arrival at the home laboratory, sediment cores were stored at 4 °C, in the dark, and processed within one day to one week of collection, depending on the type of analyses.

Porewater Analyses

The sediment core for porewater geochemistry was subsampled one day after collection. The core was sliced under a constant flow of argon to minimize oxidation of oxygen-sensitive chemical species. Sediments were sliced evenly in 1 cm increments. Sediments for methane concentration analysis were immediately transferred to glass vials containing 2.5% NaOH solution. The vials were then crimp sealed, shaken vigorously and stored upside down at 4 °C. Methane concentration was analyzed using a gas chromatograph (Shimadzu GC-2014) with a packed HayeSep D column and a flame ionization detector. The remaining sediment of each layer was transferred into argon-flushed 50 ml centrifuge tubes and centrifuged at 4300 X g for 20 min to separate porewater from sediment. For dissolved sulfide and ferrous iron analyses, porewater was immediately fixed with 5% zinc acetate solution (1:1 v:v) and 1 N HCl (1:4 v:v), respectively. Dissolved sulfide and ferrous iron concentrations were determined spectrophotometrically (Shimadzu UV-1800)

immediately following fixation by the methylene blue method (Cline, 1969) and the ferrozine assay (Stookey, 1970), respectively. The rest of porewater was stored at −20 °C until analysis. Sulfate and chloride concentrations were measured using an ion chromatograph (Metrohm 761). Nitrate and nitrite concentrations were analyzed spectrophotometrically by the Griess reaction with a detection limit of 0.5 μM (García-Robledo et al., 2014). Phosphate concentration was analyzed using a spectrophotometer (Grasshoff et al., 1999). The analytical uncertainties associated with porewater concentrations were determined by replicate analysis of standards, which all displayed relative standard deviations (RSD) of 2–5%.

Solid-phase Analyses

The sediment core for solid-phase geochemistry was subsampled one week after collection. Sediments were sliced into argon-flushed 15 ml centrifuge tubes for solid-phase iron extraction and organic matter analysis and argon-flushed 50 ml centrifuge tubes with 5% zinc acetate for solid-phase sulfur extraction. Sediment samples were frozen at −20 °C until analysis. Sediment for sulfur extraction was treated with a standard two-step sulfide extraction at room temperature (Fossing and Jørgensen, 1989; Kallmeyer et al., 2004), extracted with 6 N HCl to release the acid volatile sulfur (AVS, mainly Fe monosulfide) and then with chromium(II) chloride solution and dimethylformamide to release the chromium reducible sulfur (CRS, mainly pyrite and small amounts of elemental sulfur). The sulfide evolved from these extractions was flushed within a N_2 stream through 5% zinc acetate solution and trapped as ZnS. The AVS and CRS contents were determined spectrophotometrically by the methylene blue method (Cline, 1969). Replicate analyses of samples showed a relative standard deviation (RSD) of better than 5%.

Sequential iron extractions followed the protocol of Poulton (2021) using ~100 mg of wet sediment and 10 ml of the following extractants: (i) anoxic 0.5 N HCl, (ii) solidum dithionite/citrate, and (iii) ammonium oxalate/oxalic acid. This sequential extraction scheme is modified from Poulton and Canfield (2005) for modern sediments. The Fe(II) concentration of the first extract was determined spectrophotometrically by the ferrozine assay (Stookey, 1970); while total Fe concentration was determined after complexing with ferrozine and hydroxylamine hydrochloride. Poorly crystalline Fe(III) phases (e.g., ferrihydrite, lepidocrocite) were calculated as the difference between the mixed valence and the Fe(II) fractions—A phase termed microbially reducible Fe(III) (Laufer et al., 2020). The dithionite step targets crystalline Fe(III) phases such as goethite and hematite, while the oxalate step targets magnetite. Only total Fe concentrations were measured for these two steps spectrophotometrically. In general, microbial Fe(III) reduction is not thermodynamically favorable using highly crystalline Fe minerals such as hematite or magnetite under marine sediment conditions (Postma and Jakobsen, 1996). Replicate analyses of samples showed an RSD of better than 6%. All solid-phase iron and sulfur data are reported relative to the wet mass of the sediment.

For organic matter analysis, sediment was decarbonated with 0.5 N HCl. Total organic carbon (TOC), total nitrogen (TN) contents, and their isotopic compositions ($\delta^{13}C$ and $\delta^{15}N$) were analyzed on an Elementar vario MICRO cube elemental analyzer interfaced to an Elementar VisION isotope ratio mass spectrometer (IRMS) at the UC Davis Stable Isotope Facility. TOC and TN contents are reported in dry weight percent. The $\delta^{13}C$ and $\delta^{15}N$ values are expressed relative

to international standards VPDB (Vienna Pee Dee Belemnite) and Air, respectively. The long-term standard deviation is 0.2‰ for $\delta^{13}C$ and 0.3‰ for $\delta^{15}N$.

Determination of Microbial Turnover Rates

Ex-situ rates in sediment cores

Ex-situ rates of AOM and sulfate reduction were determined by Krause and Treude (2021) in sediment cores collected in June 2018 from the hypersaline pool. Cores from their study were collected from the same location as the solid-phase core from the present study. AOM and sulfate reduction rates were determined by injecting radioactive ^{14}C-methane and ^{35}S-sulfate, respectively, into small whole-round push cores at 1-cm increments. The ex-situ data and detailed methods were previously published (Krause and Treude, 2021). Note that for the calculation of AOM and sulfate reduction rates, sediment methane and sulfate concentration profiles determined by Krause and Treude (2021) were used.

Short-term Sediment Slurry Incubation Experiments

Synthesized Fe oxides and artificial seawater medium were prepared right before the field sampling. Fe(III) oxides have different bioavailability for microbial iron reduction (Postma and Jakobsen, 1996; Thamdrup, 2000), thus both amorphous Fe(III) oxyhydroxide and ferrihydrite are used here. Amorphous Fe(III) oxyhydroxide was synthesized by neutralizing a 0.4 M solution of $FeCl_3$ to a pH of 7 with NaOH (Lovley and Phillips, 1986). Two-line ferrihydrite was synthesized

using the protocol in Schwertmann and Cornell (2000). Artificial seawater medium was made following Laso-Pérez et al. (2018). Extra NaCl was added to the seawater medium to match the salinity of the hypersaline pool. Seawater was degassed with N_2/CO_2 and reduced with Na_2S. $FeCl_2$ was added in a 1:1 stoichiometic ratio to the sulfide in order to precipitate all of the added sulfide (Beal et al., 2009). The developed FeS in the seawater was allowed to settle prior to use to minimize the amount of sulfide added to the incubations. We did not use soluble iron(III) complexes (e.g., ferric citrate and ferric-EDTA) or highly crystalline Fe minerals (e.g., geothite, hematite, and magnetite) because the former may react with the abundant Fe monosulfide in the FeS-rich layer (Aller and Rude, 1988), while the latter may not be available for microbial iron reduction during our two-day incubation (Postma and Jakobsen, 1996).

One sediment core was subsampled one day after collection for slurry incubation. The upper black layer (0–6 cm; hereafter termed FeS-rich layer) and the lower grey/brown layer (6–12 cm; hereafter termed FeOx-rich layer) were each transferred into a separate argon-flushed 500-ml culture glass bottle under a constant flow of argon. Anoxic seawater medium was added to each bottle through a 0.22 μm syringe filter to avoid addition of FeS. Sediment slurries were made by mixing sediment with seawater medium at a ratio of 1:2 (v:v). The final salinity in the FeS-rich and FeOx-rich slurries were 136 and 89, respectively, determined using a refractometer. Due to the high sulfate concentrations (>86 mM) in the original sediments, sulfate was not limiting in both slurries (>28 mM) during the incubation periods.

Following the preparation of homogenous stock slurries, a total of 54 sediment slurry subsamples from each layer were prepared in an anoxic glove bag by transferring 13 ml of slurry to glass crimp vials and sealed without headspace. The glass vials from each layer were divided into two groups: one for ^{14}C-methane incubations, the other for ^{35}S-sulfate incubations. Each group had the following treatments in triplicates: (i) live control without inhibitor or substrate amendment, (ii) molybdate (30 mM; sulfate reducer inhibitor), (iii) excess sulfide (ca. 5 mM; for the removal of reducible metals), (iv) molybdate + excess sulfide, (v) excess amorphous Fe(III) oxyhydroxide (ca. 30 mM), (vi) excess amorphous Fe(III) oxyhydroxide + molybdate, (vii) excess ferrihydrite (ca. 30 mM), and (viii) excess ferrihydrite + molybdate. Assuming complete reaction of Fe(III) oxides with free and metastable sulfides, a final concentration of Fe(III) oxide exceeding 10 mM was anticipated. Killed controls were also prepared in triplicates by adding either 5% sodium hydroxide for the ^{14}C incubations or 20% zinc acetate for the ^{35}S incubations. Killed control samples incubated in parallel with the above treatments.

For AOM rate determinations, 20 µL of ^{14}C-methane tracer (dissolved in MilliQ water, activity 0.7 kBq, specific activity 185 MBq mmol^{-1}) was injected into one group of the sediment slurries. For sulfate reduction rate determinations, 10 µL of carrier-free ^{35}S-sulfate tracer (dissolved in MilliQ water, activity 234 kBq, specific activity 37 TBq mmol^{-1}) was injected into a separate group of the sediment slurries. The vials were incubated for two days in the dark at 20 °C, which closely matched the in-situ temperature. Sulfate reduction incubations were terminated by transferring the sample from the glass vial to a centrifuge tube filled with 20 ml 20% zinc acetate followed by freezing at −30°C. The sulfate reduction rate was analyzed and calculated according to the cold chromium distillation method (Kallmeyer et al., 2004). AOM incubations were terminated by

transferring samples to 50 ml glass vials filled with 20 ml 5% NaOH. The vials were sealed with rubber stoppers immediately and shaken thoroughly. The AOM rates were analyzed and calculated according to Krause and Treude (2021). Killed controls were also prepared in triplicates for each layer by adding either 5% sodium hydroxide for the ^{14}C incubations or 20% zinc acetate for the ^{35}S incubations before radiotracer addition. Samples were regarded active only if: sample value > control mean + (3 × standard deviation). If a sample value passed this threshold, the killed control mean was subtracted from the sample value. The rates are expressed as pmol per cm^3 of diluted sediment slurry per day.

RESULTS AND DISCUSSION

Geochemical Profiles

The hypersaline pool sediment was characterized by high sulfate (>86 mM) and low methane (<33 μM) concentrations (Figure 1B). The decrease in sulfate concentration downcore was likely caused by a combination of microbial sulfate reduction and the diffusion of additional sulfate from the supernatant water during the dry season, when the water becomes hypersaline and enriched in sulfate. Methane concentrations throughout the sampled sediment remained constant at 21±5 μM (one standard deviation, 1σ). The TOC content was highest (9.4 wt. %) at the sediment surface, then decreased to an average of 0.9 ± 0.2 wt. % below the upper 6 cm, reflecting strong organic matter degradation in the upper 6 cm (Figure 1C). The $\delta^{13}C_{TOC}$ was invariant below 2 cm (−24.3 ± 0.5‰), whereas its values peaked up to −3.9‰ at the sediment surface where microbial mats were present (Figure 1C). This extremely high $\delta^{13}C_{TOC}$ is consistent with a minimal isotope fractionation seen in many hypersaline microbial mats due to diffusion-limited DIC uptake and

active bicarbonate transport (Des Marais and Canfield, 1994). The organic matter degradation resulted in the release of phosphate into the porewater (Ruttenberg, 2014), leading to a progressive increase of its concentration in the upper 6 cm (Figure 1G). Porewater nitrate and nitrite were detectable only in the upper 2 cm, totaling 6.5 μM and 5.9 μM at 0–1 and 1–2 cm, respectively (Figure 1G). Vertical geochemical profiles further revealed two distinct mineralogical zones: an FeS-rich layer between 0–6 cm overlying an Fe-oxides-rich (FeOx-rich) layer between 6–15 cm (Figure 1H–J). Sulfate reduction rates, which were determined in the hypersaline pool in 2018 (Krause and Treude, 2021), peaked at the sediment surface and decreased sharply with depth in the upper 6 cm (Figure 1F), fueling aqueous sulfide accumulation in the FeS-rich layer (Figure 1E), and therefore leading to the formation of Fe sulfide minerals up to 40 μmol g^{-1} and the depletion of poorly crystalline Fe(III) minerals down to 0.5 μmol g^{-1} (Figure 1H–J).

In the FeOx-rich layer, dissolved Fe^{2+} concentration formed a broad peak at 6–13 cm, reaching its maximum up to 278 μM at 10 cm (Figure 1E). A similar pattern was observed in the abundance of poorly crystalline Fe(III) minerals with peak values up to 68 μmol g^{-1}, while the content of Fe sulfides was consistently low (3.6 ± 1.8 μmol g^{-1}) below 6 cm (Figure 1H–J). In this layer, sulfate reduction rates were below detection limit, suggesting that the dissolved Fe^{2+} was not sourced from abiotic sulfide-mediated reductive dissolution of Fe-oxides. Accordingly, the cooccurrence of abundant solid-phase Fe(III) phases and dissolved Fe^{2+} implies microbial iron reduction (Michaud et al., 2020). The reduction of Fe oxides prompted the liberation of phosphate previously adsorbed onto these oxides into the porewater (Ruttenberg, 2014). Nevertheless, a decline in phosphate concentration was observed at 10 cm where dissolved Fe^{2+} reached its peak, indicating the potential precipitation of Fe(II)-phosphate minerals, such as vivianite (Egger et al., 2015a; Liu et

al., 2018). Conversely, in the upper 6 cm, Fe was predominantly sequestered as Fe sulfides, leading to a buildup of phosphate in the porewater (Figure 1G).

Notably, the highest AOM rates (Krause and Treude, 2021) peaked and aligned with the broad dissolved Fe^{2+} peak between 6–12 cm (Figure 1E–F), pointing strongly to the occurrence of Fe-dependent AOM. Aside from Fe(III), other electron acceptors coupled to AOM include sulfate, nitrate/nitrite, humic substances, and other oxidized metal species (e.g., Mn(IV)) (Beal et al., 2009; Knittel and Boetius, 2009; Haroon et al., 2013; Scheller et al., 2016). Given that sulfate reduction rates and nitrate/nitrite concentrations were below detection limit in this depth section, AOM is likely not coupled to sulfate and nitrate/nitrite reduction. The extremely low TOC content at 6–12 cm can further eliminate humic substances, which are a major part of the TOC pool in sediments (MacCarthy, 2001; Wang et al., 2015), as electron acceptors. Mn(IV)-dependent AOM is a possible process, albeit it remains a minor contributor to metal-catalyzed AOM in natural settings. This limited impact is attributed to the relatively low abundance of manganese in sediment, with mass ratios to aluminum averaging approximately 0.005 (for Mn/Al) compared to approximately 0.6 for iron (Fe/Al) in the studied region (Shiller et al., 1985). Accordingly, Mn(IV) and its coupling to AOM were not determined in this study.

It should be noted that salinity and sulfate concentrations in the core from the Krause and Treude (2021) study were different from this study. The porewater concentrations of methane, sulfate, and salinity in the sediment core during the 2018 sampling were 26 ± 7 μM, 68 ± 3 mM, and 119 ± 7 PSU, respectively (Figure S2). Methane concentrations were similar to the 2022 core (21 ± 5 μM),

whereas sulfate concentrations and salinity were substantially higher in the 2022 core (114 ± 28 mM, and 264 ± 47 PSU, respectively), pointing to an advanced evaporation phase in the present study. However, we are confident that the vertical distribution of AOM and sulfate reduction remained very similar between the sampling events as the coloring of the sediment layers and their vertical extension did not change between sampling (Figure S2). In the following sections, we will focus on the environmental conditions under which Fe-dependent AOM occurs, as well as the relationship between AOM and the biogeochemical cycling of carbon, sulfur, and iron in the hypersaline pool.

Evolution of Sediment Property and Microbial Activity in the Hypersaline Pool

The hypersaline pool was created by human activity. In 1945, an oil company conducted an exploratory drilling operation in the CSMR (Ferren, 1985). Although the well never entered into sustained production and the derrick was dismantled, the drilling process inadvertently created a depression that served as a reservoir for water accumulation, comprising both freshwater from precipitation and seawater from storm events. The original sediments in the pool were composed of organic-poor but Fe-oxide-rich clay as ubiquitously observed in the salt marsh. Some of the Fe oxides are sourced from riverine input from neighboring mountains, while others may be due to oxidative precipitation of groundwater-derived ferrous iron (Charette and Sholkovitz, 2002). Over time, the pool started to accumulate labile organic matter such as plant debris from the surroundings and dead algae that grew in the pool, in addition to the microbial mat at the sediment surface, which has fueled enhanced organic matter degradation in surface sediment.

Among all the degradation pathways, microbial iron reduction and sulfate reduction are particularly important for the changes in the mineral composition of the sediment. Sulfate reduction competes with microbial iron reduction for the same electron donors, which are typically fermentation products (Jørgensen, 2021). Although iron reducers may be favored by the higher energy yield of their metabolism, they are limited by the availability of solid-phase Fe(III) minerals, while sulfate reducers are not electron-acceptor-limited in shallow marine sediment settings (Postma and Jakobsen, 1996; Michaud et al., 2020). The aqueous sulfide produced through microbial sulfate reduction is highly reactive and reduces Fe oxides abiotically and thereby competes with microbial iron reduction for thermodynamically favorable, poorly crystalline Fe oxides (Poulton et al., 2004; Laufer et al., 2020). The reductive dissolution of Fe oxides subsequently leads to the formation of Fe monosulfide (FeS) and ultimately pyrite (FeS_2) (Rickard and Luther, 2007), as shown by the high AVS and CRS contents in the uppermost sediment (Figure 1J). This diagenetic transformation results in the exhaustion of microbially reducible Fe(III) (Holmkvist et al., 2014; Liu et al., 2020), eliminating the occurrence of microbial iron reduction in the FeS-rich layer where sulfate reduction dominates organic matter mineralization (Figure 1F, 1H). The highest sulfate reduction rates detected at the sediment surface are driven by the recent deposition of labile organic matter as indicated by the extremely high TOC content (Figure 1C, 1F).

Sulfate reduction is below detection limit in the subsurface FeOx-rich sediments, whereas the peak in dissolved Fe^{2+} concentration indicates the occurrence of iron reduction (Figure 1E, 1F). This upside-down redox cascade is likely due to the relatively low organic carbon content below 6 cm (0.9 ± 0.2 wt. %). Here, the recalcitrant nature of the organic matter hinders its degradation rate,

and the high availability of microbially reducible Fe(III) allows microbial iron reduction to compete with, and therefore suppress, sulfate reduction (Holmkvist et al., 2014; Liu et al., 2020; Jørgensen, 2021). The upward Fe^{2+} flux further fuels the formation of Fe sulfides at the transition between the two layers, commonly referred to as the sulfidization front in the Baltic and Black Seas (Jørgensen et al., 2004; Holmkvist et al., 2014; Liu et al., 2020). Taken together, the hypersaline pool presents an example of how human activity significantly changed the biogeochemical cycles of carbon, sulfur, and iron in a coastal wetland, and how the timing of diagenetic transformations of sulfur and iron leads to very distinct microbial activity in the sediment where the FeS- and FeOx-rich layers are dominated by microbial sulfate and iron reduction, respectively.

Electron Acceptors for Anaerobic Oxidation of Methane

Based on the geochemical profiles, we suggest that AOM is primarily coupled to either sulfate reduction or iron reduction in the FeS-rich and FeOx-rich layers, respectively. Accordingly, we designed and conducted sediment slurry incubation experiments to elucidate the electron acceptors involved in AOM in each layer. In previous studies, ^{13}C-labelled methane was more commonly used as a tracer to track AOM activity in long-term incubations with a series of substrates and inhibitors (Beal et al., 2009; Sivan et al., 2011; Egger et al., 2015b; Bar-Or et al., 2017; Mostovaya et al., 2022; Vigderovich et al., 2022). The use of ^{13}C-labelled methane has the advantage of enriching the microbial biomass and allowing the track of microbial activity over an extended period of time, while the rates may not remain stable over the same period. On the other hand, ^{14}C- and ^{35}S-radiotracer techniques are highly sensitive and effective in quantifying microbial turnover rates in short-term incubations (e.g., 6 hours to 2 days) and the rate is expected to be more stable

(Segarra et al., 2013; Treude et al., 2014; Xu et al., 2021). One should note that environmental conditions in sediment slurries are strongly altered compared to the intact sediment and hence the balance and rates of processes may be affected. By further disrupting the balance of microbial processes using substrates and inhibitors, however, we can gain insights into the reactions linked to AOM.

In this study, we employed ^{14}C-methane and ^{35}S-sulfate radiotracers to track the activity of AOM and sulfate reduction. We set up a series of incubations, using amorphous Fe(III) oxyhydroxide and ferrihydrite to provide microbially reducible Fe(III), and adding molybdate to inhibit sulfate reduction and aqueous sulfide to remove microbially reducible Fe oxides and thereby inhibiting iron reduction. High sulfate reduction rates, up to 149 nmol SO_4^{2-} per cm^3 of diluted sediment slurry per day, were detected in the FeS-rich layer in incubations without molybdate, while sulfate reduction was nearly completely inhibited (down to 0.1% of the non-inhibited rate) in the molybdate incubation (Figure 2A). In the FeOx-rich layer, extremely low sulfate reduction activity was detected (10–100 pmol SO_4^{2-} cm^{-3} d^{-1}) in incubations without molybdate, and activity was undetectable in incubations with molybdate. These results are consistent with the ex-situ rates determined by the whole-round core technique (Figure 1F), where sulfate reduction was only detected in the S-rich layer. In addition to inhibitors, the introduction of electron acceptors can also lead to a reduction in the sulfate reduction rate. For example, introducing Fe oxides, in particular ferrihydrite, to the incubations tends to lower sulfate reduction rates (Figure 2A) because the microbial reduction of newly added Fe oxides yields more free energy than sulfate reduction, and thereby partially suppress sulfate reduction (Postma and Jakobsen, 1996; Thamdrup, 2000).

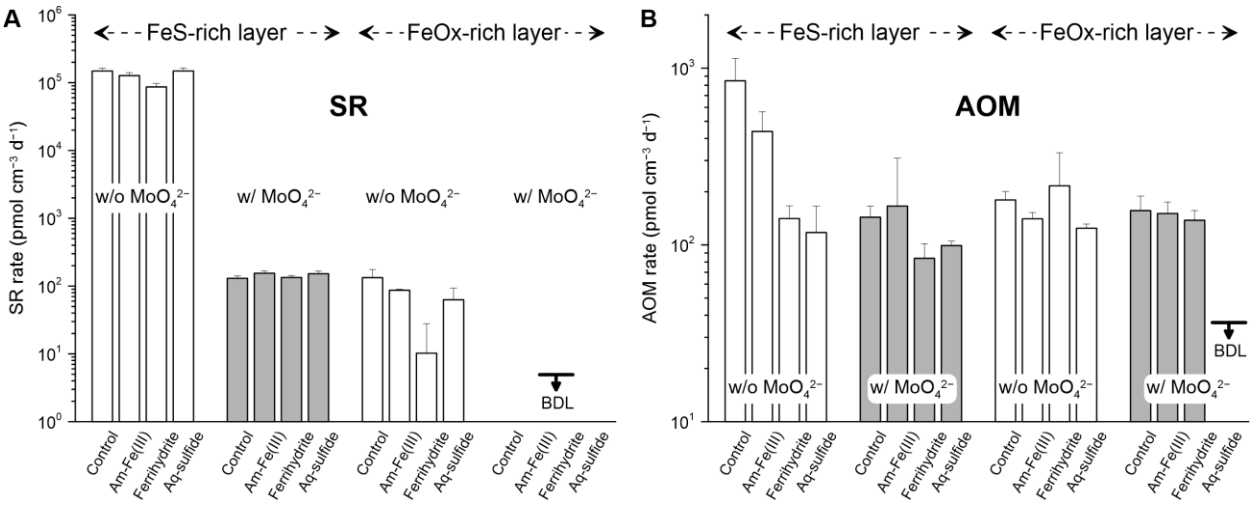

Fig. 5-2 Rates of sulfate reduction (SR) and anaerobic oxidation of methane (AOM) from slurry incubation experiments. The incubations lasted for two days. Control refers to the unamended sediment slurry, i.e., without the addition of inhibitors or substrates. Am-Fe(III), Aq-sulfide, and BDL represent amorphous Fe(III) oxyhydroxide, aqueous sulfide, and below detection limits, respectively. Amorphous Fe(III) oxyhydroxide and ferrihydrite are termed Fe oxides in the main text. The y-axes are displayed using a logarithmic scale. Error bars are 1σ error.

Similar to sulfate reduction, AOM rates in the FeS-rich layer were the highest in the incubation without molybdate (~848 pmol CH_4 cm^{-3} d^{-1}), whereas adding molybdate reduced the AOM rate by 80%, indicating that AOM is mostly coupled to sulfate reduction (Figure 2B). Notably, however, AOM was still active on the order of 100 pmol CH_4 cm^{-3} d^{-1} in incubations with molybdate, implying the use of other electron acceptors in parallel to sulfate. Two potential electron acceptor candidates are humic substances and nitrate/nitrite. Indeed, the ex-situ AOM rates from 2018 (Krause and Treude, 2021) showed one peak at the sediment surface (Figure 1F), where the highest TOC and nitrate/nitrite concentrations were found (Figures 1H, 1J). Introducing Fe oxides to the

FeS-rich layer did not stimulate AOM activity (Figure 2B), suggesting that the microbial communities here were not able to switch to Fe-driven AOM in the course of the incubation, possibly because of sluggish growth rate of minority populations of ANME performing Fe-AOM and/or the involvement of special structures such as cytochrome c proteins and pili for iron reduction (McGlynn et al., 2015; Wegener et al., 2015). As discussed, the addition of Fe oxides decreased sulfate reduction rates in the FeS-rich layer (Figure 2A). Since AOM was largely coupled to sulfate reduction, introducing Fe oxides thereby reduced AOM rates in incubations without molybdate. Another unexpected observation was that adding aqueous sulfide (5 mM) did not change the rate of sulfate reduction, but significantly decreased AOM activity (Figure 2), implying a differential toxicity of aqueous sulfide to the two groups of microorganisms.

In the FeOx-rich layer, the AOM rates were nearly constant (on average of 159 pmol cm^{-3} d^{-1}) across the four sets of incubations without molybdate (Figure 2B). The addition of Fe oxides did not stimulate AOM activity, possibly because in-situ Fe oxides were already available in non-limiting concentrations. AOM activity was not reduced in incubations with molybdate, suggesting that the process was not coupled to sulfate reduction but likely to iron reduction as implied by geochemical profiles (Figure 1). The addition of aqueous sulfide showed different results with and without molybdate. When sediment slurries were treated with both aqueous sulfide and molybdate, AOM was below the detection limit, suggesting that both iron and sulfate reduction coupled to AOM were inhibited. On the other hand, when aqueous sulfide was added without molybdate, only iron reduction was inhibited, allowing sulfate reduction coupled to AOM to gain more advantage and thereby maintaining AOM activity. Overall, the incubation data from the FeOx-rich layer demonstrates that AOM is indeed coupled to iron reduction but can be switched to sulfate reduction

when Fe oxides are not available. Further, comparing the AOM rates in both layers, we infer that the transitioning from Fe-driven AOM to sulfate-driven AOM is more feasible than the reverse scenario.

Environmental Implications

In anoxic wetland sediments, methane commonly undergoes anaerobic oxidation, effectively mitigating its release into the atmosphere (Knittel and Boetius, 2009; Segarra et al., 2013). To evaluate the importance of each AOM pathway at the study site, we convert the measured ex-situ volumetric rates (Krause and Treude, 2021) to depth-integrated areal rates. The depth-integrated sulfate- and Fe-driven AOM rates were calculated to be 0.22 and 0.78 mmol m^{-2} d^{-1}, respectively, under the assumption that sulfate and Fe oxides serve as the sole electron acceptors within each layer. This comparison indicates that Fe-AOM is the major pathway of methane oxidation in the hypersaline pool. This finding is in contrast to offshore marine sediments where most of the methane is oxidized by sulfate-driven AOM in the SMTZ (Niewöhner et al., 1998; Knittel and Boetius, 2009). In the deep subsurface of marine sediments, Fe-AOM is commonly found below the SMTZ, because methane rarely penetrates the upper iron reducing zone, but it only accounts for a very minor fraction of total methane removal in typical marine sediments (e.g., ~3% in the Baltic Sea) (Egger et al., 2015b; Wallenius et al., 2021). This can be attributed to the low reactivity of Fe oxides in the deep subsurface. As Fe(III)-bearing minerals are buried down through the surface sediments, the most reactive fraction is readily consumed by organoclastic iron reduction and abiotic reductive dissolution by sulfide, leaving the Fe(III)-minerals below the SMTZ to be less reactive and bioavailable compared to the ones at the sediment surface (Raiswell and Canfield, 2012; Riedinger et al., 2014). In coastal wetlands, however, fresh reactive Fe oxides are pervasive

from terrestrial inputs, providing ideal conditions for the occurrence of Fe-AOM. In addition to sulfate-driven AOM, Fe-AOM may act as a major sink for methane in wetland sediments, significantly mitigating methane emissions from wetlands. Given the 8:1 Fe−CH_4 stoichiometry, the strong Fe^{2+} production from Fe-AOM could enhance the sequestration of phosphorus through the formation of Fe(II)-phosphate minerals (e.g., vivianite; Figures 1J), potentially limiting the degree of coastal eutrophication (Egger et al., 2015b; Liu et al., 2018). We stress that the importance of Fe-AOM likely varies between diverse types of wetlands due to different environmental conditions, such as the availability of organic matter, sulfate, and reactive Fe oxides. Although the biogeochemical zonation observed in this study is specific to organic-rich sediment overlying organic-poor sediment (e.g., the Baltic and Black Seas), the interaction between methane and electron acceptors is broadly relevant to wetlands and other natural environments. Given that iron oxides are pervasive in wetlands (Yu et al., 2021), we conclude that Fe-AOM in FeOx-rich wetlands has the potential to significantly impact the biogeochemical cycles of carbon, sulfur, iron, and phosphorus, with intrinsic connections to climate change and eutrophication (Figure 3).

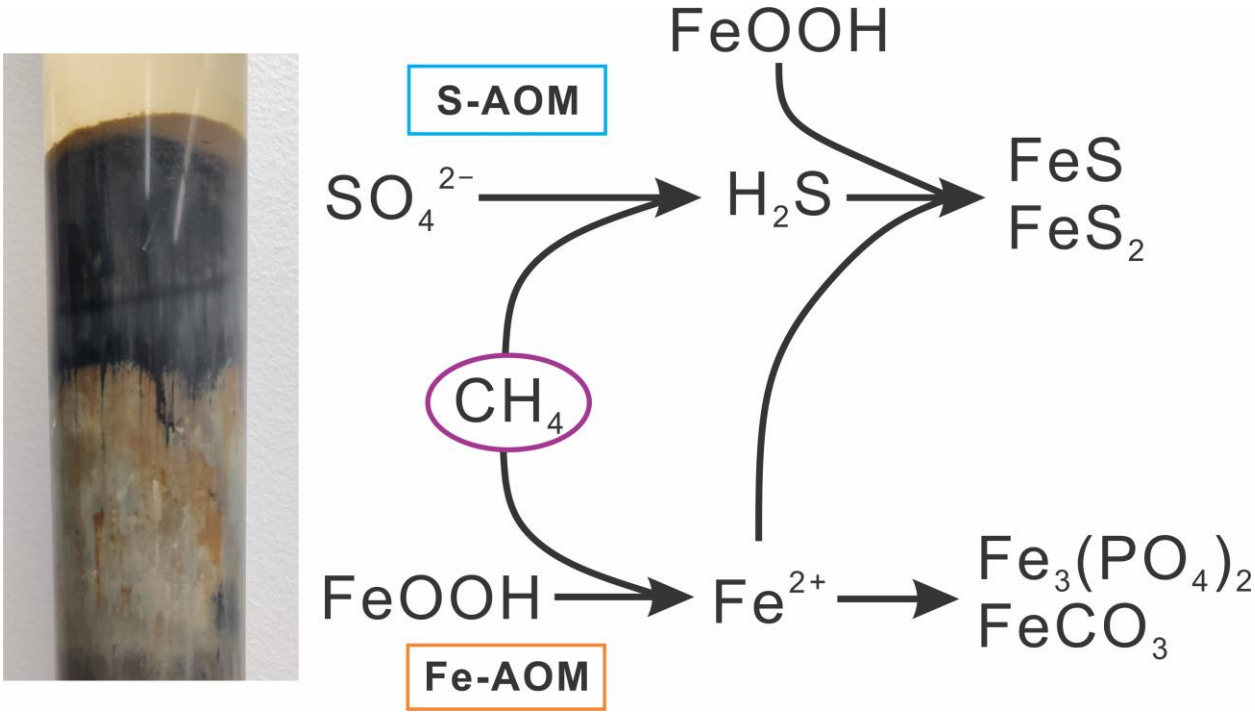

Fig. 5-3 Schematic representation of the carbon-sulfur-iron cycles within the hypersaline pool of the studied salt marsh, integrating sulfate- and iron-driven anaerobic oxidation of methane into the broader context of biogeochemical dynamics.

ACKNOWLEDGMENTS

We thank the University of California Natural Reserve System and the Project Scientist of the Carpinteria Salt Marsh Reserve, A. Brooks, for authorizing the field sampling. We acknowledge G. Vetushko, D. Robinson, M. Hasnain, E. Lim, D.J. Yousavich, T. Holzmann, B. Cloutier, M. Lin, M. Puls, and S. Lenkin for assistance during sampling and laboratory work. This work was funded by the National Science Foundation (Award No.: 1852912) and the NASA FINESST Fellowship (Award No.: 80NSSC21K1529).

References

Aller R.C. and Rude P.D. (1988) Complete oxidation of solid phase sulfides by manganese and bacteria in anoxic marine sediments. *Geochim. Cosmochim. Acta* **52**, 751-765.

Aromokeye D.A., Kulkarni A.C., Elvert M., Wegener G., Henkel S., Coffinet S., Eickhorst T., Oni O.E., Richter-Heitmann T., Schnakenberg A., Taubner H., Wunder L., Yin X., Zhu Q., Hinrichs K.-U., Kasten S. and Friedrich M.W. (2020) Rates and Microbial Players of Iron-Driven Anaerobic Oxidation of Methane in Methanic Marine Sediments. *Front. Microbiol.* **10**.

Bai Y.-N., Wang X.-N., Wu J., Lu Y.-Z., Fu L., Zhang F., Lau T.-C. and Zeng R.J. (2019) Humic substances as electron acceptors for anaerobic oxidation of methane driven by ANME-2d. *Water Res.* **164**, 114935.

Bar-Or I., Elvert M., Eckert W., Kushmaro A., Vigderovich H., Zhu Q., Ben-Dov E. and Sivan O. (2017) Iron-coupled anaerobic oxidation of methane performed by a mixed bacterial-archaeal community based on poorly reactive minerals. *Environ. Sci. Technol.* **51**, 12293-12301.

Beal E.J., House C.H. and Orphan V.J. (2009) Manganese-and iron-dependent marine methane oxidation. *Science* **325**, 184-187.

Boetius A., Ravenschlag K., Schubert C.J., Rickert D., Widdel F., Gieseke A., Amann R., Jørgensen B.B., Witte U. and Pfannkuche O. (2000) A marine microbial consortium apparently mediating anaerobic oxidation of methane. *Nature* **407**, 623-626.

Bridgham S.D., Cadillo-Quiroz H., Keller J.K. and Zhuang Q. (2013) Methane emissions from wetlands: biogeochemical, microbial, and modeling perspectives from local to global scales. *Global Change Biol.* **19**, 1325-1346.

Cai C., Leu A.O., Xie G.-J., Guo J., Feng Y., Zhao J.-X., Tyson G.W., Yuan Z. and Hu S. (2018) A methanotrophic archaeon couples anaerobic oxidation of methane to Fe(III) reduction. *The ISME Journal* **12**, 1929-1939.

Charette M.A. and Sholkovitz E.R. (2002) Oxidative precipitation of groundwater-derived ferrous iron in the subterranean estuary of a coastal bay. *Geophys. Res. Lett.* **29**, 85-81-85-84.

Chowdhury T.R. and Dick R.P. (2013) Ecology of aerobic methanotrophs in controlling methane fluxes from wetlands. *Applied Soil Ecology* **65**, 8-22.

Cline J.D. (1969) Spectrophotometric determination of hydrogen sulfide in natural waters. *Limnol. Oceanogr.* **14**, 454-458.

Des Marais D.J. and Canfield D.E. (1994) The carbon isotope biogeochemistry of microbial mats, in: Stal L.J., Caumette P. (Eds.), Microbial Mats. Springer Berlin Heidelberg, Berlin, Heidelberg, pp. 289-298.

Dlugokencky E.J., Nisbet E.G., Fisher R. and Lowry D. (2011) Global atmospheric methane: budget, changes and dangers. *Philosophical Transactions of the Royal Society A: Mathematical, Physical and Engineering Sciences* **369**, 2058-2072.

Egger M., Hagens M., Sapart C.J., Dijkstra N., van Helmond N.A., Mogollón J.M., Risgaard-Petersen N., van der Veen C., Kasten S. and Riedinger N. (2017) Iron oxide reduction in methane-rich deep Baltic Sea sediments. *Geochim. Cosmochim. Acta* **207**, 256-276.

Egger M., Jilbert T., Behrends T., Rivard C. and Slomp C.P. (2015a) Vivianite is a major sink for phosphorus in methanogenic coastal surface sediments. *Geochim. Cosmochim. Acta* **169**, 217-235.

Egger M., Rasigraf O., Sapart C.l.J., Jilbert T., Jetten M.S., Röckmann T., van der Veen C., Bândă N., Kartal B. and Ettwig K.F. (2015b) Iron-mediated anaerobic oxidation of methane in brackish coastal sediments. *Environ. Sci. Technol.* **49**, 277-283.

Ettwig K.F., Butler M.K., Le Paslier D., Pelletier E., Mangenot S., Kuypers M.M.M., Schreiber F., Dutilh B.E., Zedelius J., de Beer D., Gloerich J., Wessels H.J.C.T., van Alen T., Luesken F., Wu M.L., van de Pas-Schoonen K.T., Op den Camp H.J.M., Janssen-Megens E.M., Francoijs K.-J., Stunnenberg H., Weissenbach J., Jetten M.S.M. and Strous M. (2010) Nitrite-driven anaerobic methane oxidation by oxygenic bacteria. *Nature* **464**, 543-548.

Ettwig K.F., Zhu B., Speth D., Keltjens J.T., Jetten M.S. and Kartal B. (2016) Archaea catalyze iron-dependent anaerobic oxidation of methane. *P. Natl. Acad. Sci. USA* **113**, 12792-12796.

Ferren W.R. (1985) Carpinteria Salt Marsh: environment, history, and botanical resources of a southern California estuary.

Fossing H. and Jørgensen B.B. (1989) Measurement of bacterial sulfate reduction in sediments: evaluation of a single-step chromium reduction method. *Biogeochemistry* **8**, 205-222.

García-Robledo E., Corzo A. and Papaspyrou S. (2014) A fast and direct spectrophotometric method for the sequential determination of nitrate and nitrite at low concentrations in small volumes. *Mar. Chem.* **162**, 30-36.

Grasshoff K., Kremling K. and Ehrhardt M. (1999) Methods of seawater analysis. John Wiley & Sons.

Haroon M.F., Hu S., Shi Y., Imelfort M., Keller J., Hugenholtz P., Yuan Z. and Tyson G.W. (2013) Anaerobic oxidation of methane coupled to nitrate reduction in a novel archaeal lineage. *Nature* **500**, 567-570.

He Z., Zhang Q., Feng Y., Luo H., Pan X. and Gadd G.M. (2018) Microbiological and environmental significance of metal-dependent anaerobic oxidation of methane. *Sci. Total Environ.* **610**, 759-768.

Holmkvist L., Kamyshny Jr A., Bruechert V., Ferdelman T.G. and Jørgensen B.B. (2014) Sulfidization of lacustrine glacial clay upon Holocene marine transgression (Arkona Basin, Baltic Sea). *Geochim. Cosmochim. Acta* **142**, 75-94.

Jørgensen B.B. (2021) Sulfur Biogeochemical Cycle of Marine Sediments. *Geochem. Perspect.* **10**, 145-146.

Jørgensen B.B., Böttcher M.E., Lüschen H., Neretin L.N. and Volkov I.I. (2004) Anaerobic methane oxidation and a deep H2S sink generate isotopically heavy sulfides in Black Sea sediments. *Geochim. Cosmochim. Acta* **68**, 2095-2118.

Kallmeyer J., Ferdelman T.G., Weber A., Fossing H. and Jørgensen B.B. (2004) A cold chromium distillation procedure for radiolabeled sulfide applied to sulfate reduction measurements. *Limnol. Oceanogr. Methods* **2**, 171-180.

Knittel K. and Boetius A. (2009) Anaerobic oxidation of methane: progress with an unknown process. *Annu. Rev. Microbiol.* **63**, 311-334.

Krause S.J.E. and Treude T. (2021) Deciphering cryptic methane cycling: Coupling of methylotrophic methanogenesis and anaerobic oxidation of methane in hypersaline coastal wetland sediment. *Geochim. Cosmochim. Acta* **302**, 160-174.

Laso-Pérez R., Krukenberg V., Musat F. and Wegener G. (2018) Establishing anaerobic hydrocarbon-degrading enrichment cultures of microorganisms under strictly anoxic conditions. *Nature Protocols* **13**, 1310-1330.

Laufer K., Michaud A.B., Røy H. and Jørgensen B.B. (2020) Reactivity of Iron Minerals in the Seabed Toward Microbial Reduction – A Comparison of Different Extraction Techniques. *Geomicrobiol. J.* **37**, 170-189.

Le Mer J. and Roger P. (2001) Production, oxidation, emission and consumption of methane by soils: A review. *European Journal of Soil Biology* **37**, 25-50.

Liu J., Izon G., Wang J., Antler G., Wang Z., Zhao J. and Egger M. (2018) Vivianite formation in methane-rich deep-sea sediments from the South China Sea. *Biogeosciences* **15**, 6329-6348.

Liu J., Pellerin A., Antler G., Kasten S., Findlay A.J., Dohrmann I., Røy H., Turchyn A.V. and Jørgensen B.B. (2020) Early diagenesis of iron and sulfur in Bornholm Basin sediments: The role of near-surface pyrite formation. *Geochim. Cosmochim. Acta* **284**, 43-60.

Lovley D.R. and Phillips E.J.P. (1986) Organic Matter Mineralization with Reduction of Ferric Iron in Anaerobic Sediments. *Appl. Environ. Microbiol.* **51**, 683-689.

MacCarthy P. (2001) THE PRINCIPLES OF HUMIC SUBSTANCES. *Soil Science* **166**, 738-751.

McGlynn S.E., Chadwick G.L., Kempes C.P. and Orphan V.J. (2015) Single cell activity reveals direct electron transfer in methanotrophic consortia. *Nature* **526**, 531.

Michaud A.B., Laufer K., Findlay A., Pellerin A., Antler G., Turchyn A.V., Røy H., Wehrmann L.M. and Jørgensen B.B. (2020) Glacial influence on the iron and sulfur cycles in Arctic fjord sediments (Svalbard). *Geochim. Cosmochim. Acta* **280**, 423-440.

Mitchell J.F.B. (1989) The “Greenhouse” effect and climate change. *Rev. Geophys.* **27**, 115-139.

Mostovaya A., Wind-Hansen M., Rousteau P., Bristow L.A. and Thamdrup B. (2022) Sulfate- and iron-dependent anaerobic methane oxidation occurring side-by-side in freshwater lake sediment. *Limnol. Oceanogr.* **67**, 231-246.

Niewöhner C., Hensen C., Kasten S., Zabel M. and Schulz H.D. (1998) Deep Sulfate Reduction Completely Mediated by Anaerobic Methane Oxidation in Sediments of the Upwelling Area off Namibia. *Geochim. Cosmochim. Acta* **62**, 455-464.

Nisbet E.G., Manning M.R., Dlugokencky E.J., Fisher R.E., Lowry D., Michel S.E., Myhre C.L., Platt S.M., Allen G., Bousquet P., Brownlow R., Cain M., France J.L., Hermansen O., Hossaini R., Jones A.E., Levin I., Manning A.C., Myhre G., Pyle J.A., Vaughn B.H., Warwick N.J. and White J.W.C. (2019) Very Strong Atmospheric Methane Growth in the 4 Years 2014–2017: Implications for the Paris Agreement. *Global Biogeochem. Cycles* **33**, 318-342.

Norði K.à., Thamdrup B. and Schubert C.J. (2013) Anaerobic oxidation of methane in an iron-rich Danish freshwater lake sediment. *Limnol. Oceanogr.* **58**, 546-554.

Postma D. and Jakobsen R. (1996) Redox zonation: Equilibrium constraints on the Fe(III)/SO4-reduction interface. *Geochim. Cosmochim. Acta* **60**, 3169-3175.

Poulton S.W. (2021) The Iron Speciation Paleoredox Proxy. Cambridge University Press, Cambridge.

Poulton S.W. and Canfield D.E. (2005) Development of a sequential extraction procedure for iron: implications for iron partitioning in continentally derived particulates. *Chem. Geol.* **214**, 209-221.

Poulton S.W., Krom M.D. and Raiswell R. (2004) A revised scheme for the reactivity of iron (oxyhydr) oxide minerals towards dissolved sulfide. *Geochim. Cosmochim. Acta* **68**, 3703-3715.

Raghoebarsing A.A., Pol A., van de Pas-Schoonen K.T., Smolders A.J.P., Ettwig K.F., Rijpstra W.I.C., Schouten S., Damsté J.S.S., Op den Camp H.J.M., Jetten M.S.M. and Strous M. (2006) A microbial consortium couples anaerobic methane oxidation to denitrification. *Nature* **440**, 918-921.

Raiswell R. and Canfield D.E. (2012) The iron biogeochemical cycle past and present. *Geochem. Perspect.* **1**, 19-41.

Reeburgh W.S. (2007) Global Methane Biogeochemistry, in: Holland H.D., Turekian K.K. (Eds.), Treatise on Geochemistry. Pergamon, Oxford, pp. 1-32.

Repeta D.J., Ferrón S., Sosa O.A., Johnson C.G., Repeta L.D., Acker M., DeLong E.F. and Karl D.M. (2016) Marine methane paradox explained by bacterial degradation of dissolved organic matter. *Nat. Geosci.* **9**, 884-887.

Rickard D. and Luther G.W. (2007) Chemistry of Iron Sulfides. *Chem. Rev.* **107**, 514-562.

Riedinger N., Formolo M.J., Lyons T.W., Henkel S., Beck A. and Kasten S. (2014) An inorganic geochemical argument for coupled anaerobic oxidation of methane and iron reduction in marine sediments. *Geobiology* **12**, 172-181.

Ruttenberg K.C. (2014) The Global Phosphorus Cycle, in: Turekian K.K. (Ed.), Treatise on Geochemistry (Second Edition). Elsevier, Oxford, pp. 499-558.

Saunois M., Stavert A.R., Poulter B., Bousquet P., Canadell J.G., Jackson R.B., Raymond P.A., Dlugokencky E.J., Houweling S., Patra P.K., Ciais P., Arora V.K., Bastviken D., Bergamaschi P., Blake D.R., Brailsford G., Bruhwiler L., Carlson K.M., Carrol M.,

Castaldi S., Chandra N., Crevoisier C., Crill P.M., Covey K., Curry C.L., Etiope G., Frankenberg C., Gedney N., Hegglin M.I., Höglund-Isaksson L., Hugelius G., Ishizawa M., Ito A., Janssens-Maenhout G., Jensen K.M., Joos F., Kleinen T., Krummel P.B., Langenfelds R.L., Laruelle G.G., Liu L., Machida T., Maksyutov S., McDonald K.C., McNorton J., Miller P.A., Melton J.R., Morino I., Müller J., Murguia-Flores F., Naik V., Niwa Y., Noce S., O'Doherty S., Parker R.J., Peng C., Peng S., Peters G.P., Prigent C., Prinn R., Ramonet M., Regnier P., Riley W.J., Rosentreter J.A., Segers A., Simpson I.J., Shi H., Smith S.J., Steele L.P., Thornton B.F., Tian H., Tohjima Y., Tubiello F.N., Tsuruta A., Viovy N., Voulgarakis A., Weber T.S., van Weele M., van der Werf G.R., Weiss R.F., Worthy D., Wunch D., Yin Y., Yoshida Y., Zhang W., Zhang Z., Zhao Y., Zheng B., Zhu Q., Zhu Q. and Zhuang Q. (2020) The Global Methane Budget 2000–2017. *Earth Syst. Sci. Data* **12**, 1561-1623.

Scheller S., Yu H., Chadwick G.L., McGlynn S.E. and Orphan V.J. (2016) Artificial electron acceptors decouple archaeal methane oxidation from sulfate reduction. *Science* **351**, 703-707.

Schwertmann U. and Cornell R.M. (2000) Ferrihydrite, Iron Oxides in the Laboratory, pp. 103-112.

Segarra K.E., Comerford C., Slaughter J. and Joye S.B. (2013) Impact of electron acceptor availability on the anaerobic oxidation of methane in coastal freshwater and brackish wetland sediments. *Geochim. Cosmochim. Acta* **115**, 15-30.

Shi L.-D., Guo T., Lv P.-L., Niu Z.-F., Zhou Y.-J., Tang X.-J., Zheng P., Zhu L.-Z., Zhu Y.-G., Kappler A. and Zhao H.-P. (2020) Coupled anaerobic methane oxidation and reductive arsenic mobilization in wetland soils. *Nat. Geosci.* **13**, 799-805.

Shiller A.M., Gieskes J.M. and Brian Price N. (1985) Particulate iron and manganese in the Santa Barbara Basin, California. *Geochim. Cosmochim. Acta* **49**, 1239-1249.

Sivan O., Adler M., Pearson A., Gelman F., Bar-Or I., John S.G. and Eckert W. (2011) Geochemical evidence for iron-mediated anaerobic oxidation of methane. *Limnol. Oceanogr.* **56**, 1536-1544.

Stookey L.L. (1970) Ferrozine---a new spectrophotometric reagent for iron. *Anal. Chem.* **42**, 779-781.

Thamdrup B. (2000) Bacterial Manganese and Iron Reduction in Aquatic Sediments, in: Schink B. (Ed.), Advances in Microbial Ecology. Springer US, Boston, MA, pp. 41-84.

Treude T., Krause S., Maltby J., Dale A.W., Coffin R. and Hamdan L.J. (2014) Sulfate reduction and methane oxidation activity below the sulfate-methane transition zone in Alaskan Beaufort Sea continental margin sediments: Implications for deep sulfur cycling. *Geochim. Cosmochim. Acta* **144**, 217-237.

Vigderovich H., Eckert W., Elul M., Rubin-Blum M., Elvert M. and Sivan O. (2022) Long-term incubations provide insight into the mechanisms of anaerobic oxidation of methane in methanogenic lake sediments. *Biogeosciences* **19**, 2313-2331.

Wallenius A.J., Dalcin Martins P., Slomp C.P. and Jetten M.S.M. (2021) Anthropogenic and Environmental Constraints on the Microbial Methane Cycle in Coastal Sediments. *Front. Microbiol.* **12**.

Wang P., Liu Y., Li L., Cheng K., Zheng J., Zhang X., Zheng J., Joseph S. and Pan G. (2015) Long-term rice cultivation stabilizes soil organic carbon and promotes soil microbial activity in a salt marsh derived soil chronosequence. *Scientific Reports* **5**, 15704.

Wankel S.D., Adams M.M., Johnston D.T., Hansel C.M., Joye S.B. and Girguis P.R. (2012) Anaerobic methane oxidation in metalliferous hydrothermal sediments: influence on carbon flux and decoupling from sulfate reduction. *Environ. Microbiol.* **14**, 2726-2740.

Wegener G., Krukenberg V., Riedel D., Tegetmeyer H.E. and Boetius A. (2015) Intercellular wiring enables electron transfer between methanotrophic archaea and bacteria. *Nature* **526**, 587.

Xu L., Zhuang G.-C., Montgomery A., Liang Q., Joye S.B. and Wang F. (2021) Methyl-compounds driven benthic carbon cycling in the sulfate-reducing sediments of South China Sea. *Environ. Microbiol.* **23**, 641-651.

Yan Z., Joshi P., Gorski C.A. and Ferry J.G. (2018) A biochemical framework for anaerobic oxidation of methane driven by Fe (III)-dependent respiration. *Nat. commun.* **9**.

Yao X., Wang J., He M., Liu Z., Zhao Y., Li Y., Chi T., Zhu L., Zheng P., Jetten M.S.M. and Hu B. (2024) Methane-dependent complete denitrification by a single Methylomirabilis bacterium. *Nature Microbiology* **9**, 464-476.

Yu C., Xie S., Song Z., Xia S. and Åström M.E. (2021) Biogeochemical cycling of iron (hydr-)oxides and its impact on organic carbon turnover in coastal wetlands: A global synthesis and perspective. *Earth-Sci. Rev.* **218**, 103658.

Yu H., Skennerton C.T., Chadwick G.L., Leu A.O., Aoki M., Tyson G.W. and Orphan V.J. (2022) Sulfate differentially stimulates but is not respired by diverse anaerobic methanotrophic archaea. *The ISME Journal* **16**, 168-177.

Zhao Q. and Lu Y. (2023) Anaerobic oxidation of methane in terrestrial wetlands: The rate, identity and metabolism. *Sci. Total Environ.* **902**, 166049.

Supplementary Material: Liu et al. Iron oxides fuel anaerobic oxidation of methane in the presence of sulfate in hypersaline coastal wetland sediment

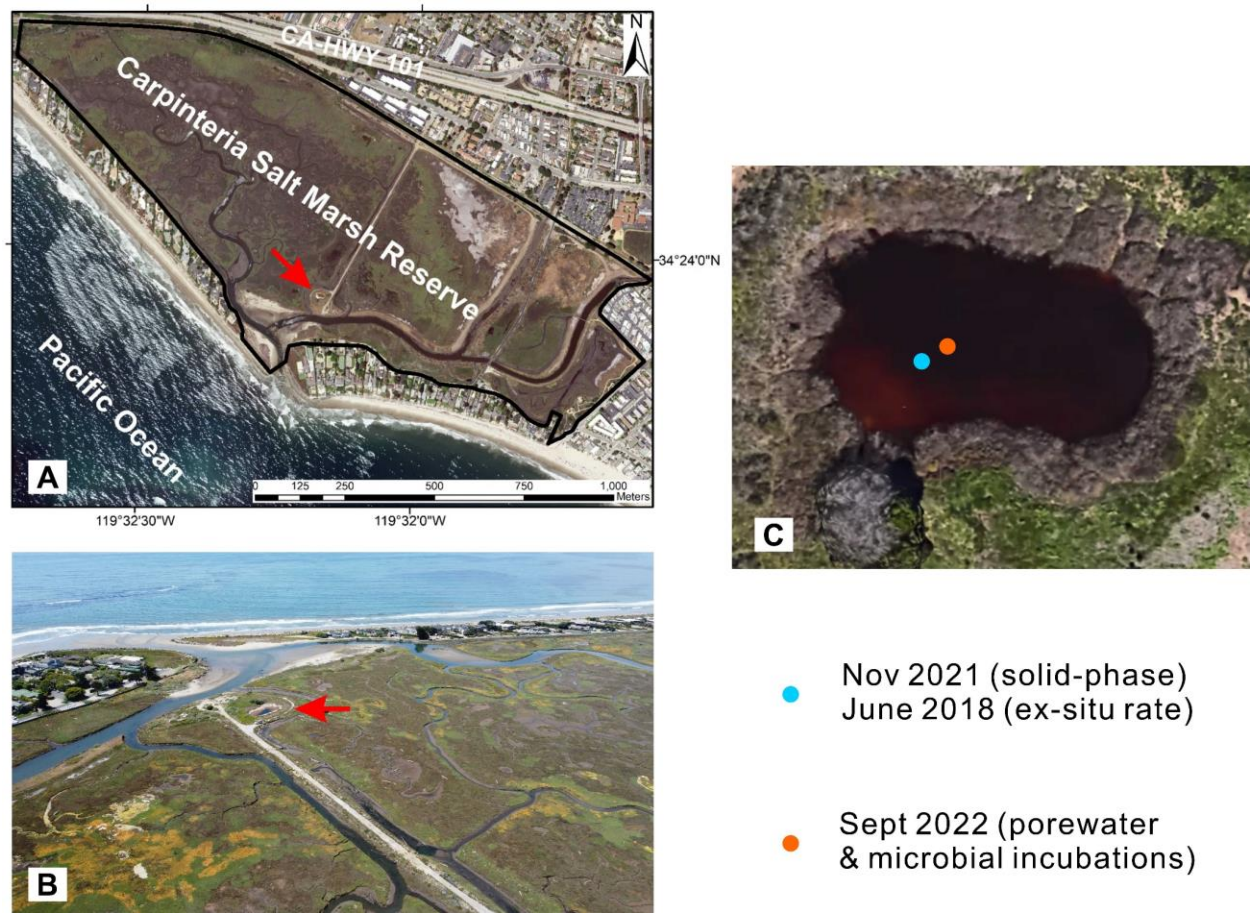

Figure 5-S1. Location of the sampled hypersaline pool. (A) Map of the Carpinteria Salt Marsh Reserve (Silva et al., 2022). (B) Aerial image of the hypersaline pool within the wider salt marsh (photo: J. Liu). The red arrows point to the hypersaline pool. (C) Satellite image of the hypersaline pool (Google Earth). The blue and orange dots represent the locations of sediment cores.

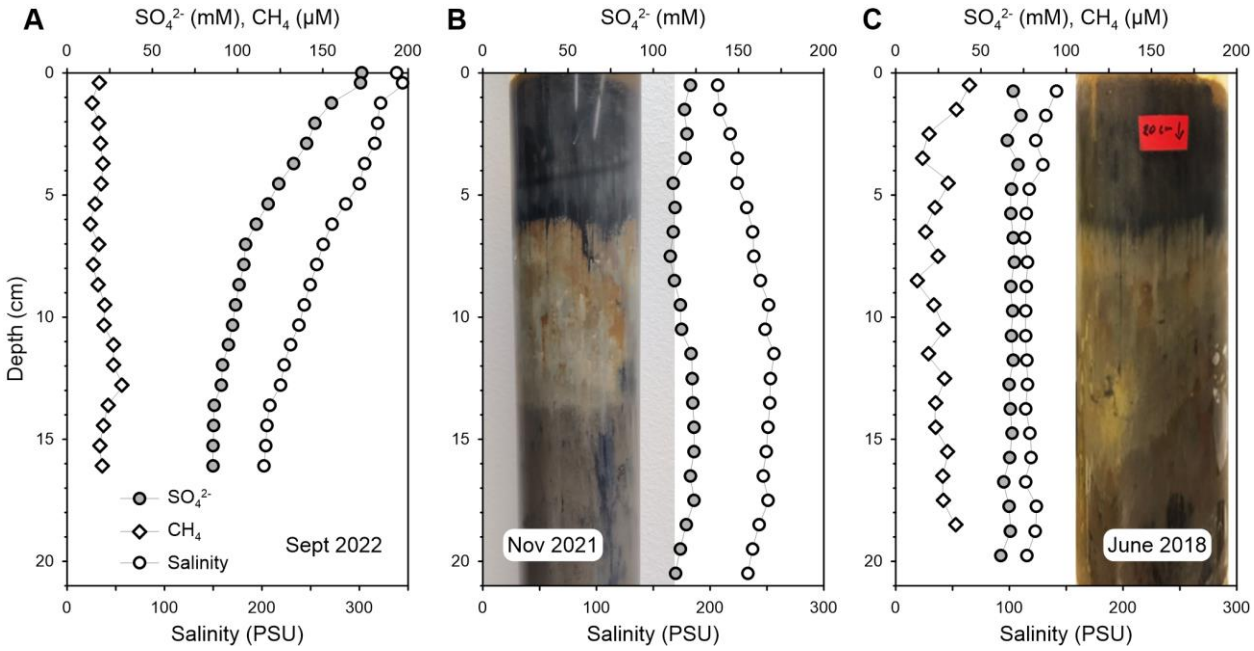

Figure 5-S2. Comparison of porewater geochemistry (sulfate, methane, salinity) across three sampling events. (A) Porewater core collected in September 2022. (B) Solid-phase core from November 2021, accompanied by a core image. (C) Ex-situ rate core from June 2018, also accompanied by a core image (Krause and Treude, 2021).

References

Krause S.J.E. and Treude T. (2021) Deciphering cryptic methane cycling: Coupling of methylotrophic methanogenesis and anaerobic oxidation of methane in hypersaline coastal wetland sediment. *Geochim. Cosmochim. Acta* **302**, 160-174.

Silva G.D., Roberts D.A., McFadden J.P. and King J.Y. (2022) Shifts in Salt Marsh Vegetation Landcover after Debris Flow Deposition. *Remote Sensing* **14**, 2819.

Chapter 6: Summary and future directions

1. Clumped isotope effects of anaerobic oxidation of methane

Chapters 2–4 focus on the clumped isotope effects of microbial methane metabolisms in anoxic environments, specifically AOM and methanogenesis. In chapter 2, we performed clumped isotopologue analysis on methane samples from laboratory microbial incubations and natural environments to elucidate the range of clumped isotope effects caused by AOM under different conditions. We present the most comprehensive dataset to date on methane clumped isotope compositions during AOM, including novel incubations with the Mcr enzyme, and a suite of sediments and fracture fluids from diverse marine and terrestrial settings across the globe. We established a connection between the isotopologue compositions of methane and the reversibility of intracellular AOM pathways. In the Svalbard slurry incubation and in Mariana natural fluids, we found extremely positive $\Delta^{12}CH_2D_2$ and $\Delta^{13}CH_3D$ values in residual methane. The measured data are modeled using closed- and open-system calculations, suggesting that the kinetic isotopologue fractionation does not differ substantially between laboratory incubations and natural environments. Additionally, the trajectories of kinetically-driven AOM remain largely consistent, regardless of the system's openness or steady-state conditions. We find that with a lower degree of reversibility, thermodynamic isotopic bond-order equilibrium in methane is achieved, observed notably in the Mcr experiment and Santa Barbara Channel and deep biosphere slurry incubations. We developed a simple, one-step isotopologue fractionation model to interpret the observed differences in $\Delta^{13}CH_3D$ and $\Delta^{12}CH_2D_2$ signatures as the thermodynamic drive and the reversibility change. We propose that the methane clumped isotope signatures of AOM, especially the kinetic

behavior, could have the potential to be diagnostic of AOM on Earth and perhaps throughout the solar system where methane has been detected. The data presented in this thesis offer new insights into distinguishing primary signatures of methane formation from biologically driven overprinting, enhancing the utility of methane clumped isotopes as effective tracers for methane formation and its subsequent processing.

The data outlined in chapter 2 have addressed many key questions regarding the clumped isotopologue effects of AOM. However, several important questions remain to be explored. For example, does clumped isotopologue fractionation vary when different electron acceptors are used? What specific conditions are needed for an AOM incubation to shift from expressing kinetic clumped isotope effects to achieving thermodynamic equilibrium among methane molecules? Why are clumped isotope fractionation and bulk isotope fractionation decoupled in the Svalbard slurry incubation? Why does AOM preferentially alter $\Delta^{13}CH_3D$ but not $\Delta^{12}CH_2D_2$ in most equilibrium-driven experiments? And how do bulk isotopes respond when clumped isotopes reach intra-species equilibrium?

Despite the global significance and widespread occurrence of AOM, no pure culture isolation of ANME is currently available (Chadwick et al., 2022). Thus, laboratory incubations of ANME enrichments remain the only viable approach to address these questions and to explicitly derive the kinetic clumped isotopologue fractionation factors for AOM. Future research should focus on sediment-free ANME enrichments from various sampling sites, conducting incubations under different conditions and with different electron acceptors. In addition, more work on natural samples is needed to understand the clumped isotope evolution of AOM in natural environments, including the diffusive sulfate-methane transition zone and advective methane seeps.

2. Clumped isotope effects of secondary methanogenesis

In chapter 3, we present data on clumped isotope compositions of methane gas from mud volcanoes in Azerbaijan, a well-characterized terrestrial methane seepage system, to better constrain the origins of methane sourced from oil and gas reservoirs. Typically, methane in petroleum reservoirs primarily originates from thermogenic sources in sedimentary basins, and its clumped isotope compositions have been reported to record thermodynamic equilibrium at the formation temperature of ca. 100–250 °C. Approximately half of the world's existing oil has undergone biodegradation, a process in which microorganisms break down heavy hydrocarbons to produce additional methane (Milkov, 2011). However, the scale of biodegradation in global petroleum accumulations and the significance of its terminal product, secondary microbial methane, in the global gas endowment and carbon cycle remain largely unknown.

To our surprise, the clumped isotope compositions of these mud volcano gases approach low-temperature thermodynamic equilibrium, reaching their ambient temperature of ~20 °C. This result is due to secondary microbial methane production from petroleum biodegradation catalyzed by the Mcr enzyme, which promotes isotopic bond re-ordering in the subsurface. This study provides the first direct evidence of clumped isotopes for microbial alteration of thermogenic methane to ambient temperature in $\Delta^{12}CH_2D_2$ vs. $\Delta^{13}CH_3D$ space, which enables secondary microbial methane to be clearly identified. More importantly, we discovered that the methane emitted into the atmosphere was predominantly a result of the microbial degradation of petroleum rather than the abiotic breakdown of organic molecules at high temperatures. During petroleum biodegradation, hydrocarbons are converted to methane, potentially significantly increasing methane emissions into the atmosphere. Therefore, it is crucial to consider the role of secondary microbial methane in biological contributions to global methane budgets. Clumped isotopes of

methane offer a unique perspective for tracking the fate of methane in oil and gas reservoirs. We propose, as others have with more circumstantial evidence, that clumped isotopes may serve as a distinct biosignature to track the activity of the Mcr enzyme in the deep biosphere.

Chapter 3 presents a compelling dataset of natural samples on secondary methanogenesis. The next step is to conduct laboratory incubations focused on methanogenic hydrocarbon biodegradation, which can occur either through syntrophic partnerships between hydrocarbon-degrading bacteria and methanogenic archaea or via alkylotrophic methanogenic archaea (Zhou et al., 2022). Future studies should aim to determine whether the clumped isotopologue effects of secondary methanogenesis observed in laboratory incubations mirror those found in natural environments.

3. Clumped isotope effects of methanogenesis

In chapter 4, we conducted clumped isotopologue analysis on methane samples from both laboratory incubations and natural environments to explore the range of clumped isotope effects from methanogenesis. Our aim was to sample methane on-site, where methanogenesis rates far exceeded AOM, and to incubate sediments for methanogenesis while adding AOM inhibitors. We show that methane molecules in thermodynamic isotope equilibrium can be produced by microbial methanogenesis alone and in the absence of anaerobic oxidation of methane. For the first time, we combined laboratory incubations with natural samples to demonstrate that this near-equilibrium methane results from limitations of free energy during methanogenesis. We support the hypothesis that slow methanogenesis with limited substrate availability leads to methane formation in or near both intra- and inter-species isotope equilibrium, providing a robust framework for interpreting

methane isotope data. Our results are analogous to expressions of equilibrium isotope effects during anaerobic oxidation of methane and microbial sulfate reduction (Holler et al., 2011; Sim et al., 2011; Leavitt et al., 2013; Yoshinaga et al., 2014; Wegener et al., 2021), highlighting the fundamental nature of isotope effects during microbial metabolisms. In addition, we link methane clumped isotope signatures to the energetic landscape, specifically substrate availability, of methane metabolisms. Accordingly, we find that clumped isotopes of methane may serve as a tracer of bioenergetics in the environment. Moreover, we find that different methanogenic pathways exhibit distinct methane clumped isotope compositions. This discovery enables us to trace the pathways of methane production in natural environments.

Our results have important implications for the origin of methane. The presence of near-equilibrium methane in the deep subsurface has been interpreted as either a consequence of slow methanogenesis or the involvement of AOM. Our data suggest that methane exhibiting intra- and inter-species isotope equilibrium essentially indicates the dominance of Mcr-catalyzed isotope exchange, near equilibrium, regardless of whether the net process is methanogenesis or AOM. The Mcr-catalyzed isotopic bond re-ordering drives methane towards equilibrium and is responsible for the widely observed near-equilibrium clumped isotope signatures in substrate-limited anoxic natural environments where microbial methane production and/or oxidation occur.

To directly calculate the ΔG of hydrogenotrophic methanogenesis, it is necessary to measure porewater hydrogen concentrations. The two most commonly used techniques, the headspace equilibration method and the extraction method, may produce systematic discrepancies due to technique-related challenges (Lin et al., 2012). Consequently, isotope clumping in methane molecules can be used to monitor the chemically-available energy in environments hosting methanogenesis, where estimates of hydrogen concentrations are not readily available to calculate

ΔG. Moving forward, future research should extend our sediment slurry incubation experiments to pure-culture methanogens, allowing for a more detailed investigation of the energy controls on methane isotopologue compositions.

Globally, microbial methane emissions into the atmosphere primarily arise from shallow terrestrial environments, with only a small fraction originating from the marine realm (Saunois et al., 2020). The $\Delta^{12}CH_2D_2$ signature in microbial methane substantiates this conclusion. Terrestrial sources exhibit markedly negative $\Delta^{12}CH_2D_2$ values due to kinetic and combinatorial effects, while marine sources have $\Delta^{12}CH_2D_2$ values near equilibrium. Here we show that this difference is a direct consequence of the availability of chemical energy in these respective environments. Because of the very different $\Delta^{12}CH_2D_2$ values of these sources, recent measurements of $\Delta^{12}CH_2D_2$ values in atmospheric methane demonstrate that the primary microbial sources of methane in air must indeed be terrestrial and not marine, alongside contributions from fossil fuel emissions (Haghnegahdar et al., 2023; Sivan et al., 2024). Methane isotopologues thereby provide an additional constraint on global methane budgets.

Through the work in chapter 4, we developed a method to extract sufficient methane from low-concentration sediments for clumped isotope analysis. We modified glass Mason jars with screw plastic lids and airtight silicone gaskets to accommodate the low methane concentrations at the sites. A hole was drilled in the lid to install a blue butyl rubber stopper for gas sampling. In the field, we transferred sediment into each jar, added solid sodium chloride and saturated sodium chloride solution, and then sealed the lids, leaving an air headspace. The jars were shaken vigorously, stored at 20 ºC for one week, and then the headspace gas was transferred to evacuated crimp vials. We initially applied this method to salt marsh sediment, where cryptic methane cycling results in methane concentrations in the range of tens of micromoles per liter (Krause and Treude,

2021). Subsequently, we used this method to extract methane from the sulfate-methane transition zone of marine sediments. The technique has the potential for application in other low-methane environments in the future.

4. Iron-driven anaerobic oxidation of methane

In chapter 5, we shift our attention to the environmental controls on electron acceptors involved in AOM in natural environments. Coastal wetlands have been regarded as a minor source of methane emissions compared to freshwater wetlands, primarily because high sulfate concentrations facilitate AOM. We conducted comprehensive porewater and solid-phase geochemical analyses, along with microbial radiotracer incubations, in hypersaline coastal wetland sediment. We demonstrate that, despite the high concentrations of sulfate, AOM is not associated with sulfate reduction but is instead coupled with the reduction of an unconventional electron acceptor—iron oxides—in subsurface sediment. This finding highlights the role of wetland sediments enriched in iron oxides as an effective sink for the greenhouse gas methane. Fe-dependent AOM in sulfate-free sediments has been extensively studied. Extending these observations into sulfate-rich sediments significantly advances the earlier observations and hypotheses, while suggesting that Fe-AOM is an under-considered sink for methane in wetlands.

Moving forward, future research should better incorporate molecular analyses, such as 16S rRNA sequencing, into the incubation experiments to identify the microorganisms responsible for Fe-AOM. Recent studies showed that methanogens can reverse key reactions of methanogenesis coupled to the reduction of ferric iron and humic substances (Yan et al., 2018; Yan et al., 2023).

Therefore, it would be valuable to investigate whether methanogens can operate in reverse to perform Fe-AOM in natural environments.

Utilizing tracer incubations, porewater profile modeling, and identification of authigenic minerals, the occurrence of Fe-AOM has been documented across various aquatic environments, including both marine and freshwater systems. However, incubation experiments remain the only definitive method to directly confirm the presence of Fe-AOM. Compared to the widely used ^{13}C-tracer method, ^{14}C- and ^{35}S-radiotracer techniques are more sensitive and effective for quantifying microbial turnover rates in short-term incubations, offering greater stability in the measured rates. Therefore, radiotracer techniques are better suited for tracking ex-situ rates and can be used alongside porewater profile modeling to quantify the budget of Fe-AOM.

References

Chadwick G.L., Skennerton C.T., Laso-Pérez R., Leu A.O., Speth D.R., Yu H., Morgan-Lang C., Hatzenpichler R., Goudeau D., Malmstrom R., Brazelton W.J., Woyke T., Hallam S.J., Tyson G.W., Wegener G., Boetius A. and Orphan V.J. (2022) Comparative genomics reveals electron transfer and syntrophic mechanisms differentiating methanotrophic and methanogenic archaea. *PLoS Biol.* **20**, e3001508.

Haghnegahdar M.A., Sun J., Hultquist N., Hamovit N.D., Kitchen N., Eiler J., Ono S., Yarwood S.A., Kaufman A.J., Dickerson R.R., Bouyon A., Magen C. and Farquhar J. (2023) Tracing sources of atmospheric methane using clumped isotopes. *P. Natl. Acad. Sci. USA* **120**, e2305574120.

Holler T., Wegener G., Niemann H., Deusner C., Ferdelman T.G., Boetius A., Brunner B. and Widdel F. (2011) Carbon and sulfur back flux during anaerobic microbial oxidation of methane and coupled sulfate reduction. *P. Natl. Acad. Sci. USA* **108**, E1484-E1490.

Krause S.J.E. and Treude T. (2021) Deciphering cryptic methane cycling: Coupling of methylotrophic methanogenesis and anaerobic oxidation of methane in hypersaline coastal wetland sediment. *Geochim. Cosmochim. Acta* **302**, 160-174.

Leavitt W.D., Halevy I., Bradley A.S. and Johnston D.T. (2013) Influence of sulfate reduction rates on the Phanerozoic sulfur isotope record. *P. Natl. Acad. Sci. USA* **110**, 11244-11249.

Lin Y.-S., Heuer V.B., Goldhammer T., Kellermann M.Y., Zabel M. and Hinrichs K.-U. (2012) Towards constraining H2 concentration in subseafloor sediment: A proposal for combined analysis by two distinct approaches. *Geochim. Cosmochim. Acta* **77**, 186-201.

Milkov A.V. (2011) Worldwide distribution and significance of secondary microbial methane formed during petroleum biodegradation in conventional reservoirs. *Org. Geochem.* **42**, 184-207.

Saunois M., Stavert A.R., Poulter B., Bousquet P., Canadell J.G., Jackson R.B., Raymond P.A., Dlugokencky E.J., Houweling S., Patra P.K., Ciais P., Arora V.K., Bastviken D., Bergamaschi P., Blake D.R., Brailsford G., Bruhwiler L., Carlson K.M., Carrol M., Castaldi S., Chandra N., Crevoisier C., Crill P.M., Covey K., Curry C.L., Etiope G., Frankenberg C., Gedney N., Hegglin M.I., Höglund-Isaksson L., Hugelius G., Ishizawa M., Ito A., Janssens-Maenhout G., Jensen K.M., Joos F., Kleinen T., Krummel P.B., Langenfelds R.L., Laruelle G.G., Liu L., Machida T., Maksyutov S., McDonald K.C., McNorton J., Miller P.A., Melton J.R., Morino I., Müller J., Murguia-Flores F., Naik V., Niwa Y., Noce S., O'Doherty S., Parker R.J., Peng C., Peng S., Peters G.P., Prigent C., Prinn R., Ramonet M., Regnier P., Riley W.J., Rosentreter J.A., Segers A., Simpson I.J., Shi H., Smith S.J., Steele L.P., Thornton B.F., Tian H., Tohjima Y., Tubiello F.N., Tsuruta A., Viovy N., Voulgarakis A., Weber T.S., van Weele M., van der Werf G.R., Weiss R.F., Worthy D., Wunch D., Yin Y., Yoshida Y., Zhang W., Zhang Z., Zhao Y., Zheng B., Zhu Q., Zhu Q. and Zhuang Q. (2020) The Global Methane Budget 2000–2017. *Earth Syst. Sci. Data* **12**, 1561-1623.

Sim M.S., Bosak T. and Ono S. (2011) Large Sulfur Isotope Fractionation Does Not Require Disproportionation. *Science* **333**, 74-77.

Sivan M., Röckmann T., van der Veen C. and Popa M.E. (2024) Extraction, purification, and clumped isotope analysis of methane (Δ13CDH3 and Δ12CD2H2) from sources and the atmosphere. *Atmos. Meas. Tech.* **17**, 2687-2705.

Wegener G., Gropp J., Taubner H., Halevy I. and Elvert M. (2021) Sulfate-dependent reversibility of intracellular reactions explains the opposing isotope effects in the anaerobic oxidation of methane. *Sci. Adv.* **7**, eabe4939.

Yan Z., Du K., Yan Y., Huang R., Zhu F., Yuan X., Wang S. and Ferry J.G. (2023) Respiration-driven methanotrophic growth of diverse marine methanogens. *P. Natl. Acad. Sci. USA* **120**, e2303179120.

Yan Z., Joshi P., Gorski C.A. and Ferry J.G. (2018) A biochemical framework for anaerobic oxidation of methane driven by Fe (III)-dependent respiration. *Nat. commun.* **9**.

Yoshinaga M.Y., Holler T., Goldhammer T., Wegener G., Pohlman J.W., Brunner B., Kuypers M.M.M., Hinrichs K.-U. and Elvert M. (2014) Carbon isotope equilibration during sulphate-limited anaerobic oxidation of methane. *Nat. Geosci.* **7**, 190-194.

Zhou Z., Zhang C.-j., Liu P.-f., Fu L., Laso-Pérez R., Yang L., Bai L.-p., Li J., Yang M., Lin J.-z., Wang W.-d., Wegener G., Li M. and Cheng L. (2022) Non-syntrophic methanogenic hydrocarbon degradation by an archaeal species. *Nature* **601**, 257-262.